Université de Strasbourg

UNIVERSITÉ DE STRASBOURG

École doctorale
Sciences de la terre et de l'environnement | ED 413
Université de Strasbourg

École doctorale no 413 : Sciences de la Terre et Environnement

Institut Terre et Environnement de Strasbourg

THÈSE **présentée par / DISSERTATION presented by :**

Kusnahadi SUSANTO

Soutenue le /defended on : 18 décembre 2024

pour obtenir le grade de / to obtain the grade of :
Docteur de l'Université de Strasbourg / Strasbourg University Doctor

Discipline/Spécialité / Discipline/Specialty : Géophysique

Mesures distribuées de la température du sol pour l'hydrologie proche de la surface : utilisation de la technologie passive des fibres optiques pour déduire l'humidité du sol dans un bassin versant Méditerranéen

THÈSE dirigée par / DISSERTATION supervisor :

Jean-Philippe Malet	Prof. Dr, Université de Strasbourg

RAPPORTEURS :

Thom Bogaard	Prof. Dr, Delft University of Technology, Water Ressources Section
Thomas Lebourg	Prof. Dr, GeoAzur, University Nice-Sophia-Antipolis, France

AUTRES MEMBRES DU JURY / OTHER MEMBERS OF THE JURY :

Renaud Toussaint	Prof. Dr, Université de Strasbourg, EOST, Strasbourg, France
Catherine Bertrand	Prof. Dr, Université de Franche-Comté, LCE, Besançon

---

INVITÉS (le cas échéant) / INVITED MEMBERS (if applicable):

Julien Gance	Dr, IRIS-Instruments, Orléans, France

Avertissement au lecteur / Warning to the reader

Licence attribuée par l'auteur / Licence attributed by the author

[*Veillez à ne conserver que la licence qui vous convient* / Make sure you only keep the licence that suits you best]

https://creativecommons.org/licenses/?lang=fr-FR

Kusnahadi SUSANTO

Mesures distribuées de la température du sol pour l'hydrologie proche de la surface : utilisation de la technologie passive des fibres optiques pour déduire l'humidité du sol dans un bassin versant Méditerranéen

Résumé

La connaissance de la dynamique de la teneur en eau de la surface du sol fournit des informations précieuses sur l'interaction sol-eau et les changements dans les eaux souterraines. CeLe variabilité peut être mesurée par des méthodes directes et indirectes. CeLe thèse traite de la relation entre l'observation de la température et la teneur en eau du sol. L'observation de la température est utilisée comme méthode indirecte pour comprendre l'hydrologie et la thermo-physique du sol lors de l'écoulement de l'eau. Afin d'améliorer les connaissances sur l'interaction entre l'eau et le sol en surface peu profonde, la technologie DTS à fibre optique a été utilisée pour mesurer la température du sol à long terme. On s'aLend à ce que ceLe stratégie permeLe de recueillir des informations hydrologiques plus détaillées. Trois types de sol ont été considérés dans ceLe expérience sur le terrain : la forêt de colluvions, les buissons ou prairies de colluvions et les marnes noires.

Mots clés :
Passive DTS, soil moisture, thermal diffusivity, Hydrus

Abstract

Knowledge of soil surface water content dynamics provides valuable information on soil-water interaction and changes in groundwater. This variability can be measured by direct and indirect methods. This thesis deals with the relationship between temperature observation and soil water content. Temperature observation is used as an indirect method to understand the hydrology and thermo-physics of soil water flow. To improve knowledge of the interaction between water and soil in the shallow surface, fiber-optic DTS technology was used to measure long-term soil temperature. This strategy is expected to provide more detailed hydrological information. Three soil types were considered in this field experiment : colluvial forest, colluvial shrubland or grassland, and black marl.

Keywords :
Passive DTS, soil moisture, thermal diffusivity, Hydrus

This work is dedicated:

To my late father, who always supported me by carrying the burdens, and whose memory lives on.

To my mother, whose love, resilience, and constant prayers have been my foundation.

To my beloved wife, whose patience, love, and strength made this possible, and whose belief never failed me.

And to my dear children, whose smiles make every struggle worthwhile.

Acknowledgments

This thesis would not have been possible without the contribution and support of colleagues from *Ecole et Observatories des Sciences de la Terre* (EOST) and other institutions. I would like to acknowledge the support of many people below.

First, I would like to express my sincere gratitude to my Ph.D promotor, Dr. Jean-Philippe Malet, for his professional guidance, advice, enormous encouragement, and continuous support of this research progress in this challenging subject. His support and energy have been invaluable to me in performing the various stages of this thesis. This thesis would not have been possible without his guidance. Second, I would like to thank Dr. Julien Gance for helping to start this research project and allowing me to access his datasets. Third, I extend my profound gratitude to the late Prof. Dr. Bernard Y Tumbelaka for his support of my international collaboration at the beginning.

I would like to extend my gratitude as well to Dr. Xavier Chavanne (IPGP-Université Paris Diderot) and Dr. Vincent Marc (EMMAH, Université d'Avignon) for the fruitful discussion and for being the reviewers of my thesis. I also thank another jury member, Assoc Prof. Dr. Thom Bogaard (Technische Universiteit Delft, Netherlands), for agreeing to assess my work.

To achieve the success of this thesis, I received generous support from several programs and institutes: the research project HYDROSLIDE and the extensive infrastructure project CRITEX, funded by the French Research Agency (ANR). Support of Indonesia Endowment Fund for Education (LPDP), Ministry of Finance of the Republic of Indonesia, for providing the funding that allowed me to undertake this Ph.D. program. We should highlight the support from Universitas Padjadjaran (Indonesia) in realizing this Ph.D. program.

I also would like to thank my colleagues from the IRSTEA team for allowing me to access their research facility. Thank Sebastien Klotz for the unforgettable Jurassic-past traveling and Firmin Fontaine for helping me provide the best network connection and data measurement.

Throughout my campus and field life, everyone who accompanied me supported me. I want to thank the Dynamic active group team for making me feel at home in the institute and the field. Thanks to Floriane Provost, Pierrick Bornemann, Clément Hibert, Gilbert Ferhat, Myriam Lajaunie, Odin Marc. Thanks to Mathilde Desrues for our conversations. I will remember your daily greeting and sneezing. Thanks to the good first adaptation in the institute: André Stumpf, David Michéa, and Mohammed Benbachir. A big thank you to Alexandre Remaître for his musical sound and conversations. I will keep perfect memories of those days.

I thank all Indonesian PhD students, Dwinarto Sukamto, Titin A Nengsih, Gianto Gianto, and Siti Aisyah Rahman, for their kind help and great discussions. It has been an enjoyable and unforgettable working and learning experience with all of them.

I also want to highlight my gratitude for all support from my beloved family and parents, without which my effort would have been more difficult. All great things worth having require great sacrifices worth giving.

Finally, I must acknowledge Husneni Mukhtar for her great daily support and for making things easier from any perspective. I cannot wait for our travels, crossing the cold and warmth of the world in the future away.

This page intentionally left blank.

Résumé Long

La connaissance de la dynamique de la teneur en eau de la surface du sol fournit des informations précieuses sur l'interaction sol-eau et les changements dans les eaux souterraines. Cette variabilité peut être mesurée par des méthodes directes et indirectes. Cette thèse traite de la relation entre l'observation de la température et la teneur en eau du sol. L'observation de la température est utilisée comme méthode indirecte pour comprendre l'hydrologie et la thermo-physique du sol lors de l'écoulement de l'eau. Afin d'améliorer les connaissances sur l'interaction entre l'eau et le sol en surface peu profonde, la technologie DTS à fibre optique a été utilisée pour mesurer la température du sol à long terme. On s'attend à ce que cette stratégie permette de recueillir des informations hydrologiques plus détaillées. Trois types de sol ont été considérés dans cette expérience sur le terrain : la forêt de colluvions, les buissons ou prairies de colluvions et les marnes noires. Cette attente soulève la question suivante quant aux objectifs de recherche énoncés dans le **Chapitre 1** :

- Comment surveiller la teneur en eau du sol et quantifier les propriétés hydrologiques du sol à l'aide de méthodes directes et indirectes ?
- Quelles informations sur les types de sol des arbres peut-on déduire de la distribution spatiale et temporelle de l'observation de la température ?
- Les ensembles de données de température peuvent-ils être utilisés pour calculer indirectement les propriétés hydrauliques du sol couplées à d'autres variables ?
- Peut-on comprendre le comportement historique du sol en se basant sur des simulations et des prédictions du passé ?

Le **Chapitre 2** présente une synthèse de la littérature sur l'application de la détection de température distribuée par fibre optique (FODTS) dans les études hydrologiques, ainsi que les concepts de base de la technologie distribuée. De plus, des techniques de traitement des données sont également exposées pour améliorer la sensibilité des mesures. La correction et l'étalonnage de la température sont décrits pour éviter les erreurs de mesure résultant des interférences internes des câbles à fibres optiques et des perturbations environnementales externes, telles que le rayonnement solaire. En effet, la longueur du câble à fibre optique entraîne une atténuation de l'énergie lumineuse le long de la fibre, qui a une incidence sur l'amplitude de la rétrodiffusion Raman, utilisée comme détecteur de température.

Le décalage de fréquence de la lumière n'est pas un problème comme pour la rétrodiffusion Brillouin, mais l'atténuation peut perturber la mesure de température car la rétrodiffusion Raman utilise le décalage d'amplitude de la lumière. De plus, le rayonnement solaire incident doit être quantifié pour corriger la température du câble à fibre optique installé à la surface du sol. L'installation à la surface du sol a été conçue pour mesurer la température de l'interface entre l'air et le sol, qui est ensuite utilisée comme condition limite supérieure dans la simulation. Cependant, le traitement des données techniques doit être effectué selon les procédures standard de mesure de température utilisant la fibre optique DTS.

Le **Chapitre 3** porte sur l'observation sur le terrain, la collecte de données et les méthodes. Le site de Draix est un bassin versant intéressant. Situé dans les Alpes, Draix se trouve entre le système climatique alpin et méditerranéen qui a été étudié pendant plusieurs décennies par de nombreux géoscientifiques. Le cadre géologique de Draix est généralement montagneux et dominé par la formation de marnes noires appelée "badland" qui est fortement affectée par les conditions climatiques. En conséquence, le sol subit des processus

d'érosion périglaciaire qui contribuent à la topographie et à la morphologie. Dans ce chapitre, l'installation permanente de la fibre optique DTS et des autres instruments de mesure des paramètres hydrologiques et météorologiques est décrite. On s'attend à ce que l'installation de Draix techno soit en mesure de fournir des mesures à haute résolution et de démontrer l'importance de la résolution de l'échantillonnage sur le site. La collecte des données a été effectuée avec une très haute résolution. La température du sol a été mesurée par fibre optique DTS toutes les 6 minutes sur 354 mètres de longueur, puis la station météorologique a fonctionné avec un échantillonnage de données toutes les 5 minutes. La configuration de Draix techno a été équipée d'un réseau de communication établi qui permet la télédétection et la surveillance. Par la suite, l'ensemble des données observées a été traité pour estimer les propriétés hydrologiques et thermophysiques et pour réaliser la simulation historique. L'estimation des paramètres a été réalisée à l'aide du logiciel de simulation Hydrus 1D et de l'inversion non linéaire développée.

De plus, une discussion détaillée est présentée dans les trois articles de recherche. Le premier article, présenté au **Chapitre 4**. L'article montre la stratégie d'amélioration de la précision de l'estimation de la teneur en eau volumétrique (VWC) à long terme à l'aide d'une détection de température distribuée par fibre optique chauffée passivement (FO-DTS). Nous améliorons la précision du calcul de la diffusivité thermique du sol en utilisant une méthode combinant la discrétisation numérique et le traitement du signal pour effectuer une procédure de validation. Après simulation et examen, cette stratégie est pratique à utiliser dans les expériences de chauffage passif utilisant des sources de chaleur diurnes, où des données fiables de diffusivité thermique et de VWC peuvent être obtenues sans sources d'application actives et avec des ajustements appropriés pour augmenter ses performances. **Chapitre 5**, décrit la mise en place technique de l'observation permanente à haute résolution de la température à l'aide du FO-DTS pour surveiller les changements des eaux du sol dans un bassin versant méditerranéen. La température à long terme et la teneur en eau du sol calculées dans la série chronologique sont également analysées. La conclusion de ce chapitre décrit que les séries chronologiques de la teneur en eau du sol, de la température et des précipitations calculées sont assez cohérentes. L'étude des cycles hydrologiques saisonniers montre les différences de comportement de l'eau dans le sol pour chaque type de sol. Ce résultat préliminaire pourrait donner un aperçu des influences saisonnières sur l'étude du site Draix.

Le deuxième article, rédigé au **Chapitre 6**, rend compte de la modélisation directe de l'humidité du sol dans la région méditerranéenne. La mesure indirecte de la teneur en eau du sol nécessite une méthode d'inversion pour estimer les paramètres optimaux. Dans ce cas, la pression d'entrée d'air, la distribution de la taille des pores et la conductivité hydraulique ont été optimisées et utilisées en modélisation directe pour simuler la teneur en eau du sol à Draix. Les propriétés hydrologiques du sol sont très spécifiques pour chaque type de sol. Il ne peut donc pas être généralisé en raison des différences dans la teneur en argile et d'autres facteurs. Il ne peut être généralisé que pour la modélisation directe à long terme des changements dans l'eau du sol pour les types de sol spécifiques. Par la suite, la conclusion de cet article est que ces simulations expérimentales montrent clairement que l'observation de la température en tant que paramètre de substitution influe considérablement sur le modèle direct à long terme des changements dans l'eau du sol.

Le troisième article est le **Chapitre 7**. Il présente une simulation de la teneur en eau souterraine dans le temps. Le comportement historique à long terme du sol est prédit par des modèles hydrologiques directs. Les bases de données des précipitations et de la température de l'air sont utilisées comme données d'entrée principales pour la simulation. Cependant, l'historique de la température du sol n'est pas disponible car aucune mesure n'a été effectuée dans le passé. Par conséquent, la simulation 1D-Hydrus est utilisée pour caractériser le système de sol. Ceci est fait pendant la période d'étalonnage, puis testé pendant la période de validation avant

d'être appliqué pour établir les températures historiques du sol. Plusieurs analyses statistiques ont été utilisées pour tester cette méthode. De plus, les températures historiques du sol peuvent être prédites à partir des mesures de la température de l'air. Les résultats de la simulation montrent que les précipitations ont un impact direct sur la série chronologique dynamique des changements des eaux souterraines. Le décalage temporel de l'écoulement des eaux souterraines et la propagation de la température à une certaine profondeur sont discutés. Bien que les résultats simulés de la teneur en eau souterraine correspondent bien aux événements pluvieux et aux mesures de la nappe phréatique, les résultats peuvent ne pas être généralisables en raison de certaines simplifications du modèle.

Enfin, cette thèse se termine par une discussion générale au **Chapitre 8**, qui traite de l'observation de la température à long terme concernant la simulation de l'humidité du sol. Quelques propriétés physiques sont décrites pour clarifier les trois types de sol étudiés. Le **Chapitre 9** est consacré à la conclusion et à la perspective de la recherche, ce qui conclut le manuscrit de la thèse.

Contents

List of Figures

List of Tables

Chapter 1: Introduction

1.1 Problem definition

Natural hazards have a significant impact on society. Numerous disasters have occurred due to hydro-geomorphological processes such as landslides, rockfalls, snow avalanches, debris flows, and riverbank collapses. Increasing our understanding of environmental processes is necessary to comprehend their causes and assess risks. Numerous studies have documented environmental processes; however, much of this knowledge remains challenging to acquire due to the hydrological complexity of factors such as soil-water interaction, erosion, and soil alteration. The complexity of environmental processes compels us to conduct detailed research on soil-water interaction using environmental and soil temperature data.

The hydro-geomorphology process greatly influences the natural hazard, especially in a critical zone. In 2001, The National Council for Research proposed the concept of the critical zone in the US to denote the skin of the earth. The researchers have been encouraged to develop a holistic understanding of the future. Since then, with extreme climate changes, critical zone science has become a global initiative in numerous observatories such as America, Europe, China, Australia, and the Mediterranean (Figure 1.1). In critical zone research, soil water content monitoring is essential for various environmental studies. However, assessing soil water content is more complex, especially in clayey soils, because it can be non-linear.

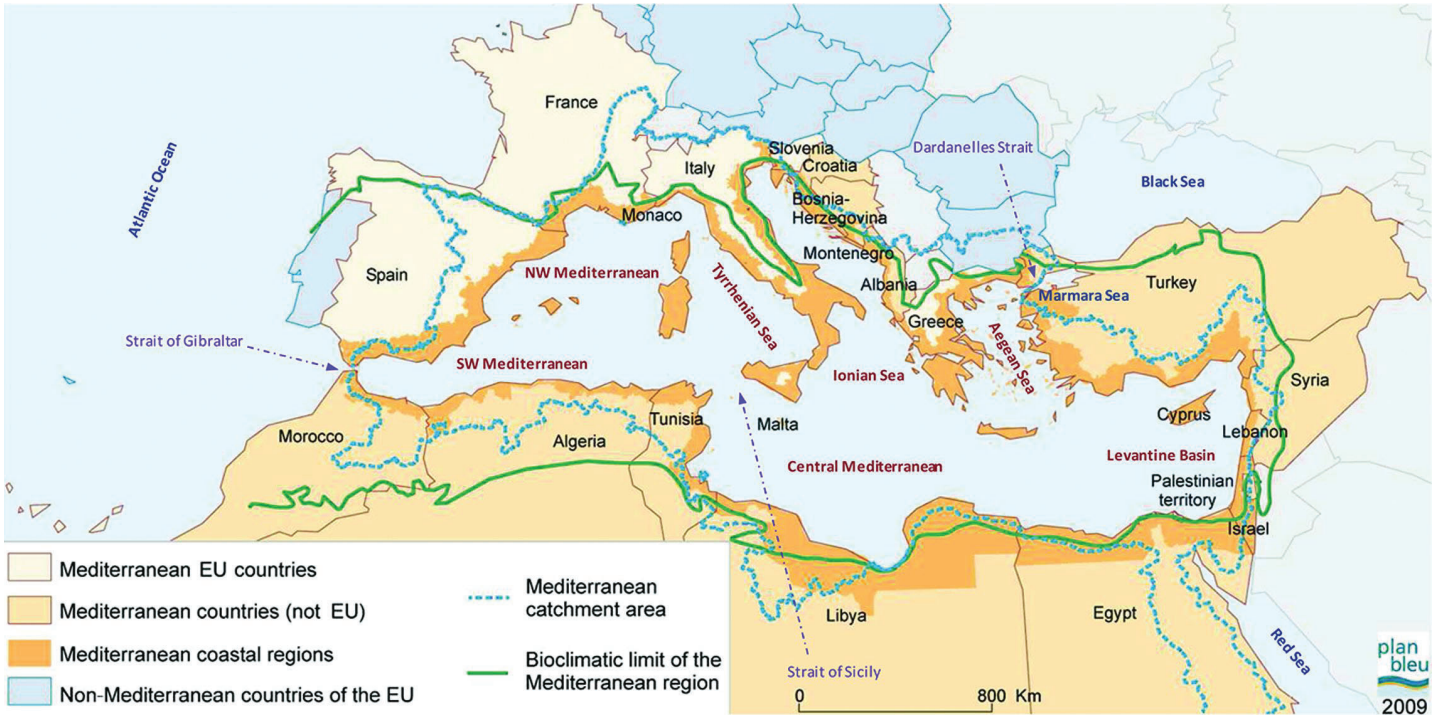

Figure 1.1 The Mediterranean areas are located around the sub-basins of the Mediterranean Sea (Castro-Jiménez et al., 2013).

On the other hand, the climate system has a solid relationship with the soil moisture situation. The impact of climate change could prompt the soil into a very severe drought situation. The lack of groundwater causes the death of plants and turns the ground into a giant CO2 trap due to the cessation of photosynthesis (Green et al., 2019). Figure 1.2 presents the schematic of slope hydrology with a drought area as a carbon trap when the plants die. In the Mediterranean, soil moisture experiences high fluctuations due to temperature, wind, and vegetation coverage. A long-term assessment of soil moisture in the Mediterranean area is needed. In the short term, changes in soil moisture affect drought intensity, water runoff, and erosion patterns. For a long time, this situation has triggered more severe global climate change and has affected the stability of the ecosystem and changes in biodiversity (Seneviratne et al., 2010).

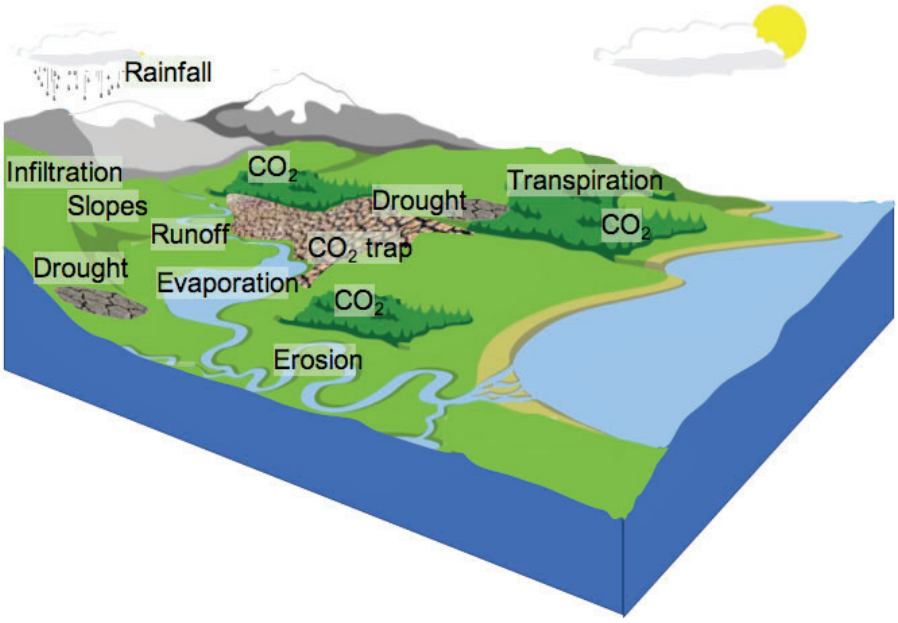

Figure 1.2 Schematic representation of slope hydrology with arid and wet areas. The drought area becomes a carbon trap when plants die.

In recent years, technology and strategies have actively dedicated themselves to protecting human life against natural risks. Many physical properties in the shallow surface, from the atmospheric to lithospheric layers, are studied to identify and predict the possibility of hazards. In this concept, physical properties do not change except if an external factor changes them. In this context, temperature changes and water behavior in the soil play some of the most crucial roles in the environmental change mechanism. Additionally, geomorphology and lithology are other aspects of shallow disasters. Slope stability is often the critical factor combined with the increasing ground level.

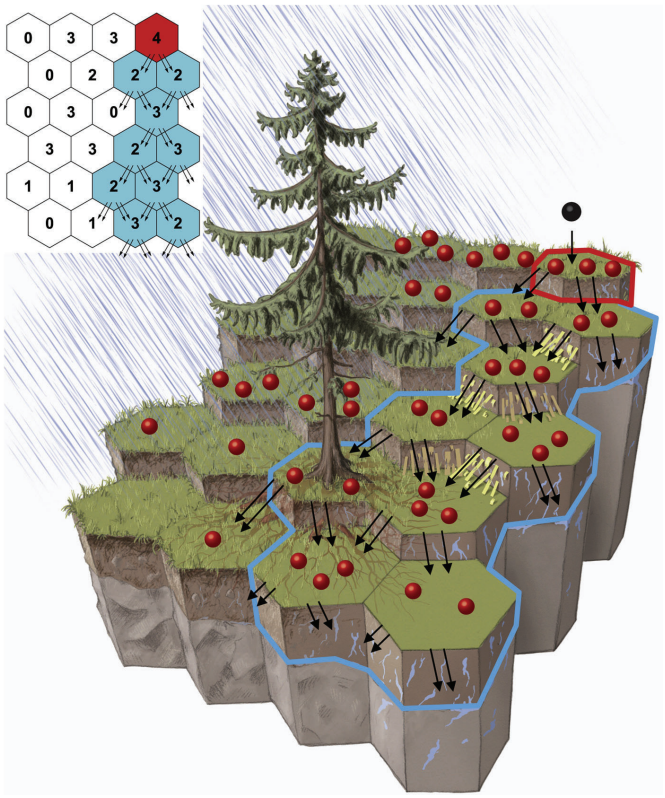

Figure 1.3 The illustration shows water flowing as a hydromechanical trigger. Water infiltration, represented by the black sphere, acts as a local perturbation and initiates a chain reaction in the hillslope, causing a load in the downslope direction (Lehmann and Or, 2012).

The analogy of a breaking soil system is perfectly illustrated in Figure 1.3. Scientists have made significant progress in understanding the physical properties that act on the shallow surface during the 20th century, thanks to the development of soil sensing instrumentation, multiplication of instruments for more expansive subject areas, and continuous effort in data processing, diffusion, and interpretation. In soil science and research, tracing water infiltration and monitoring soil water content in the vadose zone is essential for various hydrological, agronomical, ecological, and environmental studies. Researchers have developed direct and indirect methods to recognize water content associated with water-soil interaction. However, the vast area as a spatial factor and fluctuation of infiltration and evaporation as a time factor forces us to develop high spatial and temporal frequency observations.

Currently, the limitation of the direct method is its implementation as a single-point measurement. The wider the subject area, the more soil moisture sensors are needed. This condition provides excellent motivation for developing an indirect method for multiple-point measurement implementation. The indirect method utilizes another soil property with a physical relationship with soil moisture. In this case, temperature propagation inside the soil becomes critical to identifying moisture. Some inversion and modeling techniques solve the physical connection between temperature and soil water content.

1.2 Research objectives

Researchers have conducted numerous studies to understand preferential water flow in many soils and to recognize the influence of soil water distribution concerning environmental studies. Regarding the critical zone, hydrology studies can be viewed from the perspective of soil temperature and humidity observation (see Figure 1.4). We expect the developed method to monitor water content fluctuations in the shallow surface with high spatial and temporal resolution. The water content fluctuation is affected by infiltration, evaporation, and attenuation percolation towards the groundwater system, which can change quickly in the Mediterranean area. Moreover, the developed method is expected to present not only a time series of temperature and calculated soil moisture but also to obtain typical hydraulic and thermal properties at the field scale.

In this work, we conducted observations to develop an indirect soil moisture measurement based on permanent long-term temperature measurements. Soil thermal properties were used as proxy parameters to obtain soil moisture content. Therefore, this method can simultaneously monitor temperature and soil moisture. We applied this method to clay-rich soils in general. We analyzed soil moisture and temperature in three soil types in the Mediterranean areas: soil colluvium forest, soil colluvium bushes, and black marls. These three soil types have unique water-soil interactions (Wildung, Garlan,d and Buschbom, 1975; Descroix and Gautier, 2002; Weiler and Naef, 2003).

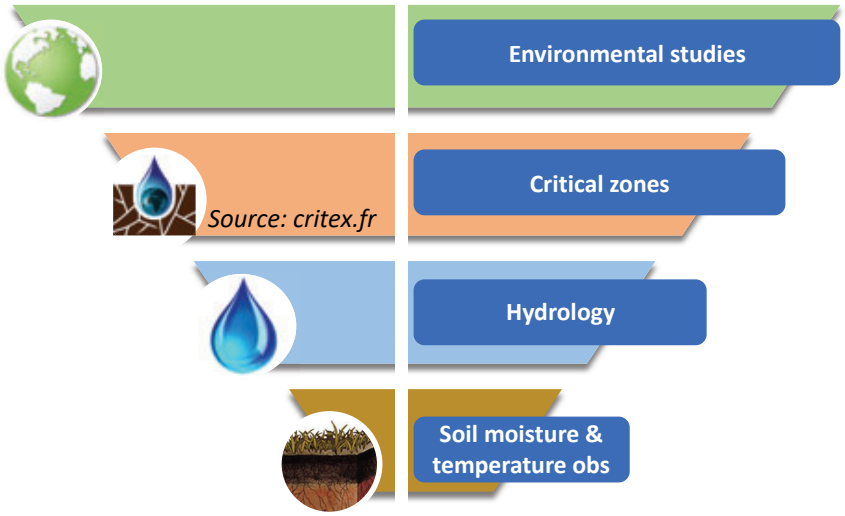

Figure 1.4 The research structure demonstrates the relationship between global environmental studies and technologies for observing groundwater.

Principally, the temperature propagation in the soil is influenced by soil diffusivity, which is the ratio of soil heat conductivity and capacity that depends on pore and water content. Consequently, temperature measurement provides a double advantage: soil thermal information and calculated water content. The soil water content changes the specific heat capacity of the soil porosity, and the relation between both variables is linear (Campbell and Norman, 1998). Nevertheless, the link between calculated water content and temperature is complicated. Hence, the general soil moisture assessment in clay-rich soil is more difficult because the hydrological response can be non-linear. On the other hand, accurate soil temperature measurement is needed to obtain the calculated soil moisture. Some calibration and correction should be made to reduce measurement errors in the actual soil temperature, which is a particular challenge in this thesis.

This thesis aims to monitor temperature and soil moisture variability and identify and quantify three soil types of hydrological properties using direct and indirect methods. The research questions are as follows:

1. How can we monitor soil moisture and quantify soil hydrological properties based on indirect methods in long-term observations?
2. What information on the three soil types can we deduce from the spatial and temporal distribution of temperature observations by using a combination of innovative sensors?
3. Can the temperature datasets be used for indirectly calculating the soil hydraulic properties coupled with other variables, and can they be used for hydrological model forecasting?

To answer the research questions, we installed permanent hydrological and meteorological observation instruments in the field to document the long-term hydrological situation. The study site is at the Draix catchment, representing different environments, including dense vegetation and uncovered land areas. The instruments are designed to work long-term with high spatial and temporal resolutions. The primary device used is a fiber optic distributed sensor buried by incision. The fiber optic cable was spread out through the three soil types: black marls, colluvium under the forest, and colluvium bushes. This thesis contributes to developing an indirect method that enables low-cost field-scale hydrological observation.

1.3 Thesis outline

The structure of this thesis is composed of three main parts divided into a total of seven chapters. The first part consists of three chapters introducing this thesis and state of the art. **Chapter 1** provides a general introduction and outline. **Chapter 2** presents a detailed description of the state-of-the-art temperature

observation for hydrology studies. It discusses numerous methods for understanding environmental processes based on temperature measurement, such as electrical and optical measurement strategies.

Additionally, the chapter describes the theoretical background and application information of Fiber Optic Distributed Temperature Sensors (FODTS) to provide a general knowledge of distributed temperature sensor technology. Furthermore, calibration and correction methods are also described. **Chapter 3** presents a detailed description of the Draix techno setup. It describes the location, geology, morphology, and climate information of the Draix Bléone catchment, part of the Mediterranean area in southern France. The chapter also covers instrumentation deployment and data collection. Long-term data collection is not only on soil temperature by FODTS but also includes meteorological and hydrological datasets to complete standard geohydrological research.

The second part is adapted from an article focused on the methodologies and analysis of hydrological observations at Draix Bléone. It is divided into four chapters. **Chapter 4** introduces a technique called "Passively Heated Fiber Optic Distributed Temperature Sensing for Long-Term Soil Moisture Observation". Our approach offers a practical solution for conducting passive heating experiments using diurnal heat sources, which enables the collection of accurate thermal diffusivity and VWC data without the need for active application sources. With the appropriate adjustments, the performance of this technique can be improved. **Chapter 5** presents permanent temperature observations using FODTS to monitor soil water change in the Mediterranean areas from January 2016 to April 20ea. The combination of meteorological and hydrological data in characterizing soil can help understand environmental processes over an extended observation period that highlights significant changes in the Mediterranean area. Furthermore, this chapter discusses the statistical spatio-temporal analysis of temperature and calculated soil moisture concerning hydrological cycles such as seasonal wetting-drying processes and winter-storm conditions. **Chapter 6** focuses on parameter inversion to perform the direct model using Hydrus 1D. The inversion model of hydrology observation consisting of hydraulic and thermal properties estimates the soil hydraulic parameters that can be used to forecast soil water changes. Hydrus simulation was run as the inversion strategy. The time series and water retention curve fitting approaches were used. **Chapter 7** discusses historical simulations with limited observation data to predict hydrologic behavior in past sessions. The hydrological and thermophysical properties are assumed to be constant over time to simplify the simulation. Unavailable databases are generated by a mathematical algorithm and examined in the calibration and validation period.

The third part consists of **Chapter 8**, which provides a general discussion of the results of the long-term temperature observations concerning soil moisture simulation. In terms of this, the hydraulic and thermophysical properties are emphasized as essential parameters in slope hydrology. Furthermore, the historical soil moisture simulation is analyzed and compared with the current situation. The cross-correlation shows that water infiltration in the past was longer than in the current situation. In summary, **Chapter 9** of this thesis concludes with general conclusions and perspectives on using long-term temperature observations to monitor soil moisture. Additionally, the chapter proposes using FODTS to observe shallow groundwater and offers recommendations for future enhancements.

Chapter 2: Soil Moisture And Temperature Observation For Hydrology Studies

2.1 The soil moisture observation strategy on slope hydrology

Many strategies have already been developed for measuring soil moisture (see Table 2.1). The direct method has advantages in terms of accuracy; however, it cannot be used for high-resolution time-series observations. On the other hand, the indirect method uses electrical or thermo-physics sensor principles, which are suitable for long-term and high-resolution observations. The main disadvantage of the indirect method is the complicated correction and calibration that must be done dynamically over time. Electrical-based sensors use permittivity, capacitance, and resistivity around the rod for soil moisture measurement. For instance, Hymenet is an electrical-based sensor that uses permittivity and conductivity simultaneously (Chavanne and Frangi, 2017). In terms of thermo-physics-based sensors, the method uses thermal diffusivity for indirect soil moisture measurement. PT107 and fiber optic DTS are commonly used sensors for soil temperature observations. PT107 works as a pointed temperature sensor, while fiber optic DTS works as a distributed one.

Table 2.1 Several direct and indirect methods were applied to measure soil moisture.

Types	Technologies	Measurement	Volume coverage
Direct method	Volume mass ratio	Gravimetric	Depends on diameter soil sampling
Indirect method "Electrical based"	Frequency Domain Reflectometry (FDR)	Permittivity on oscillation frequency around the probe	± 8 cm^3
	Combination of time Domain Transmission (TDT) and Reflectometry (TDR)	permittivity on the speed of propagation along a buried transmission	± 10 cm^3
	Neutron moisture gauges	Neutron scattering	15 cm
	Soil resistivity	Resistance	Depends on configuration
	Galvanic cell	voltage based, water acts as an electrolyte.	1 cm between the electrodes
Indirect method "Thermo-physics based"	Fiber optic DTS	Thermal diffusivity	Distributed, wide field

This work focuses on the application of thermo-physics sensors. In hydrology studies, the environmental temperature usually refers to the soil's air and surface layer temperatures being studied for water movement phenomena. The sun's radiation is a heat source, heating the soil in diurnal cycles. Temperature alone does not provide enough information about prevailing environmental processes unless combined with other meteorological observations, such as precipitation or soil moisture. Additionally, the temperature indirectly relates to soil moisture through soil thermal diffusivity calculations, which can be used to expand hydrology studies. The amplitude, phase, and waveform of diurnal temperature in the sub-surface layer are crucial for evaluating the balance of surface energy and mass transfer, such as water movement (An et al., 2016). Field observations of thermal conduction also make it possible to monitor soil moisture based on the relationship

between thermal diffusivity and thermal conductivity (Adams, Watts, and Mason, 1976). The heat carried by groundwater can also be used to identify surface water flow infiltration in hydrological studies.

2.1.1 Direct soil moisture observation

The direct method measures the amount of water in the soil pores to determine how wet the soil is. However, this method only applies to the specific position in the soil where the measurement was taken. Most people use the gravimetric method, which involves taking a sample of soil, weighing it before and after drying it, and then figuring out how much water it has. This method is the oldest way to determine how much water is in the soil, but it is still widely used. Technically, the soil sample is taken using a core sampler or a tube auger with a known volume. The amount of water in the soil sample is estimated by drying it in an oven (as shown in Eq 2.1). The volumetric moisture content can also be calculated from the moisture content on a dry mass basis.

$$\theta_m(\%) = \frac{M_s - M_d}{M_d} \times 100 \qquad \text{Eq 2.1}$$

Where θ_m is the soil moisture on a mass basis, M_s is the soil mass immediately after sampling (i.e., before any water is lost), and M_d is the mass of the soil after drying in the oven. If the volume of the sample V_s is known, then the volumetric water content in $m^3\ m^{-3}$ can be calculated by converting the mass of water lost on drying $M_s - M_d$ to a volume and assuming the density of water to be 1 Mg m^{-3}.

2.1.2 Indirect soil moisture observation

The indirect method estimates the amount of water in the soil through its properties. The most used instruments for assessing soil moisture through indirect methods are the neutron probe, frequency domain reflectometry (FDR), time domain transmission-reflectometry (TD-T/R), galvanic, and soil resistivity apparatuses (as shown in Table 2.1).

Time and frequency-domain reflectometry is a new device developed to measure soil moisture. These devices use two parallel rods or stiff wires inserted into the soil. The electromagnetic pulse or wave generated by the instrument is transmitted along the rods. The rate at which the wave of energy is transmitted into the soil and reflected on the soil surface is related to the average water content of the soil. This indirect method estimates the apparent dielectric permittivity of the soil by measuring the travel time a step-voltage pulse takes to propagate the energy along the probe and back (Raffelli et al., 2017).

The neutron moisture meter quickly and continuously estimates soil moisture without disturbing the soil. This type of sensor can scan approximately 15 cm in diameter around the probe in wet conditions and 50 cm in dry situations. A two-year study was conducted at a grazing pasture site in central Saskatchewan, Canada, to identify soil moisture using a downhole neutron probe (Peterson, Helgason, and Ireson, 2016). The probe contains a fast neutron source, a mixture of radium and beryllium or americium and beryllium, released from the probe and scattered into the soil. The speed of the neutron decreases when the particles encounter the hydrogen atoms of the water nuclei. The slow neutron speed is directly proportional to the count of water molecules.

Furthermore, soil resistivity sensors and galvanic cell sensors use electrical tension to measure the water in the soil. The electrical resistance of soil water is affected by substances dissolved in the water. Hence, soil resistivity is highly affected by salinity. In addition, the galvanic method works as a potentiometric sensor in which the redox energies of aluminum and polyaniline are exploited to design the sensor. The sensing

mechanism is identical to a battery-type discharge reaction, in which the polyaniline redox energy changes from the conducting to the non-conducting state with a resulting voltage shift in the presence of soil moisture (Gaikwad et al., 2015). The above discussion is regarding the indirect method based on electrical principles. The indirect method based on thermo-physical principles is discussed in subsections 2.2 and 2.3.

2.1.3 Non-linear inversion for hydraulic parameter estimation

The inversion method determines the soil's hydraulic properties, especially for clayey soil that is not entirely wet. It can be obtained by using long-term temperature and soil moisture observations. This observation aims to understand the hydrological behavior of unsaturated clayey soil from a thermal perspective. This section describes inversion strategies for estimating soil thermal and hydraulic parameters step-by-step. The inversion methods emphasize the minimum root mean squared error (RMSE) of the objective function, such as the Johansen model (1975) for soil thermal properties and the Van Genuchten model (1976) for soil hydraulic properties.

The hydraulic properties of soil are vital to understanding water flow in unsaturated soil. Accurate measurement of the pressure head and soil moisture enables the estimation of the Van Genuchten parameters through an inverse procedure (Schaap and Van Genuchten, 2006). The purpose of this section is to describe the inversion technique for estimating the air entry pressure and pore size distribution from the highly non-linear Van Genuchten equation. The objective function of the Van Genuchten equation is expressed in Eq 2.2.

$$\theta(h) = \theta_r + \frac{\theta_s - \theta_r}{[1 + |\alpha h|^n]^{1-1/n}} \qquad \text{Eq 2.2}$$

The symbol $\theta(h)$ is the soil moisture, h is the water potential, θ_s and θ_r are the saturated and residual soil water content, α and n are air entry pressure and pore size distribution, respectively. A modification to Eq 2.2 is needed to find a solution. Non-linear inversion with least-squares regression approximation is applied to estimate α and n. Similar to the previous method for diffusivity calculation, the error modification should be zero based on the estimated parameters. By modifying the soil moisture to effective soil moisture (Eq 2.3), we can obtain Eq 2.4.

$$\Theta_i = \frac{\theta_s - \theta_r}{\theta(h) - \theta_r} \qquad \text{Eq 2.3}$$

$$\Theta_i = [1 + |\alpha h|^n]^{1-1/n} \qquad \text{Eq 2.4}$$

The logarithmic transformation that is applied to Eq 2.4 produces a simple solution. It can be modified to become a linear equation.

$$\log \Theta_i = \left[1 - \frac{1}{n}\right] \log[1 + |\alpha h|^n] \qquad \text{Eq 2.5}$$

$$= (n-1)\log(\alpha h_i)$$

$$\left(\frac{1}{n-1}\right) \log \Theta_i = \log(\alpha) + \log(h_i) \qquad \text{Eq 2.6}$$

Considering that some variables are modified, as in Eq 2.7.

$$a_1 = \frac{1}{n-1} \qquad \text{Eq 2.7}$$

$$a_0 = \log(\alpha)$$

$$x_i = \log \Theta_i = \log\left[\frac{\theta_s - \theta_r}{\theta(h) - \theta_r}\right]$$

$$y_i = \log(h_i)$$

Finally, the least-squares regression equation is obtained as shown in Eq 2.8, where a_1 represents the modified pore size distribution, a_0 represents the logarithmic value of air entry pressure, and x_i and y_i represent the effective soil moisture and water potential on a logarithmic scale. To account for the existence of misfits, the residual error e_i is added as a prediction error.

$$y_i = a_1 x_i - a_0 + e_i \qquad \text{Eq 2.8}$$

Hereafter, the error minimization function of the least squares regression is applied to estimate the air entry pressure and pore size distribution, similar to the estimation of soil thermal parameters. This step uses the observed soil water potential and moisture as inputs. The number of available datasets, m, should be sufficient to reduce the root mean square of this strategy.

$$E(a_0, a_1) = \sum [y_i - a_1 x_i - a_0]^2 \qquad \text{Eq 2.9}$$

The error function should have the minimum value. It can be obtained by calculating the differential error for each optimized parameter, shown in Eq 2.10 and Eq 2.11.

$$\frac{\partial E(a_0, a_1)}{\partial a_0} = 0, \qquad \frac{\partial E(a_0, a_1)}{\partial a_1} = 0 \qquad \text{Eq 2.10}$$

$$\frac{\partial E(a_0, a_1)}{\partial a_0} = \frac{\partial}{\partial \lambda_s} \sum [y_i - a_1 x_i - a_0]^2 = 0$$

$$\frac{\partial E(a_0, a_1)}{\partial a_1} = \frac{\partial}{\partial \lambda_s} \sum [y_i - a_1 x_i - a_0]^2 = 0 \qquad \text{Eq 2.11}$$

In the end, the non-linear inversion method can be expressed by the inverse matrix solution $M = [G^t G]^{-1} G^t D$, where G is a Kernel matrix, M is the estimated Van Genuchten parameters, and D is a matrix that contains the observed data of soil water potential and moisture. Referring to Eq Eq 2.9 and Eq 2.11, the solution can be arranged as shown in Eq 2.12.

$$\begin{bmatrix} m & \Sigma x_i \\ \Sigma x_i & \Sigma x_i^2 \end{bmatrix} \begin{bmatrix} a_0 \\ a_1 \end{bmatrix} = \begin{bmatrix} \Sigma y_i \\ \Sigma x_i y_i \end{bmatrix} \qquad \text{Eq 2.12}$$

The root means squared error (RMSE) describes the goodness of fit between observed and calculated variables. The RMSE analyzes soil thermal and hydraulic parameter estimation (Eq 2.13).

$$\text{RMSE} = \sqrt{\frac{\Sigma (Y_i - Y_o)^2}{m}} \qquad \text{Eq 2.13}$$

2.2 Pointed temperature measurement

The temperature probe sensor is widely used to measure soil temperature. This method uses the electrical properties as a proxy parameter on the electrical conductor rod junction. The thermoelectric effect accurately converts the temperature differences into electric voltage. However, the application of this method needs more simultaneous multi-point observation in a wide area. The sensor probes must be spread for every

single temperature point observation using too much cable, making it a more complex application. An example of such a sensor is the Hymenet probe, a soil moisture sensor complete with a temperature sensor developed by IPGP (Chavanne and Frangi, 2017; Chavanne and Jean-Pierre, 2014). This sensor comprises five soil moisture sensors and a temperature sensor on the rod device for several depths (see Figure 2.1). The device simultaneously measures the vertical profile of soil moisture and temperature.

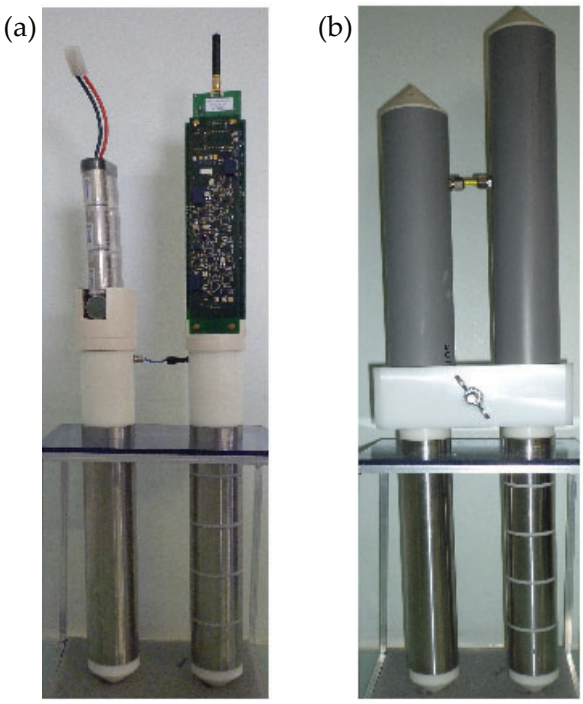

Figure 2.1 Photograph of the probe with a five-channel sensor for measuring soil moisture and temperature based on electrical properties (Chavanne and Jean-Pierre, 2014).

2.3 Distributed temperature measurement

Over several decades, numerous studies have proposed using optical fiber for communication transmission and as a sensor (Ciocca et al., 2012; Sayde et al., 2010; Steele-Dunne et al., 2010; Suárez et al., 2011; van de Giesen et al., 2012a). The high spatiotemporal resolution of temperature measurement has been the subject of numerous investigations using fiber-optic distributed sensors. The advantage of light pulses propagating and interacting inside the optical fiber contributes to the sensor technology. Physical properties such as temperature and strain distribution can be revealed along the fiber in small areas, broad areas, and multiple kilometers into the subsurface.

One advantage of fiber optic distributed sensors is the reduced cable wires needed to observe temperature over a wide area. In addition, the fiber optic method reduces power consumption during observation. The pulse generator can provide light excitation for the fiber optic with less power than electrical excitation on a conductor cable of the same length. At an experimental scale, fiber optic distributed sensing has demonstrated great success in locating and quantifying distributed ground-surface water interaction (Mamer and Lowry, 2013).

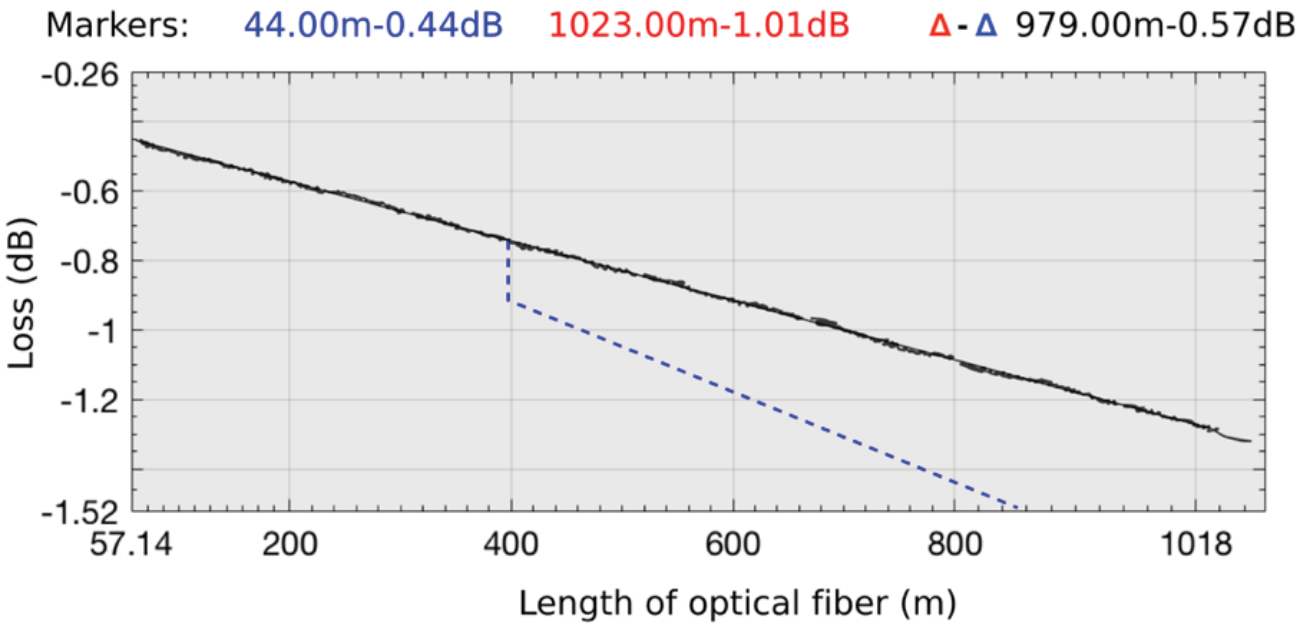

Figure 2.2 The typical signal power loss graph over distance along the optical fiber. The blue dashed line is the loss of signal power after connector or splice at 400 m, i.e., fiber optic cable Linear Pro Series DTS-N4386B, which was manufactured by AP Sensing Advance Photonic, Germany (AP Sensing Linear Pro DTS-N4386B, 2013).

Several agronomical, natural resource, hazard, and environmental studies (Dorleus et al., 2009; Liu et al., 2008; Marasigan and Olivar, 2015; Paulsson et al., 2013; Rizkalla, 1997; Sayde et al., 2010; Tyler et al., 2009) have looked at how fiber optics can be used. The wide range of parameters that can be measured with fiber optic distributed sensing makes it very useful for research indoors and outdoors under any right conditions. As an ecological application, Krause et al. (2013) showed how fiber optics can get accurate information about how temperature patterns change over time in woodlands (Krause et al., 2013).

In environmental studies, fiber-optic applications measure distributed temperature and strain (Nikles et al., 2004; Suárez et al., 2011; Weng et al., 2011). The fiber optic sensor is easy to deploy as a distributed sensor. The fiber cable works as a transmission medium and array sensor along the cable. In addition, the fiber optic cable has high-speed information transmission because it works using photonic propagation inside the cable. The speed of light propagating inside the fiber ranges between 1.7×10^{8} and 2.0×10^{8} ms^{-1}. Unlike electrical transmission, which has resistance along the cable, fiber optic transmission depends on the refractive index of the core and cladding inside. Briefly, fiber cables are thin glass wires with a thickness of about 100 μm. The waveguide theorem is applied to this technology. The series of reflections inside the fiber cable maintain the ability of the light to travel along the fiber even if the fiber is bent quite sharply. Therefore, it can be used for long cable applications with low-cost energy light resources. The maximum signal loss is around 1.52 dB for fiber cables of 1000 m in length (Figure 2.2).

Table 2.2 The fiber cable types for commercial DTS (Schenato, 2017)

Type / fiber type	Operating wavelength	Spatial resolution	Sensing range	Temperature resolution	Acquisition time
Short-range/MMF	904 nm	7.5 m	2km	0.4 °C	12 s
		n/a	3km	2°C	70 s
	975 nm	2m	4km	0.1 °C (*)	600 s
	680 nm	n/a	2km	1°C (*)	60 s
Middle-range/MMF	1064 nm	n/a	5km	2°C	120 s
		n/a	12 km	2°C (*)	600 s
		1.4 m	5km	0.28 °C (*)	10 s
		1.4 m	8km	1°C (*)	10 s
		1.4 m	10 km	2.25 °C (*)	10 s
		0.35 m	5km	0.2 °C	180 s
Long-range/MMF	1550 nm	5m 1	15 km	1°C	600 s
		0m	30 km	1.5 °C (*)	600 s
		2m	30 km	2.75 °C (*)	10 s
		n/a	10 km	1.2 °C (*)	60 s
		n/a	32 km	6.0 °C (*)	300 s
		n/a	16 km	1.8 °C (*)	180 s
Raman OFDR/MMF	980 nm	1m		0.80 °C	200 s
		1.5 m	4 km	0.29 °C	158 s
		3m		0.88 °C	27 s
	1480 nm	3m	10 km	3.0 °C	60s
Raman OFDR/SMF	2 m	2m		1.9 °C	300 s
Pulse Compression Raman/MMF	1.5 m	1.5 m	4 km	0.15 °C	600 s
			8 km	0.65 °C	600 s

(*) Resolution at the maximum specified range

Fiber-optic sensors provide a very promising alternative for the longest space measurement. Fiber optics has a robust system against any disturbances during long-term measurements because it is insensitive to electromagnetic interference (EMI) around the cable. Fiber is beneficial for long-term monitoring and observation (J. S. Selker et al., 2006). Some commercial interrogators achieve specific characterization for the particular fiber cable purposes. Table 2.2 presents the performance of the fiber cable obtained after proper calibration (Schenato, 2017).

In any application, the limit for fiber optics to work properly is a temperature below ~700 °K. In some extraordinary experiments, fiber optics can be used intermittently up to 1300 °K (Cheng, 2014). As a distributed temperature sensor, fiber optics works with a potential temperature resolution below 0.1 °C (van de Giesen et al., 2012a) and a temporal and spatial resolution of 1–60 s and 0.5 m, respectively (Suárez et al., 2011; Susanto et al., 2017), for cables up to 30 km (Suárez et al., 2011; Ukil et al., 2012). On the other hand, the achievement of strain measurement is also demonstrated by the highest accuracy of ±1.5 με (Zhou et al., 2013; Monsberger, Woschitz, and Hayden, 2016) and the highest precision of 1 μm m^{-1}. However, most fiber optic sensing technologies demonstrate fairly good distributed measurement along the cable in their application (Nikles et al., 2004).

The basic idea behind fiber optics is that light is scattered inside the fiber cable. Scattering happens when outside disturbances change the way the core's materials behave. Changes in temperature and strain can cause outside disturbances and scatter light because of how light and changes in the crystalline structure interact. There are three types of scattering inside the fiber: Rayleigh, which is elastic scattering, and Raman and Brillouin, which are inelastic scattering (Suárez et al., 2011).

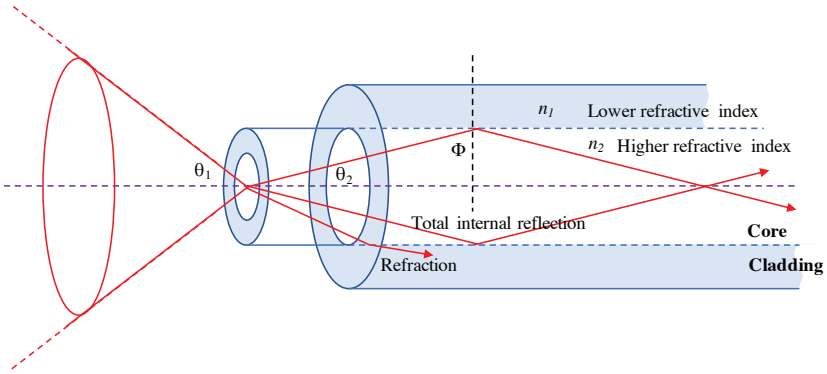

Figure 2.3 Internal propagation of light in a cross-section of a fiber optic. The total internal reflection becomes a waveguide inside the fiber. The core and cladding glasses have different refractive indexes coated by the outer jacket.

The molecules of wire glass, which serve as the core of the fiber for thermal sensing purposes, will theoretically vibrate due to thermal excitation, resulting in the scattering of light by the photon and electron of the electron molecule (Hausner et al., 2011; Koudelka et al., 2010; Ukil et al., 2012). Numerous studies have aimed to produce high-quality fiberglass using various materials, expecting to produce fiber cables with very low attenuation. Fiber cables commonly use the silicon dioxide (SiO_2) molecular structure as a silica-based glass molecular structure, with an optical fiber attenuation of only 0.15 dB Km^{-1} (Rogers, 1999). Other studies have investigated using different materials, such as Barium titanate ($BaTiO_3$), based on perovskite structure, which Kauffmann, Kokanyan, and Fontana (2019) examined.

In addition, impurities and density fluctuations contribute to the light returned in the backscattering process (Ciocca, Lunati, Van de Giesen, and Marc B. Parlange, 2012). The source light generator emits the laser pulse into the fiber cable, which consists of a glass core surrounded by cladding and coating (the jacket). Most laser generators have a wavelength range of 850–1300 nm, and the permissible power is around 20 mW. Both the core and cladding have different refractive indices. The refractive index of the glass core (n_1) is higher than that of the cladding (n_2) to achieve a total internal reflection of light through the glass core, which is influenced by the incident angle and critical angle (Φ) (see Figure 2.3). Total internal reflection guides the light for propagating along the fiber cable.

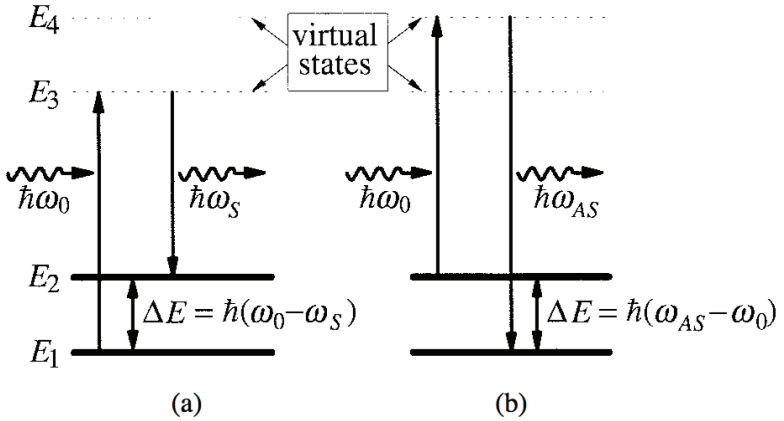

Figure 2.4 The schematic diagram of Rayleigh and Raman scattering. (a) Stokes scattering and (b) anti-Stokes scattering (Farahani and Gogolla, 1999).

Predictive frequencies and intensity shifting result from the interaction between light and molecular vibrations to measure temperature along the fiber. This phenomenon is called Raman and Brillouin backscattering. The frequency shifted lower than the incident light is called the backscattered Stokes signal (ω_S). In contrast, the frequency shifted higher than the incident light signal is called the backscattered anti-Stokes

(ω_{AS}) (Farahani and Gogolla, 1999). The angular frequency of the incident light is denoted as $\omega_0 = 2\pi f_0$, where $\hbar$ is Planck's constant and f_0 is the incident light frequency (see Figure 2.4). In the anti-Stokes frequency range, the intensity of Raman backscattering and the frequency of Brillouin backscattering strongly depend on the temperature of SiO_2. In contrast, the frequency and intensity of Stokes backscattering have weak temperature influences (Figure 2.5). The energy changes during the backscattering processes, as expressed by Kauffmann, Kokanyan, and Fontana (2019), are shown in Eq 2.14.

$$\hbar\omega_{BS} = \hbar\omega_i \mp \hbar\omega_p \qquad \text{Eq 2.14}$$

where ω_{BS}, ω_i, and ω_p are the frequencies of the scattered photon, incident photon, and phonon, respectively. In temperature measurement applications, the light source DTS control unit emits an initial pulse of light with a specific intensity and collects the backscattered light. The ratio of intensities between the Stokes and Anti-Stokes signals can be used to determine the fiber's temperature at a specific scattering point. Eq 2.15 and Eq 2.16 present the intensities of Raman Anti-Stokes and Stokes backscattering in fiber cables, as Rogers (1999) expressed. The DTS instrument collects the signal intensity during temperature measurements along the fiber.

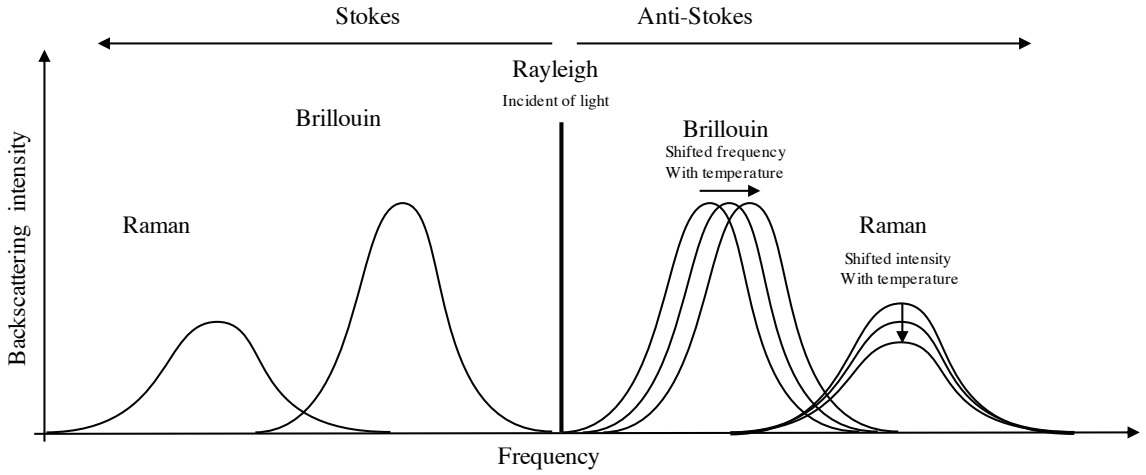

Figure 2.5 The shifting frequency and intensity of Rayleigh, Raman, and Brillouin backscattering on the Stokes and Anti-Stokes ranges indicate the system's state.

$$I_{AS}(x) = I_0 \exp(-\alpha_0 x)\exp(-\alpha_{AS} x)\wp_{AS}\Gamma_{AS} \qquad \text{Eq 2.15}$$

$$I_S(x) = I_0 \exp(-\alpha_0 x)\exp(-\alpha_S x)\wp_S\Gamma_S \qquad \text{Eq 2.16}$$

where x is the length of the fiber cable, $I_s(x)$ and $I_{As}(x)$ are the Raman Stokes and anti-Stokes signal intensities, respectively. I_0 is the initial light intensity emitted by the light source in the main DTS controller. At the same time, α_0, α_S, and α_{AS} are the coefficients of cable attenuation that affect the emitted light along the fiber, Stokes, and anti-Stokes backscattered signals, respectively. $\wp_S$ and $\wp_{AS}$ are the distribution probabilities of Bose-Einstein of phonons, and Γ_S and Γ_{AS} are the capture coefficients of the Stokes and anti-Stokes backscattering signals (Suárez et al., 2011).

The emitted light from DTS would encounter resistance in the form of internal optical resistance, which is known as attenuation along the fiber. The longer the fiber cable, the higher the attenuation. The optical attenuation within the fiber follows an exponential function concerning its length, x. Additionally, the attenuation is affected by the natural resonance of the molecule. The type of fiber cable used also influences the

interaction between light and material (Kauffmann et al., 2019; Rogers, 1999). The attenuation characteristic is influenced by specific materials that modify the absorption spectrum (refer to Figure 2.6). The absorption of material due to attenuation along the fiber leads to energy depletion from the forward-propagating light (Rogers, 1999).

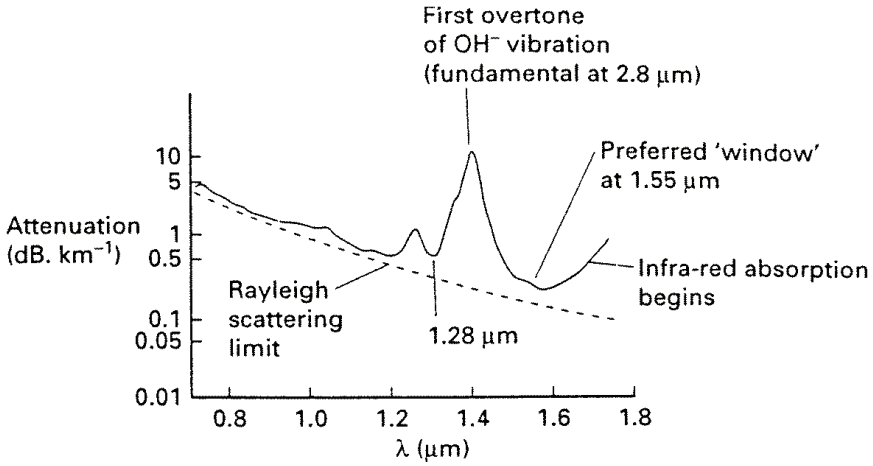

Figure 2.6 The absorption spectrum of silica fiber (Rogers, 1999).

Because of attenuation, the ratio of Stokes to Anti-Stokes intensity should be fixed and calibrated. Many solutions have been made to deal with this problem, such as the double-ended configuration and using a reference bath in the calibration process. However, the manufacturer provides internal calibration (refer to Figure 2.9d). Eq 2.17 calculates the temperature along the entire fiber optic, including the backscattering intensity ratio, attenuation factor, and calibration parameter (van de Giesen et al., 2012a).

$$T(x,t) = \frac{\gamma}{\ln[R(x,t)] + C(t) - \int \Delta\alpha(x')dx'} \qquad \text{Eq 2.17}$$

In the equation, $T(x)$ represents the temperature along the entire fiber optic cable in Kelvin, γ is dependent on the distribution of quantum state in Kelvin, R is the ratio of backscattering intensity between Stokes and Anti-Stokes, x is the distance, $\Delta\alpha(x')$ is the differential attenuation of the backscattering Stokes and Anti-Stokes along the fiber cable at different (x_0), and $C(t)$ is a calibration parameter that depends on the frequency of the incident light, which may vary over time. Dynamic calibration is required to obtain accurate temperature measurements periodically. The ambient and heated baths installed at the beginning and end of the fiber cable can be used as a reference for dynamic calibration. The temperature of the reference baths is maintained under constant temperature conditions. However, if the temperature of the baths fluctuates slightly, corrections can still be calculated periodically using the temperature contrast between the ambient and heated baths as a guideline.

Moreover, to determine the location of scattering occurrence along the fiber cable, the propagation time of light must be known. The optical time domain reflectometry (OTDR) method is the most common way to determine where scattering occurs. After backscattering in space, the OTDR measures how long light bounces forward and backward. The distance can be estimated using the two-way travel time of light in a specific refractive index of the fiber (Eq 2.18). A light pulse generator emits light with a specified pulse width, then transmits it through the fiber cable and reflects it due to internal backscattering. The two-way travel time of light provides an opportunity to estimate the distance of local scattering. The pulse width of light affects the spatial resolution of the temperature reading.

Moreover, to determine the location of scattering occurrence along the fiber cable, the propagation time of light must be known. The optical time domain reflectometry (OTDR) method is the most common way to determine where scattering occurs. After backscattering in space, the OTDR measures how long light bounces forward and backward. The distance can be estimated using the two-way travel time of light in a specific refractive index of the fiber (Eq 2.18). A light pulse generator emits light with a specified pulse width, then transmits it through the fiber cable and reflects it due to internal backscattering. The two-way travel time of light provides an opportunity to estimate the distance of local scattering. The pulse width of light affects the spatial resolution of the temperature reading.

$$x(t) = \frac{c\,t}{2\,n} \qquad \text{Eq 2.18}$$

where x represents the distance in meters (m), t is the two-way time light travels in seconds (s), c is the speed of light in a vacuum in meters per second (m/s), and n is the refractive index of the fiberglass core (Yilmaz and Karlik, 2006). To obtain various locations of temperature anomalies along the fiber, the laser pulse width of light becomes an essential factor. Commercially available distributed temperature instruments typically use a 10 to 20-nanosecond laser pulse width of the light.

2.3.1 The basic of Fiber optic distributed sensing (FODTS)

A distributed temperature sensor device comprises a light pump generator, an optical splitter as a light deflector, a photodetector as a light reflection receiver, a signal analyzer, and a fiber cable. For the FODTS backscattering probing method to work, the light pulse must go to the fiber cable and then back to the light detector. The shifted light intensity indicates the ratio of Raman scattering as a function of temperature and distance. The spontaneous Raman backscattering distributed temperature sensor requires a high-intensity light pulse to induce the Stokes and Anti-Stokes signal reflections. The reflected Stokes and Anti-Stokes signals are returned through the same fiber cables and deflected by the optical splitter towards the light photodetector. In an OTDR system, almost 97% of the returned light has the same optical frequencies as the source (Bolognini and Hartog, 2013).

Regarding backscattering reflection, the Stokes and Anti-Stokes signals have different attenuations (Bao and Chen, 2012). Figure 2.7 shows a schematic of FODTS, the spectrum of light scattering, the difference in intensity of backscattering between Stokes and Anti-Stokes, and the temperature profile along the fiber cables. Attenuation along the fiber cable may occur over distance and time. Not detecting it could lead to errors in the temperature profiles (Fernandez Fernandez et al., 2005), making it difficult to interpret the results. Furthermore, in many applications, it has been found that the aging effect can influence the background transmission properties of fiber optic cables in very long installations (Stoddart et al., 2005).

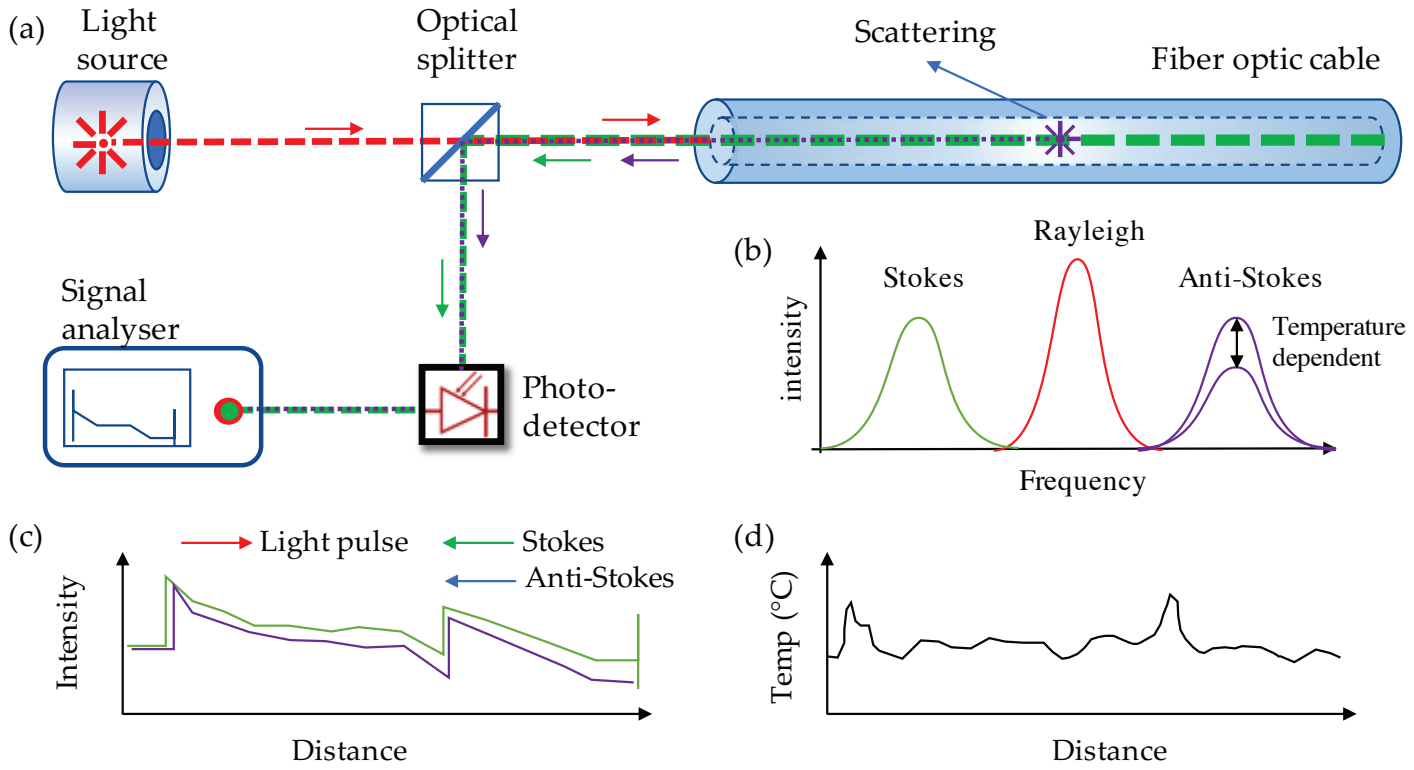

Figure 2.7 Typical fiber optic distributed sensing diagram and responses. (a) Schematic of FODTS work, (b) Backscattering signal corresponds to Rayleigh, Stokes, and Anti-Stokes, (c) The intensity of backscattering Stokes and Anti-stokes along the fiber cable, and (d) Temperature signal as a ratio of Stokes and Anti-Stokes. Attenuation also takes effect.

In Raman scattering, the light spectrum is considered to determine the Stokes Raman band and the Anti-Stokes Raman band. Before the signal analyzer can calculate the temperature profile along the fiber, it should be able to identify the spectrum of the signal components. Based on Figure 2.7b, the Stokes signal has a longer wavelength than the photon entering the fiber, but the Anti-Stokes signal is vice versa. Moreover, the intensity of the Stokes signal is insensitive to temperature changes, but the intensity of the Anti-Stokes signal is temperature-dependent (Bolognini and Hartog, 2013; Koudelka et al., 2010; Schenato, 2017).

$$R(x,T) = \frac{I_{AS}(x,T)}{I_S(x,T)} = C(t)\exp\left(-\frac{\hbar\,\Delta\omega}{k\,T}\right)\exp(\Delta\alpha x) \qquad \text{Eq 2.19}$$

The dependence of Raman scattering intensity on temperature refers to the ratio of Eq 2.15 and Eq 2.16. The Bose-Einstein probability of phonons, $\wp_{AS}$ and $\wp_S$, depends on temperature and frequency shifting, representing the difference in molecular energy states that drive the Raman scattering (Eq 2.14). The ratio of the capture coefficients, Γ_{AS} and Γ_S, is considered a calibration parameter $C(t)$ that varies over time (see Eq 2.19).

2.3.2 Dynamic calibration and Aerial radiation correction

In Raman scattering thermometry, the ratio of Stokes to Anti-Stokes is not only a temperature function but also influenced by cable attenuation. There are two types of attenuation: one due to material selection and the other due to step losses. Hausner and Kobs (2016) developed a simple correction to solve step losses. They used the constant slope of the natural log of the Stokes and Anti-Stokes. The undamaged fiber cable has a linear ratio of Stokes and Anti-Stokes with distance and uniform temperature along the fiber cable (see Figure 2.8a and b). However, step losses create a discontinuity and an offset. Nevertheless, the constant slope can be applied to

the entire fiber cable, starting from the far side of the step losses to correct the ratio of Stokes and Anti-Stokes signals.

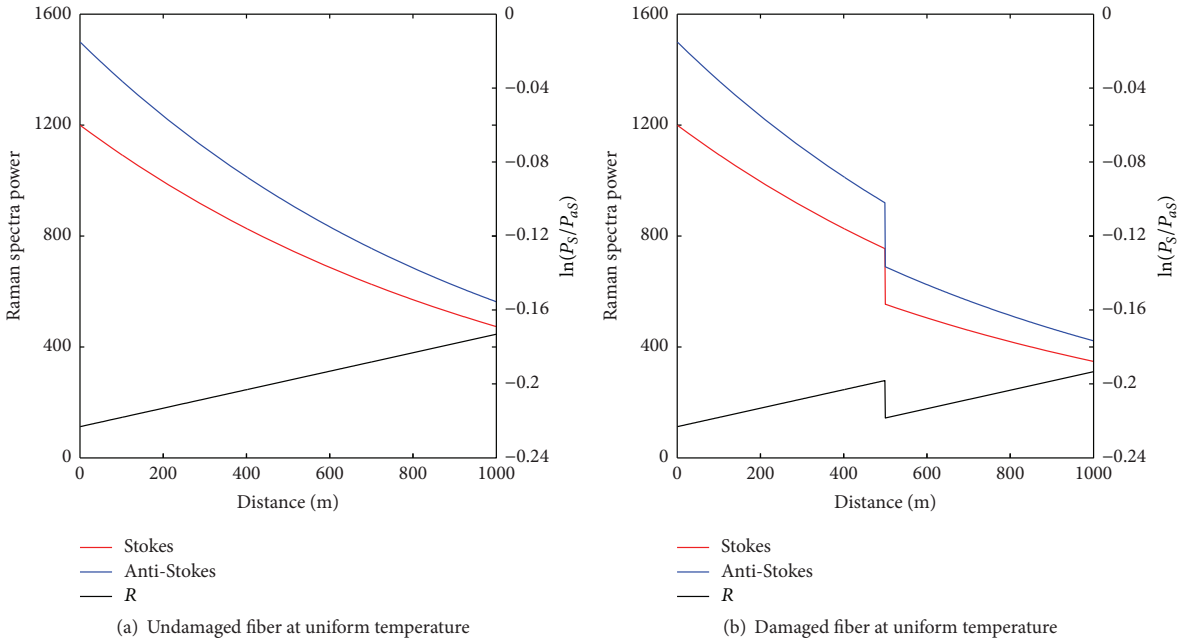

Figure 2.8 The situation of the fiber cable is shown by the ratio of signal backscattering between Stokes and Anti-Stokes signals when the temperature is the same: (a) undamaged fiber cable, (b) damaged fiber cable (Hausner and Kobs, 2016).

As mentioned above, fiber-optic distributed sensors have an excellent advantage for temperature measurement with high accuracy and precision. However, the temperature profile error along the fiber can be highly disruptive. Most commercial FODTS have already set up internal calibration on the DTS main instrument using internal references in a static operating condition (see Figure 2.9a and b). However, external calibration is often used in many environmental applications to prevent the magnitude of the offset during measurement because of the dynamic operating conditions of environmental processes (see Figure 2.9c and d). The accuracy of the distributed temperature sensor in a static operating condition is ± 0.2°C.

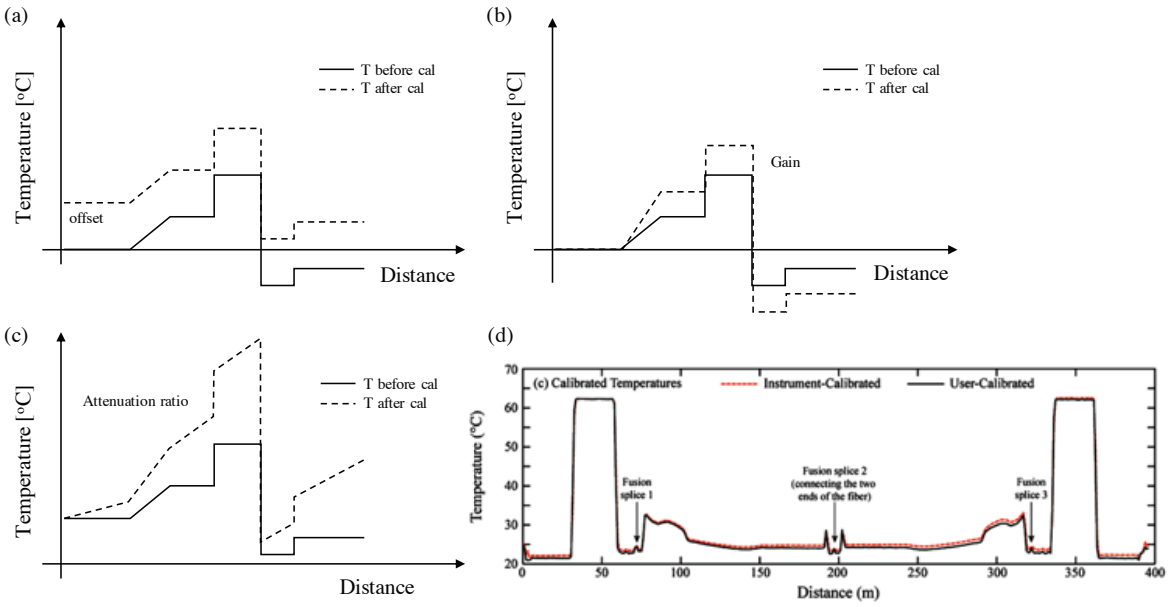

Figure 2.9 The fiber cable calibration process is affected by offset, gain, and attenuation influences. (a) offset. (b) Gain. (c) Attenuation ratio. (d), i.e., different temperatures between the manufacturer's internal and external user calibrations (Hausner et al., 2011).

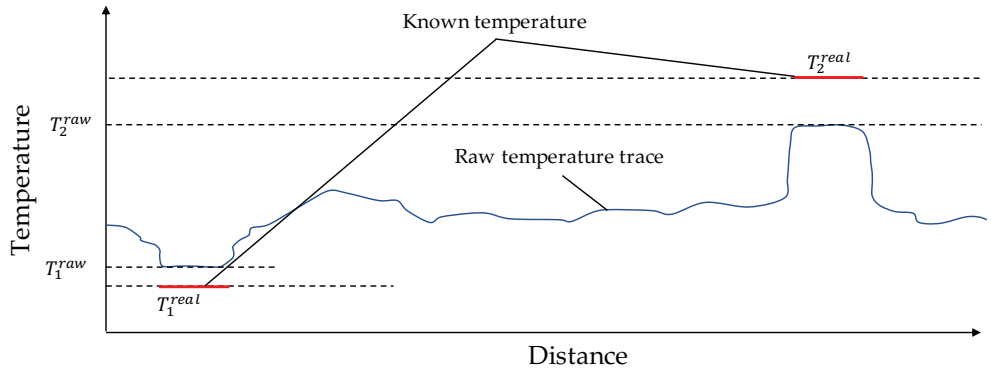

Figure 2.10 The known temperature in two places is used for gain and offset correction on the raw temperature trace.

According to the programming guide from AP Sensing DTS, temperature correction consists of temperature gain and offset correction. The strategy uses the trace and absolute temperatures measured by an independent temperature sensor at two locations (see Figure 2.10). The gain and offset correction can be calculated according to Eq 2.20 through Eq 2.22 from these known temperatures as absolute independent temperatures. Nevertheless, the correction method only considers the temperature difference and neglects the distance between the two locations traversed by the fiber cable.

$$G_a = \frac{T_2^{real} - T_1^{real}}{T_2^{raw} - T_1^{raw}} \qquad \text{Eq 2.20}$$

$$O_f = \frac{\left(T_1^{real} \cdot T_2^{raw}\right) - \left(T_1^{raw} \cdot T_2^{real}\right)}{T_2^{raw} - T_1^{raw}} \qquad \text{Eq 2.21}$$

$$T_{corr} = O_f + T_{raw} \cdot G_a \qquad \text{Eq 2.22}$$

where G_a is the temperature gain correction, T_1^{real} and T_2^{real} are the known temperatures at two different locations, T_1^{raw} and T_2^{raw} are the raw temperature traces simultaneously positioned as T_1^{real} and T_2^{real}, respectively. O_f is the temperature offset correction, and T_{raw} and T_{corr} are the raw temperature trace and corrected temperature along the fiber cable.

A different temperature ΔT as a function of distance x is proposed to elaborate on the temperature drift along the fiber cable. The basic calculation of the method uses linear temperature between two places like the above. However, it is added with a different function temperature between the measured trace and the absolute independent temperature (see Figure 2.11a). The slope of different temperatures $\Delta T(x)$ along the fiber has negative and positive possibilities (see Figure 2.11b). The complete temperature correction is presented in Eq 2.23 through Eq 2.25.

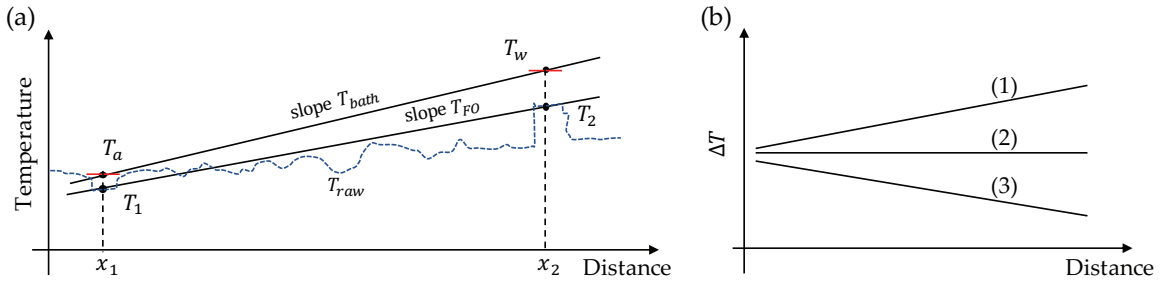

Figure 2.11 Temperature drift correction along the fiber cable. (a) the difference in temperature between ambient and warm baths for correcting raw temperature. (b) the slope of possibility along the fiber.

$$\Delta T(x) = T_{bath}(x) - T_{FO}(x) \quad \text{Eq 2.23}$$

$$\Delta T = \left[\frac{T_w - T_a}{x_2 - x_1}(x - x_1) + T_a\right] - \left[\frac{T_2 - T_1}{x_2 - x_1}(x - x_1) + T_{a1}\right] \quad \text{Eq 2.24}$$

$$T_{corr}(x) = T_{raw}(x) + \Delta T(x) \quad \text{Eq 2.25}$$

where x_1 and x_2 are ambient and warm bath reference positions, respectively. $\Delta T(x)$ is the slope temperature difference between the real and raw temperatures on the baths. T_a and T_w are the absolute temperatures of the ambient and warm baths, respectively. T_1 and T_2 are the raw temperatures of the ambient and warm baths, measured by the fiber optic, respectively.

Two typical configurations, single-ended and double-ended calibration, are widely used in many applications using Raman scattering deployment based on fiber cable deployment. Up to three known temperature zones are required for external calibration strategies to improve precision. The single-ended and duplexed single-ended configurations use two and three known temperature calibration zones, respectively. Furthermore, the double-ended calibration is sufficient with only two known temperature calibration zones (Schenato, 2017). Generally, the known temperature zones consist of heated and ambient baths filled with water and maintained during the observation. Technically, the temperature reference becomes a calibration point in a precise position, from which the calibration parameter can be obtained. Sometimes, the ambient zone uses the water temperature in natural situations as a reference to reduce the experiment's cost (V.F. Bense et al., 2016).

Dynamic calibration

Aside from using temperature references, two calibration methods have been developed based on light direction strategies. Single-ended and double-ended configurations are commonly used in fiber optic distributed temperature sensing applications. The single-ended configuration uses one light direction for calibration, while the double-ended configuration uses two (Hausner et al., 2011; Schenato, 2017; van de Giesen et al., 2012a).

In a simple test, a single-ended installation usually assumes that the properties of light transmission along the fiber cable are the same all the way along. It refers to a one-way light direction on the entire fiber path. Hence, single-ended calibration only needs a single light launcher. The simple single-ended configuration allows for high precision in a short-range fiber cable. The third temperature reference should be located at the end of the cable, far from the DTS main instrument (see Figure 2.12a). Often, the end of the fiber cable is placed in a difficult-to-reach location, such as downhole hydrology observation (V.F. Bense et al., 2016). Otherwise, an independent temperature sensor is attached to the end of the fiber cable or fusion splice as the third temperature reference (Hausner et al., 2011; Schenato et al., 2017). Another way is a duplex single-ended configuration, which returns the end of the fiber cable to the known temperature zones that are the same as the beginning of the fiber. Hence, the fiber cable must be twice as long as the other configuration (see Figure 2.12b). However, the advantage of a duplex single-ended configuration is that it can correct the non-uniform attenuation of the entire fiber cable.

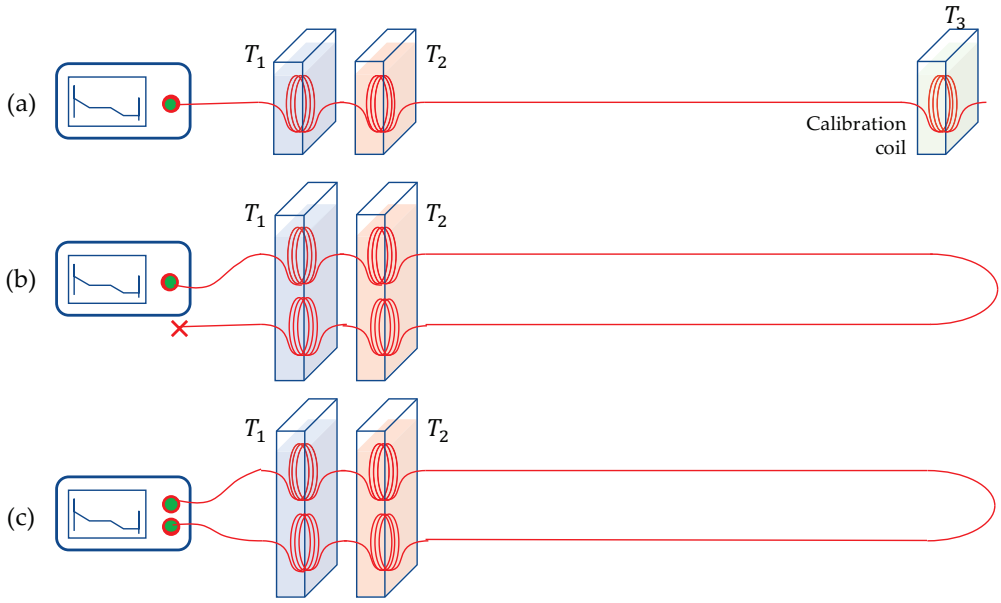

Figure 2.12 Typical deployment and configuration of FODTS. (a) A simple single-ended cable needs the third temperature reference at the end of the fiber cable. (b) A single-ended duplex does not need the third temperature reference separately, but the fiber cable should be returned to the temperature reference at the beginning. (c) double-ended configuration with dual light pulse launchers on both sides.

Measuring the backscattered light from both ends of fiber cables is expected to recover the differential attenuation caused by splice, connectors, and bend. This way is called a double-ended configuration (Tyler et al., 2009; van de Giesen et al., 2012a). Closed-loop fiber cable enables the light pulses to be injected and monitored from both sides over time intervals (see Figure 2.12c). The motivation of this strategy is to reduce the cumulative differential attenuation along the fiber. The intensity of backscatter light may change over time because of minor inconsistencies in the system, such as power supply fluctuation and laser light parameters. Technically, the pulses are launched into the fiber twice from different sides. In the first transmission, the pulse light is launched from one cable end during the first measurement period called " forward," starting at $x = 0$ m. It is launched from the other one during the next measurement period called " reverse," starting at $x = l$ m, with l being the fiber cable's length. The non-uniform attenuation along the fiber can be corrected using the double-ended configuration. Moreover, the temperature references can be installed close to the main DTS instrument to control and maintain temperature more efficiently.

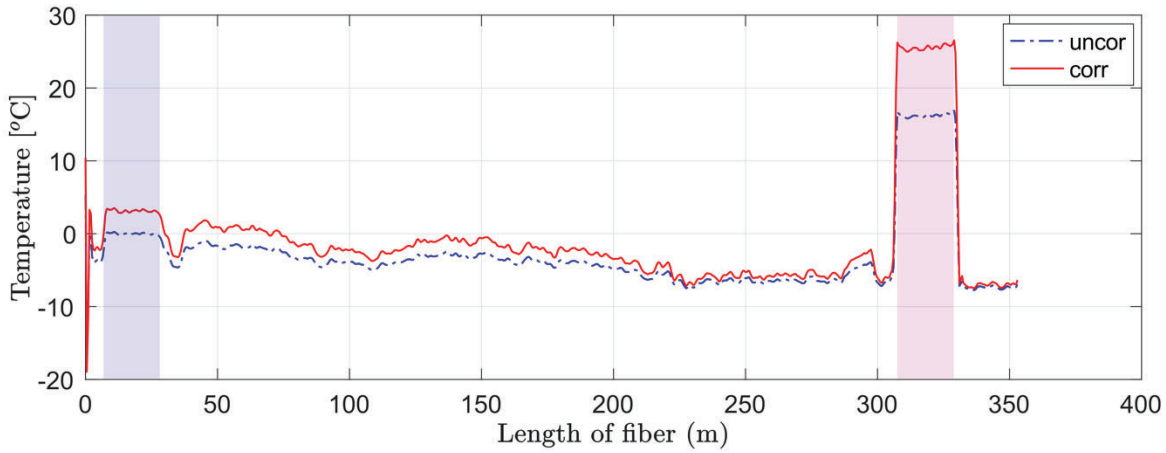

Figure 2.13 Temperature response. Around 20 m of fiber cable were rounded in ambient and heated baths. The blue area is a fiber cable rounded in the ambient bath, and the red one is in the heated bath. The dotted line is uncalibrated, and the solid line is calibrated along the fiber.

The above discussions show that temperature calibration is essential in applying fiber optic distribution sensors. This thesis uses a simple double-ended configuration, where the first coil of fiber is immersed in the ambient bath, and the second is in the heated bath. The first and second coils are rolled up near the beginning and end of the fiber cables, respectively. Several temperature sensors are assembled as references in the ambient and heated baths. Comparing temperatures in the baths is calculated as a drift correction along the fiber cables, which becomes the temperature calibration (see Figure 2.13).

Aerial radiation correction

Fiber optic distributed temperature sensing has recently been used to figure out the temperature of the air (Keller et al., 2011; De Jong, Slingerland, and Van De Giesen, 2015; Hilgersom et al., 2016). At the surface, optical fiber measures the temperature difference between the air and the soil, which radiation, rain, and other things affect. However, in the subsoil, fiber optics only measure soil temperature, which is mainly affected by moisture. The soil temperature variability in complex terrain has a different solar input strongly modified by surface conditions (Neilson et al., 2010; Seyfried et al., 2016). Regarding the experiment conducted by Sigmund (2017) (see Figure 2.14b), the shortwave and longwave solar radiation flux affects the surface area of fiber optics. Physically, the fiber cable jacket has a specific fiber cable albedo, emissivity, and heat transfer coefficient.

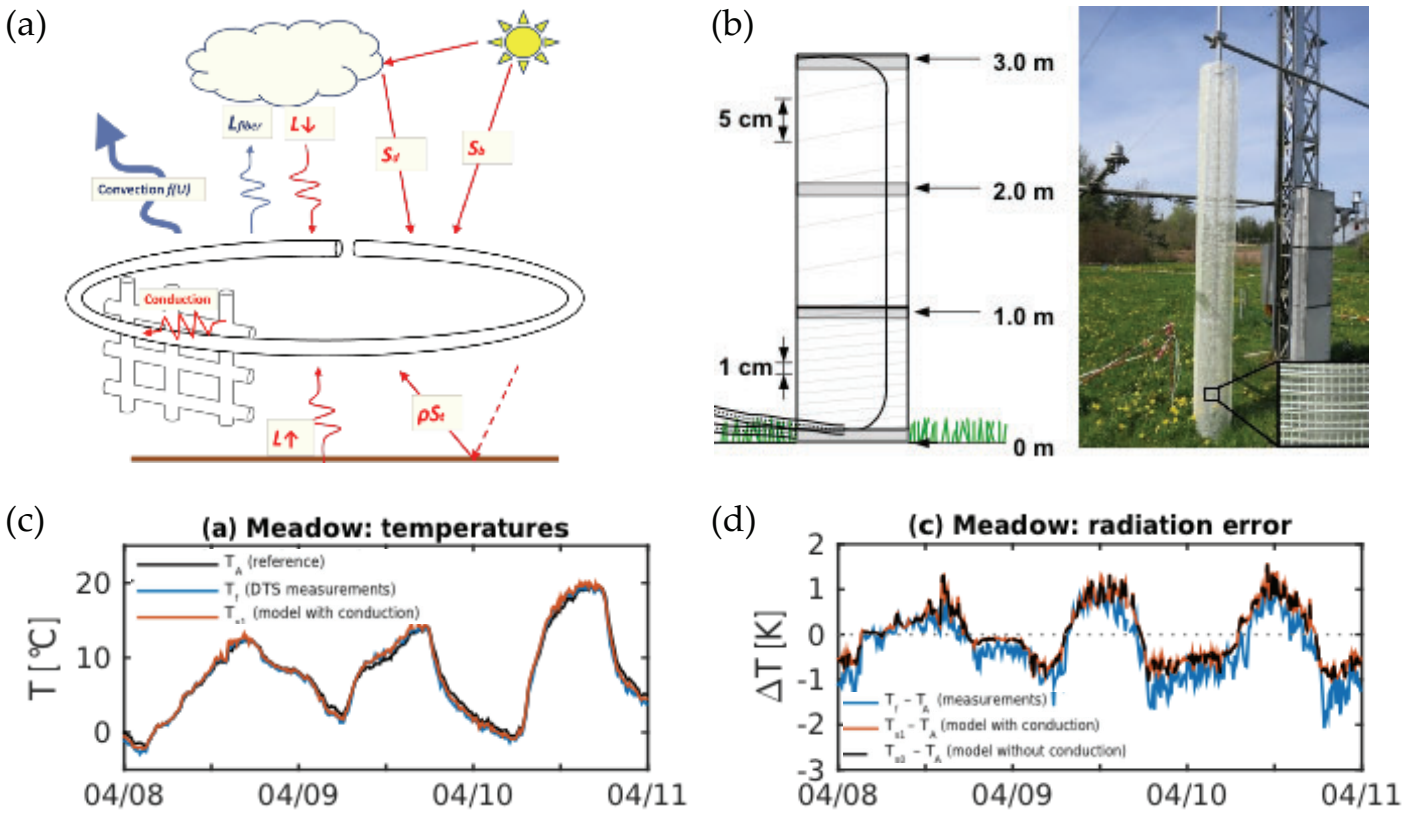

Figure 2.14 Aerial fiber optic experiment for quantitative analysis of radiation error (Sigmund, Pfister, Sayde, and Christoph K. Thomas, 2017). (a) Schematic of incoming and outgoing wave radiation through the fiber cable. (b) Experiment design and instrument installed at the meadow. (c) Meadow temperature during observation. (d) Aerial radiation error obtained from meadow temperature.

The quantification of energy balance helps us remove aerial radiation errors caused by solar radiation (see Figure 2.14a). The basic principle of this method is to use the shortwave, longwave, convective, and conductive heat transfer around the fiber for quantifying the modeled radiation. An energy balance model (see Figure 2.14a) measures radiation from the sky and eliminates the errors caused by solar radiation. The basic

principle of this method is to use shortwave, longwave, convective, and conductive heat transfer around the fiber to quantify the modeled radiation. Eq 2.26 describes the temperature along the entire fiber cable.

$$T_c = T_s + \frac{1}{h}\left[\frac{1}{2}C_p \rho r \frac{dT_s}{dt} - \bar{S}(1-a) - \bar{L}\varepsilon + \varepsilon\sigma T_s^4\right] \quad \text{Eq 2.26}$$

where T_c and T_s are the temperatures along the fiber (°C) after and before radiation correction, respectively; C_p is the specific heat capacity of the fiber (kJ kg^{-1} K^{-1}); ρ is the density of the fiber (kg m^{-3}); r is the radius of the fiber optic; $\bar{S}$ and $\bar{L}$ are the shortwave and longwave radiation (J s^{-1} m^{-2}) around the fiber; a is the albedo of the fiber; ε is the emissivity of the fiber; σ is the Stefan-Boltzmann constant (J s^{-1} m^{-2} K^{-4}), and h is the convection heat transfer coefficient (J s^{-1} m^{-2} K^{-4}) that mainly depends on wind velocity (Sayde et al., 2015).

2.3.3 Determination of soil diffusivity by using passively heated fiber optic

Two common strategies employing different temperature source configurations estimate soil moisture changes over time through temperature sensing. The passive configuration uses the diurnal temperature cycle as a heat source (Steele-Dunne et al., 2010). The active configuration uses an electric current in the metal sheath as a heat pump generator (Ciocca et al., 2012). The advantage of a passive heat source is the simplicity of DTS installation, which only requires the burial of the cable. However, due to uncontrolled temperature circumstances, the difficulty lies in properly processing the temperature data to obtain the soil heat parameters. On the other hand, the active heat source requires more power consumption because the heat is injected into the soil by the power heat source generator. Therefore, the active heated DTS is suitable for laboratory-scale experiments that do not have external temperature disturbances.

In this work, the passive heat DTS setup was used to measure the temperature of the soil and the surrounding area in the field. Soil moisture concerning soil heat diffusivity was estimated using a standard procedure consisting of several steps. As a natural heat source, temperature contains multiple frequencies and amplitudes, not only annual and diurnal cycles as periodic responses but also aperiodic responses such as rainfall events, cold or warm wind flow, and cloudy weather. This section presents the simulation procedure for estimating soil heat diffusivity contained in the diurnal temperature cycle and how to extract it while ignoring disruptions in temperature from other sources. A temperature simulation is generated by the heat equation solution (Carslaw and Jaeger, 1959; Jong van Lier and Durigon, 2013) at various depths for two days as an example simulation (see Eq 2.7).

$$T(z,t) = T_a + A_0 \exp\left(\frac{-z}{d}\right)\sin\left(\frac{2\pi t}{\tau} - \frac{z}{d}\right) \quad \text{Eq 2.27}$$

where temperatures $T(z,t)$ are in the spatial and time domain, the average temperature in a day is represented by 'T_a', the surface temperature amplitude is represented by 'A_0', the depth position is represented by 'z', the diurnal period is represented by 'τ', and the damping depth that depends on soil diffusivity is represented by 'd'. Regarding temperature simulation, synthetic diffusivity 'D' is generated to represent dry, wet, and drainage circumstances. When the thermal diffusivity is known, soil temperature can be predicted in time and depth (see Figure 2.15a).

Figure 2.15 shows the overview of the soil diffusivity estimation in the diurnal temperature simulation. This experiment sets the predetermined soil diffusivity values around 4×10^{-7} [m^2 s^{-1}] and 5.8×10^{-7} [m^2 s^{-1}]

for dry and saturated circumstances, respectively; the experiment periods are 15 days. Peak diffusivity is assumed to be the increased soil moisture due to water infiltration. Furthermore, the soil temperature is predicted using Eq 2.7, and the signal indicates the disrupted temperature at a similar time with a high diffusivity. After inverse calculation by using the 1D finite difference method, the diffusivity changes can be traced locally.

Figure 2.15 provides an overview of the estimation of soil diffusivity in diurnal temperature simulations. This experiment sets predetermined soil diffusivity values at around 4×10^{-7} [$m^2 s^{-1}$] and 5.8×10^{-7} [$m^2 s^{-1}$] for dry and saturated circumstances, respectively, and the experiment periods are set to 15 days. Peak diffusivity is assumed to result from increased soil moisture due to water infiltration. Furthermore, the soil temperature is predicted using Eq 2.7, and the signal indicates disrupted temperature at a similar time with high diffusivity. After inverse calculation using the 1D finite difference method, changes in diffusivity can be traced locally.

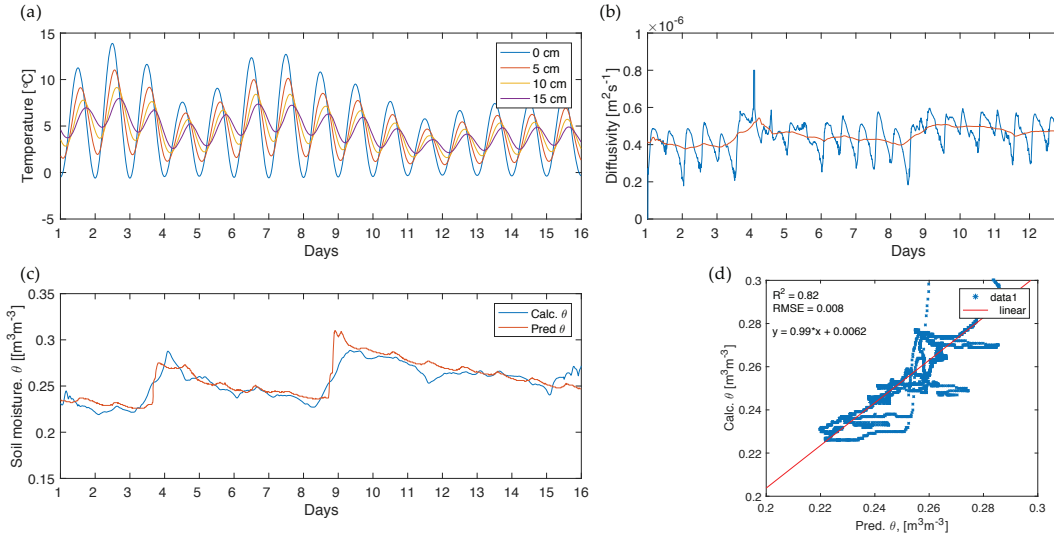

Figure 2.15. Overview of a passively heated experiment with diurnal temperature simulation. (a) Synthetic diffusivity and predicted soil temperature, (b) estimated diffusivity after inverse calculation, (c) comparison of synthetic and calculated diffusivity, (d) analysis goodness using linear regression.

However, undesirable diffusivity appears as a periodic artifact due to the temperature gradient in the finite-difference solution. Therefore, the high pass filter reduces the low frequency, usually caused by a periodic response such as annual and diurnal cycles. Figure 2.15b shows the original and filtered soil diffusivity. The predetermined and calculated diffusivities are converted to soil moisture to validate the strategy using the Johansen model and Kersten coefficient (Eq 2.32). Further, the model-fitting analysis shows a pretty good comparison between calculated soil moisture and the predetermined one (see Figure 2.15c). The discrepancy between the calculated and the predetermined soil moisture is relatively minor. In the analysis provided here, the determination coefficient R^2 of both soil moisture is 0.82, and the root mean square error (RMSE) is 0.008 (see Figure 2.15d), so the strategy above provides a possible way for soil moisture estimation concerning passively heated soil temperature observation through soil thermal properties.

2.3.4 Non-linear inversion for soil thermal parameter estimation

By tracing temperature in space and time, thermal soil diffusivity can be estimated using the second Fick's law regarding the heat transport equation (Eq 2.28). Analytical and numerical methods can be applied to calculate soil thermal diffusivity. The analytical solution for the heat transport equation, considering boundary

and initial conditions, is presented in Eq 2.29 (Carslaw and Jaeger, 1959). It separately emphasizes the amplitude or time of temperature propagation through amplitude and phase-shifting analysis (Eq 2.30).

By tracing temperature in space and time, thermal soil diffusivity can be estimated using the second Fick's law regarding the heat transport equation (Eq 2.28). Analytical and numerical methods can be applied to calculate soil thermal diffusivity. The analytical solution for the heat transport equation, considering boundary and initial conditions, is presented in Eq 2.29 (Carslaw and Jaeger, 1959). It separately emphasizes the amplitude or time of temperature propagation through amplitude and phase-shifting analysis (Eq 2.30).

$$\frac{\partial T}{\partial t} = D(\theta)\frac{\partial^2 T}{\partial z^2} \qquad \text{Eq 2.28}$$

$$T(z,t) = T_0 + A_0 \exp\left(\frac{-z}{d}\right)\sin\left[\frac{2\pi t}{\tau} - \frac{z}{d}\right] \qquad \text{Eq 2.29}$$

$$D_{amp} = \frac{\omega}{2}\left[\frac{z_2 - z_1}{\ln\left(\frac{A_1}{A_2}\right)}\right]^2 \quad \text{or} \qquad \text{Eq 2.30}$$

$$D_{phase} = \frac{\tau}{4\pi}\left[\frac{z_2 - z_1}{t_2 - t_1)}\right]^2$$

where T represents the temperature (°C), t represents time (s), z represents depth position (m), θ represents soil moisture, and $D(\theta)$ represents soil diffusivity (m^2s^{-1}), which is affected by soil water content. T_0 represents the average soil temperature, A_0 represents the amplitude of surface temperature, and ω represents the angular frequency of diurnal temperature changes. The estimated diffusivity is addressed by D_{amp} and D_{phase} as amplitude analysis and phase-shifting diffusivity.

The numerical method is slightly more complex than the analytical one because it simultaneously employs the second-order differential solution to examine temperature and time. The implicit or explicit finite difference scheme is applied to a homogeneous half-space (Béhaegel, Sailhac, and Marquis, 2007; Krzeminska *et al.*, 2012a).

$$\frac{T(z_i, t_{j+1}) - T(z_i, t_j)}{\Delta t} = D(\theta)\frac{T(z_{i-1}, t_j) - 2T(z_i, t_j) + T(z_{i+1}, t_j)}{\Delta z^2} \qquad \text{Eq 2.31}$$

where Δt and Δz represent time and profiling differences, respectively, while i and j denote the depth and time indices. Furthermore, the conductivity and heat capacity are also calculated to determine the soil moisture within the soil porosity. Saturated and dry conditions are required to estimate the constant volumetric heat capacity and soil heat conductivity. For this purpose, a time series of temperature profiling observations is used to drive the diffusivity calculation, which depends on soil water changes in the soil pores. The Johansen model (1975) describes this calculation as a combination of saturated and dry soil thermal conductivity, while the Kersten coefficient (Kersten, 1949) formulates the normalized thermal conductivity between dry and saturated situations, which is used in the Johansen model. Eq 2.32 illustrates the relationship between soil thermal properties and soil water content in saturated and dry conditions.

$$D(\theta_i) = \frac{\left[\log_{10}\left(\frac{\theta_i}{\emptyset}\right) + 1\right](\lambda_s - \lambda_d) + \lambda_d}{(1 - \emptyset)C_s + \theta_i C_w} \qquad \text{Eq 2.32}$$

where $\emptyset$ is soil porosity, λ_s and λ_d are the saturated and dry conductivity of soil, C_s and C_w are the volumetric heat capacity of soil and water, respectively. The non-linear least-squares regression method is applied in terms

of soil thermal inversion. Eq 2.32 is reformed to become a linear equation for simplification. Linear regression as a simplification solution is presented in Eq 2.33 by considering some modified variables in Eq 2.34.

$$D(\theta_i) = \lambda_s x_i + \lambda_d y_i - C_s z_i \qquad \text{Eq 2.33}$$

$$x_i = \frac{\log_{10}\left(\frac{\theta_i}{\emptyset}\right) + 1}{\theta_i C_w} \quad , \quad y_i = \frac{\log_{10}\left(\frac{\theta_i}{\emptyset}\right)}{\theta_i C_w} \quad , \quad z_i = \frac{D(\theta_i)}{\theta_i C_w} \qquad \text{Eq 2.34}$$

Furthermore, the error minimization function on least squares regression estimates the soil's thermal properties. This step uses the observed soil moisture from EC5 Decagon and soil diffusivity from FODTS as an inversion input. Soil porosity and volumetric water heat capacity are assumed as constant coefficients. Eq 2.35 and Eq 2.36 present the error function of this strategy. $P(x_i, y_i, z_i)$ is a model that contains the estimated parameters, and D_i is the observed dataset.

$$P(x_i, y_i, z_i) = \lambda_s x_i + \lambda_d y_i - C_s z_i \qquad \text{Eq 2.35}$$

$$D_i = P(x_i, y_i, z_i) + e_i \qquad \text{Eq 2.36}$$

The modification of the error provides the possibility to calculate thermal properties. To reach the minimum value of the error function, the error that depends on each parameter should be zero. Therefore, the solution can be arranged as shown in Eq 2.37 to Eq 2.39.

$$E(\lambda_s, \lambda_d, C_s) = \sum [D_i - \lambda_s x_i - \lambda_d y_i + C_s z_i]^2 \qquad \text{Eq 2.37}$$

The error function is essential to attain the minimum value. It helps to ensure optimal performance of the non-linear inversion process. Achieving this requires us to calculate the differential error for each optimized parameter, as demonstrated in Eq 2.38 and Eq 2.39. By doing so, we can determine the optimal values for these parameters that minimize the error function and improve the overall accuracy of our model.

$$\frac{\partial E(\lambda_s, \lambda_d, C_s)}{\partial \lambda_s} = 0, \quad \frac{\partial E(\lambda_s, \lambda_d, C_s)}{\partial \lambda_d} = 0, \quad \frac{\partial E(\lambda_s, \lambda_d, C_s)}{\partial C_s} = 0 \qquad \text{Eq 2.38}$$

$$\frac{\partial E(\lambda_s, \lambda_d, C_s)}{\partial \lambda_s} = \frac{\partial}{\partial \lambda_s} \sum [D_i - \lambda_s x_i - \lambda_d y_i + C_s z_i]^2 = 0$$

$$\frac{\partial E(\lambda_s, \lambda_d, C_s)}{\partial \lambda_d} = \frac{\partial}{\partial \lambda_s} \sum [D_i - \lambda_s x_i - \lambda_d y_i + C_s z_i]^2 = 0 \qquad \text{Eq 2.39}$$

$$\frac{\partial E(\lambda_s, \lambda_d, C_s)}{\partial C_s} = \frac{\partial}{\partial \lambda_s} \sum [D_i - \lambda_s x_i - \lambda_d y_i + C_s z_i]^2 = 0$$

The non-linear inversion method can be expressed through an inverse matrix solution: $M = [G^t G]^{-1} G^t D$, where G is a Kernel matrix, M is the estimated parameters, and D is a matrix containing observations of soil moisture and soil diffusivity. Referring to Eq 2.34 and Eq 2.39, the solution can be arranged as shown in Eq 2.40.

$$\begin{bmatrix} \Sigma x_i^2 & \Sigma x_i y_i & \Sigma x_i z_i \\ \Sigma x_i y_i & \Sigma y_i^2 & \Sigma y_i z_i \\ \Sigma x_i z_i & \Sigma y_i x_i & \Sigma z_i^2 \end{bmatrix} \begin{bmatrix} \lambda_s \\ \lambda_d \\ C_s \end{bmatrix} = \begin{bmatrix} \Sigma D_i x_i \\ \Sigma D_i y_i \\ \Sigma D_i z_i \end{bmatrix} \qquad \text{Eq 2.40}$$

2.4 The insight of fiber optic temperature sensing applications in environmental geophysics

Fiber optic technology is a revolutionary technique for measuring distributed temperature in various applications. It offers several potential advantages, including cost-effective installation and wide-area deployment. Fiber optic cables with metal cladding can also be used for active heated experiments. Currently, fiber-optic sensing is widely used in many fields, such as industry, engineering, environmental science, and shallow and deep geophysics. Besides temperature sensing, fiber optics can also measure physical aspects such as pressure, strain, acoustic waves, and chemical composition.

Heat transfer mechanisms are essential to developing environmental geophysics because they provide complex insights into multiparameter characterization ((Lienhart, 2015; Suárez et al., 2011; Zeni et al., 2015). Heat moving through the soil is a beneficial way to learn more about its properties and how to describe it. The sun's heat, which warms up the earth occasionally, can be used as a free heat source. Geophysical methods use this kind of heat source called a passive heat source. In the surface zone, heat exchange depends on many things, such as the texture of the soil, the amount of water in the pores, the plants, and whether the soil is covered with mulch or left bare (Hillel, 2004).

In environmental geophysics, numerous fiber optic applications have been reported. One of these applications is in the southern Mojave Desert. Fiber optic sensing was installed at Devil's Hole, which has a surface area of barely 30 m^2 and a depth of 30 m from the surface to monitor the carbonate aquifer (Riggs and Deacon, 2002). The researchers observed the water temperature in Devil's Hole because it is home to the Devil's Hole pupfish called *Cyprinodon diabolis*, which is very sensitive to temperature changes (Moyle, 2002). The temperature tolerance for most species in Devil's Hole is 33-35 ºC (Otto and Gerking, 1973). Figure 2.16 shows the temperature profile at Devil's Hole for the winter and summer periods. As shown in Figure 2.16, the temperature along the fiber from top to bottom can be more easily observed and confidently quantified during the observation period. Therefore, the vertical temperature profile gradient can be estimated as an indication of the seasonal system. This case shows the advantages of fiber optic sensing in environmental studies.

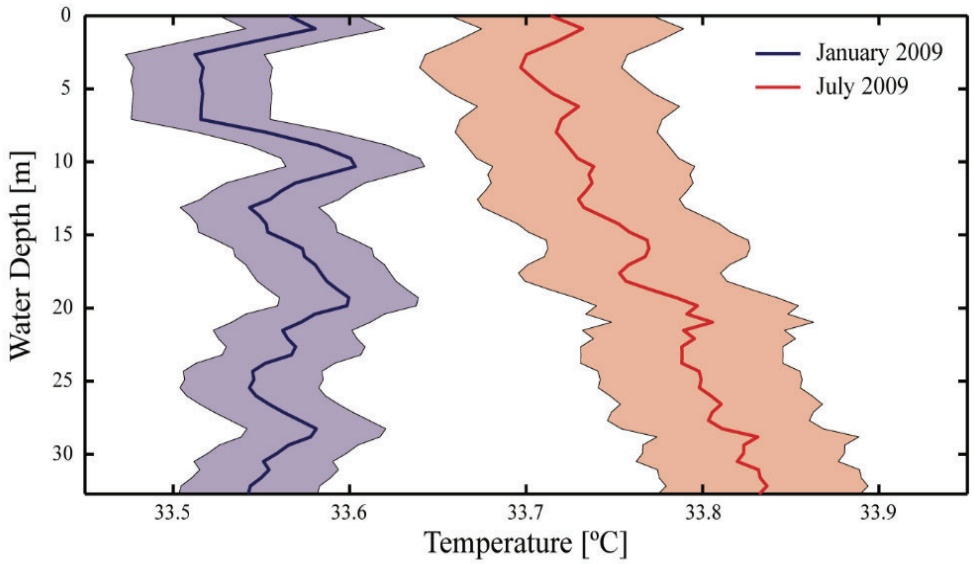

Figure 2.16 The water temperature profile on Devil's Hole is a perfect example of fiber optic temperature sensing application in environmental monitoring (Suárez et al., 2011).

Fiber optic sensing can also find levee leaks between the river and the field. The heat exchange in the levees contains information about embankment leakage (Schenato, 2017). The schematic experiment is presented in Figure 2.17. Like Devil's Hole, the gradient method provides specific information regarding the

temperature across the levees. Some authors call this method "natural-occurring temperature gradients and fluctuations" (Schenato, 2017). Technically, fiber optic temperature sensing deployed in the levees measures temperature spatially and temporally. Great effort should be made analytically and numerically to compute the differences in soil thermal models inside the levees because infiltration water flows from the riverside. A well-designed experiment with appropriate analytical and numerical methods makes fiber optic temperature sensing a standard for quantifying groundwater-surface water exchange fluxes (Vandersteen et al., 2015). Therefore, detecting leaks in levees becomes more manageable in the field.

In addition to the examples of research given above, many studies have been done on the development and use of FODTS for other types of environmental research. FODTS applications can measure air temperature, soil temperature, and water needs. The usage of FODTS installed on land and water can reach up to very far distances of 5 km (van de Giesen et al., 2012a), with laboratory accuracy up to 0.01 °C and typical field accuracy of 0.08 °C (De Jong et al., 2015) FODTS provides a significant advantage because it can reduce costs and simplify sensor installation. Using FODTS, measuring temperature along the fiber cable allows for very efficient measurements. In air temperature measurement, a quantitative analysis of radiation errors on FODTS has also been analyzed (Sigmund, Pfister, Sayde, and Christoph K. Thomas, 2017). This strategy was developed to improve the performance of air temperature measurement where FODTS is affected by solar heat radiation in the field (Westhoff et al., 2007).

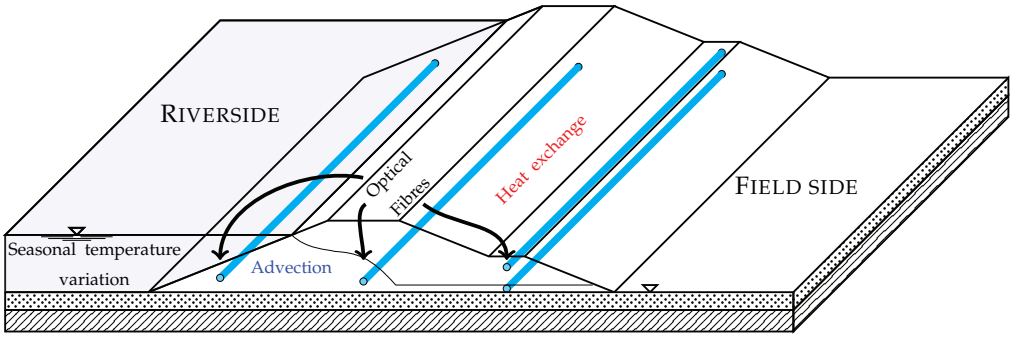

Figure 2.17 The leakage detection in the levees between the riverside and field side uses heat exchanges measured by fiber optic temperature sensing (Schenato, 2017).

In simple terms, fiber optic temperature sensing measures temperature along the fiber. In other words, the fiber optic cable acts as a temperature sensor with multiple observation points along the fiber. Physically, fiber optic temperature sensing works by measuring the backscattering of light inside the fiber cable. The physical parameter of the fiber temporarily changes depending on the effect of temperature. Generally, the fiber optic temperature sensing principle is well-known from fiber Bragg grating, Raman scattering, and interferometric point sensors (Hoffman et al., 2007). This thesis discusses the application of Raman scattering for observing soil temperature with high spatiotemporal resolution. Raman scattering is highly distinctive and is used for temperature observation. The molecular vibration frequency inside the fiber cable is driven by temperature. Figure 2.18 illustrates an excellent 3D temperature observation along the fiber in distance and frequency (Nikles et al., 2004).

Environmental processes can be observed naturally by putting sensors all over the observation site. The way the fiber cable is set up should remain the same as how the light moves through it, except in cases where it is bent or stretched. Sharp bends and strains in the fiber cable installation can sometimes cause significant localized losses of light transmission, which reduces the light intensity and causes noise in temperature data

readings. Calibration design should be considered to handle these light losses (Hausner and Kobs, 2016). Single-ended and double-ended calibrations are recommended as calibration designs. These calibration strategies can be adjusted for a specific application. Single-ended calibration provides more precision for short fiber cables, but strains highly influence it and bend along the fiber cable. The double-ended calibration allows noise to be distributed evenly along the fiber, but the noise level is higher than in the single-ended calibration.

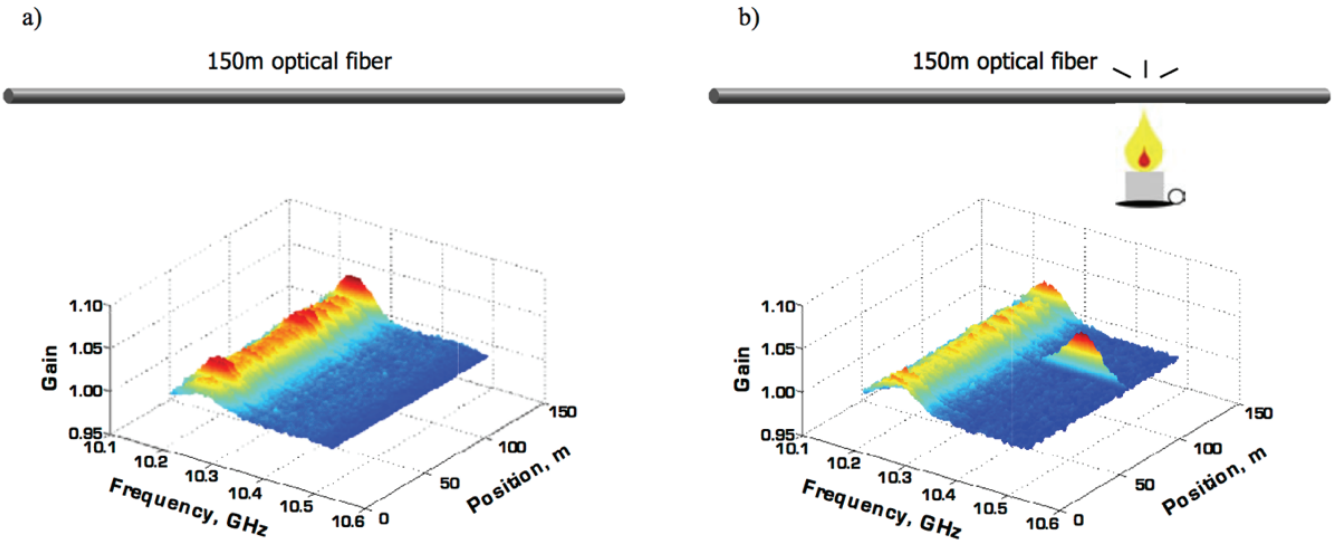

Figure 2.18 The 3D illustration of temperature observation along fiber as a function of frequency and distance. (a) fiber with uniform temperature, (b) the temperature anomaly is detected at the specific location and shown by frequency anomaly (Nikles et al., 2004).

Using fiber optic sensing to measure temperature depends on how the user sets up, calibrates, and fixes the fiber cable based on how it will be used. The above application examples show different deployment strategies for each case. The temperature observation in Devil's Hole, shown in Figure 2.16, used a single typical calibration, while the leakage detection in Figure 2.17 used a double-ended configuration. This thesis focuses on detecting soil water content in shallow surface soil porosity over time. Therefore, specific configuration, calibration, and correction is necessary for temperature observation. For instance, the interface temperature between soil and air, which acts as an upper boundary condition, is highly affected by solar radiation. Therefore, an aerial temperature correction is needed for fiber cables installed in the upper soil surface (Sigmund, Pfister, Sayde, and Christoph K. Thomas, 2017).

Chapter 3: Field Experiment: Draix Technological setup, Data Collection & Inversion

3.1 General introduction of the study site

The shallow weathering zone in the Mediterranean catchments is highly affected by soil and water changes in space and time. The study site is in the Digne—Valensole basin region. Specifically, the observation was situated in the Draix—Laval catchment area. The observatory facility was developed by the Observatory for Research in the Environment (ORE), French Ministry, in 2002 and has been managed by the Institute *National de Recherche en Sciences et Technologies pour l'environnement* (IRSTEA) until now. Some studies were conducted regarding erosion (Descroix and Claude, 2002; Esteves et al., 2000; Mathys et al., 2003), soil hydraulic properties (Esteves et al., 2005), and water flow modeling (Esteves et al., 2000). Draix is an exciting observation site for environmental and soil studies as part of a large watershed. It was passed by the Ravin de Laval watershed, yielding intense erosion. Because of exposed roots, the medium-term erosion rates vary from 6 to 7 mm y^{-1} depending on the uplift of roots after exposure (Corona et al., 2011).

Figure 3.1 The general view of Draix site observation comprises Laval and Moulin (Mathys et al., 2005).

In the weathering zone, soil-water interaction is critical for soil deformation. Additionally, the presence of trees affects soil-water interactions in the subsoil (Zribi et al., 2010). In the Draix area, the weathering has resulted in soil with increasing compactness and density with depth (Maquaire et al., 2002). Several studies have been conducted to understand the infiltration processes in the unconfined shallow aquifer, which is highly reactive to rainfall pulses (Garel et al., 2012; Travelletti et al., 2012). These studies investigate the groundwater level to observe the infiltration capacity and macrospore connectivity on clay-shale slopes. They confirm that several parameters control surface runoff and subsurface flow patterns, such as water infiltration, slope gradient, soil surface characteristics, and initial soil moisture conditions (Esteves et al., 2005; Striegl and Loheide, 2012; Travelletti et al., 2012).

3.1.1 Localization and climate information

As part of the Mediterranean catchment area, the observation site is Draix Bléone, located 44°8'N., 6°21'E 13 Km northeast of Digne town, in southern France's Alpes de Haute-Provence region. The primary groundwater source is the infiltration of rainfall and snowmelt, although snow does not permanently cover the area during winter (Corona et al., 2011). Precipitation is highly variable, ranging from 0 to 80 mm/day, and the average annual rainfall from 1984 until 2008 was 912 mm ± 188 m (Garel et al., 2012; Marc et al., 2017a). Solar radiation reaches an intensity of up to 1133 W/m^2 during the summer and approximately 25 W m^{-2} during the winter. The climate in the area is characterized by mountains, with maximum precipitation in the summer and frequent freeze-thaw cycles during the winter. The average annual temperature at the study site is 9.8 °C, rising

to 28 °C during the summer (Rovéra and Robert, 2005). The *Laboratoire Rhodone de Geomorphologie* confirmed that the extreme temperatures of each freeze-thaw cycle were fixed at -15 and +15 °C (Descroix and Claude, 2002).

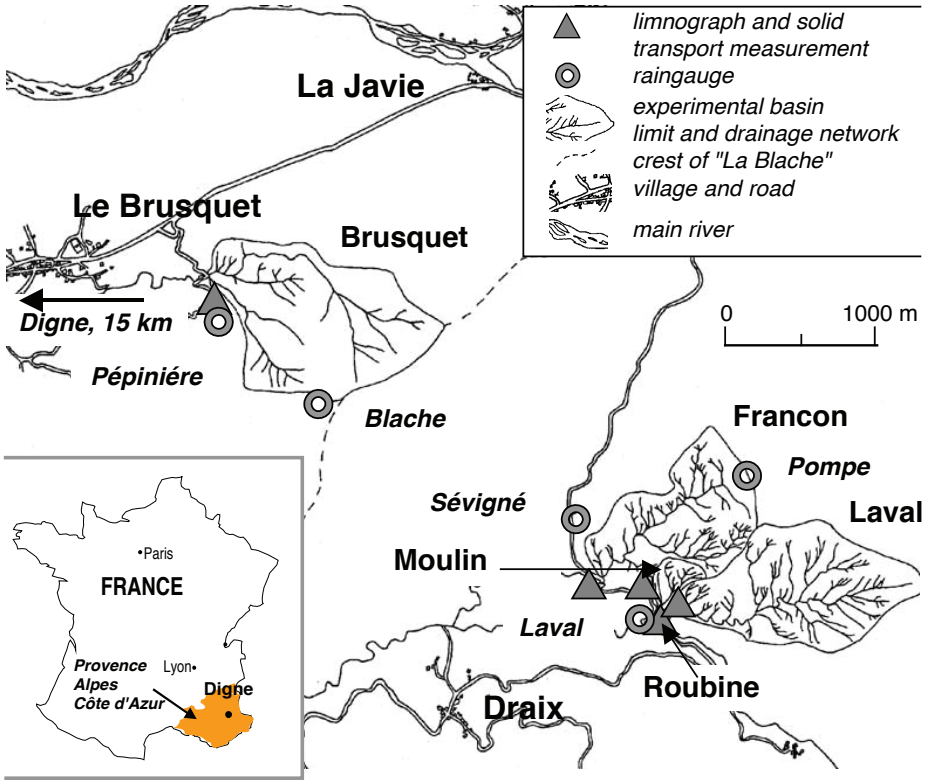

Figure 3.2 Localization of the Draix catchment area comprises the Moulin, Laval, and Roubine basins (Mathys et al., 2005).

Draix Bléone comprises three large catchment basins: Moulin, Laval, and Roubine. Figure 3.1 and Figure 3.2 show the localization features and the experimental design for runoff and erosion observation conducted by Mathys (2005). The high rainfall intensity in the marly catchment area results in sedimentation and gully development. Water erosion has produced a solid sedimentary filling in the riverbed around the location, and water runoff is the main factor controlling gully development (Esteves et al., 2005). The erosion rates vary between 6 and 7 mm/year for Moulin, Laval, and Roubine basins (Corona et al., 2011), with 6.4 mm/ year and 6.3 mm/ year for Moulin and Laval basins, respectively.

The Draix site area is highly affected by winter climatic conditions, resulting in periglacial erosion processes contributing to the Marly Badlands' topography and morphology. The Cemagref-RTM experimental basin at Digne recorded temperature and soil erosion during the winter 2000–2001 to identify periglacial morphogenetic characteristics. They confirmed the presence of 114 freeze-thaw cycles in the air, a morphoclimatic contrast between the north and south slopes at the gully, frost creep and gelifluction on the marly surface, and the seasonally frozen ground's presence down to a depth of 30 cm on the north slopes (Rovéra and Robert, 2005).

3.1.2 Geological setting of the Draix—Laval catchment area

This thesis is mainly about the Draix-Laval catchment area, where black marl, sensitive to weathering and erosion (Descroix and Claude, 2002), makes up most of the soil. Draix-Laval is in Jurassic marine black marls, specifically in the Bajocian, Bathonian, and Callovo-Oxfordian units (Mathys et al., 2003). The area is part of the Digne-Valensole basin, established between the Miocene and Pliocene periods. Generally, the Laval basin

covers an area of almost 86 hectares, and its maximum elevation is 1259 m.a.s.l. The main site area locally features a dextral strike-slip fault, with the oriented fold N140 (Marc et al., 2017b). The Draix-Laval elevation ranges from 850 to 925 meters, with 46% of the catchment area covered by pine trees (Esteves et al., 2005), and the main slope is 30°. Additionally, the catchment area has colluvial material dispersed in a silt-clay matrix (Maquaire et al., 2002). Figure 3.3 presents the conceptual hydrological model of the Draix-Laval area. On the east side, a local recharge area drives shallow and deep groundwater flow, with a strike slip separating another local recharge below. Draix-Laval is situated between them, close to a strike-slip zone.

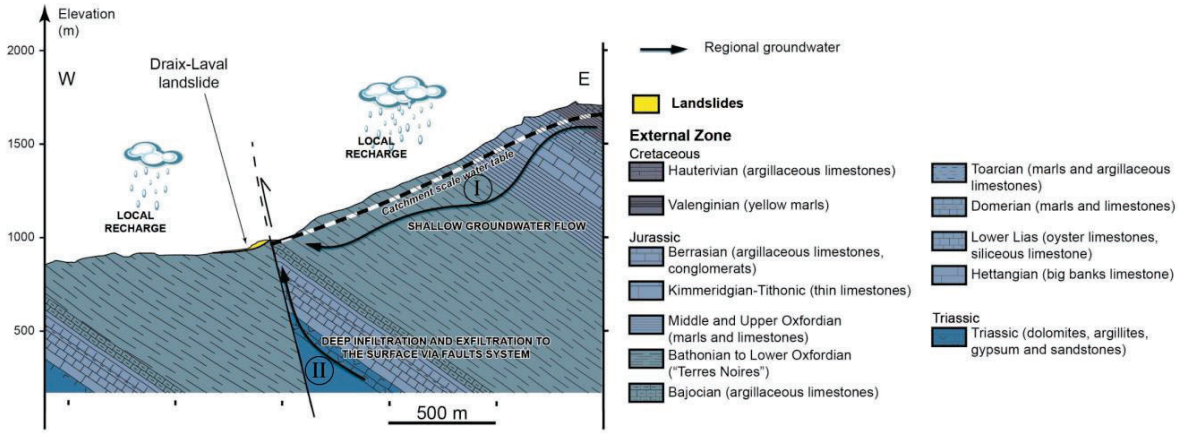

Figure 3.3 Conceptual model of the hydrogeological system at the Draix catchment area (Marc et al., 2017b).

The geological and environmental condition of Draix, as part of the Marly formation, is very complex. This site is sensitive to weathering and erosion, which have formed extreme topography, badland soil conditions, steep slopes, and highly eroded slopes (Antoine et al., 1995). The topography is controlled by moderately resistant limestones that cover the edge of the formation, forming elongated monoclinal ridges with elevations up to 2000 m.a.s.l (Oostwoud Wijdenes and Ergenzinger, 1998).

The landscape of the study site is characterized by at least three soil types: soil covered by forest and grass in the vegetation area and black marls that are uncovered. Pine trees dominate the northeast side, which has a slightly higher elevation. The grassland is distributed in the center, while the black marls elongate on the west side of the forest and grassland, with ridges and gullies in the center. Figure 3.4 presents a simplified topographic view of the study site, highlighting some of its features.

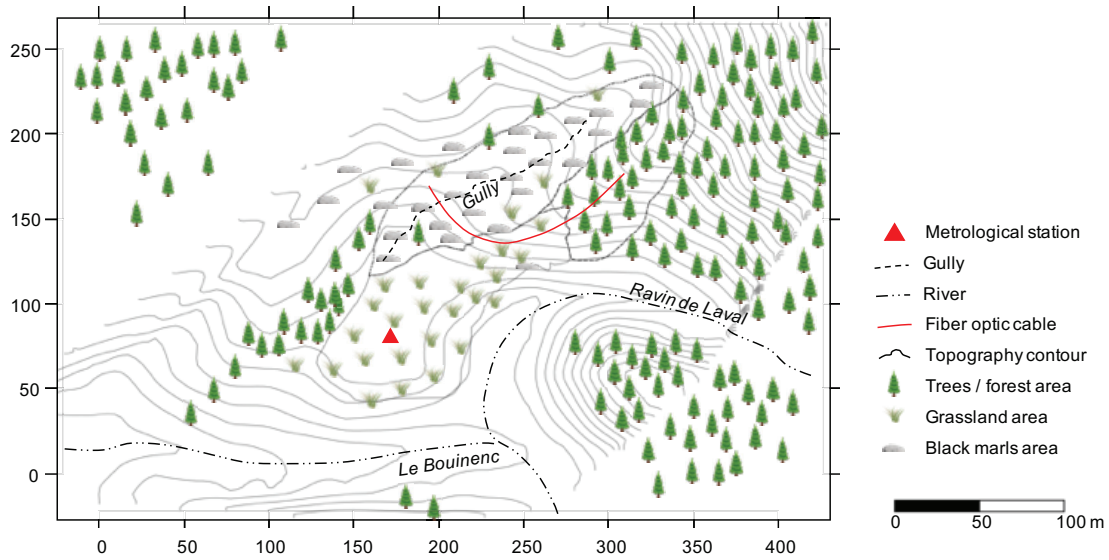

Figure 3.4 Fiber optic sensing was used to pass through three soil types at the study site, shown on a simplified topographic map.

3.1.3 Hydrology of the Draix—Laval area

The study of soil hydraulic properties in Draix, published in 2005 (Esteves et al., 2005), was done on slopes to show that runoff is one of the main factors affecting how gullies form. When rainfall intensity exceeds the soil infiltration capacity, flow velocity discharge produces concentrated erosion flows. The infiltration tests were performed during a 2-week dry period in June 2001, using tension disc infiltrometers of 125, 100, 40, and 25 mm radii (Vandervaere et al., 2000) at six different regolith types. Figure 3.5 shows the infiltration equipment installed in the field. The multiple potential tests were performed using four supply pressure heads, such as h = -100, -70, -40, and -10 mm, with a disc radius of 125 mm.

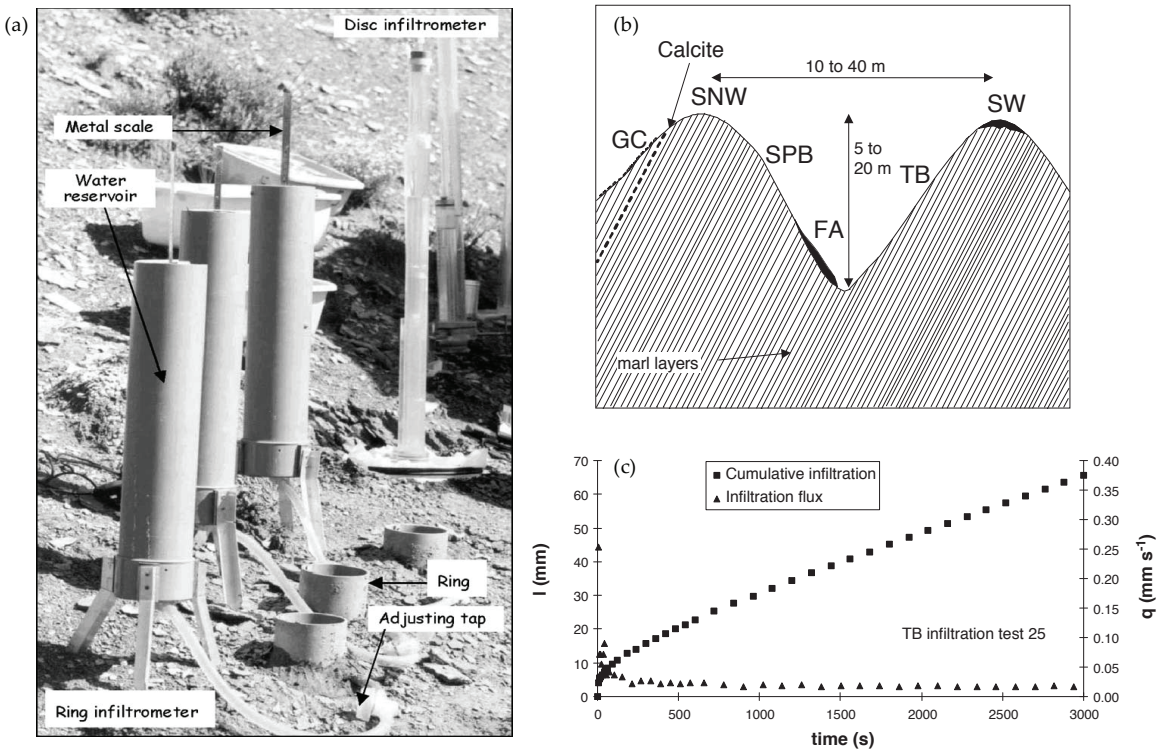

Figure 3.5 The infiltration testing was conducted over two weeks in June 2001 (Esteves et al., 2005). (a) The infiltrate-meter equipment consists of a metal scale, a water reservoir, and an infiltrate-meter disk. (b) The description of experimental site topography. (c) For example, the time series data record cumulative infiltration at the TB position (TB = top of bedding).

In 2005, Esteves experimented on six regolith types in an outcrop land area, testing three main criteria: slope gradient, dip angle, and gravel cover. The six regolith types are GC, SNW, SPB, FA, TB, and SW, which correspond to gravel-covered surfaces, summits without weather marls, perpendicular slope bedding, foot accumulation of marls, top bedding, and summits with weather marls, respectively.

Table 3.1 The statistical analysis of the infiltration testing and volumetric soil water content for six regolith types located at a gully catchment in Draix, France (Esteves et al., 2005).

	Initial VSWC				Final VSWC Disc infitrometer				Final VSWC Ring infiltrometer			
	n	Minimum	Maximum	mean	n	Minimum	Maximum	Mean	n	Minimum	Maximum	Mean
SW	4	0.045	0.075	0.058	12	0.174	0.301	0.228	9	0.285	0.455	0.354
SNW	4	0.052	0.077	0.066	9	0.189	0.267	0.214	5	0.268	0.445	0.376
SPB	4	0.04	0.065	0.048	10	0.171	0.284	0.211	7	0.266	0.343	0.312
TB	4	0.031	0.062	0.042	11	0.128	0.338	0.215	9	0.282	0.459	0.359
FA	4	0.02	0.078	0.057	12	0.167	0.327	0.245	9	0.36	0.545	0.436
GC	4	0.019	0.061	0.045	9	0.234	0.321	0.281	9	0.3	0.469	0.402

The hydraulic conductivity and volumetric soil water content were calculated as functions of the pressure heads. Table 3.1 presents a statistical analysis showing that the volumetric soil water content of the gully catchment varies from 0.019 to 0.545 (m^3/m^3). Moreover, the near-saturation hydraulic soil conductivity (K) with pressure head differences between $h = -100$ mm and $h = 0$ has main values ranging from 2.56×10^{-7} to 6.26×10^{-5} m/s. Several studies indicate a similar propensity for significant increases in $K(h)$ as the soil becomes saturated (Clothier and White, 2010; Oh et al., 2015; Smettem and Ross, 1992; van Genuchtan M, 1980). The variation of soil hydraulic conductivity near saturation is shown in Figure 3.6. Meanwhile, the unsaturated hydraulic soil conductivity with an imposed pressure head of $h = -100$ mm has values less than 8.33×10^{-7} m/s[1]. These values are claimed to be not significantly different from the previous studies on black marls formation in the literature (Caris and Van Asch, 1991).

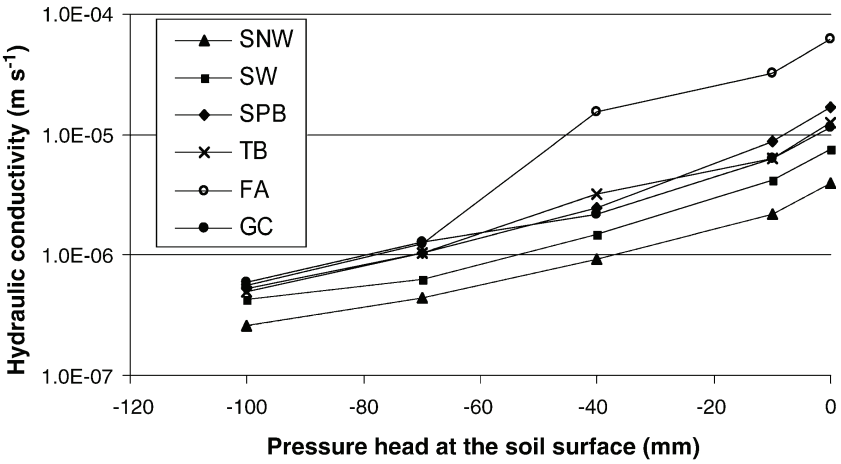

Figure 3.6 The estimated hydraulic conductivity near saturation for six regolith types as a function of pressure head (Esteves et al., 2005).

The hydrological investigation was also conducted by Caris and Van Asch (1991), which entailed measurement of saturated permeability and pressure head, which indicate instability because of long-term wet conditions and little evapotranspiration. The experiments were run to assess the stability of the slope in the marls area. The saturated hydraulic conductivity was evaluated by evaluating the permeability decrease. They experimented on two different depth intervals, from 0.3 to 0.8 m and 1.5 to 2.0 m, with results of 1.82×10^{-6} and 8.11×10^{-8} m/s[1], respectively.

Moreover, there have been many suggestions for hydrology studies to help predict floods in headwater catchments, especially at Draix Bleoné. The soil moisture mapping approach has been conducted to identify changes in soil properties down to a depth of 3 m (Mallet, 2018). The already developed method is valuable for investigating surface runoff generation processes.

3.2 Experimental and observation setup

Long-term hydrological observations provide potential information for understanding environmental processes. Most hydrological research uses simple instruments to assess water and soil conditions over time (Mittelbach et al., 2012), with data collected manually. The behavior of soil-water interaction is mainly studied at the laboratory scale to avoid uncertainties in the field (Gallage et al., 2013). However, in situ observations at the field scale provide more detailed information about environmental processes.

In the study of hydrological processes in the Mediterranean catchment area, several instruments have been permanently installed in the field, such as a meteorological station, fiber optic distributed temperature sensing, and a soil moisture sensor, since 2015. All data measurements were collected by several data loggers

and stored on IRSTEA computer servers. Furthermore, the IRSTEA data center maintains and distributes the data using internet network communication during observation. High-voltage electricity around the observation site was equipped to ensure the research works appropriately.

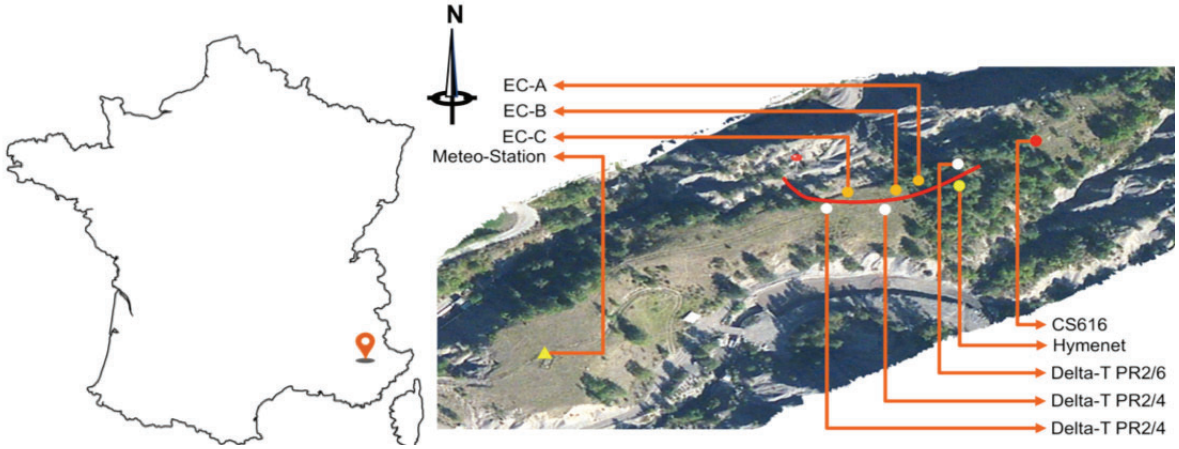

Figure 3.7 The instruments, which include the FO-DTS and cable (shown by the red line) and the meteorological station, were put in place, and their sensors were set up. The sensors installed include those for temperature, soil moisture, and more.

The thesis presented in this work discusses using FO-DTS for long-term observation of environmental temperature and soil moisture at the Draix Bléone catchment hydrological observatory, which is in the Mediterranean area (as shown in Figure 3.7). The main priority was to demonstrate the design and procedures in field trials. A permanent system installation was performed to ensure the long-term implementation of sensing and observation. The design requirements for this purpose were completed with additional considerations for independent environmental temperature and meteorological observations (as shown in Table 3.2). The completed observation dataset during multi-cycle hydrology is helpful for unambiguous interpretation.

Table 3.2 The instrument and experimental setup consist of hydrological observation and meteo-station sensors.

	Instruments	Measured parameters	Installation
Hydrological observation sensors	Fiber optic DTS ® Brugg Cables sensing technologies-Switzerland	T° along the fiber	Depths are 0cm, - 5cm, -10cm, -15cm. ~1cm
	DTS instrument ® AP Sensing DTS	Light pulse generator and DTS main controller	
	PT100 at baths reference	T° references	5 in cold bath 5 in warm bath
	EC5 Soil water sensor (*)	In situ soil moisture	Depths are -5cm, -10cm, -15cm and -30cm
	CS625 water content reflectometer (**)	Soil volumetric water content (VWC)	Depths are -5cm, -10cm, -15cm and -30cm, -50cm
	Soil potential sensor 253/257 (**)	Soil matrix potential	Depths are -5cm, -10cm, -15cm and -30cm
Meteo – station (**)	PT107	Air temperature	height ± 1.7 m above surface
	Tipping bucket rain gauge	Rain event	
	CS300 Pyranometer	Total solar wave radiation sensor	
	Anemometer	wind speed and direction	2 m above surface
	CS215 temperature and rel. Humidity probe	air humidity	

(*) Decagon device. Inc
(**) Campbell scientific. inc

Three different soil units were considered in this study to understand the behavior of water-soil interaction. The FO-DTS setup consisted of a 352 m long reinforced fiber optic cable buried at depths of 0 m, -0.005 m, -0.010 m, and -0.015 m and crossing the three soil units, which were argillaceous weathered black marls (BM), silty colluvium under grassland (GR), and silty colluvium under forest (FR). The hill-slope direction drove the water runoff from the northeast to the southwest, with different altitudes ranging from around 870 to 876 m.a.s.l (see Figure 3.8).

In this research, the fiber cable was manufactured by Brugg Cables Sensing Technologies-Switzerland ((http://www.bruggcables.com) and the FO-DTS unit system by AP-Sensing Advanced Photonic-Germany (https://www.apsensing.com). The FO-DTS measured the soil temperature every 6 minutes with a time interval of 0.5 m using a double-ended configuration. The optical fiber was installed by an incision in the soil to minimize soil damage around the fiber. Soil damage caused by mistaken trenching procedures can affect the porosity and temperature propagation, leading to errors in distributed temperature sensing, as pointed out by O'Donnell Meininger, and Selker (O'Donnell Meininger and Selker, 2015). In addition to the soil unit difference, this thesis also considers solar radiation.

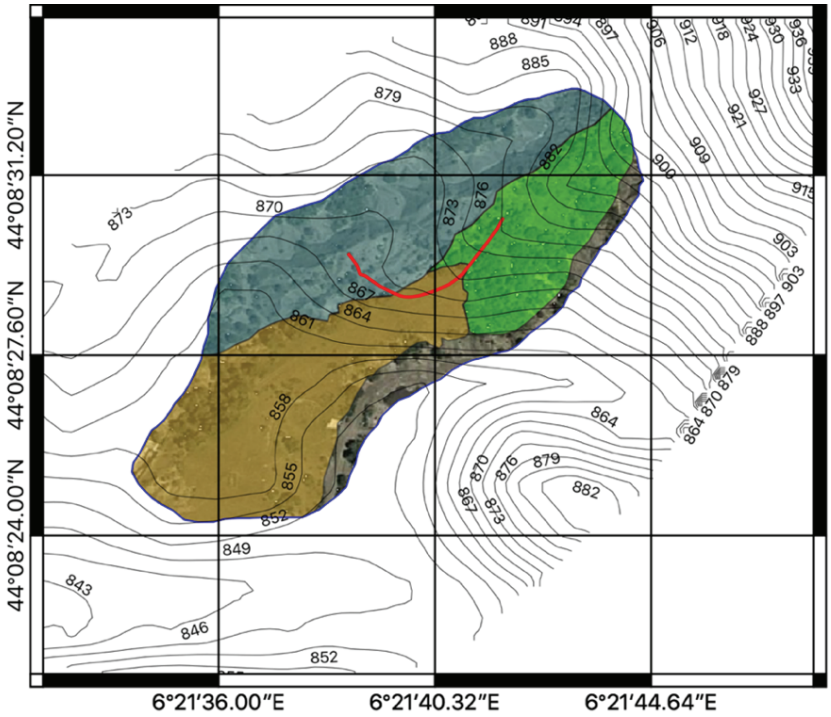

Figure 3.8 The Draix Bléone catchment hydrological observatory (South French Alps, Réseau de Basins-Versants/RBV) consists of three soil units. Those are the argillaceous weathered black marls (a gray area), silty colluvium under grassland (brown area), and silty colluvium under forest (green area). The red line illustrates the fiber cable installation.

At the soil surface, the fiber cables adhere to the soil and spread out to sense the air temperature. This condition allows the fiber cable to sense the temperature interface between the soil and the upper environment (Hilgersom et al., 2016; Keller et al., 2011; Krause et al., 2013). The upper boundary condition must be based on the temperature interface for heat transfer solutions. However, the diurnal temperature oscillation can act as a heat source for changes in soil temperature (see Figure 3.9). In other cases, Ciocca (2012) says that many advanced soil thermal studies use an active heat source, a coil, or a source of electrical current through the wire cable or fiber jacket (the part made of stainless steel).

The lateral observation site spans around 60 m from top to bottom (see Figure 3.10). The forested area with dense vegetation covers the colluvium bushes and fiber optic cables for 20 m. In this part, solar radiation

cannot directly heat the fiber cable. Therefore, the aerial radiation correction to the fiber cable is ignored. Furthermore, the fiber optic captures the soil temperature under the grass for 20 m. Following the same pattern, the 20 m long fiber was passed through the black marls, which have gully features as part of the erosion area. In the grassland and black marls area, the top layer of fiber cable senses the temperature interface between the soil and air temperatures.

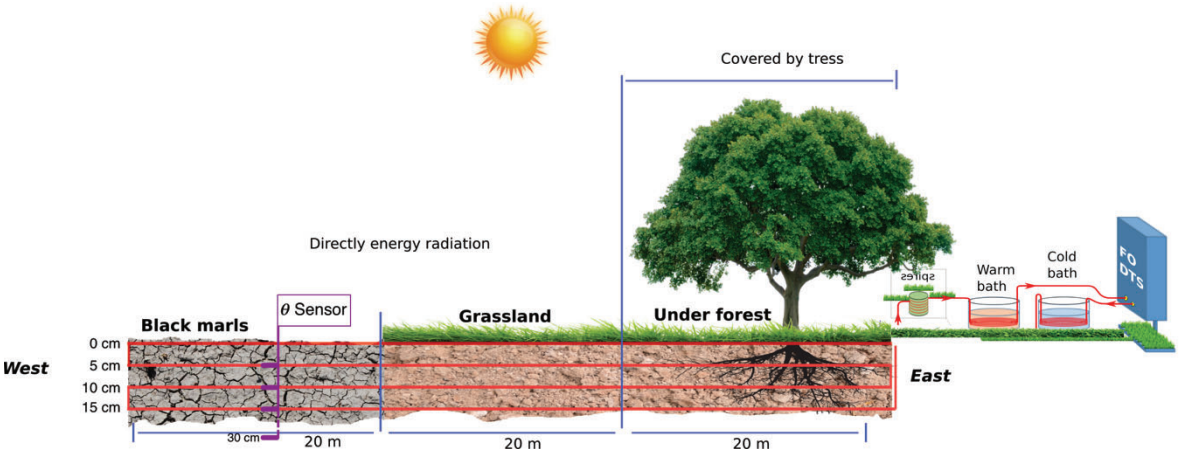

Figure 3.9 Observation setup. The baths were wired with a 352-meter fiber optic cable. The DTS instrument is configured for double-ended measurement through three soil units: colluvium under forest (20 m), silty colluvium under grassland (20 m), and argillaceous weathered black marls (20 m). The soil porosity ranged from 43% to 49%, and the clay content ranged from 19.89% to 28.66%.

Additionally, solar radiation directly heats the fiber cable, influencing the temperature reading. Solar radiation can increase the temperature uncertainty by more than 5 °C and less than 1.5 °C for relatively uniform areas (Seyfried et al., 2016; Vercauteren et al., 2011). Hence, aerial radiation should be corrected. In the subsurface, the fiber optic sensor only senses soil temperature affected by diurnal temperature oscillation as a passive heat source (Vogt et al., 2012). The temperature gradient and difference lead to the characterization of soil thermal properties, which are influenced by soil moisture (Béhaegel et al., 2007; Krzeminska et al., 2012b).

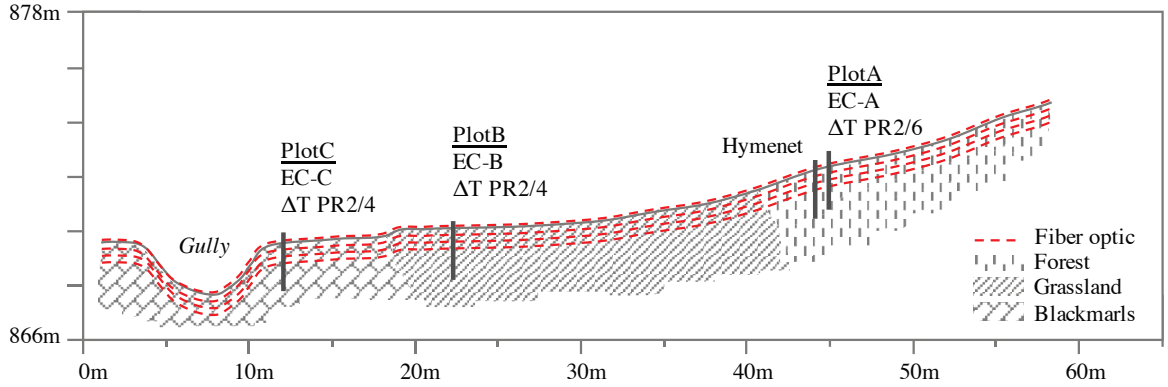

Figure 3.10 The $x = 0$ m is black marls (left side), and the $x = 60$ m is silty colluvium under the forest (right side). The other sensors were installed to complete the hydrological data observation.

Several data loggers were set up around the study site and connected to the internet service provider. This equipment recorded all data collection over time. Not only do the data loggers keep track of soil temperature, but they also keep track of soil moisture and soil matrix potential. The layout of the sensor and data logger positions is presented in Figure 3.11. Since solar radiation can heat the construction and lead to

inaccuracies in DTS temperature measurements, the main instrument and data logger are placed in the forest area.

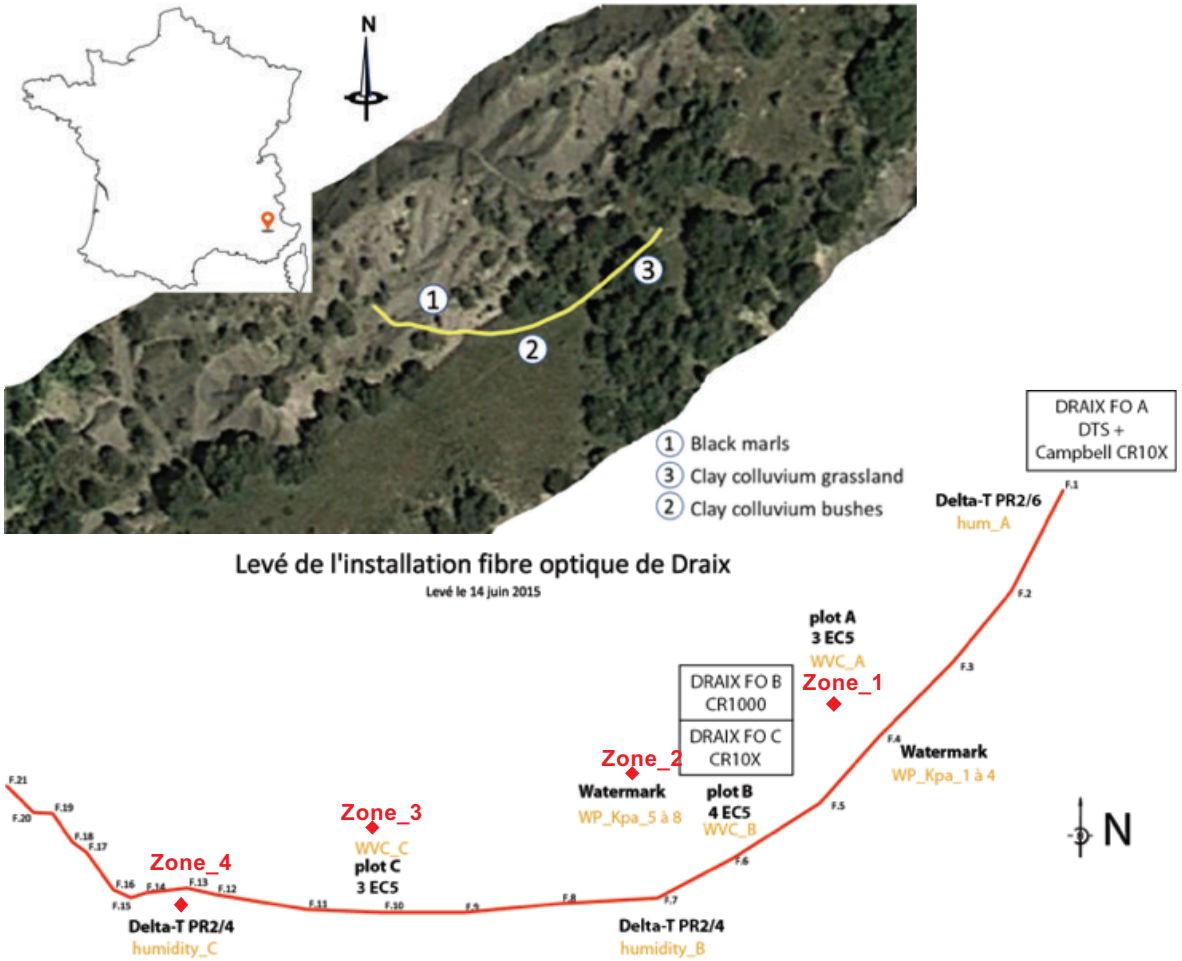

Figure 3.11 The layout of sensors and datalogger positions at the study site.

Figure 3.12 shows the two-ended setup used to measure changes in temperature at a depth of 15 cm. The configuration consists of 0 cm at the top surface as the upper boundary and -5 cm, -10 cm, and -15 cm as the lower boundaries. The deployment is expected to resemble Fick's second-law diffusion problem, making it easy to obtain predictions of soil thermal properties and models based on the heat equation solution (Krzeminska et al., 2012b). Vertical profiling is emphasized more for the 1D heat equation solution than the horizontal one (see Figure 3.13). Ten PT100 water temperature sensors are used in the calibration baths, with five sensors placed in the cold and warm baths, respectively. The cold and warm baths are installed at the beginning and end of the fiber cable, respectively. Around 40 meters of cable are also rolled in the cold and warm baths for calibration procedures. This configuration ignores step losses inside the fiber cable and can be used assuming the fiber cables are undamaged. However, this configuration can still correct attenuation along the fiber cable. The temperature in the warm bath in the reference is kept constant using an electric water heater. On the other hand, the cold reference uses the ambient temperature absorbed by the water in the baths. In the calibration procedure, the average of warm and ambient baths was used as temperature references, with standard deviations less than ±1.87 °C and ± 0.54 °C, respectively.

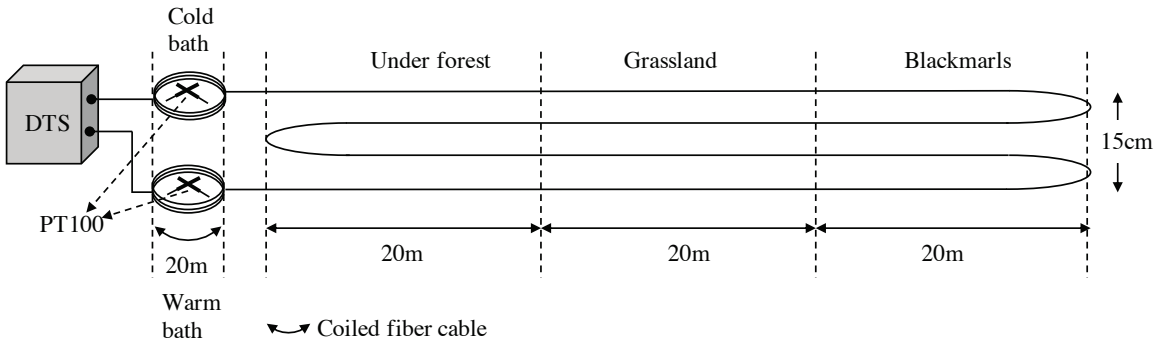

Figure 3.12 Double-ended configuration. The fiber was deployed through warm and cold baths and spread through three soil types. Ten sensors are placed in both baths as the reference temperature for dynamic correction.

The temperature along the fiber is determined by the ratio of Stokes and anti-Stokes intensity, which is influenced by attenuation (α) and capture coefficient (C). The heat propagation can be detected using a vertical grid configuration, as shown in Figure 3.13. This configuration enables the collection of temperature data in a grid and 2D matrix, with x and z representing distance and depth, respectively. The optical fiber measures the interface temperature between the soil and air at the soil surface. This is an essential initial condition for finite difference calculations. The heat equation can be solved by accounting for the diurnal temperature at the surface. This configuration is passively heated configuration (Steele-Dunne et al., 2010). The gridding setup is potentially suitable for further processing, such as 1D finite difference calculations for determining soil thermal properties and estimating soil moisture.

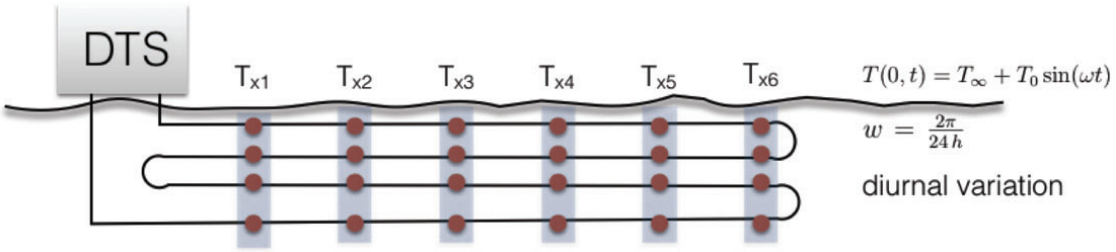

Figure 3.13 Gridding schemes approach Fick's law of diffusion equation. Vertical gradient accuracy is preferred for the 1D heat equation solution application.

Based on the schematic drawing in Figure 3.13, the temperature data collection is periodically rearranged to create a 2D slice profile. This profile can show the temperature propagation at a depth of 15 cm. The temperature variability can be analyzed for each depth in the time domain. At the surface, the optical fiber measures the air and soil temperature interface, which is influenced by radiation and precipitation. However, in the subsoil, the optical fiber only measures soil temperature, which is affected by water content.

3.3 Long-term observation and data collection

3.3.1 Temperature data observation and calibration

The long-term temperature observation at Draix using a fiber optic DTS instrument started at the end of 2015 and continued until the beginning of 2020. Fiber optic cables and ten PT100 sensors submerged in two reference baths were used to measure the temperature. With a measurement sampling time of 6 minutes, the DTS main control stored the data collected in a 16 GB data logger. This memory would be complete in about two years. The temperature datasets from the reference baths were stored in a Campbell datalogger, which has 128 KB of memory. However, unlike the DTS storage memory, the dataset on the Campbell datalogger could be automatically overwritten when the memory becomes full.

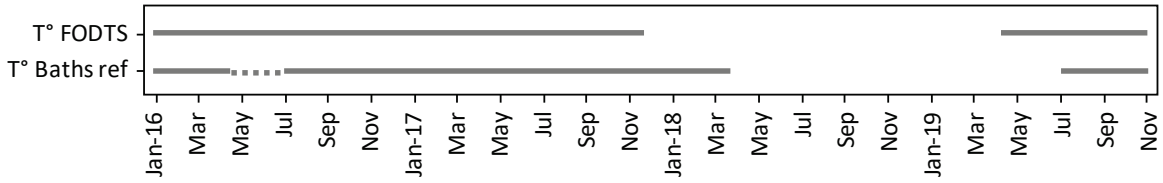

Figure 3.14 Overview of temperature data collection based on fiber optic DTS observation.

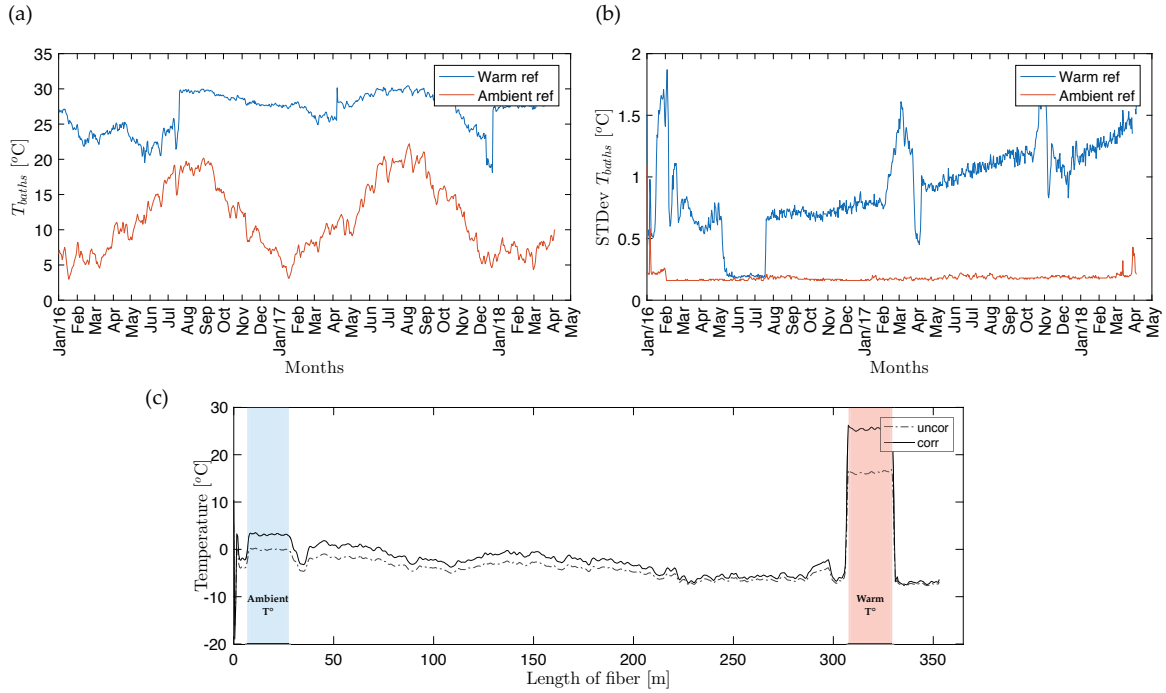

Figure 3.15 The corrected temperature along a 352 m fiber cable was obtained using known bath temperatures as references, including (a) daily average temperature, (b) standard deviation of known bath reference temperatures, and (c) both corrected and uncorrected temperature data.

In this thesis, the discussion focuses on 28 months, starting in January 2016. Two pairs of hydrological cycles are expected to provide environmental information and validation for the fiber optic DTS experiment. The soil thermal properties are also calculated as a proxy for soil moisture during the experimental period, combined with meteorological observations.

The raw temperature measurements along 352 m are corrected using temperature references installed at an ambient temperature reference and a warm temperature reference (see Figure 3.15a). Ten PT100s, submerged in two baths, are used; the averages are used as known temperature references. The standard deviation of the temperature measurements on the baths provides accuracy (see Figure 3.15b). In contrast to the warm bath reference, the ambient bath has the highest accuracy in temperature measurement. The ambient temperature in the water is evenly spread over time, while the water temperature in the warm bath is not heated evenly. The water heater is a source of heat from the inside, but the heating process is very dynamic and depends on the heat power pump from the coil heater; moreover, the outside temperature could cause uneven heating. The standard deviation of temperature references is about 0.25 °C and ranges from 0.27 °C to 1.87 °C for ambient and warm baths, respectively. The temperature increases after the correction process (see Figure 3.15c). The temperature variability along the fiber is calibrated periodically. Although the heat equation solution only uses the temperature differential along the fiber, the corrected temperature is used for the time-lapse temperature difference. Indeterminate disturbances in temperature are possible and are considered random disturbances.

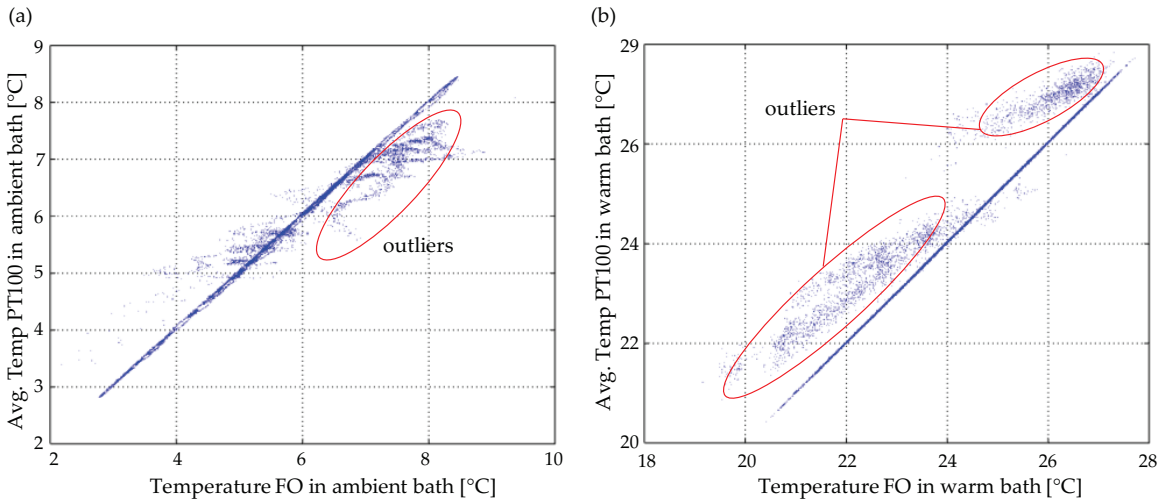

Figure 3.16 For example, compare the corrected and known temperatures on baths in the winter session. (a) ambient bath reference, and (b) warm bath reference.

Although the temperature of the fiber has already been corrected using the baths, due to some errors, slight temperature differences still occur (see Figure 3.16). The scattered points outside the linearity line are considered outlier datasets and are not used in the next level of processing. After the calibration, the remaining temperature is assumed to be affected only by aerial radiation errors (see Figure 3.17). The magnitude of the error can be calculated using a quantitative energy balance model.

Table 3.3 Material properties of fiber cable used in aerial radiation correction.

Description	Symbol	Values	Unit
Specific heat capacity [a)]	c_p	1.06	kJ kg^{-1} K^{-1}
Thermal Conductivity [b)]	λ	0.3 – 0.35	W^{-1} M^{-1} K^{-1}
Density of fiber [b)]	ρ	1.41	g cm^{-3}
Radius of fiber plus jacket [c)]	r	1.7	mm
Albedo of fiber [a)]	a	0.7	-
Emissivity [a)]	ε	0.92	-
Weight [c)]	W	18	kg km^{-1}
Length of fiber was heated by solar radiation	x	60	m

Material information source :
a) Sigmund et al., 2017
b) Neilson et al., 2010
c) BRUsteel ™ cable (Brugg, Switzerland)

The next important step after the calibration process is aerial radiation correction. The temperature error on the fiber-distributed sensing caused by aerial radiation is highly influenced by the material and environmental properties of the surface layer. In this case, the fiber cable located in the surface layer is 60 m long, and it is possible to have an aerial error reading (see Table 3.3). The albedo and emissivity values are kept constant and are based on the fabric's datasheet, which varies by a maximum of ± 20% and -12% to +33% for albedo and emissivity, respectively.

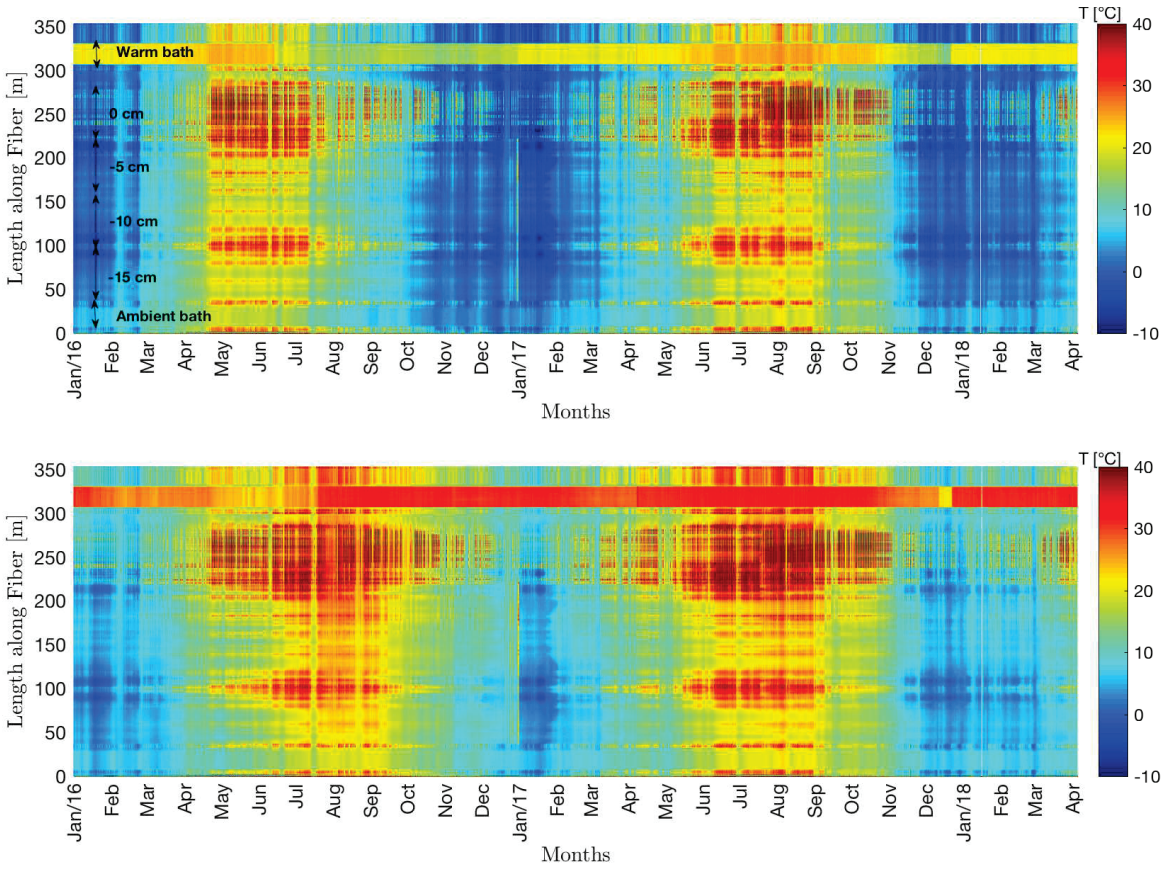

Figure 3.17 The temperature along the fiber over time, before (top) and after correction (bottom).

For example, on April 1, 2017, the modeled radiation error was 0.7°C because the sun's rays came in at 235.5 W m^{-2} (cloudy) and rained 3.04 mm/day. This correction considers the incoming energy flux from the conduction of the fiber cable and the outgoing convective energy exchange with the moving air, as well as shortwave and longwave radiation. The higher the incoming solar radiation, the higher the radiation error obtained, shown during the 08:00–17:00 CET. The

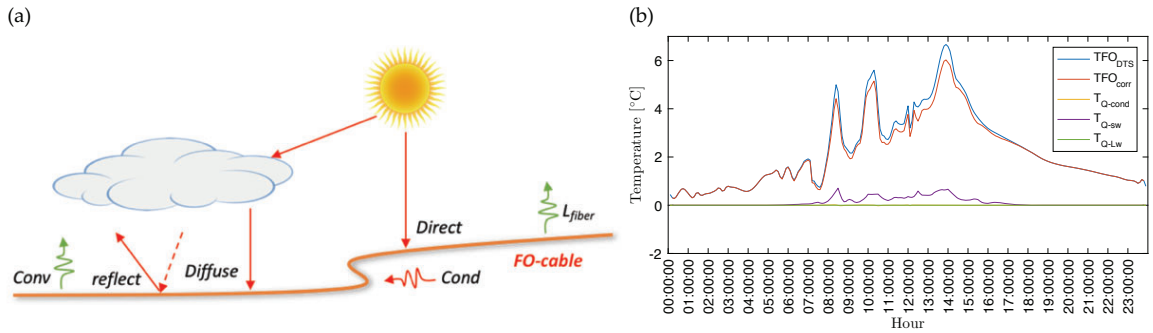

Figure 3.18 Quantitative correction of aerial radiation errors in fiber optic distributed temperature sensing. The correction process aims to replace the sun's radiation effect measured by the pyranometer. (a) The energy balance component consists of incoming and outgoing wave radiation around the fiber. (b) e.g., aerial radiation correction on fiber optic temperature $z = 0$ cm on April 1, 2017.

solar radiation correction for April 1, 2017, is shown in Figure 3.18b. The fully corrected temperature is obtained by combining dynamic calibration and solar radiation correction. Additionally, the complete correction and calibration of the fiber-distributed sensing temperature are arranged following the grid scheme (refer to Figure 3.13) and topographic setting. The temperature propagation is traced inside the soil occasionally (refer to Figure 3.19). However, the two-dimensional heat transfer equation approach does not yield a significant diffusivity calculation due to the relatively long-distance measurement ($\Delta x = 50$ cm). In contrast, the vertical

one-dimensional heat equation is more convincing in obtaining the diffusivity as a function of soil moisture, with a vertical depth difference of $\Delta z = 5$ cm ±1 cm.

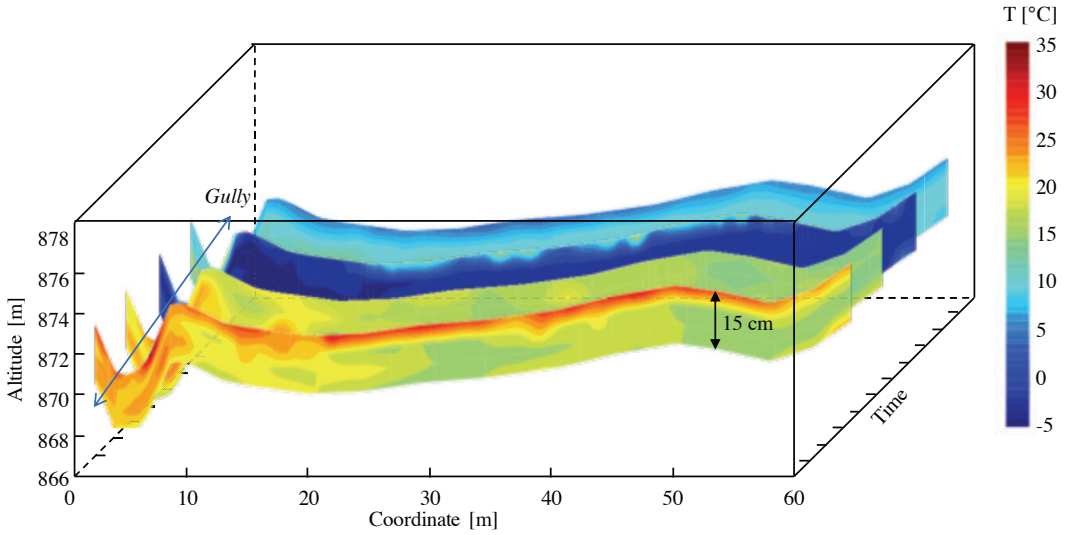

Figure 3.19 The temperature profile after full correction is presented in distance, altitude, and time during the observation, providing a comprehensive overview of the temperature changes over time and space.

The passively heated fiber optic scheme utilizes diurnal solar radiation as a heat source, and the diurnal temperature variation can serve as an initial numerical condition. Monitoring the upper surface is essential for constraining the numerical shallow surface model. Heat transfer and energy balance at the interface between air and the top layer of soil must be considered. The estimation of heat flux and the control surface index for evaporation are studied for monitoring soil moisture related to atmospheric exchanges (Castle and Elliott, 1999). However, the diurnal temperature fluctuation also affects the diffusivity calculation, and the periodic artifact always appears for the same 24-hour period (Jong van Lier and Durigon, 2013; Krzeminska et al., 2012b). The temperature at the atmospheric surface significantly impacts the boundary layer and may indicate different forcing mechanisms (Thomas et al., 2012).

3.3.2 Meteorological data collection

The fact that meteorological observations are needed is a big part of how well shallow surface hydrological observations work. Several instruments were put in place at the study site to record the air temperature, humidity, precipitation, solar radiation, wind speed, and wind direction (see Table 3.2). Figure 3.20 shows that these instruments were about 140 meters from the fiber optic installation. The meteorological station was precisely placed at 44°8’25.069"N 6°21’36.421"E, with an altitude of 872 meters above sea level. The meteorological sensors collected the atmospheric dataset every 5 to 10 minutes to record the weather fluctuations during observation. In most cases, the meteorological conditions play a crucial role in general hydrological investigations in the French Alps and Mediterranean areas (Caris and Van Asch, 1991; Peñarrocha et al., 2002).

Figure 3.20 Location of the meteorological station.

The objective of the meteorological observation is to present the climate regime during the measurement campaign in the Draix-Bléone catchment area. However, the meteorological time series measurement is not always continuous and reliable (see Figure 3.20). In this case, the meteorological observation stopped in April 2018 and resumed at the beginning of 2019 until now due to problems with the datalogger instruments. The internal battery of the datalogger survived for around 1.5 years of observation.

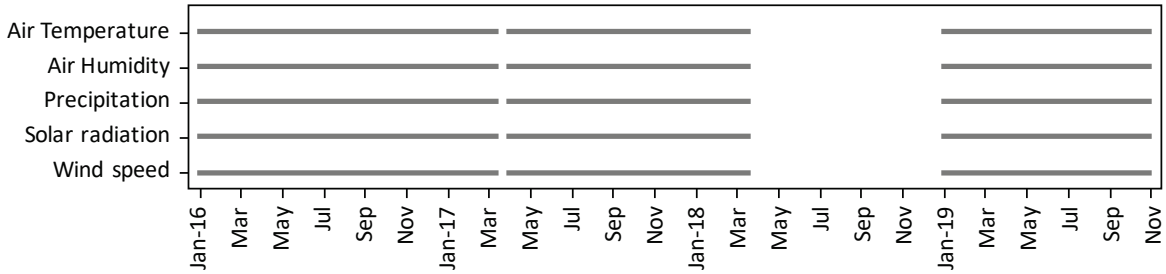

Figure 3.21 Overview of meteorological data collection and estimation.

Air temperature and precipitation

The region is characterized by a Mediterranean climate system with an average daily air temperature ranging from -7.15 to 29.37 °C for winter and summer, respectively (see Figure 3.22a), and a highly variable and irregular rainfall regime (see Figure 3.22b). During the observation period, a tipping bucket was installed to record rainfall events and measure precipitation with a precision of 0.2 mm and a measurement frequency of every 10 minutes. However, the average monthly air temperature shows weak correlations with precipitation, with a correlation coefficient of -0.17 for 2016 and -0.41 for 2017.

The rain gauge recorded 343 rainy days from January 2016 to April 2018 (825 days), with a cumulative precipitation of 1913 mm, averaging 2.3 mm per day. The rainfall intensity was calculated monthly to determine precipitation characteristics. At least two winter storms were reported in November 2016 and December 2017, with a rainfall intensity of more than 70 mm per day (see Figure 3.22c and d). No episodes of torrential rain were observed during the study. However, the distribution of rainfall was highly complex. The different cumulative rainfall amounts indicate the complexity of the annual rainfall distribution, with 920.8 mm in 2016 and 653.6 mm in 2017.

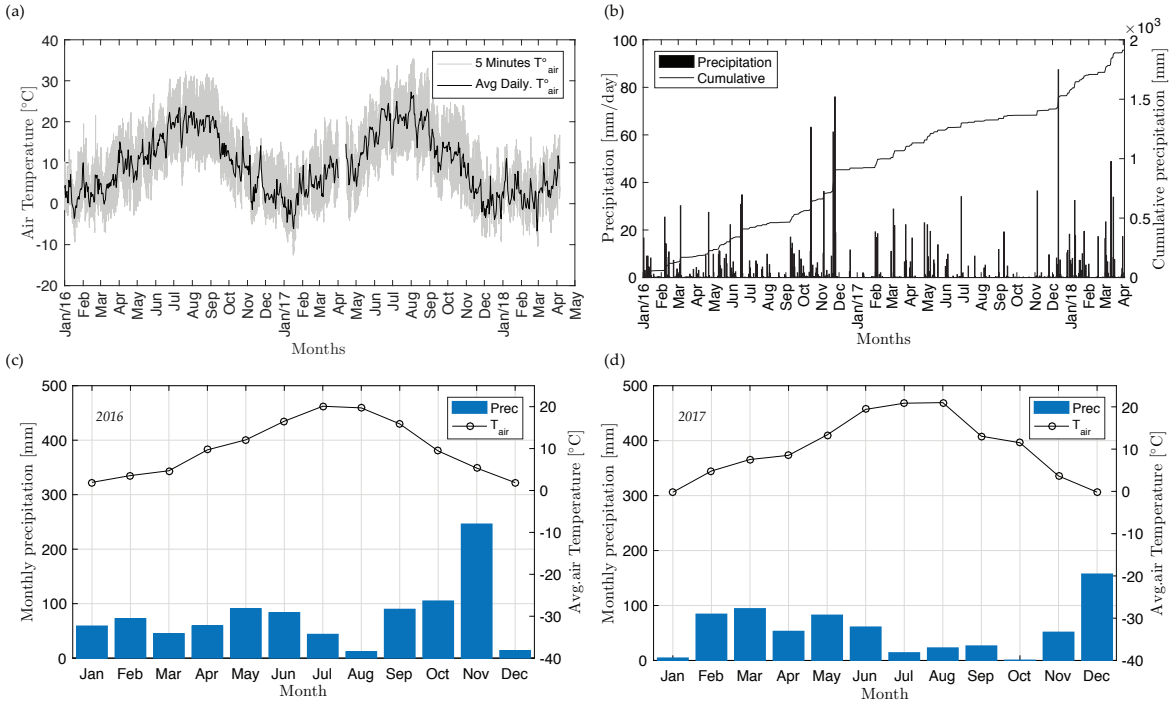

Figure 3.22 Meteorological data collection during the observation period. (a) air temperature variation, (b) precipitation and cumulation, (c) and (d) are monthly precipitation indicating rainfall distribution in 2016 and 2017, respectively.

Solar radiation, wind speed, and air humidity

At the same station, sensors were set up at different heights above the surface to measure solar radiation, wind speed, air humidity, wind direction, air temperature, and rainfall. The height of each sensor was adjusted as necessary; for example, the anemometer was installed at a height of 2 meters above the surface to measure wind speed and calculate potential evaporation. The psychrometric was estimated based on empirical calculations to determine potential evapotranspiration. The determination of psychometrics considered the altitude, air temperature, and corresponding atmospheric pressures.

Table 3.4 Climate characteristics for the Draix Bléone catchment area

	Avg. Air Temperature [°C]	Precipitation [mm]	Evapotranspiration [mm]	Avg. Air Humidity [%]	Avg. Wind speed [m s^{-1}]	Sunshine duration [h]
2016						
Annual	10.10	974.20	792.89	64.81	0.96	4617.6
Max. monthly	20.10	258.60	140.22	72.79	1.33	482.20
Min. Monthly	1.88	11.80	5.83	56.48	0.56	296.10
2017						
Annual	10.37	650.80	816.64	61.51	1.01	4753.3
Max. monthly	21.00	157.40	148.78	71.02	1.32	542.00
Min. Monthly	-0.20	0.60	13.78	51.98	0.84	292.90
2018						
Jan-March 2018	2.90	338.20	79.00	68.47	0.88	986.7
Max. monthly	4.41	186.40	58.20	70.14	1.01	379.20
Min. Monthly	0.38	23.40	2.80	67.18	0.72	303.10

Evapotranspiration

In addition to measuring precipitation in the field area, wind speed, air humidity, and solar radiation were recorded for potential evaporation calculations, and aerial correction radiation is presented in section 3.3.3. The Penman-Monteith method was used to calculate daily potential evapotranspiration (ETp). The effective precipitation (PE), calculated by subtracting potential evaporation from precipitation, shows a surplus of

precipitation from March to October and a deficit from November to February for each year, respectively (see Figure 3.23). The maximum effective precipitation is almost 6 mm per day, with an average of 2.4 mm per day.

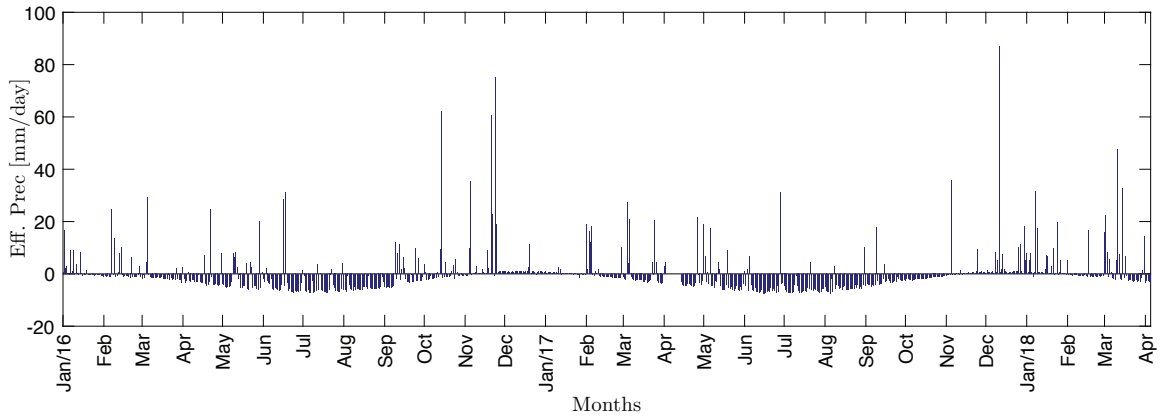

Figure 3.23 Effective precipitation at the study site meteorological station in 2016–2018.

Referring to the climatic characteristics of the Draix area as outlined in Table 3.4 and the effective precipitation plot in Figure 3.23, it can be seen that the annual precipitation excess fluctuated, with values of 181.31 mm per year in 2016, 165 mm per year in 2017, and 279 mm from January to March 2018. In 2017, the annual temperature was 0.27 °C higher than in 2016, the average wind speed was 0.05 m/s higher, and the sunshine duration was 135.7 hours longer, confirming that the drought period was particularly severe in 2017.

3.3.3 Hydrological data collection

Soil characterization

Martin (2016) gave information about the porosity and density of the soil in the study site area. He reported that the soil moisture in the grassland was no more than 0.3 mm^3/mm^3, while in the forest, it was 0.42 mm^3/mm^3. This value indicates that the soil moisture reached saturation, filling the soil porosity. Furthermore, he estimated soil porosity based on soil density measurements (see Table 3.5). The maximum porosity in the forest area reached up to 51%, which may be attributed to the high concentration of organic matter.

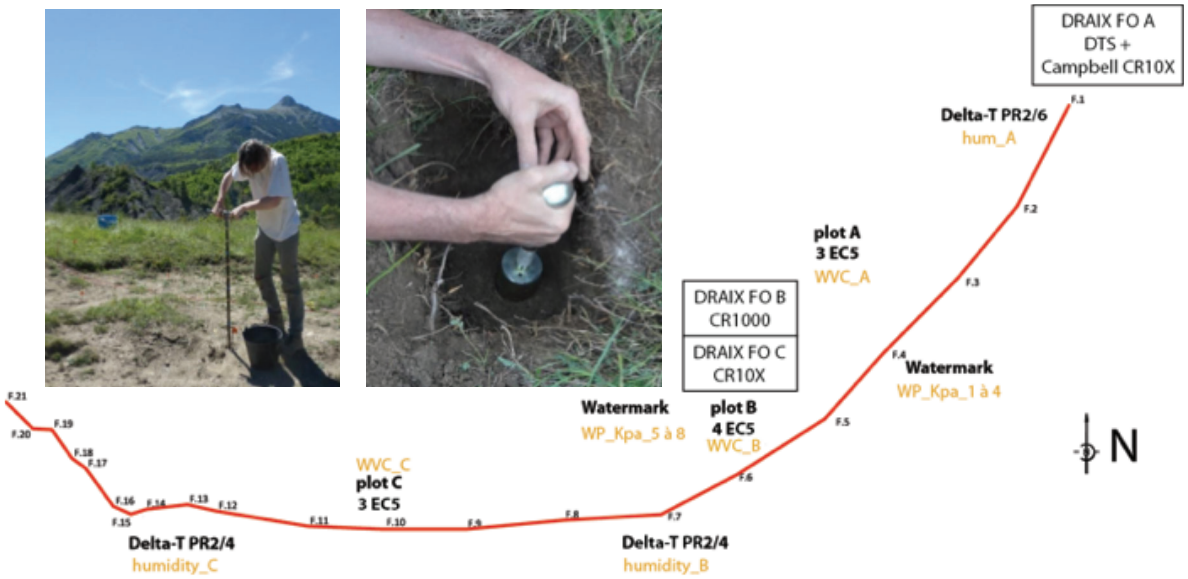

Figure 3.24 Soil sampling location. Augers or metal cylinders picked up the soil. Plots A, B, and C are the point locations of soil sampling. Further, soil samples are analyzed in the laboratory to obtain the hydrodynamic properties of the soil. Photograph source: Martin, 2016.

Table 3.5 The density and porosity of soil types (Martin, 2016).

Soil Types	Density, ρ [g cm^{-3}]	Porosity, ϕ [%]	Remarks
Forest	1.27 to 1.56	40 to 51	verified
Grassland	1.33 to 1.47	43 to 49	verified
Blackmarl	1.72 to 1.86	28 to 34	no verified

Table 3.6 The percentage and classification of soil composition show the textural terms applied to soils with various fractions of sand (50 – 20 μm), silt (2 – 50 μm), and clay (2 μm) composition.

Sample	Sand (%)	Silt (%)	Clay (%)	CDA	USDA	SSEW	INTL
Draix_A	28.67	51.44	19.89	silty loam	silty loam	clay loam	silty loam
Draix_B	1.07	71.32	27.6	silty clay loam	silty clay loam	silty clay loam	silty clay loam
Draix_C	5.76	68.58	25.66	silty loam	silty loam	silty clay loam	silty loam
Draix_D	5.25	66.09	28.66	silty clay loam	silty clay loam	silty clay loam	silty clay loam

CDA : Canadian Department of Agriculture
USDA : U.S. Department of Agriculture
SSEW : Soil Survey for England and Wales INTL : International Soil Association

In addition, soil texture and fraction measurements were taken from four locations around the study site, including soil under forest, grassland, and black marls (Draix_A, Draix_B, Draix_C, and Draix_D). The samples were then examined in a soil lab to determine the texture and fraction of the soil. Most of the textural soil fraction at the study site was found to be silty clay loam (see Table 3.6 and Figure 3.25), which shows that the soil has a uniform grade. Porosity, bulk density, and water in the soil significantly affect hydraulic conductivity and specific discharge.

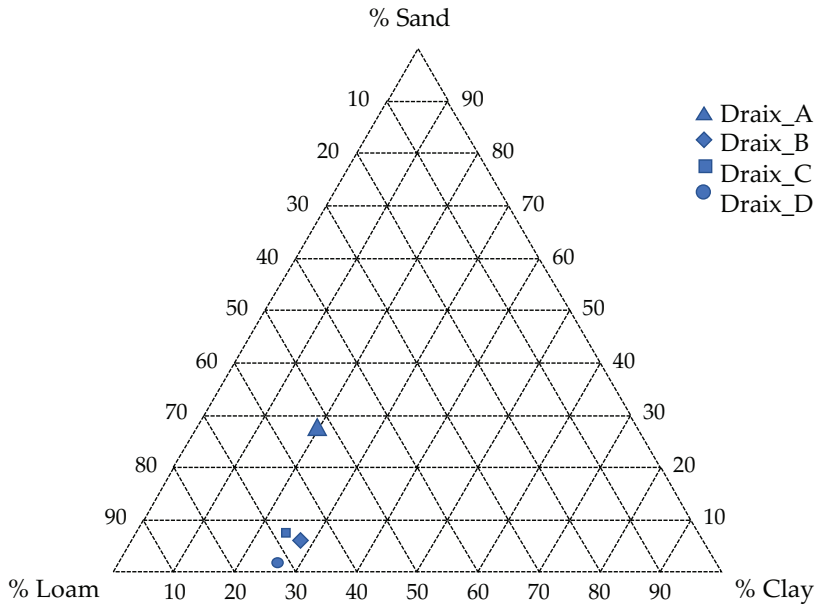

Figure 3.25 The soil texture triangle shows the textural terms applied to soils with various sand, silt, and clay composition fractions.

Generally, the texture of the soil, comprised of the weight of clay, silt, and sand, determines how its particles are spread out. Clay is defined by a grain diameter of less than 2 μm, while silt has a diameter ranging from 2 μm to 50 μm, and sand has a diameter ranging from 50 μm to 2000 μm. Examination of the soil samples revealed that the grain size is dominated by particles smaller than 100 μm (see Table 3.7), categorizing it as silty

loam clay. Furthermore, the organic fraction in the samples was found to be 9.36%, 8.90%, 6.88%, and 6.32% for samples Draix_A to Draix_D, respectively.

Table 3.7 The completed soil determination texture determines the grain sizes of samples.

Diameter [µm]	DRAIX_A [%]	DRAIX_B [%]	DRAIX_C [%]	DRAIX_D [%]
< 2	19.89	27.60	25.66	28.66
2 - 20	40.69	57.86	53.16	54.45
20 - 50	10.75	13.46	15.42	11.63
50 - 100	3.13	1.06	4.36	3.29
100 - 200	4.64	0.01	1.40	1.97
200 - 500	18.11	-	-	-
500 - 1000	2.79	-	-	-
1000 - 2000	-	-	-	-

Soil saturation laboratory testing

As part of this research, Julian Gance, in 2015, measured the saturated hydraulic conductivity (κ_{sat}) and in situ volumetric water content (θ_{sat}) of soil at the study site for three days in August 2015. Samples were taken from several depths, -5 cm, -10 cm, -15 cm, and -30 cm, at four locations around the fiber optic cable (zones 1, 2, 3, and 4, see Figure 3.11). The sample collection comprised three samplings for each depth position to increase measurement precision. The sample number is 84, divided into 42 samples for saturated volumetric water content and 42 for saturated hydraulic conductivity. The average saturated volumetric water content and hydraulic conductivity were obtained as the best values for each depth position.

Hydraulic conductivity plays an essential role in water flow through the soil medium in saturated soil. The saturated hydraulic conductivity at the study site was determined using the permeameter charge constant applied to 42 soil samples (zones 1 to 4). Laboratory testing revealed that the volumetric water content θ_{sat} for the soil under the forest (zone 1) ranged from 0.2 cm³/cm³ to 0.33 cm³/cm³. For the grassland (zone 2), it was slightly higher, reaching up to 0.4 cm³/cm³, while for the black marl (zones 3 and 4), it was slightly lower, at only around 0.28 cm³/cm³. Generally, the soil at deeper positions was found to be more compact than the upper layer, as indicated by the lower saturated volumetric water content at deeper positions compared to the upper ones (see Figure 3.26).

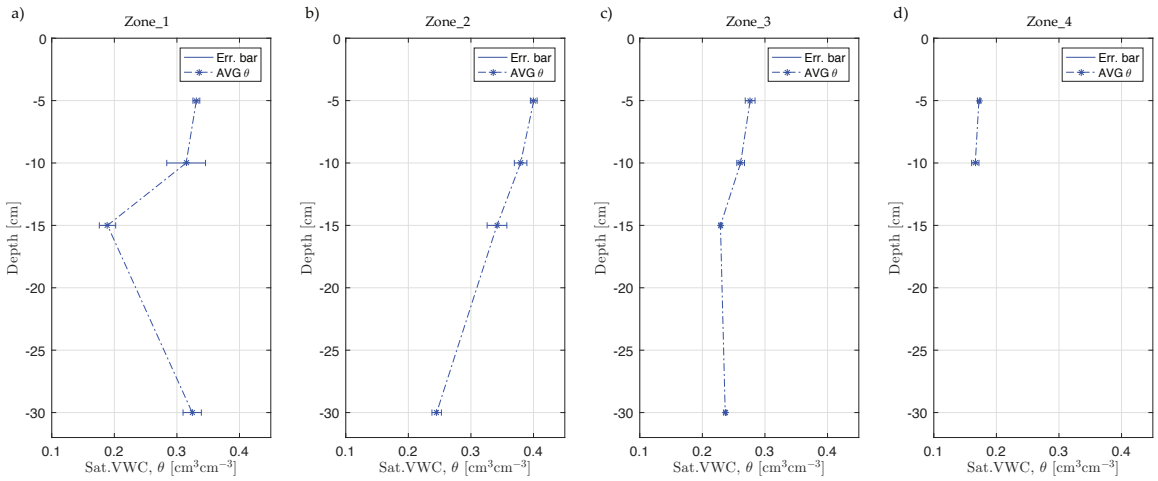

Figure 3.26 The saturated volumetric water content is based on soil laboratory testing. a) Zone_1 is in the forest, b) zone_2 is in the grassland, and c) zone_3 and d) zone_4. Zones 3 and 4 are in the black marls.

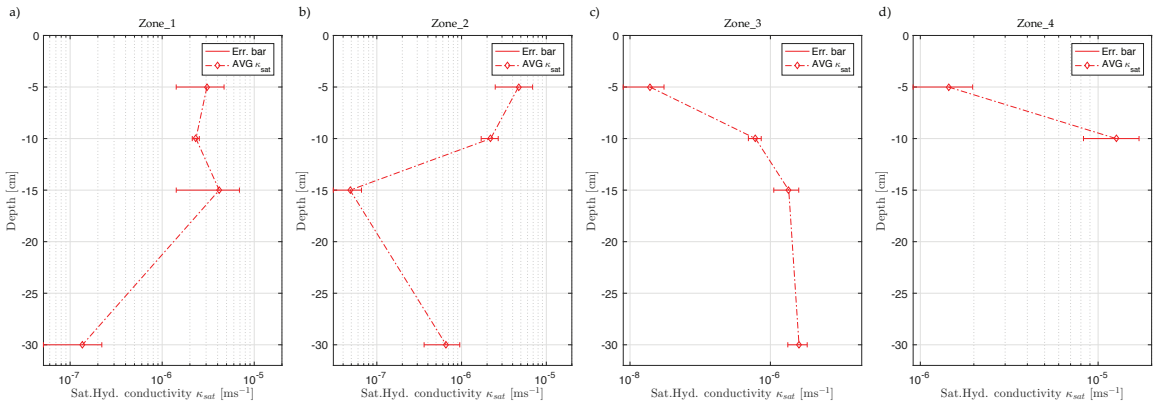

Figure 3.27 The saturated hydraulic conductivity is K_{sat} based on soil laboratory testing. a) zone_1 at the forest, b) zone_2 at the grassland, c and d) zone_3 and zone_4 at black marls area.

The mean value of κ_{sat} is obtained by averaging three samples for each depth position, like examining saturated volumetric water content. The hydraulic conductivity of the soil under forest and grassland is higher at the upper layer than at the deeper position (see Figure 3.27a and b). This situation is consistent with the saturated volumetric water content, indicating that water flows more easily on the upper layer. However, the saturated hydraulic conductivity of black marls tends to be higher at the deeper position (see Figure 3.27c and d) because the black marls area is dominated by silty clay. In contrast, a sand fraction dominates the soil under the forest, and the grassland is dominated by different vegetation.

Soil moisture measurement using ML3 and EC5 Decagon

In this study, soil moisture measurements were taken directly with a standard soil moisture sensor probe and indirectly using temperature as a proxy parameter. For the standard measurement method, there were two ways to find out how much water was in the ground: short-term fieldwork with the ML3 probe sensor and long-term observations with the EC5 decagon probe sensor. In May and June 2016, Romain Martin and Colas Bohy Provost went into the field to collect soil moisture data at almost 110 points around the fiber cable as part of the fieldwork campaign. The point measurements were taken 1 to 2 meters from the fiber cable, as shown in Figure 3.28. The study aimed to connect the different zones in the Laval basin by checking and comparing the soil moisture sensors installed in the basin, as Martin (2016) explained. This method made it easier to compare different zones based on how the ground was used in each one.

(a) (b)

Figure 3.28 Soil moisture was measured using ML3 during a fieldwork campaign by Romain Martin and Cola Bohy Provost in May and June 2016.

Another strategy used for soil moisture measurement is long-term observation. Since 2016, the time series of soil moisture has been measured using an EC5-Decagon with a 5-minute sampling period and recorded by a Campbell Scientific datalogger. The sensor probes were installed at EC-A, B, and C locations near the fiber optic and at depths of -5, -10, and -15 cm below the surface (refer to Figure 3.7). The objectives of this approach are to monitor soil moisture changes, estimate soil hydraulic properties, and validate the calculated soil moisture from fiber-optic observation and the Hydrus model. However, the data collected from EC-B and EC-C had very noisy errors, rendering them unusable (Figure 3.30).

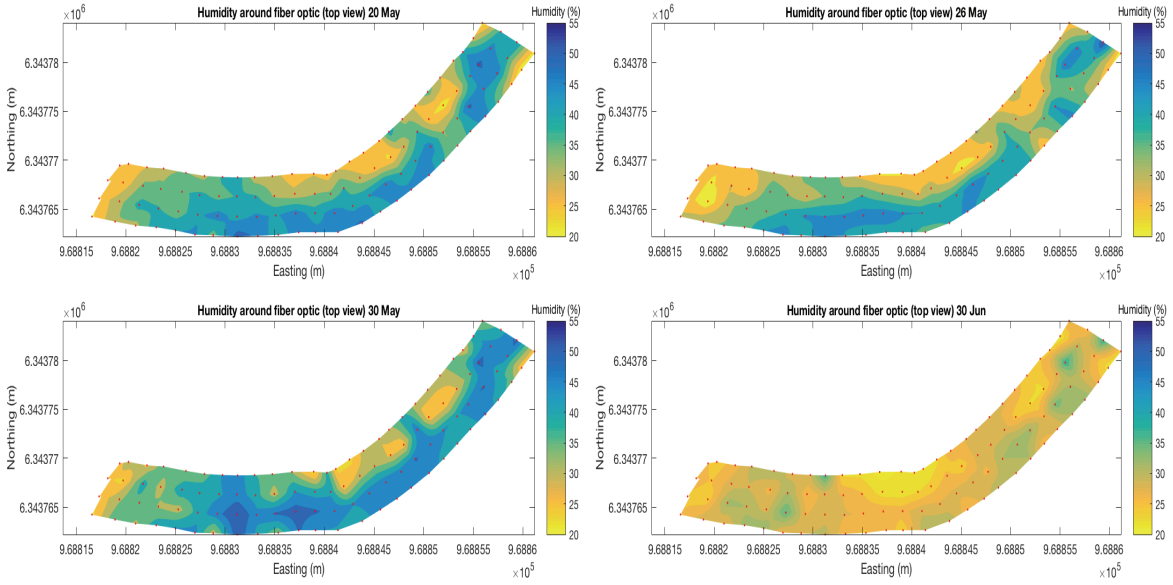

Figure 3.29 Variability of soil moisture during fieldwork campaigns (20, 26, 30 May, and 30 June 2016) following Figure 3.28a.

During the fieldwork campaigns conducted on May 20th, 26th, 30th, and June 30th, 2016, soil moisture was measured on the surface to observe the influence of vegetation on the variability of soil moisture after rainfall events near the fiber cable. It was concluded that the grassland part of the site was the wettest during all the fieldwork campaign periods, and the little vegetation present in this area made it the most exposed to rain, as reported by Bohy Provost (2016) and Martin 2016) (see Figure 3.29).

The soil moisture recorded by the EC5 Decagon on plot A fluctuated coherently with precipitation data, as shown in Figure 3.23 and Figure 3.30. However, between February and June 2017, the data record contained

noise and erroneous readings. The maximum soil moisture rose to 0.43 mm^3/mm^3, and the surface layer dried out more quickly than the lower layer. The soil moisture fluctuated less during the summer, even though rainfall occurred. The situation is likely due to the negative values of effective precipitation, as shown in Figure 3.23. The soil experienced rapid drought during the summer session, and the probe sensor could not measure effectively.

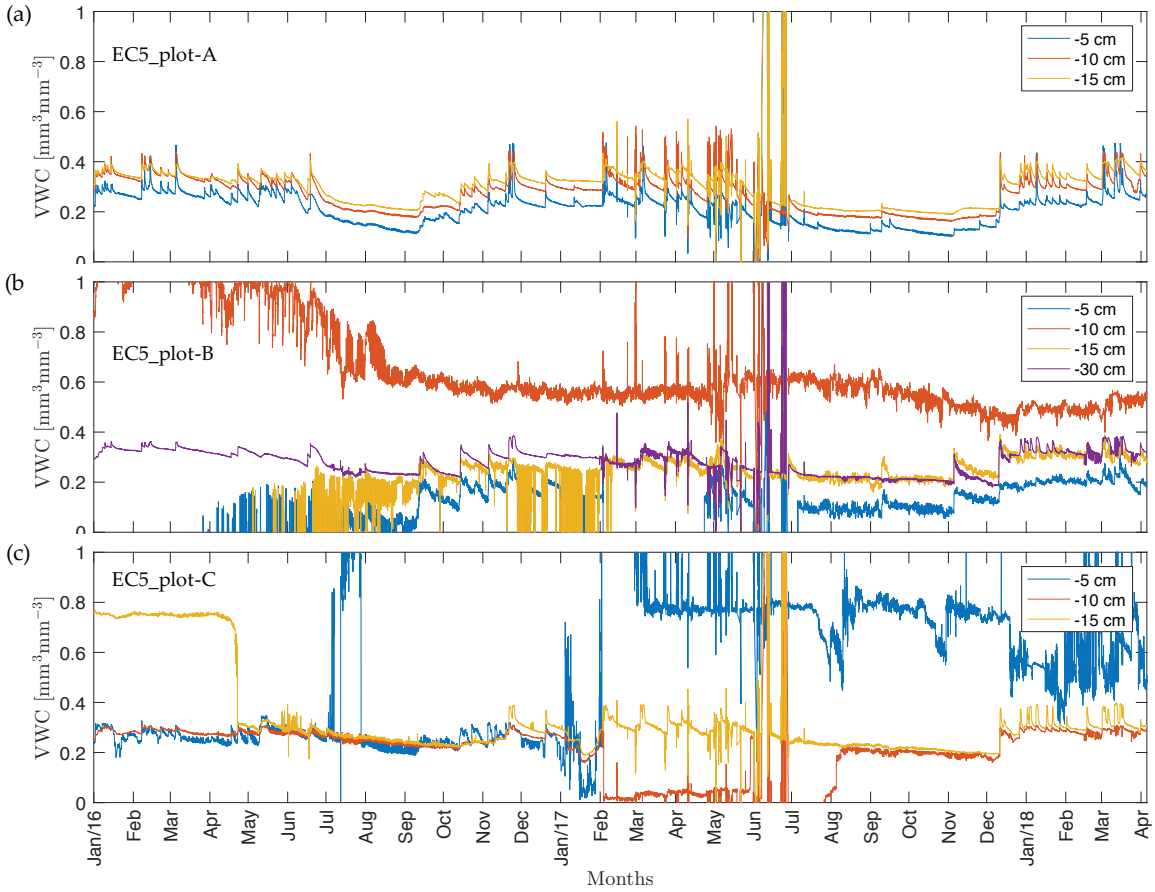

Figure 3.30 The EC5 Decagon measured long-term soil moisture. (a) EC-A, (b) EC-B, and (c) EC-C. The EC plots B and C show errors in reading, so they are neglected in hydrology analysis.

In the last part of this subsection, we talk about how sensor 253/257 from Campbell Scientific measured the soil water potential. The data was gathered to determine the soil's hydraulic properties using the inversion method, which involves nonlinear fitting curves and fitting time series. The Van Genuchten model is used in the nonlinear curve fitting approach, while Hydrus 1D serves as standard software for hydrology analysis in the time series fitting approach. The soil water potential readings are then converted to groundwater, which is essential for the water-flow lower boundary condition in Hydrus 1D simulation and for the "S form" curve on the Van Genuchten model. The sensors were installed at different depths, including 5, 10, and 30 cm below the surface, as shown in Figure 3.31.

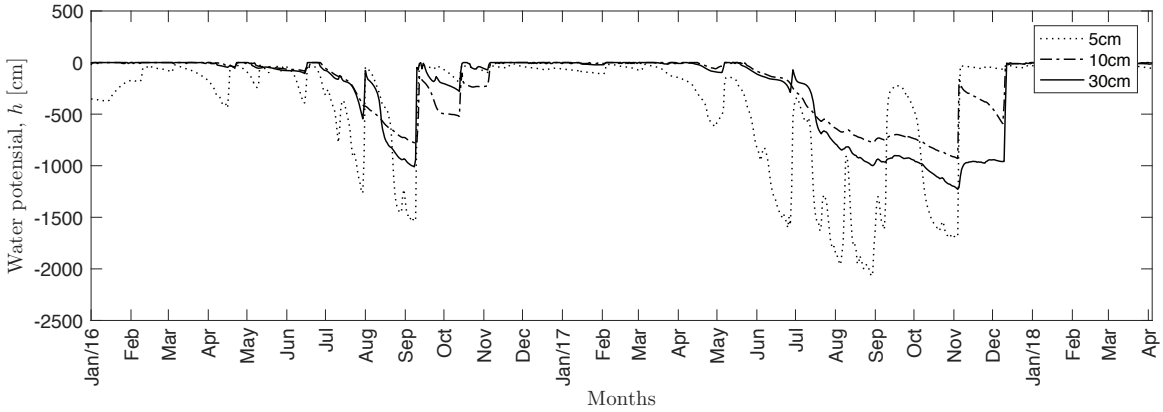

Figure 3.31 The water-soil potential was measured at the same position as the EC5 decagon at Draix in 2016–2018.

The potential water data plotted during the observation period reveals that the soil went through a period of drought from July to November, with an extreme drought occurring during the summer of 2017. Despite this, the sensors still detected some rainfall events during this period, which confirms the discussion above regarding long-term soil moisture measurements and excess precipitation during the observation. Notably, the soil water potential at a depth of 5 cm can decrease to 2000 cm during the drought period but significantly increase when rainfall occurs.

This page intentionally left blank.

Chapter 4: Passively Heated Fiber Optic Distributed Temperature Sensing For Long-Term Soil Moisture Observations

The work presented in this chapter is based on Kusnahadi Susanto, Jean-Philippe Malet, Xavier Chavanne, Vincent Marc, Julien Gance. (submitted): "Passively Heated Fiber Optic Distributed Temperature Sensing For Long-Term Soil Moisture Observations", Vadose Zone Journal.

Abstract : This paper presents a strategy to improve spatial and temporal volumetric water content (VWC) using passive DTS observation. We demonstrate this method using 22 months of passive fiber optic distributed temperature (FO-DTS). This method has previously encountered challenges, primarily due to noise effects and instability of diurnal temperature. We improve the water traceability by employing numerical estimation of the soil thermal diffusivity. This method was tested on a slope catena at the Draix–Bléone Mediterranean catchment (South-East France) and with synthetic data prior to applying it to field-scale scenarios. The results show a good performance as indicated by a determination coefficient of 0.92, a root mean square error of 0.06 m^3/m^3 and a mean relative percentage error of 1.41%. We conclude that the proposed strategy is convenient for analyzing passive DTS experiments using diurnal heat sources, where reliable thermal diffusivity and VWC data can be obtained without the use of active application sources.

Keywords: passively heated FO-DTS, soil moisture, thermal diffusivity, Hydrus

4.1 Introduction

Numerous techniques have been devised to monitor space and time variations of soil-water content, including direct manual soil sampling, and indirect methods using electromagnetic, thermophysical and radiation-based instruments. The direct manual technique of soil sampling and further gravimetric weighting can be considered as the reference method, but it is limited by the spatial representativity of the samples. Consequently, indirect methods emerged as promising approaches for wide areas survey and long-term continuous monitoring. Various active and passive radiation instruments, (such as neutron and cosmic-ray probes), electromagnetic and thermophysical-based sensors are used as indirect measurement techniques. Hybrid sensing methods combining soil permittivity and temperature have also been proposed (Chavanne and Frangi, 2014).

Soil temperature is a readily measurable environmental parameter that enables the derivation of volumetric water content (Béhaegel et al., 2007). Fiber Optic Distributed Temperature Sensing (FO-DTS) has been employed as a primary method for soil temperature measurements (Bense et al., 2016) and indirect estimations of soil moisture using active and passive measurements (Steele-Dunne et al., 2010; Dong et al., 2017). In practice, FOR TDS can measure a lot of temperature data from optical fibers embedded in shallow soil and on the ground surface with a vertical grid configuration. FO-DTS temperature measurements use many other scatterings such as Brilloin and Raman scattering. Raman scattering in the optical fiber to achieve a temperature resolution as small as ± 0.01°C.

In active FO-DTS mode, an active thermal source is created by a heat source, maintained for a few seconds to minutes, and influences a shielded cable *via* the Joule effect (Sayde et al., 2010, Ciocca et al., 2012). Analyzing the temperature decay with time allows the volumetric water content (VWC) of a soil to be determined with an error of less than 7% (Weiss, 2003; Cao et al., 2015). The accuracy of the active mode measurements exhibits a first-order proportional relationship with the water content. When the volumetric moisture content is 0.05 m^3m^{-3}, the standard deviation of the readings is 0.001 m^3m^{-3}, whereas, at a volumetric moisture content of 0.41 m^3m^{-3}, the standard deviation is 0.046 m^3m^{-3} (Sayde et al., 2010). The main drawback of active FO-DTS is that an external power source is required to generate the thermal source, which is complex to setup in remote areas and for long-term measurements.

In the passive measurement of VWC FO-DTS mode, the thermal source is created by the surface energy flux. Temporal variations in energy follows a diurnal period independent of local and global weather changes and shifts in vegetation cover (Sigmund et al., 2017). Several strategies for tracing soil VWC using passive temperature observations were developed (Halloran et al., 2016) using local measurements (e.g., point probe sensors) either installed on vertical profiles (Bechkit et al., 2014) or placed along cross-sections (Anderson, 2005).

For soil VWC estimations based on thermophysical properties, passive FO-DTS is simpler but less accurate than active heated DTS (Steele-Dunne et al., 2010; Suárez et al., 2011; Ciocca et al., 2012). Indeed, using natural heat fluxes as a thermal source requires the characterization of radiative, convective and conductive components; such measurements are rarely achievable in the field. Consequently, estimating soil VWC using this mode is sensitive to many factors (Cao et al., 2015), including air temperature differences, vegetation cover, seasons and weather condition. One of the common approaches for calculating VWC involves data assimilation, utilizing temperature measurements to determine VWC. This method ensures the accuracy of the results by incorporating correlations between temperature and soil moisture in the shallow soil layers (i.e., the top ~50 cm; Dong et.al., 2015). A second, approach is to estimate soil VWC using thermal diffusivity by solving the heat transfer equation. Durigon (2013) proposed a method to calculate soil thermal diffusivity based on temperature measurements at multiple depths. This analytical approach analyzes the amplitude damping and phase lag between temperature measurements (Durigon, 2013). This approach is strongly dependent on the sinusoidal waveform of soil temperature, which varies on diurnal, seasonal and annual periods (Carslaw and Jaeger, 1959; Jong van Lier and Durigon, 2013). Therefore, diffusivity estimated from time resolution techniques can only be used to determine daily values of VWC. Another study (Tabbagh et al., 2017) described vertical water flows by calculating thermal diffusivity using a simple numerical finite element scheme based on soil temperature profiles. This approach allows the thermal properties of a soil to be determined over short distances and at any desired time interval (Tabbagh et al., 2017). The same approach was used by Krzeminska et al. (2012) to apply an explicit finite difference scheme to track the spatial variability of soil–water saturation in an area influenced by landslides. The method is dependent on the inversion and the choice of the duration of the optimization window.

In this study, we consider the Draix–Bléone catena area, namely the Laval-Moulin divide, which represents a vadose zone under the influence of Mediterranean climate forcings. This area features slope surface erosion (gullying, shallow landslides slides) and sediment transport and has been extensively studied since 1983 (Mathys *et al.*, 2005). Documenting soil–water content changes at the scale of a catena or larger hydrological units requires the installation of local sensors, which is expensive and disturbs the environment. Hence, we used FO-DTS (Steele-Dunne et al., 2010) to monitor water content based on temperature measurements (Rutten et al., 2010) at high frequency and spatial resolution (Seyfried et al., 2016). For long-term and continuous observations, passive FO-DTS provides simpler measurement opportunities. This is different with active FO-DTS, where it requires a lot of resources to produce active heating. This need creates difficulties for measurements in the field where there is no power and shelter available.

The objective of this work is to propose a hybrid solution to the above problem by combining signal processing and numerical modeling to estimate soil VWC from passive FO-DTS along a soil catena of 60 m influenced. To achieve this, we document long-term soil–water content variations from distributed soil temperature measurements using FO-DTS technology, with the following objectives: (i) estimate soil water content at a vertical resolution of 5 cm depth and a horizontal resolution of 50 cm. (ii) describes and analyze long-term variations in soil water content over 22 months, with measurements conducted at 6-minute intervals.

4.2 Materials and Methods

4.2.1 The Draix–Bléone (South-East France) hydrological research catchment

The observation site is the Draix–Bléone catchment, which features many watersheds and catena and is representative of landscapes in the Southeast French Alps (Antoine et al., 1995; Mathys et al., 2005). The investigated catena is the Laval-Moulin divide, located on the divide separating the Moulin stream to the West and Laval stream to the East (Figure 4.1a). The catena is composed of altered regolith comprising Callovo-Oxfordian black marls with a clay shale facies (Marc et al., 2017). The catena is partly covered by grass and *Pinus Negra* trees with a vegetation density up to 45% (Matthys, 2003). Frequent freeze and thaw cycles in winter influence the weathering of the black marls and thus the soil properties.

The Draix–Bléone catchment has a Mediterranean climate with an annual rainfall of 900 mm (Mathys et al., 2003). The area has on average 200 days a year without rain, 160 days with less than 30 mm rainfall and only 5 days with more than 30 mm rainfall. The mean annual potential evapotranspiration is 650 mm (Estèves et al. 2005). Summers are dry with occasional storms and the maximum precipitation and runoff occur in spring and autumn.

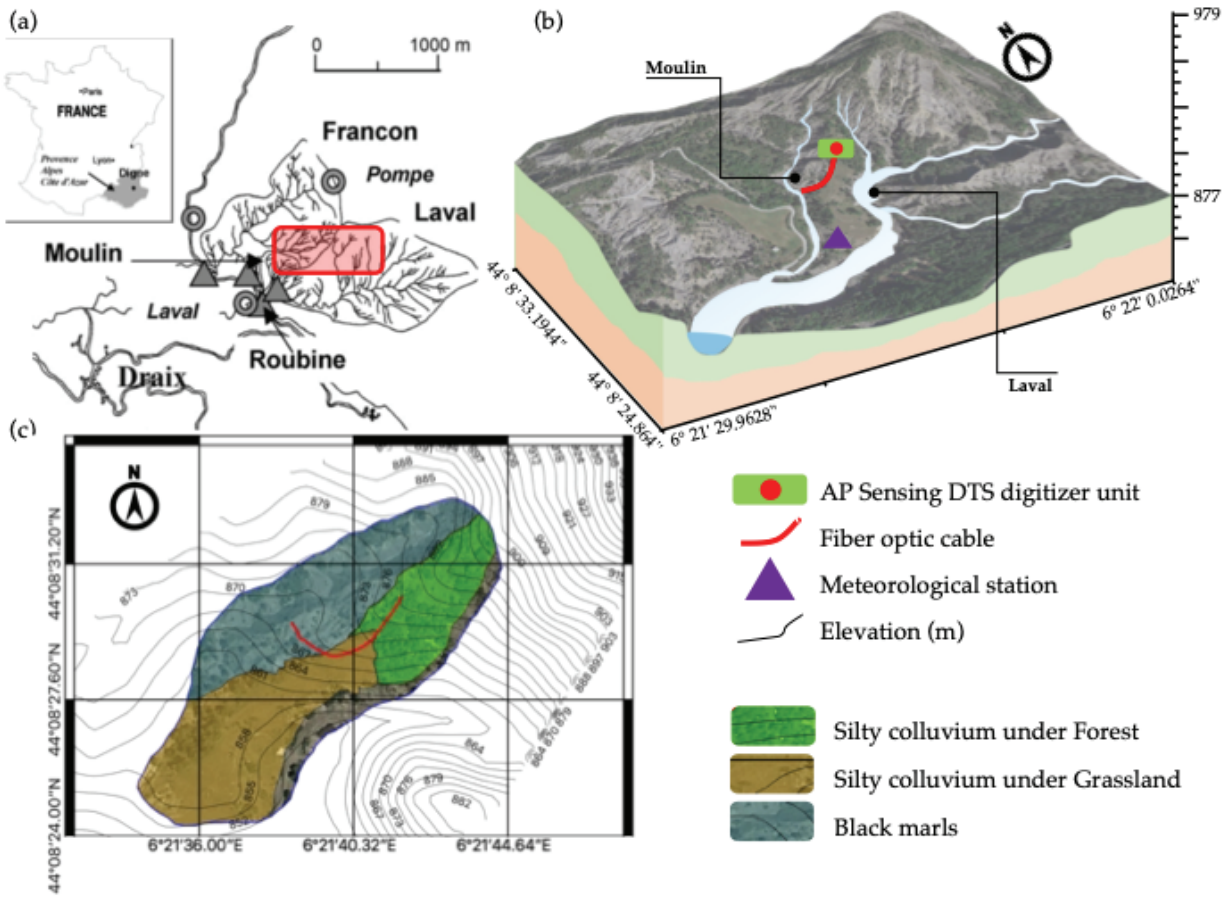

Figure 4.1 Draix–Bléone catchment hydrological research observatory. (a) Location of the investigated divide between the Moulin and Laval catchments (Mathys et al., 2005). (b) 3D view of the study site and position of the measuring instruments. (c) Soil map of the divide with colluvium soil under forest (green), colluvium soil under grass (brown), and weathered black marls (blue).

We investigated a 60 m catena crossing three soil units, consisting of argillaceous weathered black marls, silty colluvium with grassland, and silty colluvium under forest. The catena faces South (Figure 4.1a), with the weathered black marls soil unit at the West and the silty colluvium unit at the East (Figure 4.1b and 4.1c). Below the study site, the superficial formations vary considerably in thickness, texture (and thus porosity), compactness, organic matter content, and VWC depending on local structural, topographic and vegetation conditions (Maquaire et al., 2002).

Sampling was carried out to achieve a more detailed characterization of the soil grain size and hydrodynamic properties. 84 soil samples were collected at depths of 5, 10, 15, and 30 cm and analyzed using a CoulterLS particle size analyzer of the CNRS/EOST soil laboratory (LAS). The saturated hydraulic conductivity and the retention pF curves were estimated using, respectively the constant head method and the van Genuchten method (Genuchten, 1978).

4.2.2 The FO-DTS experimental setup at the Moulin-Laval divide

A 350 m long reinforced fiber optic cable was buried in the three soil units at 0 (e.g., ground level), -5, -10 and -15 cm respectively. (Figure 4.2a). Soil temperature was measured using a FO-DTS digitizer from Advanced Photonic Sensing (AP Sensing) equipped with a Brugg Fiber Optic cable manufactured by Brugg Cable AG in Switzerland (www.bruggcables.com/sensing). The fiber optic is protected by Polyamide Nylon PA12 outer sheath for outdoors harsh environments application (BRUsens Temperature LLK-BSTE 150°C 3.8 mm). The sensing cable was installed by carefully incising the soil over 20 cm (Figures 4.2b and 7.2c), thereby minimizing soil disturbance, and the vertical interlace of 5 cm was controlled using a specific mechanical template.

The AP Sensing digitizer has a power consumption of approximately 17 W at 20 °C ambient temperature (10–30 VDC). The internal memory provides 16 GB of storage space, and the LAN port connecting the digitizer to the remote network. Binary file formats are used to minimize the temperature trace file size. Hence, the digitizer can monitor temperature profiles for up to 24 months. The FO-DTS digitizer provides a raw temperature reading calibrated to the internal calibration coil; however, its internal calibration is based on default assumptions, such as connector losses, attenuation of the fiber, and environmental sensing considerations with time-varying errors that typically exceed 1K (van de Giesen et al. 2012).

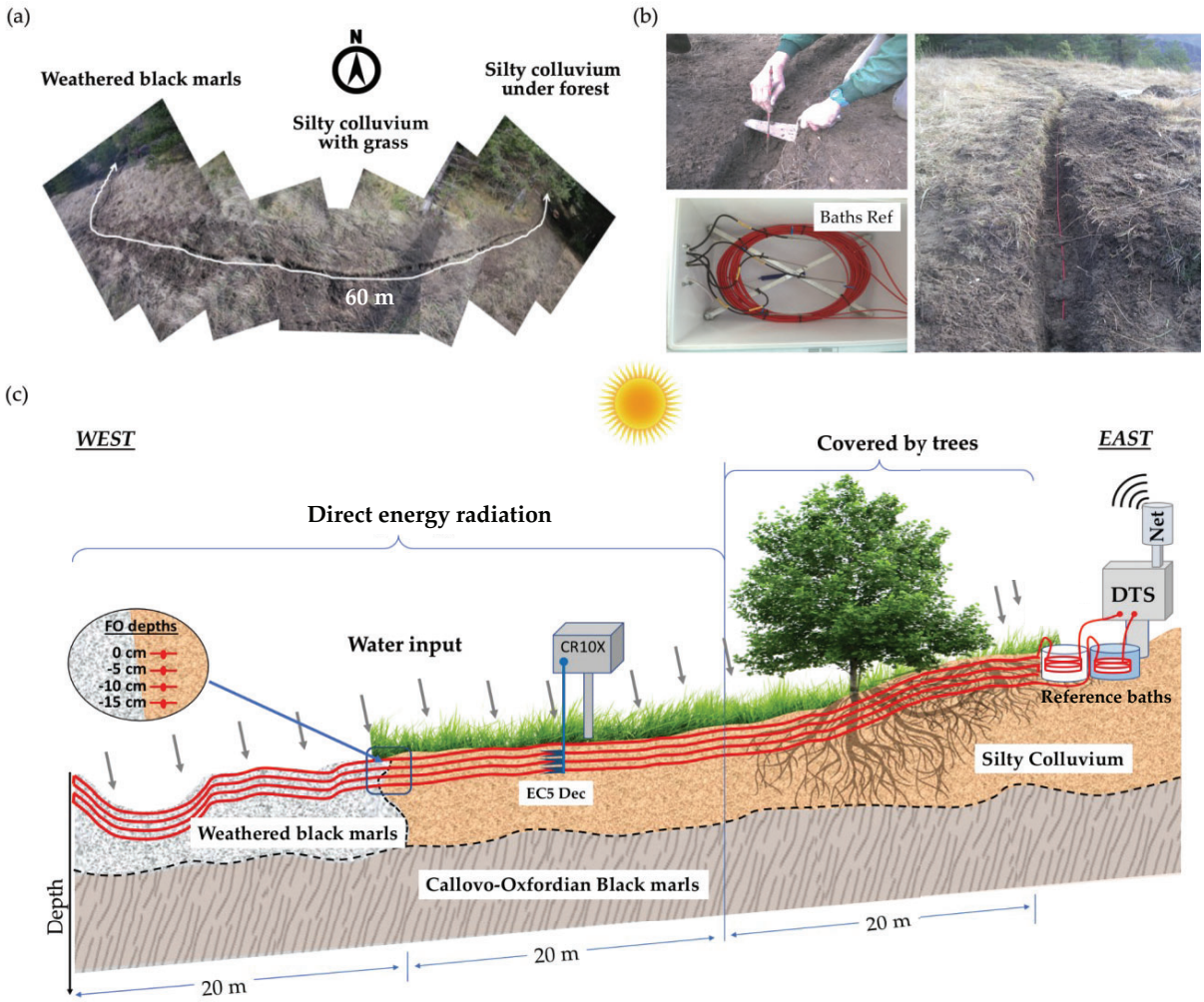

Figure 4.2 The Draix-Bléone FO-DTS instrumental setup: (a) Aerial photograph describing the fiber optic cable installation crossing the three soil types horizontally. (b) Fiber optic cable installation at the start of the experiment. (c) Schematic diagram of the network of instruments (FO-DTS, reference baths, point-based Decagon EC5 soil moisture probe sensors for validation at depths of -5, -10 and -15 cm, respectively).

Soil temperature was measured every 6 minutes at a spatial resolution of 0.50 m using a double-ended cable configuration to obtain higher accuracy temperature measurements. In this configuration, the decay of photons along the length of the sensing cable (attenuation along the fiber optic and effect of splices, effect of fiber optic heterogeneities) was compensated by loops of fiber optic cable in two reference baths filled with 10 liters of water at the start and end of the profile (Figure 4.2c).There are two baths with a different temperature, and we tried to always have a difference of ca. 20° C between each bath. The first is a bath with the ambient water temperature; this ambient reference bath is equipped with five PT100 independent temperature probe sensors and the water is mixed (to avoid layering) with a small pump. The second is a bath with a controlled water temperature called "warm reference bath". This warm reference bath is equipped with a heater (used for aquariums), five PT100 independent temperature probe sensors, and a pump to mix the water in the bath. Water temperature data on the ambient and heated baths were logged using a Campbell CR1000 datalogger. The mean and standard deviation values of water temperature in the baths were used to correct the fiber optic cable temperature according to the method proposed by van de Giesen et al (2012).

The slope catena is further instrumented with three capacitance-based soil moisture probes (EC-5 Decagon) located at 30 m distances along the fiber optic cable and buried at depths of -5, -10 and -15 cm (Figure 4.2c). A meteorological station equipped with a tipping bucket ARG100 rain gauge, a CS300 pyranometer, a CS300 anemometer and a CS215 air temperature and relative humidity probe were positioned downhill of the FO cable at a distance of 140 m. All variables were acquired at a sampling frequency of 10 minutes. The method proposed by Sigmund (2017) was used to correct the effect of radiation on the temperatures measured by the FO cable at the slope surface.

4.3 Methods

The concept addressed in this paper combines signal processing and soil temperature numerical temperature using the heat equation to reveals variations of soil moisture. Soil thermal properties, such as saturated and dry heat conductivities and volumetric heat capacity, must be estimated; however, soil thermal diffusivity depends on soil moisture and both above depend on rainfall events.

Figure 4.3 describes the data processing workflow. The workflow consists of soil temperature data acquisition, calibration and correction, determination of soil thermal properties using numerical calculation and signal processing, and non-linear inversion of soil thermal parameters. The first step is data acquisition of the soil temperature using FO-DTS (Raw T^o FO-DTS). The second step is the calibration and correction procedures. This procedure is necessary to correct the Raw T^o from attenuation losses in the fiber optics cable and the influence of air solar radiation on the cable at the soil surface (see Figure 4.2c). The third step is the determination of soil thermal diffusivity (D) using a numerical approach and applying time-series signal processing to reduce known disturbances, such as diurnal and annual variations of apparent diffusivity (D_{app}). Apparent soil thermal diffusivity was calculated using the vertical temperature profile during periods of observation between January 2016 and April 2018. A one-dimensional temperature profile consideration was used to simplify the determination of soil thermal diffusivity. The fourth step is a nonlinear inversion to retrieve the soil thermal parameters and VWC calculation. The soil thermal parameters include heat conductivity (λ_s and λ_d), heat capacity (C_s), and true soil thermal diffusivity (D). The Johansen model is used for VWC calculation. According to the constitutive workflow shown in Figure 4.3, the calculated VWC is compared with the direct measurements from EC-5 probes. The optimized soil parameters are inferred by inversion of the van Genuchten model, the input variable being the measured VWC. Error analysis is used to quantify the accuracy of the calculation.

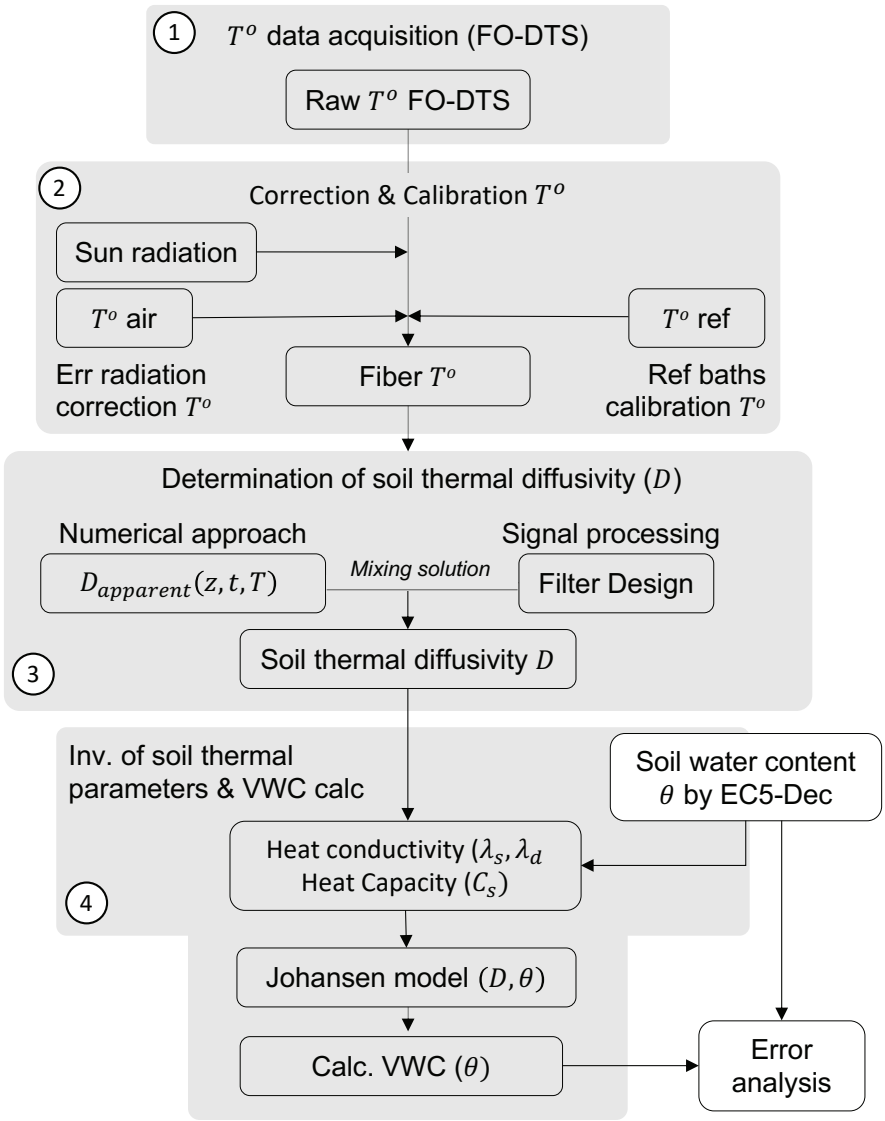

Figure 4.3 Workflow of the hybrid solution mixing soil temperature numerical modelling and signal processing to estimate soil VWC from passive FO-DTS time series.

4.4 Temperature Calibration and Correction

As shown in Figure 4.2c, the optical fiber cable is deployed on the ground using a double-ended configuration and is crossing ambient and warm reference baths. This configuration allows temperature calibration along the cable with reference to ten independent temperature sensors (PT107) spread in the two reference baths. Temperature readings along the fiber contain the dynamic calibration parameter $C(t)$ (van de Giesen et al., 2012). The values of $C(t)$ temperatures are linked to independent temperature readings measured by the PT107 sensors at several positions. We assume that $C(t)$ is a function of the linear reading of the temperature. Thus, the fiber optic temperature reading is calibrated by the $C(t)$ values.

While the buried fiber optic cable measures the soil temperature, the unburied fiber cable at the soil surface measures the temperature at the interface between the ground and the air. This configuration allows the fiber to receive heat directly from solar radiation, thus influencing soil temperature readings at the surface. This effect is corrected by subtracting the fiber optic temperatures on the topsoil with an energy balance model including the short and long-wave convective and conductive heat transfer processes (Sigmund et al., 2017). The

basic principle of this method is to use the shortwave, longwave, convective, and conductive heat transfer around the fiber for quantifying the modeled radiation. In our application, we use the CS300 pyranometer produced by Campbell Scientific for providing total wave irradiance datasets that are installed at the meteorological station (See Figure 4.1). In addition, we used PT100 to measure the air temperature around the fiber and installed it at 1.7 m above the soil. In this case, the fiber cable located in the surface layer is 60 m it is possible to have an aerial error reading. The albedo and emissivity remained constant and referred to the fabric's datasheet that varied maximum ± 20% and -12 to +33% for albedo and emissivity, respectively. This correction consists of incoming energy flux from the conduction of fiber cable and outgoing convective energy exchange with moving air, shortwave, and longwave radiation.

4.4.1 Determination of soil thermal properties

Heat transfer in relation to water content below the surface has been widely studied (Cheviron et al., 2005; Rutten et al., 2010). Estimating water content, using thermal properties as a proxy, can be performed with the heat transfer equation (Halloran et al., 2016). Vertical heat transfer describing subsurface heat flux density in soil is controlled by both conductivity and volumetric heat capacity, which are functions of water content and soil porosity (Adeniyi and Oshunsanya, 2012). The relationship between heat conductivity and heat capacity is described as soil thermal diffusivity while the combination of vertical heat transport and heat conservation can be simplified as the diffusion equation (Eq 4.1):

$$\frac{\partial T}{\partial t} = \frac{\lambda(\theta)}{C(\theta)}\frac{\partial^2 T}{\partial z^2} \qquad \text{Eq. 4.1a}$$

$$\frac{\partial T}{\partial t} = D(\theta)\frac{\partial^2 T}{\partial z^2} \qquad \text{Eq. 4.1b}$$

where C (J m^{-3} K^{-1}) is the volumetric heat capacity of soil, λ (W m^{-1} K^{-1}) is soil heat conductivity, D (m^2 s^{-1}) is soil thermal diffusivity which is ratio of λ/C, and all thermal parameters are functions of water content (θ). T (K) is soil temperature, z (m) is the depth of the soil column, and t (s) is time. In accordance with Eq. 4.1, conduction is assumed to be the dominant mode by which heat transfer occurs in the subsurface; other heat transfer modes are neglected due to their relatively low contribution to temperature dynamics (Van Wijk and Derksen, 1966; Rutten et al., 2010; Krzeminska et al., 2012). Further, subsurface vapor flows are ignored because they occur rarely in the dry seasons (Chung and Horton, 1987). Therefore, we assumed that water vapor transport was purely diffusive, and that convection was negligible. At least six methods have been developed to determine the apparent thermal diffusivity of near-surface soil (Horton, et al., 1983). One of these methods involves numerical discretization applied with the explicit finite difference to solve Eq. 4.1. This method allows thermal diffusivity to be estimated from three temperature measurement depths.

Below the surface, temperature variations follow the average temperature during one cycle and the temperature amplitude at the ground surface. In addition, rainfall events influence subsurface temperatures and temperature propagation due to water content. Considering that heat transfer is determined by the damping depth factor, which itself depends on the thermal diffusivity and temperature period of soil (Krarti et al., 1995; Wu and Nofziger, 1999; Evstatiev, 2013), temperature behavior can be predicted using Eq. 4.1 involving boundary conditions and damping depth (Cichota et al., 2004; Oyewole et al., 2018). Hence, the solution of the heat equation satisfying boundary condition is given with Eq. 4.2 (Carslaw & Jaeger, 1959; Kirkham & Powers, 1972):

$$T(z,t) = T_0 + A_0\, e^{\left(\frac{-z}{d}\right)} sin\left(\frac{2\pi t}{\tau} - \frac{z}{d}\right) \qquad \text{Eq. 4.2}$$

where T_0 is the average temperature during one cycle, A_0 is the temperature amplitude at the soil surface, d is the damping depth factor with $d = \sqrt{\tau D/\pi}$, τ is the diurnal period (in second), z is the depth (in centimeter), and t is time (in second). The apparent thermal diffusivity from the damping depth factor in Eq. 4.2 is calculated using analytical and numerical solutions. Apparent soil thermal diffusivity is obtained by selecting the value of soil thermal diffusivity to minimize the sum of temperature square differences between the model and observations (Horton et al., 1983). Horton (1983) showed in his experiment that the apparent thermal diffusivity of soil over three days is approximately 5.7×10^{-7} to 6.2×10^{-7} m^2s^{-1} with a standard deviation of less than 4.4×10^{-7} m^2s^{-1} at a depth of −5 cm; however, this approach only allow estimating a daily single apparent diffusivity.

In our approach, soil thermal diffusivity is calculated every 6 minutes. Theoretically, we could detect thermal diffusivity and, therefore, water content change between two estimations with a 6-minute resolution. In practice, the real resolution on the thermal diffusivity and on water content is higher and variable because it depends on the frequency content in the input temperature signal and on the thermal diffusivity value itself. From our dataset, we estimate the minimal resolution to be around 12 hours. Therefore, this is one of the limitations of this method in its application. On the one hand, diurnal temperature waveforms in the passive heat source application can result in minor temperature differences between the upper and lower boundaries. These situations yield overestimated soil diffusivities in the morning and evening when the upper boundary temperature encounters increasing or decreasing temperatures. This overestimation was mentioned by Krzeminska (2012) because the temperature signal was assumed to be a sinusoidal function. This frequently overestimated soil thermal diffusivity is considered an "artifact" because it appears repeatedly. Hence, the estimated soil thermal diffusivity in the time domain contains not only the water content effect but also diurnal and annual variations due to the temperature sinusoidal waveform (Eq. 4.3).

$$D(t) = D_{wc}(t) + D_{diurnal}(t) + D_{annual}(t) \qquad \text{Eq. 4.3}$$

where $D(t)$ is the calculated soil thermal diffusivity in the time domain, consisting of the response of water content variation (D_{wc}) and the artifact, namely the apparent soil thermal diffusivity due to diurnal ($D_{diurnal}$) and annual (D_{annual}) fluctuations. The apparent soil thermal diffusivity response generally experiences an extreme increase at sunrise and sunset. On the other hand, the thermal diffusivity also increases due to the presence of water content. This response is found in both analytical and numerical soil thermal diffusivity calculations on passive DTS optic setups. This artifact associated with diurnal temperature heat sources can be investigated using spectrum analysis. The Fast Fourier Transform (FFT) shown in Eq. 4.4 presents periodically overestimated soil thermal diffusivity in the frequency domain such that the artifact can be removed using a specific filter design.

$$D(\omega) = \int_{-\infty}^{\infty} D(t) e^{-j\omega t}\, \partial t \qquad \text{Eq. 4.4}$$

The aperiodic signal due to water infiltration and drainage is expected to pass as a filtering result. The filter is also expected to remove noise from the measurement uncertainty or temperature fluctuation due to wind flow, cloudy weather, or any other factors provoking different soil temperature over short time periods. The

Butterworth band-stop filter is used for removing these signals with the selection of an appropriate cutoff frequency tailored to our application.

The filtered value of soil thermal diffusivity may be impacted by noise reduction during signal filtering, but the filtered soil thermal diffusivity remains in agreement with water content changes with time. To anticipate the biased VWC from the filtered soil thermal diffusivity, we converted filtered soil thermal diffusivity into relative saturation.

4.4.2 Inversion of soil thermal parameters and VWC calculation

The inversion of soil thermal diffusivity to relative saturation in the Johansen model (Eq. 4.5) presents a constitutive relationship of the dependency of thermal diffusivity to water content. In terms of soil thermal diffusivity calculations, a nonlinear relation exists between water content (θ) and soil thermal diffusivity ($D(\theta)$) as follows:

$$D(\theta) = \frac{Ke(\lambda_s - \lambda_d) + \lambda_d}{(1 - \emptyset)C_s + \theta C_w} \quad \text{Eq. 4.5}$$

where θ is relative saturation of volumetric water content, $\emptyset$ is soil porosity, λ_d and λ_s are dry and saturated heat conductivity (W m^{-1} K^{-1}), respectively, and C_s (J m^{-3} K^{-1}) is soil matrix heat capacity. The formula in Eq. 4.5 provides physical thermal coefficients that are within the heat property ratio of the soil heat conductivity and capacity. Soil heat conductivity is a linear combination of saturated and dry heat conductivities. The Kersten number (Kersten, 1949) for unfrozen fine soil is then used to determine the normalized soil heat conductivity in dry and saturated soil (Béhaegel, et al., 2007). Kersten number is expressed by $K_e = \log_{10}\left(\frac{\theta}{\emptyset}\right) + 1$.

Estimating soil thermal diffusivity is complex even when the volumetric heat capacity is a linear function of the air–water composition (Krzeminska et al., 2012; Campbell et al., 1991). To solve the nonlinear function in Eq. 4.5, we modified the equation and used proxy variables X, Y, and Z as functions of water content (θ) as follows:

$$X(\theta_i) = \frac{\log_{10}\left(\frac{\theta_i}{\emptyset}\right) + 1}{\theta_i C_w} \quad \text{Eq. 4.6a}$$

$$Y(\theta_i) = -\frac{\log_{10}\left(\frac{\theta_i}{\emptyset}\right)}{\theta_i C_w} \quad \text{Eq. 4.6b}$$

$$Z(\theta_i) = \frac{D(\theta_i)(1 - \emptyset)}{\theta_i C_w} \quad \text{Eq. 4.6c}$$

Further, Eq. 4.6 may be rearranged by using proxy variables and applying the least square inversion method to determine saturated and dry heat conductivity (λ_s and λ_d) and soil matrix heat capacity (C_s). Here, an error (E_r) appears as a consequence of inversion. We therefore rewrite Eq. 4.6 and apply the least square method to obtain parameters of Eq. 4.7 as follows:

$$D(\theta_i) = \lambda_s X(\theta_i) + \lambda_d Y(\theta_i) - C_s Z(\theta_i) + E_r \quad \text{Eq. 4.7}$$

Using the error minimization function within the least square inversion (Eq. 4.7) enables us to obtain optimized soil heat parameters (λ_s, λ_d, and C_s). To minimize the error, the solution can be arranged as shown in Eq. 4.8:

$$\frac{\partial E_r(\lambda_s, \lambda_d, C_s)}{\partial \lambda_s \partial \lambda_d C_s} = \frac{\partial}{\partial \lambda_s \partial \lambda_d C_s}\left[\sum (D - \lambda_s X_i - \lambda_d Y_i + C_s Z_i)^2\right] = 0 \qquad \text{Eq. 4.8}$$

Finally, the nonlinear inversion method can be expressed by $m = [G^t G]^{-1} G^t d$ as an inverse matrix solution, where G is a kernel matrix, m are the estimated parameters, and d is a matrix containing data observations for soil moisture and thermal diffusivity. We emphasize that the success of inversion depends on the range of plausible apparent soil thermal diffusivity. This plausibility can be examined using the signal correlation between soil thermal diffusivity and VWC measurements.

4.5 Results And Discussion

4.5.1 Composition and hydrodynamic properties of the soil units

The soil physical properties, such as air entry pressure and pore size distribution, were obtained using modelled soil water retention curves. The calculation results that the inverse of the air entry value range from 0.039 cm^{-1} to 0.061 cm^{-1} and the pore size distribution index was found to range between 1.69 and 2.01. Table 4.1 presents the soil physical properties at the field site, which are dominated by loam and fine-textured soils (smaller than 20 μm). The porosities vary between 28 and 51%.

Table 4.1 Soil physical properties at the Moulin-Laval divide.

Soil property	Soil type			Unit
	Under Forest	Under grass	Black marls	
Coarse sand (200–2000 μm)	21	-	-	%
Fine sand (50–200 μm)	7	1	6	%
Coarse silt (20–50 μm)	11	13	15	%
Fine silt (2–20 μm)	41	58	53	%
Clay (<2 μm)	20	28	26	%
Soil porosity (∅)	40–51	43–49	28–34	%
Air entry pressure (α)	0.056	0.061	0.039	(cm^{-1})
Pore size distribution (n)	1.99	1.69	2.01	-
Saturated hydraulic conductivity (K_{sat})	0.58	1.04	3.24	($cm.hr^{-1}$)

The soils are composed of clay minerals, encompassing various types such as illite (12%), smectite/illite (31%), chlorite (6%) and kaolinite (5%) (Garel, 2010; Marc et al., 2017). A fascinating observation during the research is the remarkable ability of rainwater to infiltrate through soil cracks system. This phenomenon of rainwater infiltration holds the key to diminishing the cohesion of the soil material and triggering inter-particle repulsion among the mineral particles.

4.5.2 Temperature calibration and correction

The FO-DTS temperature dataset at depths of 0, -5, -10 and -15 cm spans over the period from 2016 to 2017. The temperature record has been calibrated and corrected using two reference baths for the application and energy balance calculation (Section 7.3). The average, maximum and minimum temperature data collections are 11.28°C, 42.83°C, and −13.21°C, respectively (see Figure 4.2c). Observations of temperature profiles at four depths are sufficient to estimate the soil thermal diffusivity below the shallow surface according to Horton et al. (1983). The temperature profile during the observation period fluctuated significantly due to the presence of water from infiltration and evapotranspiration.

Figure 4.4 presents the results of calibrated and corrected temperature during the observations. Both the calibration and correction of temperature data were successfully carried out and both annual and diurnal temperature variation are clearly observed during the two-years. It is difficult to observe temperature variations during periods of precipitation. To infer local temperature variation due to rainfall events, signal processing was applied to extract the frequency component in the temperature records. Theoretically, the influence of soil water content variation is indicated as a random frequency. Moreover, temperature data also contains two very low frequencies corresponding to annual and diurnal temperature.

The soil temperature profiles shown in Figure 4.4 indicate that temperature variations in topsoil are generally warmer and more variable than those at the subsurface. This observation supports the application of heat transfer equation for water detection. Furthermore, the measured temperature also shows a different character within each soil type, meaning that clay mineral types should be considered in the heat transfer application. For example, black marls are warmest in the summer but colder in the winter at depth. This indicates that black marls have the highest soil thermal diffusivity among the studied soil types. In areas that have a high content of interstratified illite/smectite, especially in black marls (31%), rainwater can infiltrate into the surface cracks network.

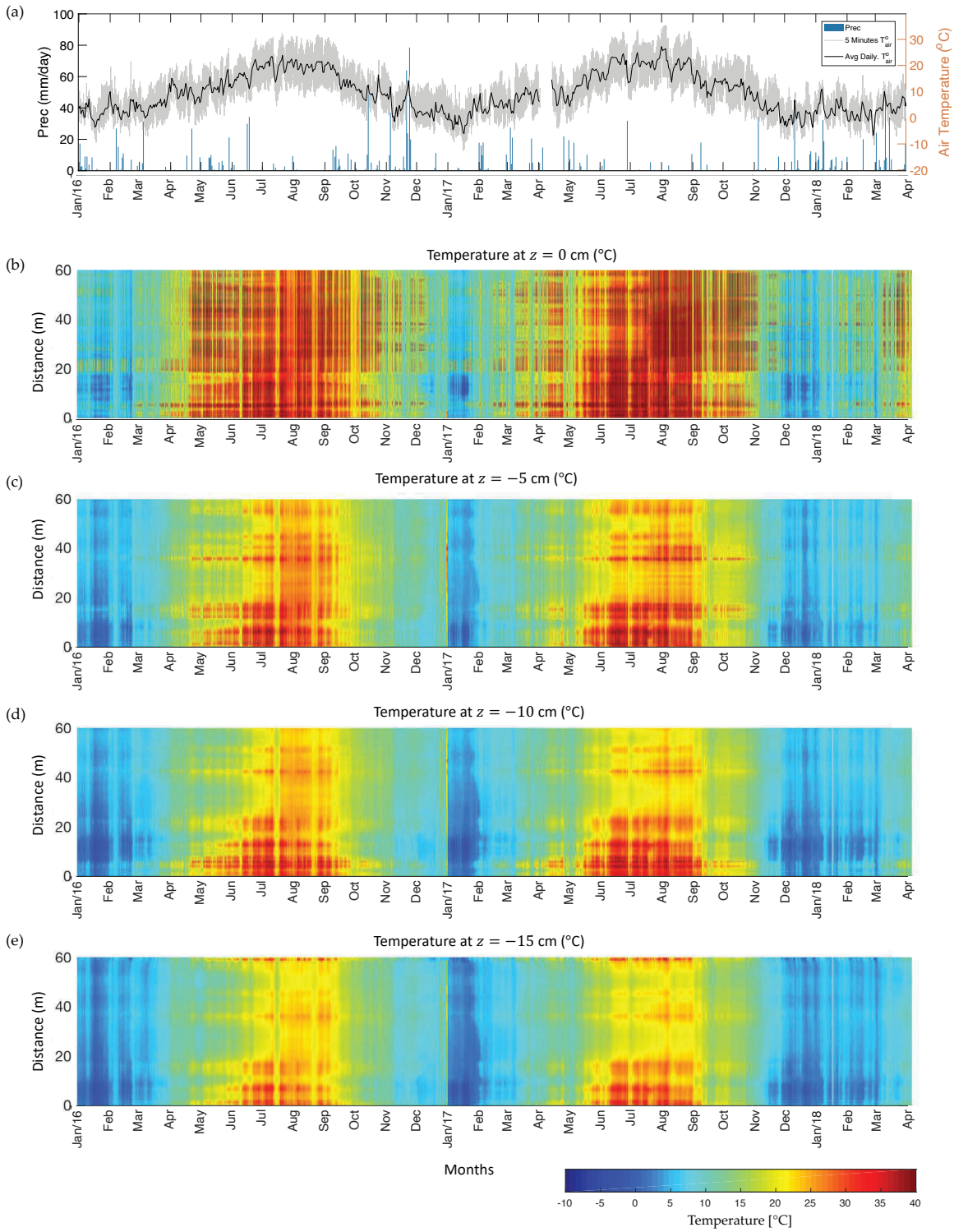

Figure 4.4 Rainfall, air and soil temperatures records at the Moulin-Laval divide. (a) Rainfall events and air temperature records. (b) Corrected long-term soil temperature profiles measured by FO-DTS during the observation period at depths of 0, -5, -10 and -15 cm.

4.5.3 Determination of soil thermal properties

Thermal parameters, such as soil heat capacity and thermal conductivity, are required to quantify the VWC of each soil type based on soil thermal diffusivity calculations (Béhaegel, et al., 2007). Parameters are estimated using a nonlinear inversion of the Johansen model. We used fifteen days of temperature and

independent soil moisture observations for the period April 15–30, 2016. We conducted this procedure to infer the soil thermal properties, such as heat conductivity and heat capacity. Independent soil moisture probes were deployed on grassland at similar depths than the fiber optic cable (see Figure 4.2c). During the inversion, some rainfall events, and thus infiltration/drainage processes, occurred. Soil moisture variations ranging from 0.15 to 0.43 m^3m^{-3} are included in this inversion step.

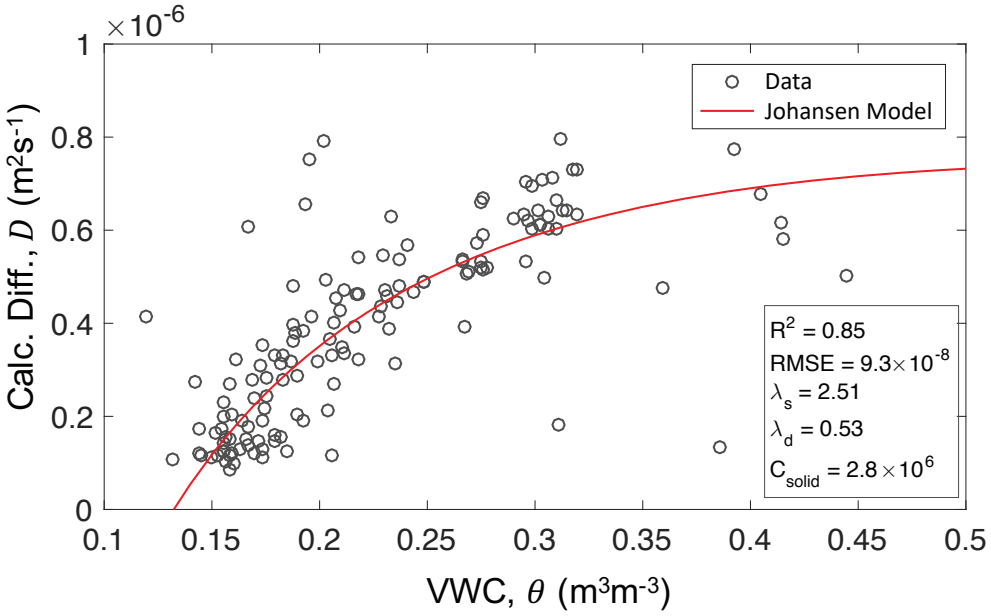

Figure 4.5 Soil thermal properties. The properties are determined using (a) a nonlinear inversion of measured soil moisture (VWC) and calculated thermal diffusivity fitted to the Johansen model during a fifteen-day observation period; coefficient of determination $R^2 = 0.85$.

Figure 4.5 presents the parameter inferred from the Johansen model linking soil moisture and diffusivity. The circles are the observation data, and the solid line curve is the best mathematical model obtained from the inversion. The results of the inversion are optimized thermal parameters, i.e., soil heat conductivity $C_s = 2.8$ $MJm^{-3}K^{-1}$, dry and saturated thermal conductivities $\lambda_d = 0.53$ $W\ m^{-1}.K^{-1}$ and $\lambda_s = 2.51$ $Wm^{-1}K^{-1}$ respectively. The fitting analysis for the inversion results presents a goodness of fit with an $RMSE = 9.8 \times 10^{-8}$ m^2s^{-1} with a coefficient of determination $R^2 = 0.85$.

In agreement with the Johansen model, we fixed the soil thermal parameters to be applied uniformly across all soil types for the VWC calculations. Our hypothesis is based on the dominance of silt and fine clay in the soil composition (Table 4.1). Consequently, we have attributed a single parameter value that adequately represents the thermal characteristics of the various soil types. This assumption ensures consistency and facilitates reliable VWC estimations throughout the analysis. These parameters may be insensitive to higher soil diffusivities in specific soil types and tend to introduce different error estimations, especially in almost saturated soils; however, low soil moisture can be inferred from low soil thermal diffusivity.

4.5.4 Implementation of the hybrid approach for VWC estimation

As discussed in section 7.3, the combination of a numerical simulation approach and of band stop filter as signal processing is used. This hybrid approach allowed determining the time series of soil thermal diffusivity. We used synthetic soil moisture variations generated by the Hydrus-1D software package as a synthetic simulation of changes in soil water content. Nevertheless, the type of mineral should be considered to achieve realistic simulation.

Step 1: Synthetic simulation of VWC

The Hydrus-1D software package (Šimůnek et al., 2013) was used to simulate synthetic water changes in a configuration similar with field experiment at a depth of -15 cm every 6 minutes for 15 days. VWC variations were simulated at a depth of -10 cm. The water flow parameters established for this simulation were residual water content = 0.08 $m^{-3}m^{-3}$, saturated water content = 0.43 $m^{-3}m^{-3}$, air entry pressure = 0.06 cm^{-1}, pore size distribution = 1.9 and saturated hydraulic conductivity of soil = 21.2 $cm.day^{-1}$. The simulation uses arbitrary data, but avoids random atmospheric effects, such as cloudy weather and cold wind flow. We took into consideration that atmospheric forcings do not impact depths below -10 cm. In our simulation, water changes from precipitation events occurred twice on the fourth and ninth days, during which precipitations of 1 $cm.day^{-1}$ and 2 $cm.day^{-1}$ were employed, respectively (see Figure 4.6a).

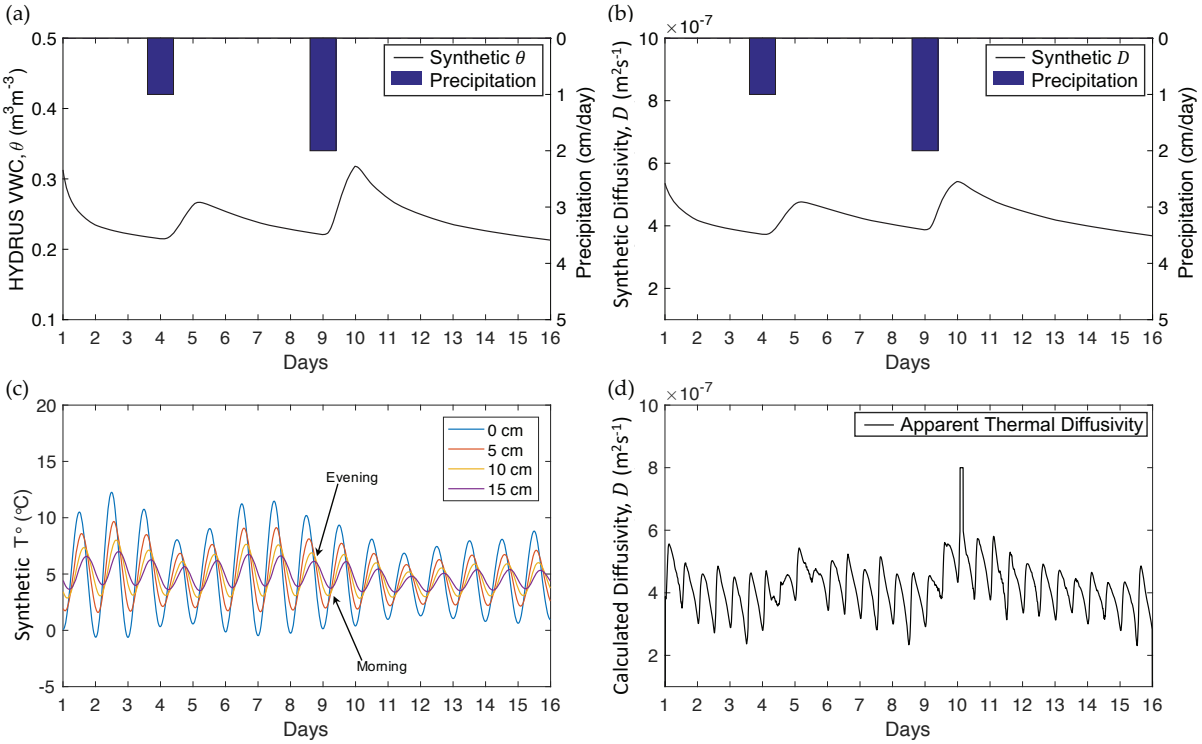

Figure 4.6 Results of the simulation and testing steps as a validation procedure. (a) Synthetic VWC generated with the Hydrus-1D software package. (b) Predefined soil thermal diffusivity converted from the Johansen model using synthetic VWC. (c) Synthetic temperature generated by considering the damping depth factor in Eq. 4.2. Each point indicated by the arrow represents a very small difference of temperature in the morning and night. (d) Calculated soil thermal diffusivity containing the artifact and signature of VWC was explicitly determined using a finite difference approach with a calculated diffusivity.

VWC from the Hydrus-1D simulation predefines synthetic soil thermal diffusivity using the Johansen model with several estimated input parameters, such as soil porosity, heat capacity, and thermal conductivity. The parameters were extracted from the inversion results, as illustrated in Figure 4.6a. Additionally, we adopted a soil porosity of 47%, which aligns with previous research conducted by Mallet (2018) about the study site. Figure 4.6b presents times series of predefined soil thermal diffusivity as a function of synthetic VWC.

As shown in Figure 4.6c, the synthetic temperature was profiled at four depths with a 5 cm vertical spacing using the sinusoidal waveform in Eq. 4.2 (Carslaw and Jaeger, 1959) and predefined soil thermal diffusivity corresponding to water change variations over 15 days. The profile exhibits small temperature

differences in the morning and evening (see arrow in Figure 7.6c). This synthetic temperature dataset involved air temperature to attain plausible variations in soil temperature. The predefined diffusivity was then used to generate synthetic temperature profiles as shown in Figure 7.6c. Please note that although the qualitative observation of VWC's signature is not seen in Figure 7.6c, the VWC change due to rainfall events can be clearly observed in Figure 4.6a. Therefore, the proposed method can effectively reacquire the apparent soil thermal diffusivity.

Step 2: Recalculation of thermal diffusivity

This step aims to re-calculate the thermal diffusivity using a combination of numerical approaches and signal processing. The synthetic soil temperature in Figure 4.6c is used in a finite difference approach to obtain the calculated thermal diffusivity. Figure 7.6d, which presents the calculated thermal diffusivity involving diurnal variation at a depth of -10 cm, shows an artifact that appears twice a day when the temperature increases in the morning and decreases in the evening. After calculating thermal soil thermal diffusivity, the signature of water changes is not an obvious response in the diffusivity time series because the artifact dominates diffusivity on all days (Figure 4.6d). Therefore, a FFT is applied to investigate the artifact of calculated soil thermal diffusivity in the frequency domain and determine the filter design to remove undesirable frequencies. In this experiment, we verified the suitable cutoff frequency based on comparisons between predefined and filtered soil thermal diffusivities, which have a minimum residual error. By examining the cutoff frequency of the band stop filter, the suitable filter design for this experiment was found to be the Butterworth fifth-order filter and the normalized cutoff frequencies were $f_{low} = 0.05$ and $f_{high} = 0.11 \times \pi$rad/samples (Figure 4.7a). However, we noted that the filter design might not be the same for other cases. The amplitudes of the filtered signal were attenuated during the filtering process such that the filtered soil thermal diffusivity might not represent the correct value. Therefore, the filtered signal seems to exhibit more ripple but has a similar temporal distribution (Figure 4.7b). In general, the thermal diffusivity of soil increases with the rainfall and thus water infiltration and decreases with drainage.

In addition, the signal-to-noise ratio of the filtered and synthetic signals demonstrated improvement during error analysis. Figure 4.7c shows the computation of the mean relative error between synthetic and calculated soil thermal diffusivity of the model experiment during a period of 15 days. The percentage of mean relative error of soil thermal diffusivity lies within the range of $3.7 \times 10^{-7}$to 5.5×10^{-7}m^2.s^{-1} while the total mean relative error for 15 days in the model is approximately 2.3%. The proposed method thus demonstrates fairly good performance and succeeds in determining soil thermal diffusivity without using the diurnal temperature period, as implemented in Jong van Lier and Durigon (2013).

Step 3: Calculation of VWC

This step consists in calculating the VWC (Figure 4.8a) by applying the filtered soil thermal diffusivity to the Johansen model. This was done to compare the calculated and synthetic VWC and investigate whether this procedure can be used in passive FO-DTS applications.

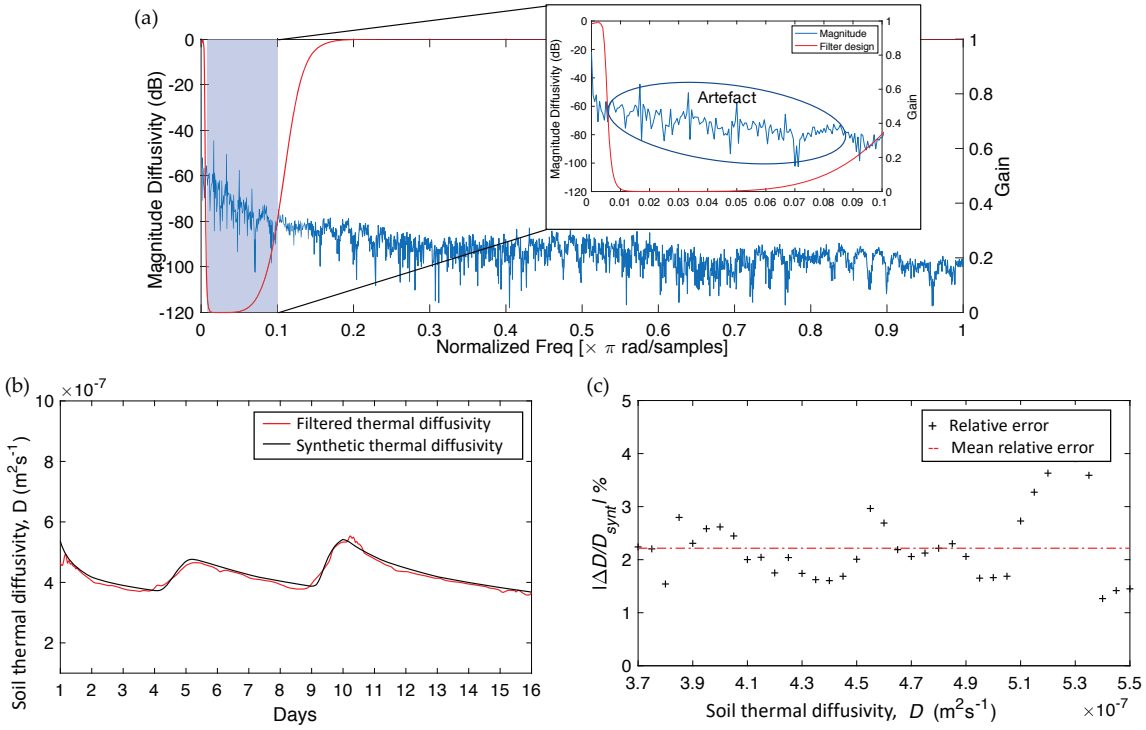

Figure 4.7 Calculated soil thermal diffusivity. The normalized cutoff frequencies were $f_{low} = 0.05$ and $f_{high} = 0.11 \times \pi$rad/samples. (a) Implemented filter design in the normalized frequency domain for a period where the artefact was removed. (b) Comparison between filtered soil thermal diffusivity and predefined thermal diffusivity. (c) Percentage of mean relative error $|\Delta D/D_{synt}|$ between calculated and predefined soil thermal diffusivities with $|\Delta D| = |D_{synt} - D_{calc}|$.

Step 4: Validation of strategy

The final step is validation. This step consists in comparing the calculated VWC and synthetic VWC generated by Hydrus-1D; the fit among the two-time series has a mean relative percentage error value of 1.4%. The scatterplot in Figure 4.8b expresses the accuracy of the calculated VWC compared to synthetic VWC using linear regression. The calculated VWC has a fairly similar value compared to the synthetic value indicated by a coefficient of determination, $R^2 = 0.92$, and a Root Mean Square Error, $RMSE = 0.06$ m³m⁻³.

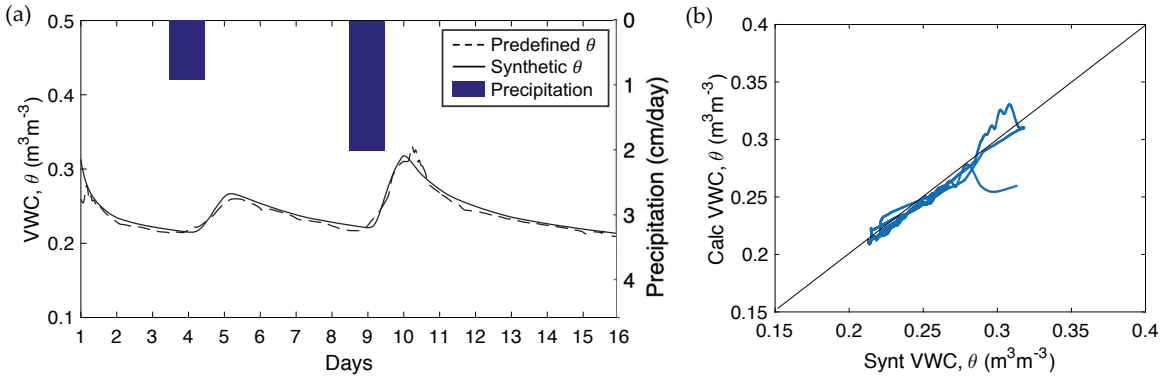

Figure 4.8 (a) Calculated VWC response overlapped with the synthetic VWC for two rainfall events. (b) Linear regression between calculated and synthetic VWC.

4.6 Implementation of VWC calculation based on field experiments.

This section describes the field implementation of the methodology for estimating VWC from soil thermal diffusivity at the clay-rich slopes of the Draix-Bléone catchment. After applying the explicit finite

difference simulation and the signal filtering to the apparent soil thermal diffusivity, water content variation in the catena can be inferred. For example, the calculation for the period 15-30 April 2016 yields the apparent soil thermal diffusivity response shown in Figure 4.9a, further post-processed using an appropriate filter. The artifact presented by the red line appeared twice in each day. Moreover, soil thermal diffusivity was more frequently overestimated.

To filter the artefact in the apparent soil thermal diffusivity response, the cutoff frequency was selected to fit to the variations in the VWC measured from the soil moisture probe. In field experiments, the cutoff frequency may not be the same for the various analyzed periods but maybe within a specific range of values. The band stop filter was designed according to the low-pass cutoff frequency range between 0.04 and 0.07 ($\times \pi$rad/sample) and the high-pass frequency range between 0.1 and 0.13 ($\times \pi$rad/sample). The black line in Figure 4.9a represents the filtered thermal diffusivity that performs acceptably for the field conditions (Fig. 4.9b). The comparison and error analysis between the FO-DTS calculated VWC and the measured VWC are shown in Figure 4.9c–d. The mean relative error of the VWC calculation is approximately 2.2% for the period and variation of soil water content due to infiltrating precipitation is revealed. The method is flexible as it allows to retrieve the measured variations in VWC, by adjusting a gain factor through normalization of the dry and saturated circumstances.

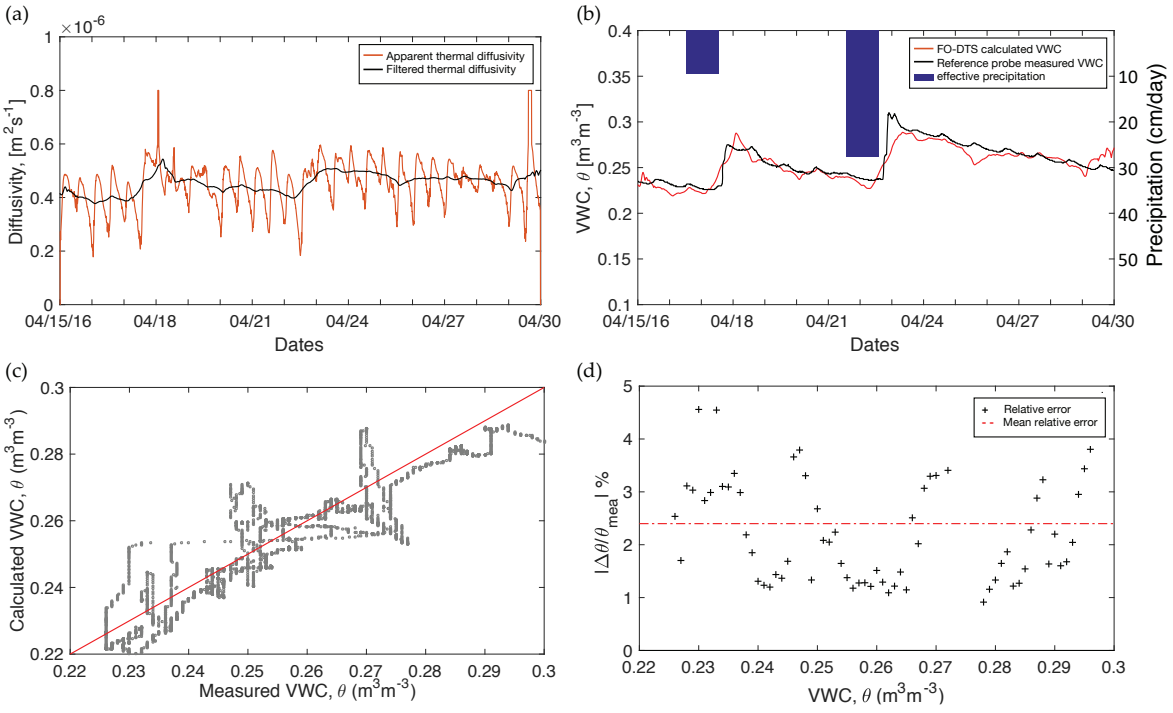

Figure 4.9 FO-DTS estimated thermal diffusivity and VWC versus reference soil moisture probe sensors for a period of two weeks, from 15 to 30 April 2016. (a) Calculated apparent and filtered soil thermal diffusivity based on FO-DTS soil temperature measurements. (b) FO-DTS calculated VWC versus reference soil moisture probe sensors. (c) Linear regression between FO-DTS calculated and reference probe measured VWC. (d) Percentage of mean relative error $|\Delta\theta/\theta_{measured}|$ between the calculated and reference probe measured VWC with $|\Delta\theta| = |\theta_{measured} - \theta_{calc}|$.

Figure 4.10a shows the measured soil moisture from 2016 to the end of 2017 as inputs to the inversion of the FO-DTS diffusivity for the three soil types. In this experiment, the depth of -10 cm corresponds to the Hydrus-1D simulation. The example period denoted by a red mark in Figure 4.10a was selected because it fits

the dry and saturated conditions of the VWC. The maximum and minimum VWC during the studied period are 0.31 and 0.22 m^3m^{-3} respectively (see Figure 4.9).

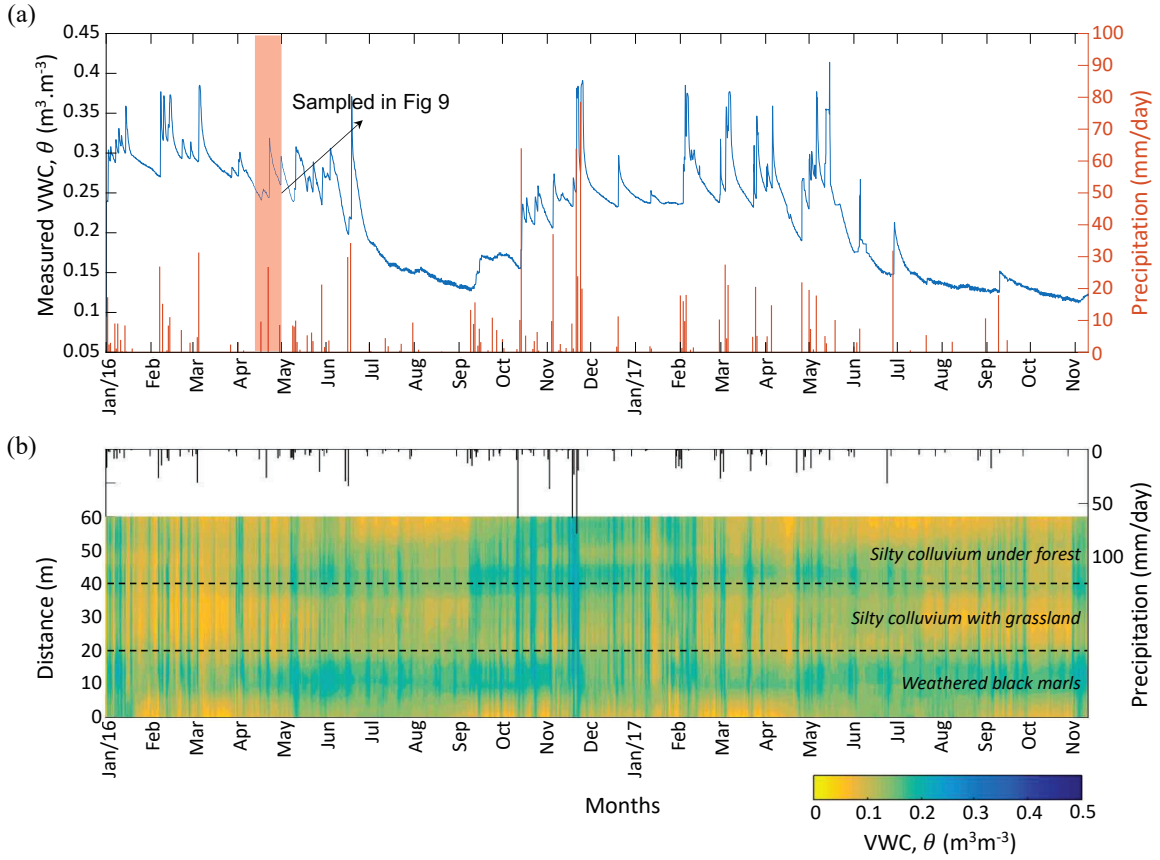

Figure 4.10 (a) VWC variations measured by the reference probe sensors during the period 2016-2017. (b) FO-DTS calculated VWC along the catena of three soil types and the precipitation. The response of the VWC calculation exhibits a delay of a few hours from the rainfall event peaks.

Soil thermal diffusivity calculations were performed for a period of two years based on the FO-DTS temperature measurements (Figure 4.4) to estimate VWC variation under natural heat sources. The soil temperature observations provide insights in the presence of water although it was very difficult to determine changes when the temperature gradient is very small, especially during the winter season when the calculated VWC exhibits its highest values. During the summer season, the diurnal heat source is relatively high, and the FO-DTS calculated VWC changes is nicely depicted in relation to infiltrating precipitation and thus soil moisture increase.

The changes in FO-DTS calculated VWC are presented in Figure 4.10b for the period 2016-2017. The weathered black marls soil tends to retain the water longer than the silty colluvium under forest during the summer season. This is explained by the presence of roots that cause high transpiration in silty colluvium under forest cover. Conversely, the presence of clay in weathered black marls prevents water from undergoing evaporation. The soil under grass is drier than the weathered black marls soil after the summer period. Indeed, solar radiation directly permeated through the soil and sparse vegetation (leaves, herbs), which result in higher evapotranspiration rates. The presence of a root zone under the grass also explains these higher evapotranspiration rates. In summary, evapotranspiration in the silty colluvium with grassland is more intense than on the weathered black marls and on the silty colluvium under forest.

The proposed processing mythology considering both hydrodynamic numerical simulations and signal processing, allows to exploit high temporal and spatial resolutions temperature observations to retrieve soil thermal diffusivity as a function of VWC in the subsoils. The method avoids any phase lag and amplitude analysis, but possibility of calculation biases must be noted. The result of the VWC calculation might not exactly represent the true volumetric water content and the filtering must be carefully designed according to reference soil moisture probe sensors. A calibration of the filter should be implemented, ideally, for each type of soil. It is also important to note that the processing parameters (e.g., cutoff frequency of the filter, soil heat properties) proposed in this work are specific to the conditions prevailing during the experiment.

4.7 Conclusion

This study developed a strategy, based on soil thermal properties used as proxy parameters, to determine soil thermal diffusivity and retrieve volumetric water content in shallow subsoils. The applied strategy combines hydrodynamic finite difference numerical simulations and spectrum analysis, allowing for the simultaneous calculation of soil thermal diffusivity from soil temperature amplitude and time differences. The calculated VWCs show that the storage of water in the subsoil is controlled by changing soil properties and evapotranspiration rates along the soil catena, which maximized in the summer season. Future work should aim to improve the accuracy of this method and reduce the calculation biases inherent to passive DTS experiments. This should enable high-resolution experiments based on water tracing to be conducted. The information obtained by the experiment described herein is important to understand the dynamics of preferential water infiltration at very high spatial and temporal resolution, and thus water resources, and to long-term soil weathering due to water–soil interactions.

This page intentionally left blank.

Chapter 5: Permanent High-Resolution Temperature Observation Using FO-DTS To Monitor Soil Water Changes In A Mediterranean Catchment

Abstract: The shallow weathering zone at Mediterranean catchments is highly affected by soil water changes in space and time. An experimental hydro-geophysical was performed to document the water storage in the topsoil. In this case, the temperature observation using fiber optic distributed sensing (DTS) is retrieved as a proxy parameter of soil moisture changes. The sensor has been installed at the Draix-Bléone hydrological observatory (South French Alps, Réseau de Basins-Versants/RBV) area since 2015. The 354 m fiber cable was buried at 0 m, -0.005 m, -0.010 m, and -0.015 m of depths and crossed three different soil units consisting of argillaceous weathered black marls (BM), silty colluvium under grassland (GR), and silty colluvium under forest (FR). The soil temperature is measured in a 6-minute time interval and 0.5 m of space. The analysis was performed in 23 months of temperature measurement (January 2016-November 2017). Several strategies were used to estimate soil moisture from thermal diffusivity using analytical and numerical solutions. Another soil moisture probe is also used as a comparison. The hydrological analysis is performed to understand the soil moisture behavior and seasonal and environmental patterns. The overall results of this study indicate permanent high-resolution temperature observation that adequately recognizes the soil moisture evolution over 23 months of observation.

Keywords: FO-DTS, soil moisture, temperature.

Kusnahadi Susanto[1], Jean Philippe Malet[1], Julien Gance[2], Vincent Marc[3]

[1] Institut de Physique du Globe de Strasbourg, CNRS UMR 7516/EOST – Université de Strasbourg, France ; susanto@unistra.fr
[2] IRIS-Instruments, Orléans, France
[3] Université d'Avignon et des Pays de Vaucluse, UFR-ip Sciences, Technologies, Santé, Fance, France

5.1 Introduction

Water content in the subsoil is essential to change the soil's physical properties. Knowing soil moisture is mainly used for agronomical and environmental studies (Al-kayssi et al., 1990). Water infiltration and evaporation influence the variation of soil moisture changes (Iverson, 2000) and evaporation. The soil moisture measurement is often used in science to recover the soil changes seasonally on the shallow surface as a hydrological behavior. Understanding soil moisture fluctuation in clay provides more benefit in slope cases (Bogaard and Van Asch, 2002). However, the water content in the active landslide is as complicated as the local hydrological regimes (Marc et al., 2017b). As an important scientific issue at the slope and catchment area, soil-water interaction is highly significant, especially in clay-rich slopes. The investigation of soil moisture by vertical temperature variation has been attempted over a long-term period and documented by indirect measurements such as temperature observation, capacitance, and electromagnetic travel time (Bechkit et al., 2014; Goran and Vesna, 2013; Krzeminska et al., 2012a).

In recent years, long-term temperature documentation has been measured by optical fiber distributed temperature sensing (J. Selker et al., 2006; Tyler et al., 2009). Optical fiber DTS based on Raman scattering and Optical Time Domain Reflectometry (OTDR) principal spatially and temporally document the temperature

changes very well (Jansen et al., 2011; Steele-Dunne et al., 2010). Optical fiber DTS has been proven accurate in measuring temperature along fiber exceeding 30,000 m and affording spatial resolution of 1 m per minute (Ciocca et al., 2012)and can be deployed with a good performance in complex terrain (Seyfried et al., 2016).

Temperature change is a significantly important factor in environmental process studies. It can be directly observed as a physical parameter of materials (Lane et al., 2008; Rutten et al., 2010). The robustness and lower cost for temperature measurement are the advantages of fiber optic DTS, which has been deployed in various environmental research and exploration, such as borehole observation, ice caves, solar ponds, soil, and groundwater (Hausner et al., 2011). Using temperature as a proxy, we estimate the soil moisture based on the thermal diffusivity model and heat capacity (Béhaegel et al., 2007; Benítez-buelga et al., 2014; Krzeminska et al., 2012a). Moreover, the performance of distributed temperature sensing allows for estimating the heat flux at the canopy layer on the soil (V. F. Bense et al., 2016). This method is also used to trace groundwater movement and distinguish the materials in dry, wet, and saturated soil conditions in the vadose zone (Weiss, 2003). Specific soil moisture influences the vadose zone hydrology and catchment area (Vereecken et al., 2008).

The heat equation indirectly states the relationship between soil moisture and temperature. Diffusivity is key for calculating water content influencing soil properties (Sayde et al., 2014). The vertical fiber optic cable can measure the soil's thermal profile and trace the temperature gradient from the surface to the subsoil. In our case, solar radiation will be a passive heat source of the observation system. Diurnal temperature variation can be used as an initial condition.

On the other hand, upper surface monitoring has been quantified for constraining the numerical shallow surface model. Heat transfer and energy balance at the interface between air and a few centimeters of soil should be a critical consideration. Heat flux estimation and index of control surface over evaporation are studied for monitoring soil moisture relevant to atmospheric exchanges (Castle and Elliott, 1999). To define the evaporation process, some sensors, such as a pyranometer, are needed. The air temperature sensor was installed at 2 meters above the soil surface. Air temperature should be measured to complete the Penman-Monteith as evapotranspiration (ETP) calculation. In addition, solar radiation properties such as shortwave and longwave radiation are needed for energy balance calculation (Sigmund et al., 2017).

In this work, long and short-term soil moisture calculations are presented. Fiber optic DTS is used for indirect long-term soil moisture monitoring by an inversion approach. The result was compared with rainfall occurrence datasets. The calculation of soil moisture informs an unsaturated zone at the shallow surface for a long time. The comparison of model calculation and another instrument observation is extended in this work.

5.2 Study site and permanent observation

5.2.1 Hydrological and site description

The observation site is at Draix Bléone [44°8'N, 6°21'E] and 13 Km northeast of Digne town, Apls de Haute-Provence, South of France. Figure 5.2 shows the location of the study site. It is dominated by black marls sensitive to weathering and erosion processes (Descroix and Claude, 2002). It consists of Jurassic marine (Bajocian, Bathonian, and Callovo-Oxfordian units) (Mathys et al., 2003). The elevation range is between 850 and 925 m, where 46% of the catchment area is covered by pine trees (Esteves et al., 2005). In addition, the catchment area also has a colluvium material dispersed in a silt-clay matrix (Maquaire et al., 2002). The primary source of groundwater is the infiltration of rainfall and snowmelt. Nevertheless, the snow is not permanently covered during the winter session (Corona et al., 2011). The precipitation is highly variable (0-80 mm/day). Moreover,

the intensity of solar radiation reached up to 1133 W/m² during the summer session and approximately 25 W/m² in the winter session. The area's climate has mountainous characteristics, with maximum precipitation in summer and frequent freeze-thaw during the winter session.

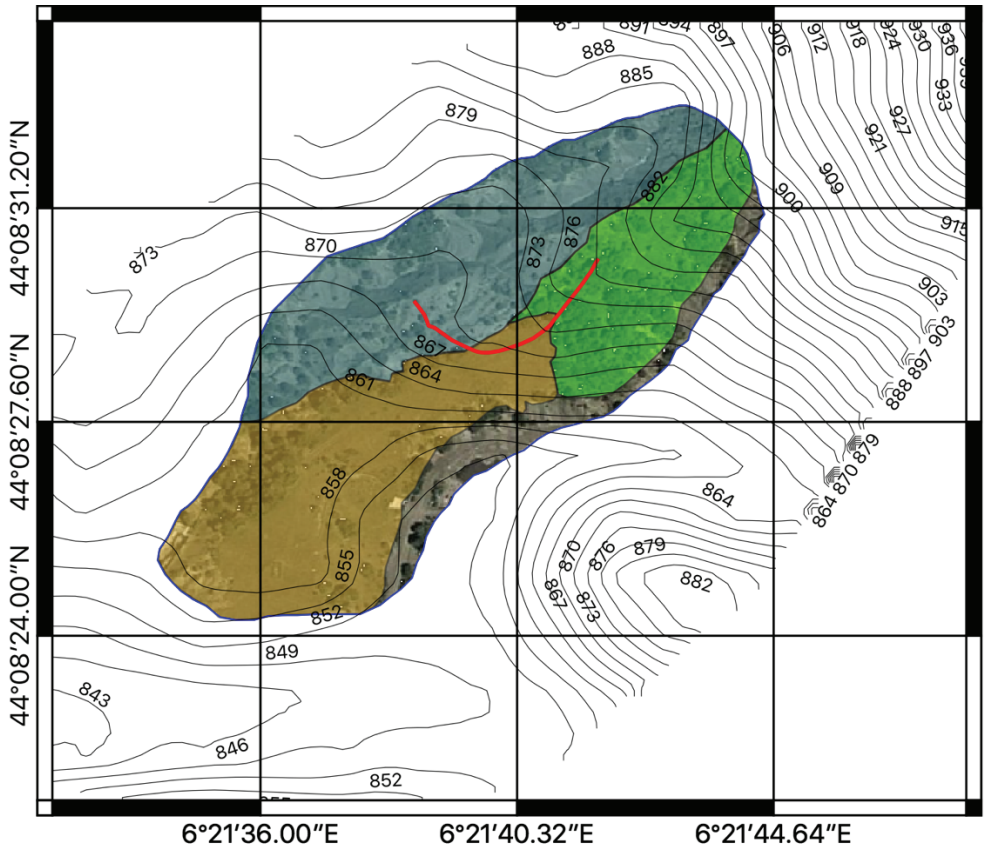

Figure 5.1 Location of hydrological observatory on the Draix-Bléone (South French Alps, Réseau de Basins-Versants/RBV).

Furthermore, the intense erosion in Draix Bléon is affected by water infiltration. This study site is susceptible to weathering and erosion (Antoine et al., 1995). Numerous studies have been conducted to understand soil water interaction on regional and river systems in this area (Corona et al., 2011). Water flow and infiltration were also modeled to reveal the environmental processes in natural hillslopes represented by topographic elevation and soil hydraulic parameters (Esteves et al., 2000). The Draix, a Mediterranean area with a mountainous climate, is called "badland" because it is a part of the black marls formation or "*Terres Noires*" in French. Historically, this area was described in detail by numerous studies in Cemagref (a French research institute on rural and forestry science) (Richard and Mathys, 1999). To understand the soil behavior that is dominated by black marl, a hydrogeological conceptual model was performed on Draix-Laval (Marc et al., 2017b). Numerous studies were conducted regarding erosion (Descroix and Claude, 2002; Esteves et al., 2000; Mathys et al., 2003), soil hydraulic properties (Esteves et al., 2005), and water flow modeling (Richard and Mathys, 1999). As a part of a large watershed, the Draix is an exciting observation site for environmental and soil study. It was passed by the Ravin de Laval watershed, yielding intense erosion. Because of exposed roots, the medium-term erosion rates vary between 6 and 7 mm/year depending on the uplift of roots after exposure (Corona et al., 2011).

In the weathering zone, soil-water interaction becomes a key parameter for soil deformation. Rainfall can be one of the most critical factors. The mean annual evapotranspiration is approximately 804 mm as a water recharge area. In addition, under high-intensity conditions, the runoff coefficient is high (20-50%) (Mathys et al.,

2005). In addition, it is a Mediterranean area that has high-temperature fluctuation. For two years (2016-2017), the average annual temperature was 11.28 °C. The maximum air temperature at the study site has been recorded to reach 42.83 °C and -13.21 °C in summer and winter sessions, respectively. The complexity of this situation makes it challenging to address the following issues: a) soil moisture behavior for land cover and uncover; b) the variability of soil moisture that is affected by hydrological cycles.

5.2.2 Observation setup

In this experiment, optical fiber DTS has been installed over two years on the Draix-Bléone (South French Alps, Réseau de Basins-Versants/RBV) hydrological observatory. It has observed the temperature since 2016. To measure the soil temperature, a 354 m long reinforced fiber optic cable manufactured by Brugg Cables (http://www.bruggcables.com) was buried at 0.05 m, -0.01 m, and -0.015 m of depths and installed at the soil surface (0 m). The total length of the monitored profile is 60 m (Figure 5.2), consisting of three different soil units. Those are argillaceous weathered black marls (BM), silty colluvium under grass (GR), and silty colluvium under forest (FR).

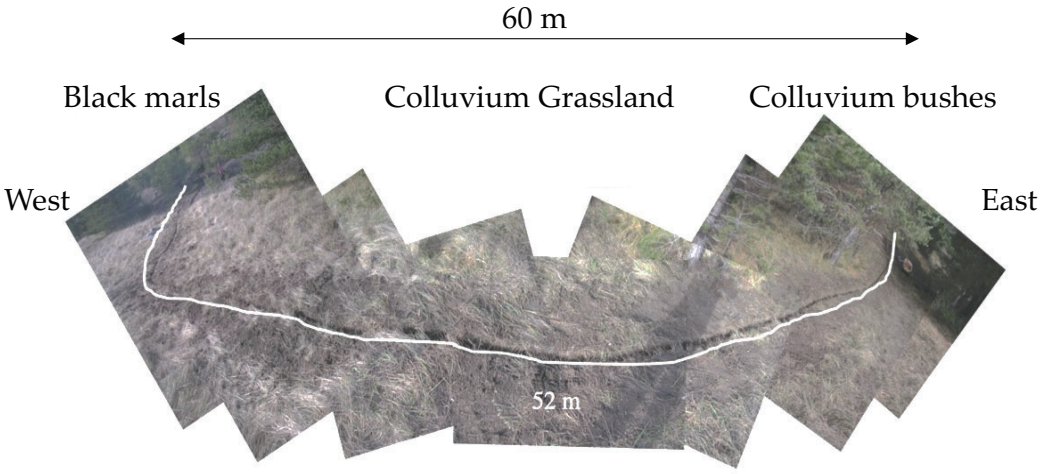

Figure 5.2 Experimental setup. Optical fiber DTS has been installed on the Draix-Bléone (South French Alps, Réseau de Basins-Versants/RBV) hydrological observatory.

The soil temperature is measured in time intervals of every 6 minutes and 0.5 m of spacing using a double-ended configuration. Therefore, we documented 484 points on the soil temperature profile area of 9 m^2 and 240 datasets for each day. The optical fiber was installed by incision way on the soil. The objective is to minimize soil damage around the fiber. The soil damage influences porosity and temperature propagation. The key to measuring temperature along the fiber is Raman scattering measurement. It uses the shift of Raman intensity of light called stoke and anti-stoke. Stoke is light intensity before scattering, and anti-stoke is light after scattering. Backscattering happened because of thermal induction around the fiber (J. S. Selker et al., 2006).

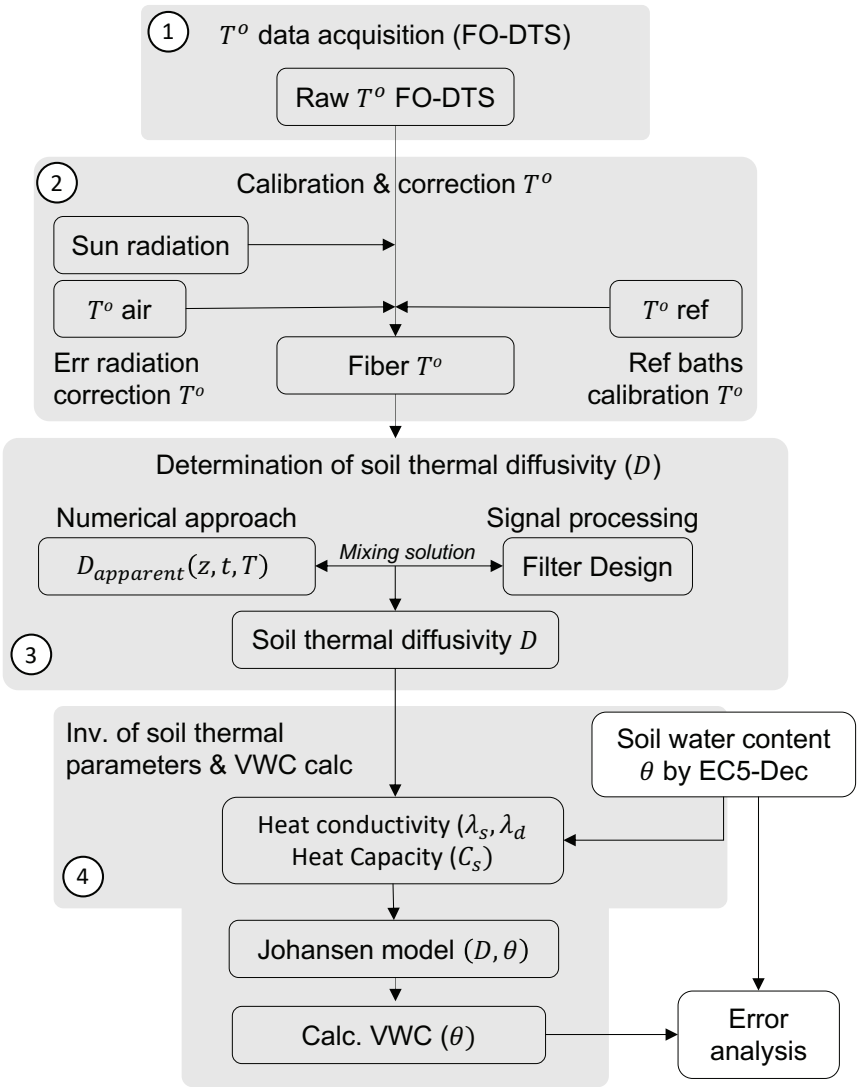

Figure 5.3 Flowchart of soil moisture estimation based on fiber optic DTS observation. Generally, the calculation is divided into the following four steps: treatment of fiber temperature datasets, diffusivity, and the other soil thermal properties estimation, then soil moisture calculation denotes water content.

To compare the performance of soil moisture calculation, we also installed EC5 Decagon as a soil moisture sensor. In principle, the EC5 Decagon used electrical permittivity and capacitance as a proxy to estimate the soil moisture. It was installed at four-depth vertical profiling close to the optical fiber cable. The accuracy of EC5-Decagon is 0-60% volume water content. The time measurement of EC5-Decagon needs 10 ms. In addition, the environmental situation was measured at the meteo-station area near the study site. The rain gauge sensor, pyrometer radiation sensor, and PT107 measure the rainfall event, solar radiation, and air temperature. The environmental measurements have been performed every 5 minutes since 2015. The meteo-station equipment aims to complete the environmental processes on the study site, especially for controlling temperature measurement and calculating soil moisture based on fiber optic distributed temperature sensing.

The general step of soil moisture estimation based on fiber optic DTS is shown in Figure 5.3. The raw temperature dataset obtained by fiber optic DTS passed through the following four steps: (1) temperature calibration using the baths reference and temperature correction because of solar radiation on the topsoil surface, (2) diffusivity calculation as soil thermal properties that will be applicable where soil water changes occur, (3) estimation of soil thermal properties such as volumetric heat capacity, dry and saturated soil heat conductivity uses nonlinear regression for a fitting approach to Johansen model curve, and the last step is (4) calculating the soil moisture using diffusivity and soil moisture relationship. Regarding calibration and

correction, the materials for solar radiation correction refer to Sigmund's calculation (2017) with the properties adjustment that is suitable for our case.

5.2.3 Dynamic calibration

The temperature along the fiber is a ratio between stokes and anti-stokes intensity influenced by an attenuation (α) and capture coefficient parameter (C). It was written by Farahani and Gogolla (1999) and rearranged by Suárez et al. (2011) in Eq 5.3. Vertical grid configuration can detect heat propagation (Figure 5.4). The configuration allows us to collect the temperature as a gridding and 2D matrix form in x and z as a distance and depth, respectively. The spatial grid temperature experiment on the x and z direction allows soil thermal properties to apply still where abrupt changes in soil moisture occur (Ross, 2014). At the soil surface, optical fiber will measure the interface of soil and air temperature. It is essential as an initial condition on finite difference calculation. The heat equation can be solved by interacting with diurnal temperature on the surface. The configuration with a diurnal temperature source is called a passive heated configuration (Steele-Dunne et al., 2010).

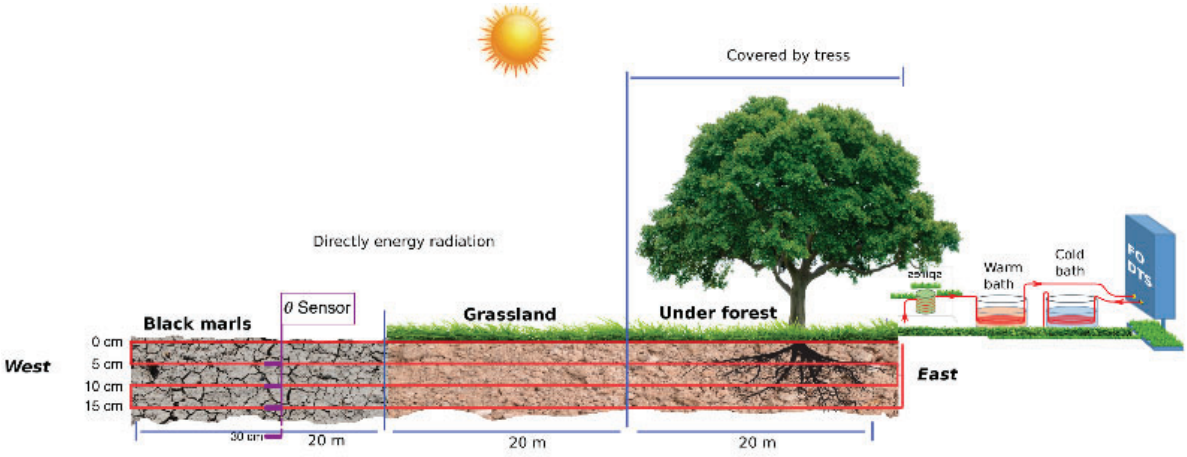

Figure 5.4 Observation setup. The 354 m fiber optic cable was spread through the baths reference. The DTS instrument is configured as a double-ended measurement through three soil units consisting of colluvium under forest (20 m), silty colluvium under grassland (20 m), and argillaceous weathered black marls (20 m). The soil porosity ranged from 37% to 49%.

Based on the schematic drawing shown in Figure 5.4, the temperature data collection is rearranged and becomes 2D slice profiling periodically. It can show the temperature propagation at a depth of 15 cm. The temperature variability can be analyzed for each depth in the time domain. At the surface, optical fiber measures the interface of air and soil temperature influenced by radiation and precipitation. In the subsoil, however, optical fiber only measured soil temperature affected by soil water content.

The temperature variability along the fiber is calibrated from time to time; even though the heat equation solution uses the differential temperature along the fiber, the corrected temperature is used for the time-lapse temperature difference. Indeterministic disturbance of temperature is possible, which is called random disturbance. The temperature reading by FO depends on laser quality. Theoretically, the laser should have a constant distribution of quantum states number $\gamma = \Omega/k$ (K). However, in practice, the Ω often has minor changes because of any disturbance, such as power supply and photon detector (van de Giesen et al., 2012a). Eq 5.1 describes the temperature along the entire fiber cable.

$$T(x) = \frac{\gamma}{\ln C - \ln[R(x)] + \Delta\alpha x} \qquad \text{Eq 5.1}$$

where T is soil temperature (K), and x is the distance along the fiber cable (m). The ratio between the power of Stoke and anti-Stoke is called R, which depends on x. The C is a calibration parameter that depends on the wavelength and frequency of the incident when the laser is in operating condition. It may vary in time (van de Giesen et al., 2012a). Therefore, we need to calibrate the temperature dynamically all the time. Then, α is the attenuation along the fiber. The correction coefficient $C(t)$ is an indefinite function of time because of random disturbance over time. Figure 5.5 shows the uncorrected and corrected temperature along the fiber optic. We used cold and warm baths for dynamic correction references.

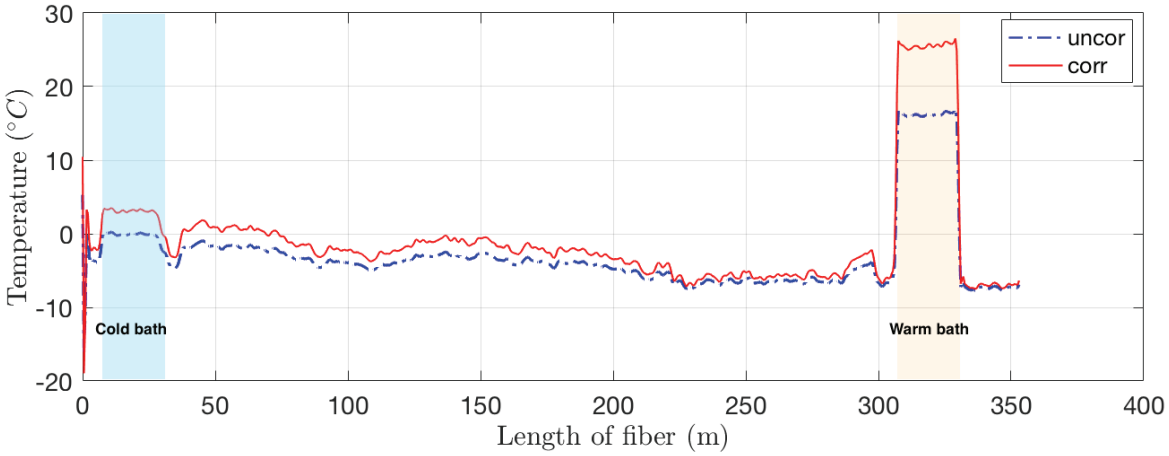

Figure 5.5 The uncorrected and corrected temperature measured by fiber optic. The reference temperature is ten pieces of PT100 at cold and warm baths. The correction process aims for temperature drift correction along the fiber. The dashed line is the temperature reading of fiber optic DTS, and the solid one is the calibrated temperature by baths reference.

5.2.4 Solar radiation correction

As shown in Figure 5.4, the first fiber optic line was deployed on the surface to measure the interface between soil and air temperature. In another case, fiber optic distributed temperature sensing was recently used to determine air temperature (De Jong et al., 2015). This situation allows the fiber optic to be directly heated by solar radiation. Therefore, the temperature measurement by fiber optic at the first line has an error reading called aerial radiation error (Sigmund et al., 2017). An energy balance calculation helps us quantify and remove the aerial radiation error caused by solar radiation (Figure 5.6a).

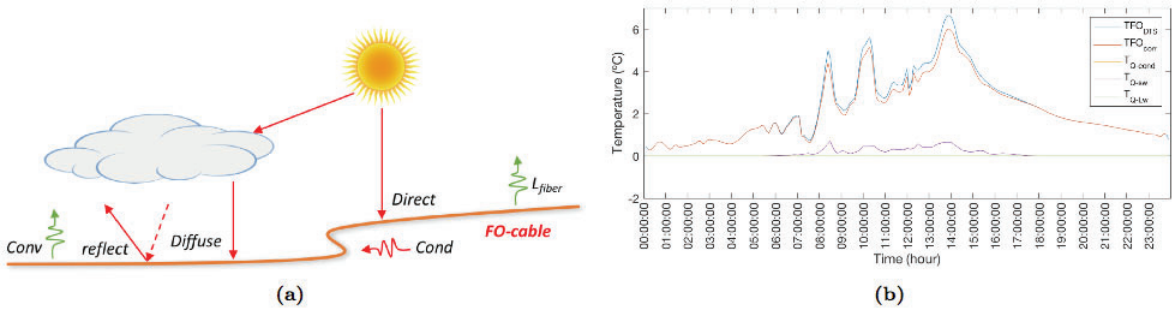

Figure 5.6 Quantitative correction of aerial radiation error on fiber optic distributed temperature sensing. The correction process aims to replace the effect of sun radiation measured by the pyranometer. (a) The energy balance component consists of incoming and outgoing wave radiation around the fiber; (b), i.e., an aerial radiation correction on fiber optic temperature at $z = 0$ cm on 1st April 2017.

The basic principle of this method is to use the shortwave, longwave, convective, and conductive heat transfer around the fiber for quantifying the modeled radiation. Our application uses the CS300 pyranometer produced by Campbell Scientific to provide total wave irradiance datasets installed at the meteo-station. In

addition, we used PT100 to measure the air temperature around the fiber and installed it at 1.7 m above the soil. The fiber optic temperature on the surface segment is inserted in Eq 5.2 to estimate the aerial radiation error. The formula consists of some material properties inside. Then, the temperature correction is calculated according to the following correction model (Sigmund et al., 2017).

$$T_c = T_s + \frac{1}{h}\left[\frac{1}{2}c_p \rho r \frac{dT_s}{dt} - \bar{S}(1-a) - \bar{L}\varepsilon + \varepsilon\sigma T_s^4\right] \qquad \text{Eq 5.2}$$

where T_c and T_s are the temperatures along the fiber (°C) after and before radiation correction, respectively; c_ρ is the specific heat capacity of fiber (kJ kg^{-1} K^{-1}); ρ is the density of fiber (kg/m^3); r is the radius of fiber optic; $\overline{S}$ and $\overline{L}$ are the shortwave (J s^{-1} m^{-2}) and longwave radiation (J s^{-1} m^{-2}) around the fiber; a is an albedo of fiber; ε is the emissivity of fiber; σ is the Stefan Boltzmann constant (J s^{-1} m^{-2} K^{-4}), and h is the convection heat transfer coefficient (J s^{-1} m^{-2} K^{-1}). For example, the modeled radiation error on the 1st of April 2017 amounted to 0.7 °C on incoming solar radiation 235.5 W/m^2 (cloudy weather) and precipitation 3.04 mm/day. The solar radiation correction is shown in Figure 5.6b. The fully corrected temperature is obtained by combining dynamic calibration and solar radiation correction.

Figure 5.7 shows the complete temperature correction for long-term observation. The slight segment contour performs the daily temperature changes. The interface temperature between soil and air above the surface is slightly higher than the subsurface during the summer and, vice versa, slightly lower throughout the winter. They also show the temperature difference in the BM, GR, and FR. The temperature of BM is slightly higher than those in GR and FR during drying periods, so it has a higher soil evaporation rate and greater heat capacity.

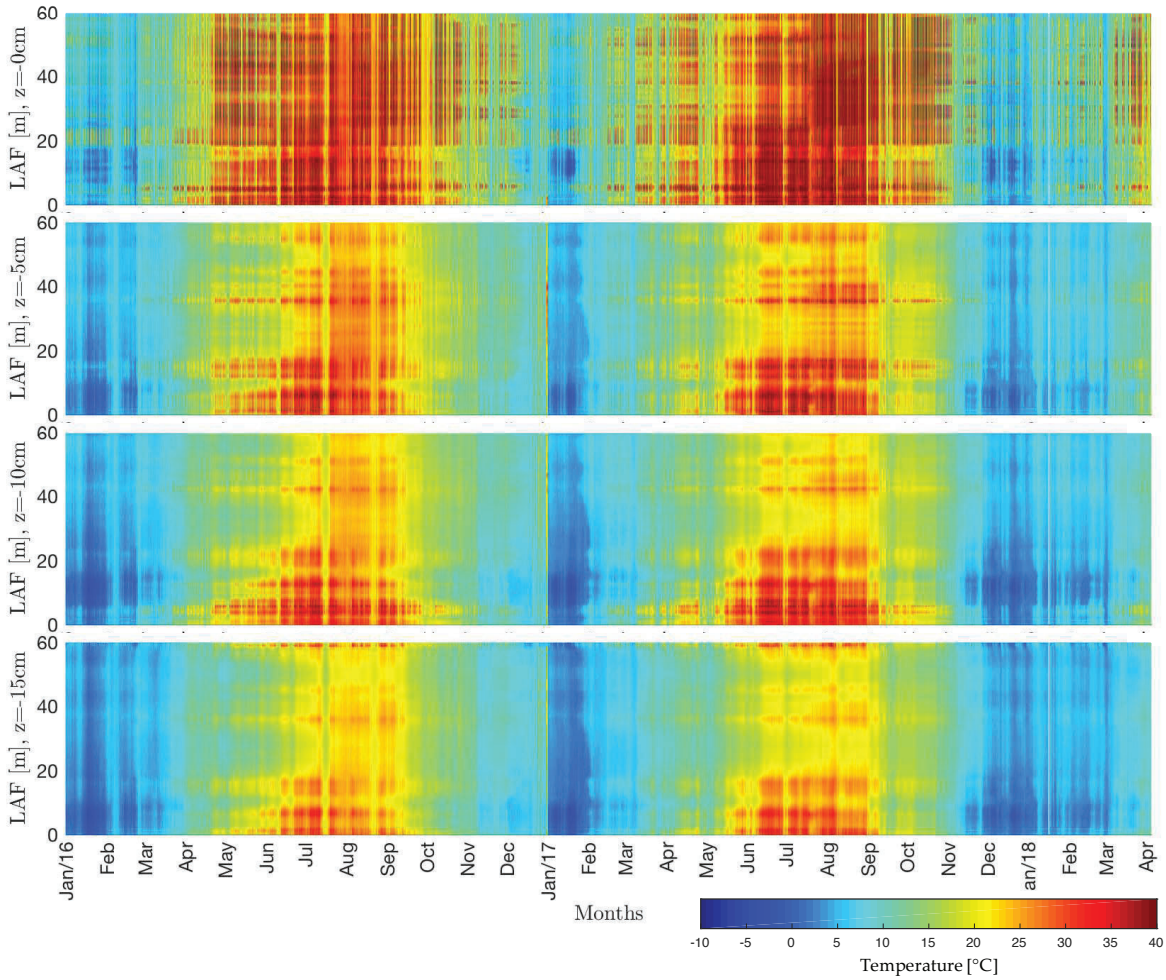

Figure 5.7 Long-term temperature observation using FO DTS was observed from Jan 2016 until March 2018 for four-point depths (0 cm, -5 cm, -10 cm, and -15 cm).

The calculation of the thermal soil properties in this paper is limited to conduction mechanisms by ignoring heat advection for simplification purposes. The heat transfer advection mechanism contributes to the heat transfer mechanism. However, it only occurs in the upper boundary condition. Figure 5.7 shows the variability of temperatures of 60 meters for each point depth (0 cm, -5 cm, -10 cm, and -15 cm) from January 2016 until November 2017. The time resolution is 6 minutes, and the spatial resolution is 0.5 meters. The minimum temperature is around -13.21 °C in the winter session, and the maximum temperature is around 42.83 °C in the summer session. The temperature propagation can be observed if the stacking temperature profile is arranged every 6 minutes. Temperature changes are always used to reveal the second-order differential equation's thermal properties.

5.2.5 Estimation of soil thermal properties

Thermal diffusivity leads us to understand the intrinsic soil property. It contains some parameters that can change the value, such as heat capacity $C(\theta)$ and heat conductivity $\lambda(\theta)$. The θ is soil moisture controlled by water infiltration due to precipitation and drainage due to evaporation. Thermal diffusivity is the ratio between thermal conductivity and heat capacity Eq 5.3.

$$D = \frac{\lambda(\theta)}{C(\theta)} \qquad \text{Eq 5.3}$$

The relationship between diffusivity and heat soil capacity is linear (Campbell et al., 1991). However, the relationship between thermal conductivity and water content is more complex. The porosity of soil heat capacity Eq 5.5 also influences thermal diffusivity. The most widely used model for finding thermal conductivity relationships with water content is a Johansen (1975) model that makes the range of dry and saturated soil conductivity and then normalizes both using Kersten's number shown in Eq 5.4 and Eq 5.5.

$$K_e = \log_{10}\left(\frac{\theta}{\phi}\right) + 1 \qquad \text{Eq 5.4}$$

$$D(\theta) = \frac{\left[\log_{10}\left(\frac{\theta}{\emptyset}\right) + 1\right](\lambda_s - \lambda_d) + \lambda_d}{(1-\emptyset)C_s + \theta C_w} \qquad \text{Eq 5.5}$$

where ϕ is porosity (%), and C is volumetric soil heat capacity (MJ m^{-3} K^{-1}). C_s and C_s are the specific heat capacity of dry soil and water heat capacity, respectively. The λ_d and λ_s are the heat conductivity of dry and saturated conditions (W m^{-1} K^{-1}). This relationship model is limited to unfrozen fine soil expressed by ($\theta/\phi > 0.1$). K_e is the Kersten coefficient (Kersten, 1949), and D is the soil diffusivity. Furthermore, dry and saturated conductivity also have their semi-empirical models (Rutten et al., 2010). Soil heat parameters are needed to obtain the relationship between diffusivity and soil moisture. The nonlinear regression estimates the volumetric soil heat capacity and soil heat conductivity of dry and saturated conditions. Using the Johansen model, the estimated parameter is optimized based on the error minimalization method (Eq 5.6 and Eq 5.7). The best-fitted parameters should produce minimal error.

$$y_i = D(\theta; \lambda_s, \lambda_d, C_s) + \epsilon_i \qquad \text{Eq 5.6}$$

$$e = \sqrt{\frac{1}{n}\sum_{i=1}^{n}\left(y_i - D(\theta_i; \lambda_s, \lambda_d, C_s)\right)^2} \qquad \text{Eq 5.7}$$

where y_i is the model soil diffusivity, ϵ_i is the misfit prediction error attended by measurement (observation) error, and e is the root mean square error (RMSE). The diffusivity variable as a function of soil water content is taken from soil temperature observation, and the soil moisture is taken from EC5 Decagon.

5.3 Results

5.3.1 Long-term thermal behavior

The temperature time series is statistically analyzed during the observation. Moreover, spectrum analysis and signal-to-noise ratio (SNR) define the quality of the temperature signal. By the spectrum analysis, the signal frequency component on long-term temperature observation should represent at least two annual and diurnal frequencies. Several causes could generate the random noise of temperature. The rainfall events, cloudy situations, and wind speed may influence temperature fluctuation, and they can reduce SNR significantly. Thus, the noise was left to exist in this temperature observation.

Figure 5.8 shows each soil type's spectrum analysis, SNR value, and depth position. Generally, the spectrum analysis represents that the temperature signals contain the annual (around 3.15×10^{-8} Hertz $\cong$ 367.4 days) and diurnal frequency (around 1.15×10^{-5} Hertz $\cong$ 24.1 hours). Other higher frequencies exist to represent seasonal periods. Besides, all frequency responses show that noise amplitude tends to decrease along with soil depth. By spectrum analysis, the average noise amplitude is 0.78 °C, 0.62 °C, 0.51 °C, and 0.35 °C on 0 cm, 5 cm, 10 cm, and 15 cm, respectively. Further, the SNR is calculated to define the temperature and noise ratio on the annual and diurnal frequencies. The annual SNR is more than 56 dB, and the diurnal SNR is more than 30 dB. Furthermore, the statistical approach, the average temperature, and the standard deviation at a specific time are used to examine the temperature for each soil type. The representative observation is associated with weather changes compared with the other sensor measurements. The comparison is performed to prove the concept of long-term observation for 23 months. An attempt was made to reveal the temperature distinction.

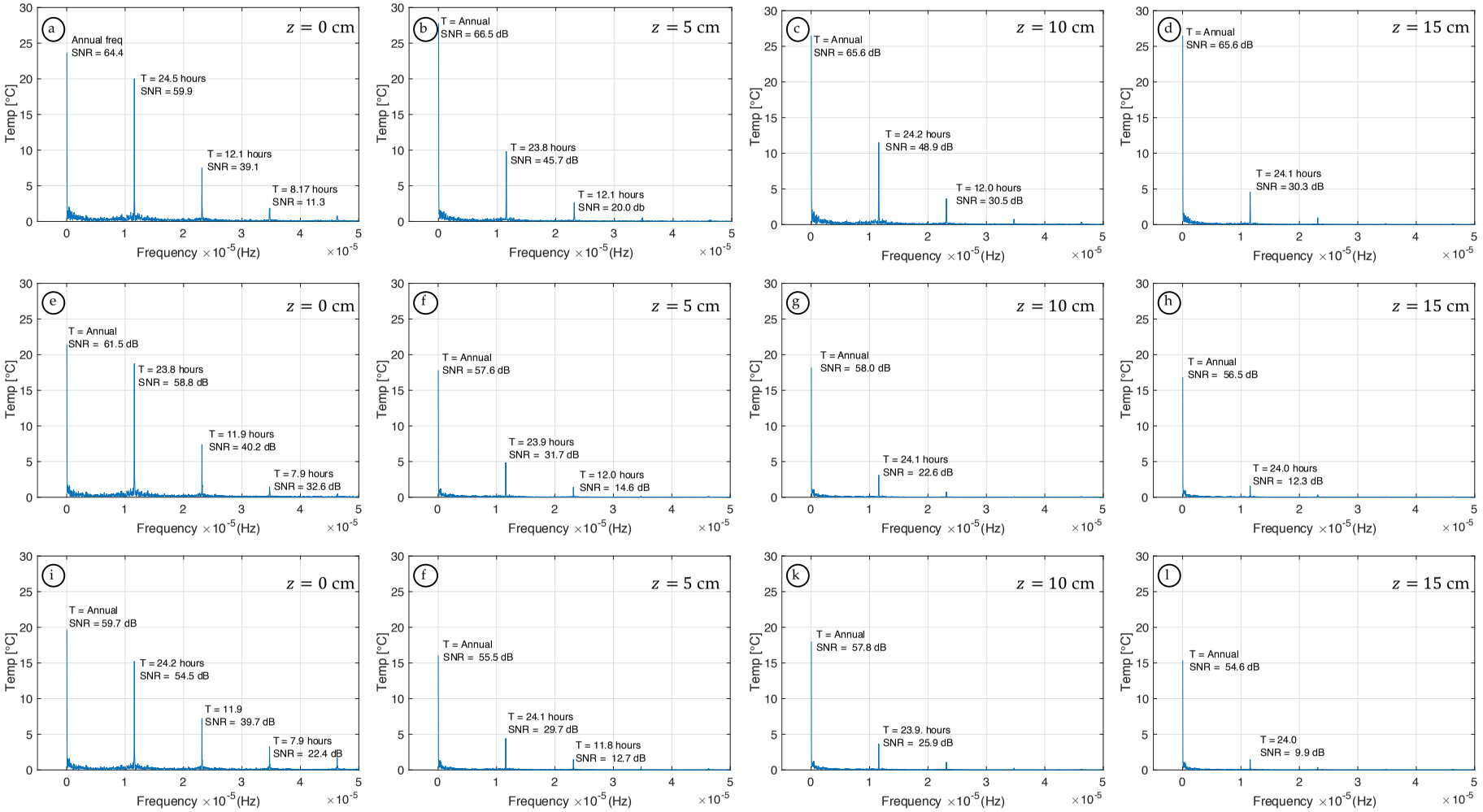

Figure 5.8 Spectrum analysis and signal-to-noise ratio (SNR) of fiber optic temperature reading. (a to d) Black marls, (e to h) Grassland, and (i to l) Soil under forest.

Table 5.1 The standard deviation of temperature measurement for each soil unit at several depths. The sampling numbers are 40 points at the same depth for each soil unit.

Depth [cm]	Standard deviation [°C]		
	FRs	GRs	BMs
0	1.38	1.25	1.99
5	0.88	0.99	1.29
10	0.84	0.91	1.85
15	0.68	0.8	1.14

The temperature observation during 2016 was measured properly with high spatiotemporal resolution at drainage and saturated soil conditions. Figure 5.9a, b, and c are the average temperature of the BM, GR, and FR, respectively. Table 5.1 shows that the temperature at BM fluctuates more than other soil types. A higher standard deviation at every depth position indicates it. Table 5.1 also shows that the surface temperature fluctuates more than in the depth position, and the standard deviation value is relatively close. The standard deviations on the surface are 1.99 °C, 1.25 °C, and 1.38 °C for BM, GR, and FR, respectively. It means the source of temperature fluctuation on the surface is likely the same for all soil units. In this case, the temperature fluctuation on the soil surface is influenced by solar radiation, cloudy weather, the shadow of trees, air temperature, and effective precipitation. The standard deviation decreases in the depths to 0.80 °C and 0.68 °C for GR and FR, respectively. It means that the temperature fluctuation is relatively lower than the soil surface.

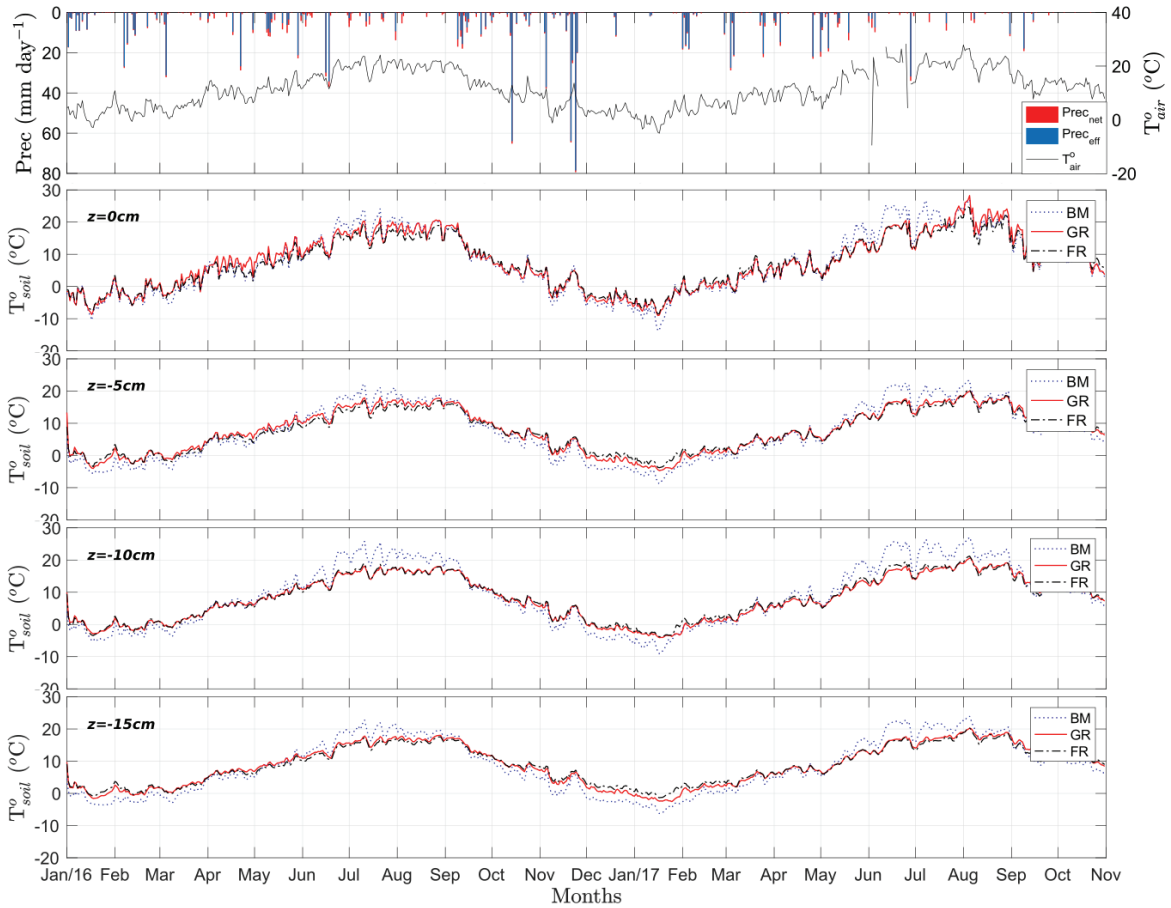

Figure 5.9 The effective precipitation and air temperature during the experiment. The red bar is a daily precipitation value, and the blue is effective precipitation. The solid line is the daily air temperature measured at +1.7 m above the soil surface. The position of profiles measured mid of BM ($x = \pm 10$ m), mid of GR ($x = \pm 30$ m), and mid of FR ($x = \pm 50$ m). The first row contains information on precipitation and air temperature variation. The second row is the temperature at $z = 0$ cm the surface, and the bottom row at $z = -15$ cm.

Figure 5.9 provides information on the environmental temperature in the air and the effective precipitation during observation. We measured the rainfall event using the AGR100 rain gauge switch. The accuracy of the rain gauge is 0.2 mm per sampling switch. Furthermore, the potential evapotranspiration is calculated by Penman-Monteith, which is proven suitable for Mediterranean climatic characterization (Ficklin et al., 2015; Longobardi and Khaertdinova, 2014). Furthermore, the spatiotemporal differences in temperature changes coincided with the "saturation" and "drainage" areas around the cable installation. Both analytical and numerical solutions can be applied to determine the wet and dry situation. Applying the analytical method for calculating diffusivity yields a moderate coefficient correlation value. In detail, we obtained a correlation of 0.52 from the 5th of May to the 15th of June 2017. The rainfall occurred seven times during this period. The observed temperature is plotted with the modeled temperature based on numerical diffusivity calculation to estimate the misfit calculation (see Figure 5.10a). The Root Mean Square Error (RMSE) obtained between observation and modeled temperature is 0.05 K, and the Mean Relative Error (MRE) is 5.67%.

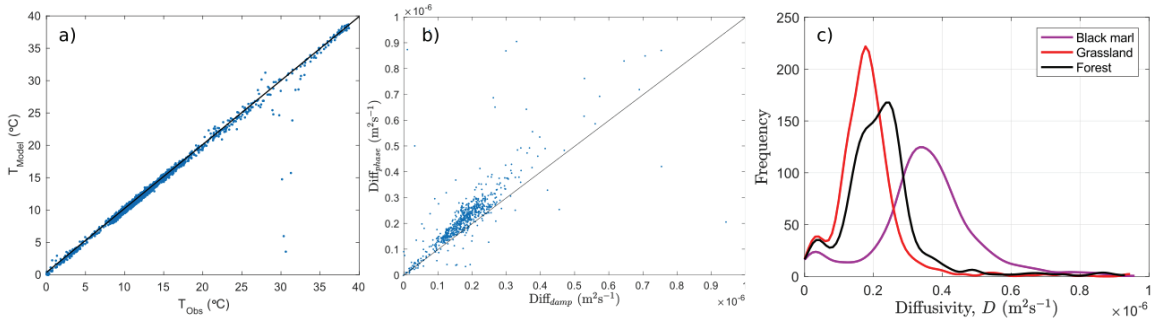

Figure 5.10 (a) The linearity of observed and modeled temperatures based on the diffusivity calculation. (b) The linearity of both damping depth and phase lag analysis. (c) Distribution of thermal diffusivity along temperature observation.

The calculated diffusivity based on damping depth and phase lag is close. Figure 5.10b shows the linearity of calculated diffusivity based on analytical methods. The high diffusivity value is slightly dispersed due to the water infiltration, and the absence of water makes them converge close to the linearity line. Regarding both analytical and numerical methods, the diffusivity on the dry and wet conditions are about 2×10^{-7} m²/s and above 3.5×10^{-7} m²/s, respectively, even more as an overestimated. However, the absolute value is unrelated to the intensity and amount of rainfall rates (Krzeminska et al., 2012a). Figure 5.10c shows the diffusivity distribution of each soil unit. A graphical distributed soil diffusivity shows that each soil unit has a relatively similar standard deviation.

On the other hand, we found specific behavior of each soil unit. The BM has the highest average soil thermal diffusivity on this observation term, followed by FR and GR, which are the lowest. The average diffusivity is 3.8×10^{-7}, 2.2×10^{-7} and 1.8×10^{-7} m²/s for BM, soil FR, and GR, respectively.

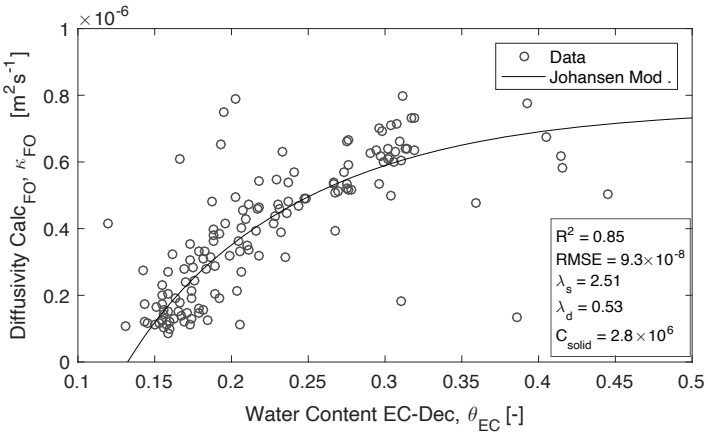

Figure 5.11 Estimation of Johansen parameters model to estimate the soil thermal properties that relate to soil moisture by using the nonlinear regression method.

Furthermore, the conversion of diffusivity to soil moisture follows the Johansen model using the parameter estimated based on nonlinear inversion. In the case of Draix, the soil porosity is obtained from Romain and Cola's experiment (2016), which describes the porosity range as 40-51%. In another experiment, F. Malet presented the detailed porosity of each soil type. The average porosity of black marls is 0.37%, and the average porosity of grassland and soil under forest is 47% (Mallet, 2018). The porosity is used for soil thermal parameters estimation, such as soil heat conductivity and capacity. The standard measurement of soil moisture was conducted by EC5 Decagon aid to estimate the soil heat properties. Figure 5.11 shows the fitting of the Johansen model curve. Based on the nonlinear inversion, the dry conductivity is 0.53 W m^{-1} K^{-1}, saturated conductivity is 2.51 W m^{-1} K^{-1}, heat capacity is 2.8 MJ m^{-3} K^{-1}, and the RMSE is 9.3×10^{-8}, and R^2 is 0.85.

5.3.2 Long-term soil moisture changes

This section analyzes the soil moisture changes depending on the effective precipitation. Daily soil moisture measurements based on numerical and analytical methods are performed to investigate soil moisture on this site. Figure 5.12a presents the complete soil moisture estimation during observation calculated based on the numerical method and the signature of the rainfall event. Despite the weak correlation of soil moisture changes with effective precipitation, the second-order finite difference and Johansen model approach are reasonably good for detecting soil moisture changes during temperature observation, especially in summer. The slight temperature gradient during the winter session is the most difficult. Winter snow completely influences the topsoil's heat transfer regime to the subsurface. We obtained regular daily signal fluctuations when analyzing soil moisture using high resolution in time. It occurs because of periodic diurnal temperature fluctuations. The moving average can eliminate fluctuations in daily soil moisture. The moving window that is suitable for eliminating this problem is 24 hours. The consequence of this strategy is the time delay. The calculation of soil moisture increases slowly with rainfall.

On the qualitative assessment, the water infiltration influences soil moisture calculation, as would have been expected on a conceptual basis. As a detailed analysis, Figure 5.12b and c compare soil moisture changes and effective cumulative precipitation. We present 21 days of fiber optic temperature observation and soil moisture calculation as detailed examples. It is taken from the 5th of May until the 15th of June 2017). The significant coefficient correlation between rainfall rate and soil moisture was estimated by damping analysis

(r = 0.41), and soil moisture was estimated by phase shifting analysis (r = 0.37). The long-time soil moisture calculation based on the finite difference method has a limitation.

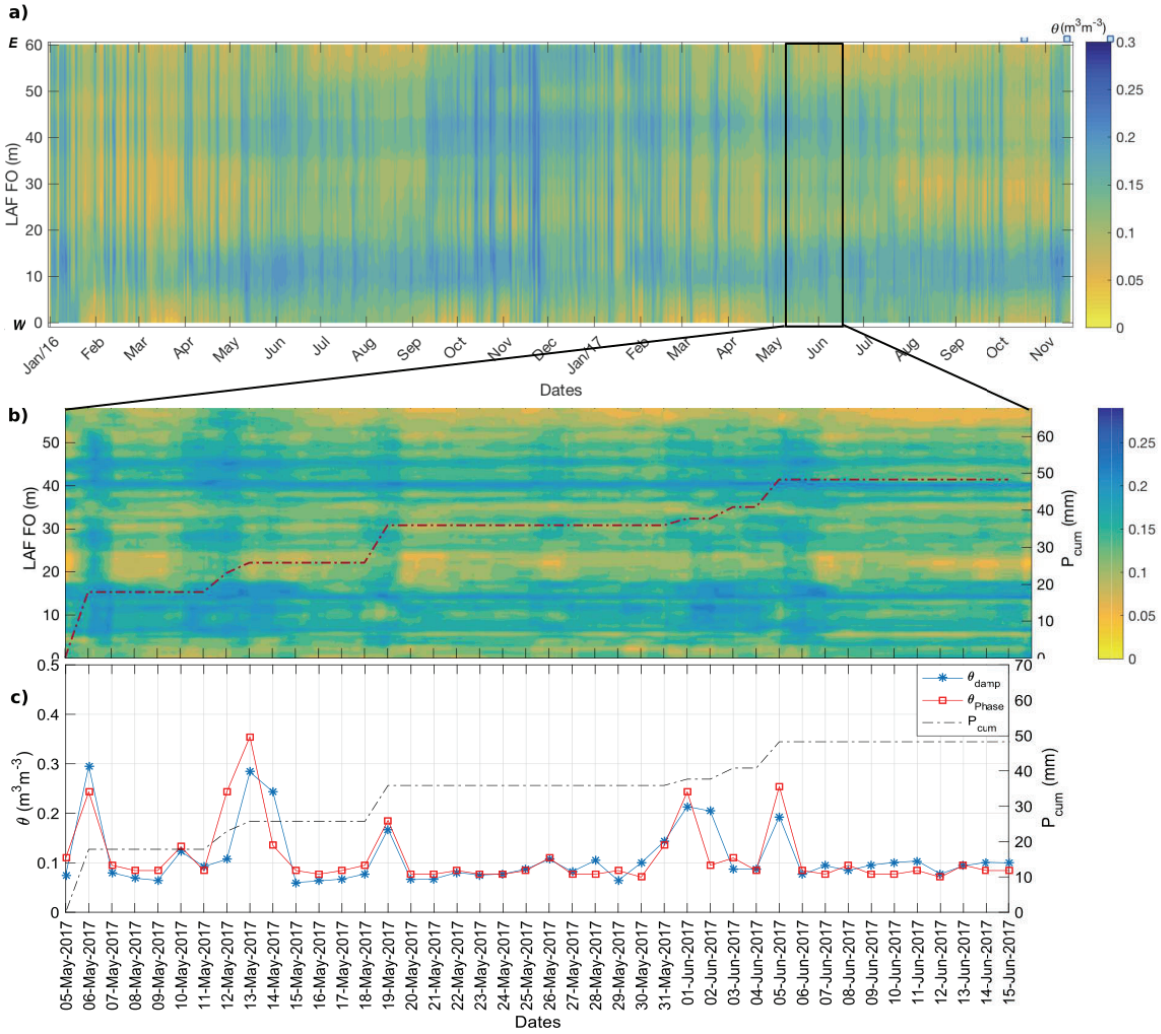

Figure 5.12 The soil moisture changes are based on high-resolution temperature measurements and numerical method calculation. (a) from January 2016 to November 2017. (b) and (c), i.e., from the 5th of May to the 15th of June 2017.

Despite having a high-frequency measurement resolution, the daily moving average is needed to avoid diurnal temperature changes. It provokes a small amount of tardiness between the soil moisture calculation and rainfall events. Moreover, it can reduce soil moisture if the rainfall rate is meager, as this study aims to monitor soil moisture and document the resolution of observations of high spatiotemporal temperatures. However, there are limitations, especially in time response and extreme rain events. The temperature differences in winter sessions do not help calculate soil moisture because of the minimal temperature gradient in time and space. In addition, the presence of snow influences the heat transfer regime. At this point, the diurnal heat temperature in the summer session was helpful as the passive heat source for calculating soil moisture based on long-term temperature observation in the field.

The variability of calculated soil moisture for each soil type has a similar pattern with a different value, which might be caused by different vegetation on the topsoil. The BM has the highest soil moisture because it does not have vegetation on the topsoil. It may not be an intensive transpiration process in this soil unit.

Evaporation is the main drainage process in the BM area. The vegetation and roots in the soil accelerate the evapotranspiration process on the GR and FR. Therefore, the GR and FR moisture dries faster than the BM.

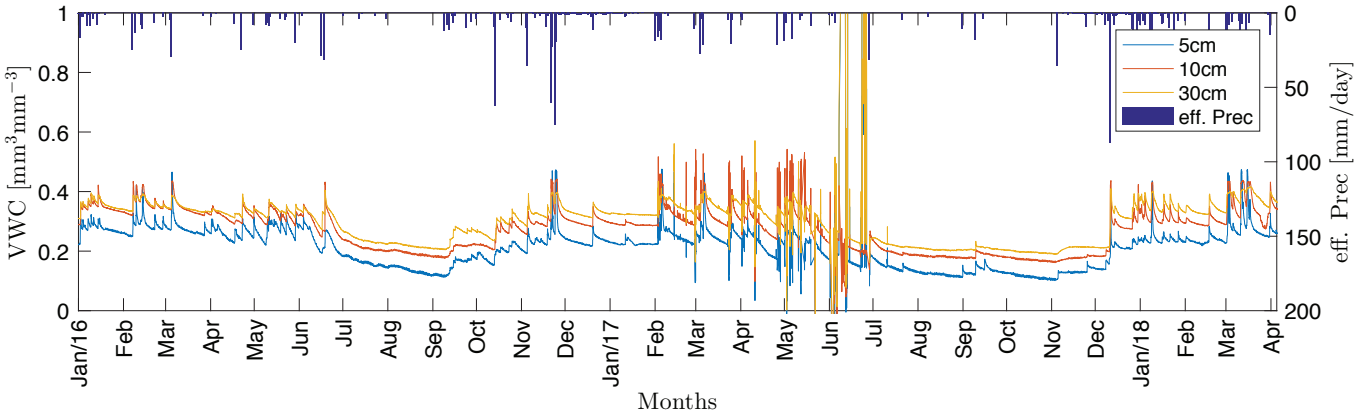

Figure 5.13 The evolution of soil moisture measured by EC5-Decagon probe related to rainfall events.

The estimated soil moisture based on fiber optic temperature sensing is compared with EC5 Decagon as another soil moisture probe (see Figure 5.13). The EC5 Decagon neglects the soil temperature and only uses electrical permittivity and capacitance to convert soil moisture. The existence of EC5 Decagon aims to validate the calculated soil moisture and makes a constraint on the Johansen model. The field capacity of the soil moisture is different for each soil unit. We examined the differences in soil moisture in several variable periods. Those are 23 studied months (long-term observation, complete datasets), winter and summer sessions, wetting and drying periods, and storm events on the study site. Statistical analysis was performed to understand the soil moisture behavior for each soil unit (see Table 5.2).

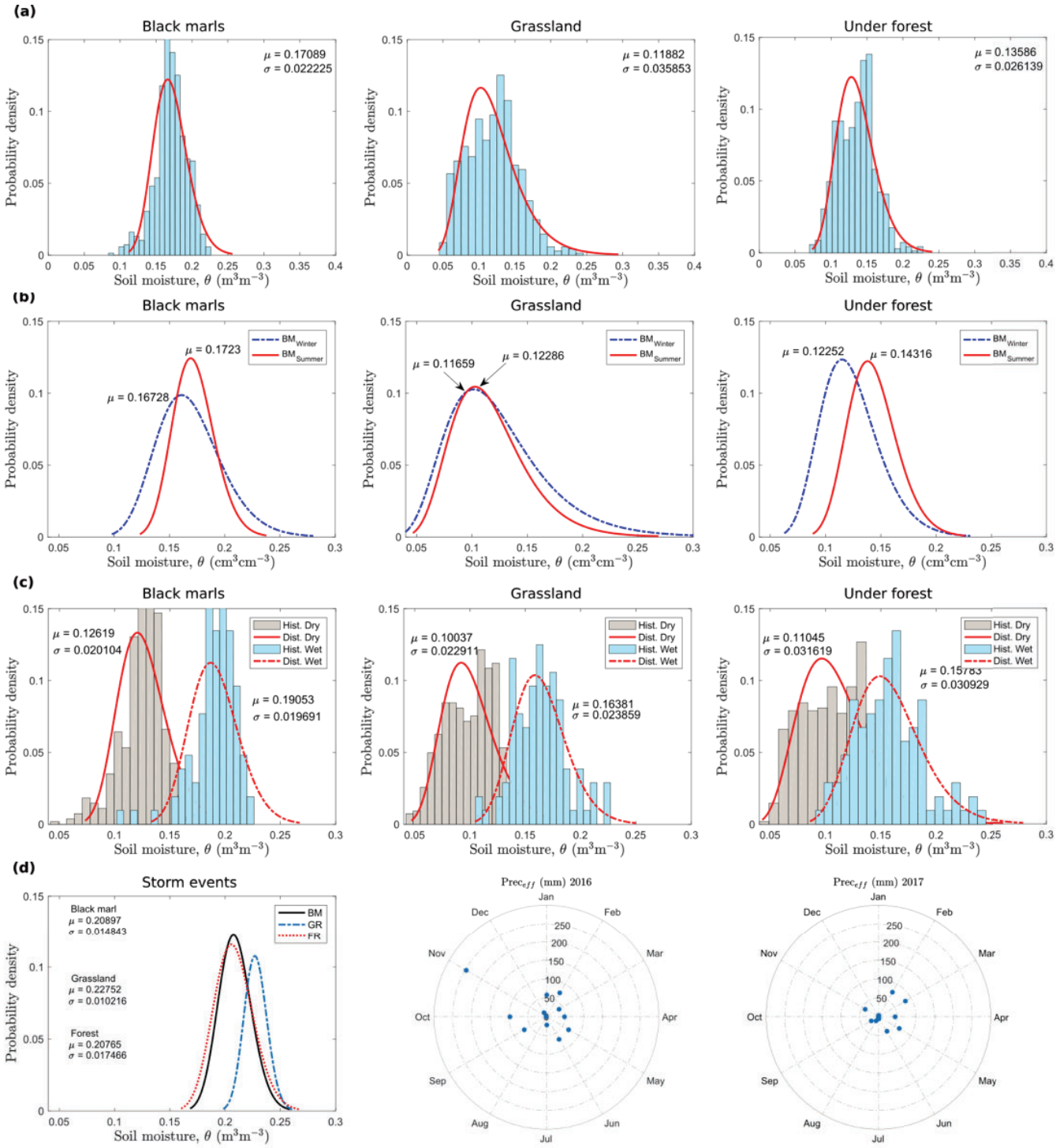

Figure 5.14 Distribution of soil moisture fitted with the log-normal analytical distribution. The red lines are the log-normal probability distribution function (pdf), and the histogram is the data distribution. (a) Twenty-three observed months, (b) summer and winter session, (c) wetting and drainage environmental process, (d) storm rainfall and monthly rainfall volume polar plot.

In another case, we analyze the soil moisture behavior for specific environmental processes such as summer and winter sessions, wetting and drainage processes, and soil moisture after heavy rainfall. Figure 5.14 presents the soil moisture distinction for each soil unit on specific hydrological processes. As shown in Figure 5.14b, the mean of BM and FR soil moisture is higher in summer than in winter sessions, but the standard deviation is relatively similar. The GR has a tiny difference in soil moisture in both summer and winter sessions.

Nevertheless, the soil moisture in summer is still higher than in winter. However, the evolution of soil moisture patterns based on fiber optic observation reveals that seasonal changes influence differences in the field capacity of soil moisture. The increase of soil moisture in summer sessions occurred in FR. It might be caused by root existence as an essential factor contributing to the evolution of soil moisture in FR.

Table 5.2 The estimation of mean and standard deviation characterizing the log-normal distribution used to soil moisture variation θ (m^3/m^3) for the soil season based on fiber optic observation.

Session	Number of days	FRs	GRs	BMs	Avg. Air T [°C]
23 months	678	0.136 ± 0.026	0.119 ± 0.036	0.171 ± 0.022	11.23
Winter	244	0.123 ± 0.028	0.123 ± 0.041	0.167 ± 0.028	3.88
Summer	434	0.143 ± 0.022	0.117 ± 0.033	0.172 ± 0.018	15.56
Wetting*	134	0.164 ± 0.024	0.159 ± 0.031	0.191 ± 0.019	9.17
Drying	544	0.100 ± 0.024	0.110 ± 0.031	0.127 ± 0.020	11.67
Storm events**	3	0.208 ± 0.017	0.229 ± 0.010	0.208 ± 0.015	10.14

Generally, the characterization of BM has the highest soil moisture than the GR and FR. The average BM soil moisture is 0.171 $m^3\ m^{-3}$ in 23 studied months, followed by soil FR 0.136 $m^3\ m^{-3}$ and GR 0.119 $m^3\ m^{-3}$ (Table 5.2 and Figure 5.14a). Evaporation is the main factor in the water movement in BM because there is no vegetation on the topsoil. Hence, the evapotranspiration rate in the BM is meager. On the other hand, the average soil moisture on GR is lower than the FR due to a more intensive evapotranspiration process.

5.3.3 Hydrological and soil moisture analysis

Table 5.3 shows the study site's soil water retention characterization and composition. Consistently, the soil water retention parameter also presents that the inverse of the air entry pressure α and pore size distribution n in BM is the lowest than the others. Hence, the BM releases the water at a lower potential. Statistically, this phenomenon will increase the mean of soil moisture based on probability density function analysis linked to local evapotranspiration on BM. Table 5.3 also present the other soil water retention parameters obtained while fitting the Van Genuchten model for each soil unit in unsaturated condition.

Furthermore, we observed the distribution of soil moisture in the wetting and drainage process. The distinction of soil moisture in the wetting and drainage process defines the field capacity of loss of water content for each of the soil units during the drainage process after rainfall events (see Figure 5.14c). The depletion of soil moisture in BM is higher than the others, meaning BM has a higher field capacity. Nevertheless, the depletion of FR describes that soil organic matter helps retain water inside. Figure 5.14d presents the distinction of soil moisture for each soil unit during heavy rainfall events in the winter storm period. The winter storm occurred thrice in late autumn 2016, with effective precipitation rates reaching around 80 mm/day. It was not a torrential rainfall event but shows the distinction between soil field capacity and water content. The monthly rainfall volume polar plots show that the highest cumulative effective precipitation rates were around 250 mm/day in November 2016. In this case, the average soil moisture of GR is the highest compared to BM and FR. This result describes that the grassroots contribute to the longer water trapping than the others. Meanwhile, the BM and FR are relatively open spaces and outcrop areas.

Table 5.3 The optimal parameters of soil water retention characteristics for each zone based on the Van Genuschten model (1980) for the Draix observation site by laboratory experiment.

Zone	Depth	θ_s [m^3m^{-3}]	θ_r [m^3m^{-3}]	α [cm^{-1}]	n	RMSE	Soil composition
FRs	5	0.505	0.141	0.0344	1.51	1.09	Silty loam
	10	0.533	0.173	0.0325	1.40	0.95	
	15	0.477	0.095	0.0340	1.57	1.44	
	30	0.446	0.090	0.0361	1.73	0.78	
GRs	5	0.636	0.109	0.0208	1.45	1.49	Silty clay loam
	10	0.574	0.156	0.0331	1.45	1.18	
	15	0.509	0.109	0.0260	1.39	1.00	
	30	0.447	0.088	0.0177	1.39	0.79	
BMs	5	0.430	0.178	0.0211	1.41	0.86	Silty loam
	10	0.425	0.108	0.0275	1.45	0.71	
	15	0.409	0.092	0.0175	1.46	0.67	
	30	0.397	0.060	0.0285	1.46	0.54	

Overall, the permanent high-resolution temperature observation for monitoring the soil moisture changes in the subsoil is reasonably good compared with other studies. The relationship between soil moisture and effective precipitation presents a strong correlation. In addition, the calculated soil moisture is correlated with another soil moisture measurement (EC5 Decagon). The results show the advantages of fiber optic thermal distributed sensing, which observes soil temperature profiling and simultaneously estimates the soil moisture behavior along thermal differences. In the future, the influence of temperature might become a significant factor in the soil-water interaction besides the existing parameters such as porosity, land covers, and roots.

5.4 Conclusions and perspectives

This work shows permanent high-resolution temperature observation by fiber optic DTS installed at Draix. We used temperature fluctuation as a proxy for calculating soil moisture over a long time. We examined several thermal soil properties to calculate the soil moisture suitable for the site observation. In general, the long-term temperature observation is suitable for 23 months. Three strategies are used for estimating the thermal diffusivity during the observation as an intrinsic soil parameter. They are damping depth and phase shifting analysis as analytical methods and finite difference as numerical methods. The soil diffusivity depends on the soil moisture in time. This mathematical relationship is highly nonlinear. The soil moisture calculation results are associated with effective precipitation as a source of water saturation. We expect the soil moisture calculation to react to water infiltration. On the other hand, the drainage process can also be detected.

Temperature observation at several depths gives us a better understanding of the temperature gradient at the shallow surface that depends on water infiltration, even for different temperature magnitudes and vegetation conditions. The results are coherent, while the temperature, soil moisture, and effective precipitation were compared. The lack of results is a time lag between rain occurrences and calculation responses. Furthermore, we analyzed the soil moisture changes to understand soil behavior. It was done based on the field's seasonal and environmental processes and unsaturated hydraulic conductivity in the laboratory experiment. Generally, the parameter value ranges are consistent with the experimental particle analyzer that interprets the soil classification.

The statistical analysis was used to understand the soil moisture behavior on several hydrological cycles. The distributed probability function is applied in winter-summer sessions, wetting-drying processes, and

winter-storm phenomenon for each soil unit. This research shows the distinction of soil moisture evidence. The result can be helpful in studies utilizing fiber optics for soil moisture estimation representing water in the catchment scale.

This page intentionally left blank.

Chapter 6: Direct Modeling Of Soil Moisture In The Mediterranean Area

Abstract: The soil hydraulic properties are necessary for developing the soil moisture model that changes in time series. Soil water retention and hydraulic conductivity are often used as the physical parameters for determining the water flow simulation. Recently, soil measurement has been carried out at Draix Bléon, Alpes-de-Haute-Provence, Réseau de Basins-Versants/RBV, France. A precise hydraulic conductivity measurement on saturated conditions and water retention test has been acquired using laboratory soil testing and long-term soil moisture monitoring. The soil composition of the site study consists of silty clay loam. The 354 m fiber cable was spread to measure the subsoil temperature and become a proxy parameter for soil moisture calculation. The fiber cable was buried at 0 m, -0.005 m, -0.010 m, and -0.015 m of depths and crossed three different soil units consisting of argillaceous weathered black marls (BMs), silty colluvium under grassland (GRs) and silty colluvium under forest (FRs). In addition, the soil moisture probe sensor was installed at several depth positions for comparison and following the fiber optic depths. This research optimizes the soil hydraulic parameters by applying a fitting approach to the soil water retention curve and the time series fitting approach on Hydrus-1D simulation. The aims are to estimate the specific parameters model, such as pore size distribution and the air entry pressure due to the pedotransfer function. Moreover, our study provides a clear difference in soil hydraulic properties in the area dominated by clay-rich soil. The soil water retention curve characterizes a significant difference in soil behavior. Analyzing soil hydraulic properties reveals the importance of elementary soil parameters to improve long-term soil moisture monitoring. Ultimately, a long-term direct soil moisture model is simulated based on meteorological and temperature observation as data input for understanding the soil water changes in time series.

Keywords: soil hydraulic properties, water retention, Hydrus 1D, Draix

Kusnahadi Susanto[1], Jean Philippe Malet[1], Julien Gance[2], Vincent Marc[3]

[1] Institut de Physique du Globe de Strasbourg, CNRS UMR 7516/EOST – Université de Strasbourg, France; susanto@unistra.fr
[2] IRIS-Instruments, Orléans, France
[3] Université d'Avignon et des Pays de Vaucluse, UFR-ip Sciences, Technologies, Santé, Fance, France

6.1 Introduction

Unsaturated hydraulic conductivity and soil water retention are some of the most essential parameters of soil water infiltration. The knowledge of water flow in the shallow, unsaturated zone has become increasingly popular over the last few years. Sub-surface hydraulic conductivity is useful in climatology, agronomy, and hazard mitigation. They are also used in hydrogeology for the water recharge and discharge rate analyses in the vadose zone (Kato et al., 2010). In the case of slope movement, the hydrologic aspects, such as infiltration and exfiltration in the marls, result in slumps and mudflows (Bogaard et al., 2000). The methods for obtaining the hydraulic properties can be classified into indirect and direct approaches (Durner and Lipsius, 2005). The indirect approach encompasses the pedotransfer function, and the direct approach is related to observing flow attributes from laboratory or field experiments.

From the Mediterranean area's perspective, groundwater transport is highly affected by precipitation and air temperature (Longobardi and Khaertdinova, 2014). Evapotranspiration plays an important role in the

environment's wetting and drying processes. Most numerical methods are optimized for the diffusion parameter model to solve the groundwater transport problem (Dehghan, 2004). The solution for soil water diffusion requires the expression of two soil hydraulic properties: hydraulic conductivity and soil water retention. Hydraulic conductivity describes the relationship between unsaturated hydraulic conductivity and soil moisture, and soil retention describes the relationship between pressure head and soil moisture (Mualem, 1978). Several studies use a conceptual-based model to obtain the soil's hydraulic properties. One of them is a conceptual model of soil water retention that has been done to define the water retention function (Assouline et al., 1998). Numerous measurement strategies were also developed to acquire soil moisture through frequency (FDR) and time domain reflectometry (TDR) techniques (Negm et al., 2017).

Furthermore, the intense erosion in Draix Bléon is affected by water infiltration. This site study is susceptible to weathering and erosion (Antoine et al., 1995). Numerous studies have been conducted to understand soil water interaction on regional and river systems in this area (Corona et al., 2011). Water flow and infiltration were also modeled to reveal the environmental processes in natural hillslopes represented by topographic elevation and soil hydraulic parameters (Esteves et al., 2000). Draix, a Mediterranean area with a mountainous climate, is called a “badland” because it is a part of the black marls formation or ”Terres Noires” in French. Historically, this area was described in detail by numerous studies in Cemagref (a French research institute on rural and forestry science) (Richard and Mathys, 1999). To understand the soil behavior that is dominated by black marl, a hydrogeological conceptual model was carried out on Draix-Laval (Marc et al., 2017b).

This paper presents our soil observation related to soil hydraulic parameters based on nonlinear inversion. We apply the Van Genuchten curve and time series fitting approaches from the Hydrus 1D simulation for the Draix site. The primary input for parameter estimation is the temperature, soil moisture, and meteorological data observation. As a consideration, Hydrus 1D is superior in accurately simulating the soil temperature and water content changes in space and time, though it requires more detailed inputs (Sándor and Fodor, 2012). Hydrus 1D could also develop a proper model for predicting soil water changes in the vadose zone (Bergvall et al., 2011; Kato et al., 2010).

6.2 Material and methods

6.2.1 Study site

In the weathering zone, soil-water interaction becomes a key parameter for soil deformation. Rainfall can be one of the most critical factors. Draix, as a catchment area, has a high rate of precipitation. As a water recharge area, the precipitation around the site study is 0-80 mm/day, and the mean annual evapotranspiration is approximately 804 mm. In addition, under high-intensity conditions, the runoff coefficient is high (20-50%) (Mathys et al., 2005). The area's climate is mountainous, with characteristics of maximum precipitation in summer and frequent freeze-thaw during the winter session. In addition, it is a Mediterranean area that has high-temperature fluctuation.

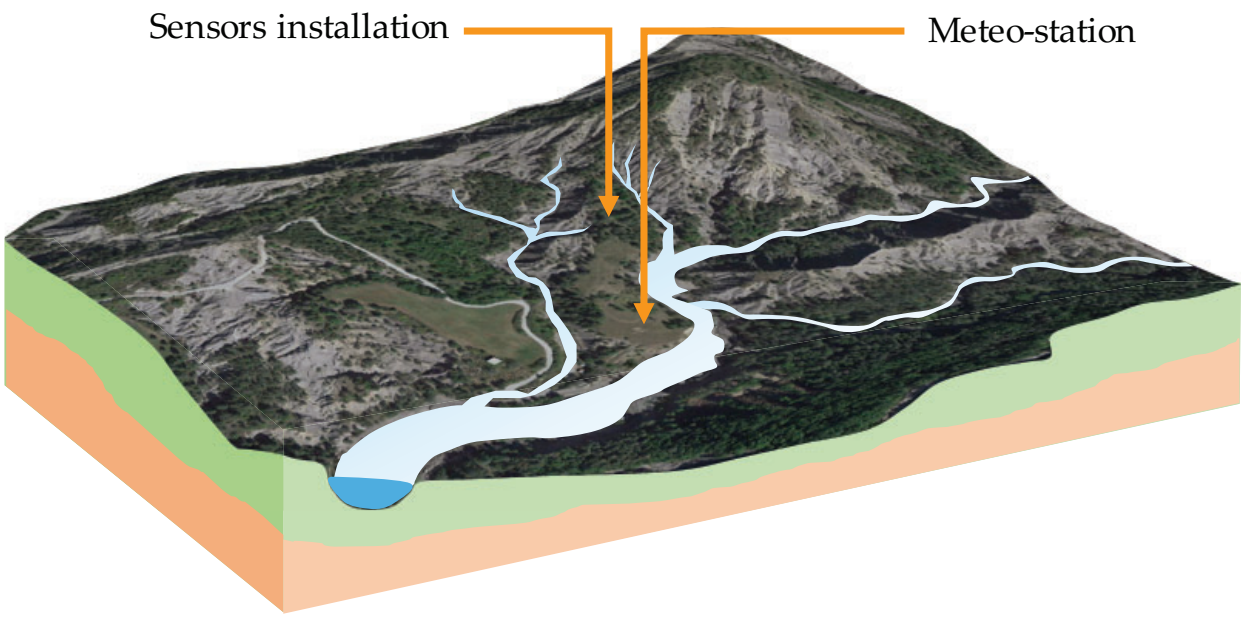

Figure 6.1 The Draix Bléon catchment is a Mediterranean area. The location of soil moisture and soil matric potential sensors are marked on the hillslope photo.

For two years (2016-2017), the average annual temperature is 11.28 °C. The maximum and minimum air temperature at the site study has been recorded to reach 42.83 °C and -13.21 °C in summer and winter sessions, respectively. The tree's existence also influences the soil-water interaction in the subsoil (Zribi et al., 2010), and Draix has 46% that are covered by pine trees (Esteves et al., 2005) (see Figure 6.1). Soil hydraulic properties describe the water's existence in soil pores. Both soil moisture and suction in the water retention curve model contain the soil condition information with pores size distribution, unsaturated water hydraulic conductivity, the interaction between water content, and air entry pressure. Numerous studies were performed to improve the Van Genuchten-Mualem model that was carried out for specific soil conditions. For instance, a modified Van Genuchten-Mualem hydraulic conductivity model was applied to Korean residual soils (Oh, Kim and Kim, 2015), and the unsaturated behavior of hydraulic conductivity was obtained in very small section conditions.

6.2.2 Estimation of soil hydraulic parameters

The methodology for estimating the soil hydraulic properties is the nonlinear regression as a fitting approach on the soil water retention curve and Hydrus 1D simulation as a time series fitting approach. The long-term soil moisture is obtained from indirect measurement by EC5 Decagon probe sensor and indirect measurement by temperature observation as a proxy of soil moisture condition. Furthermore, the soil water potential was measured directly at several depth positions. Those datasets are the main input for both methods besides the meteorological data observation (see Figure 6.2).

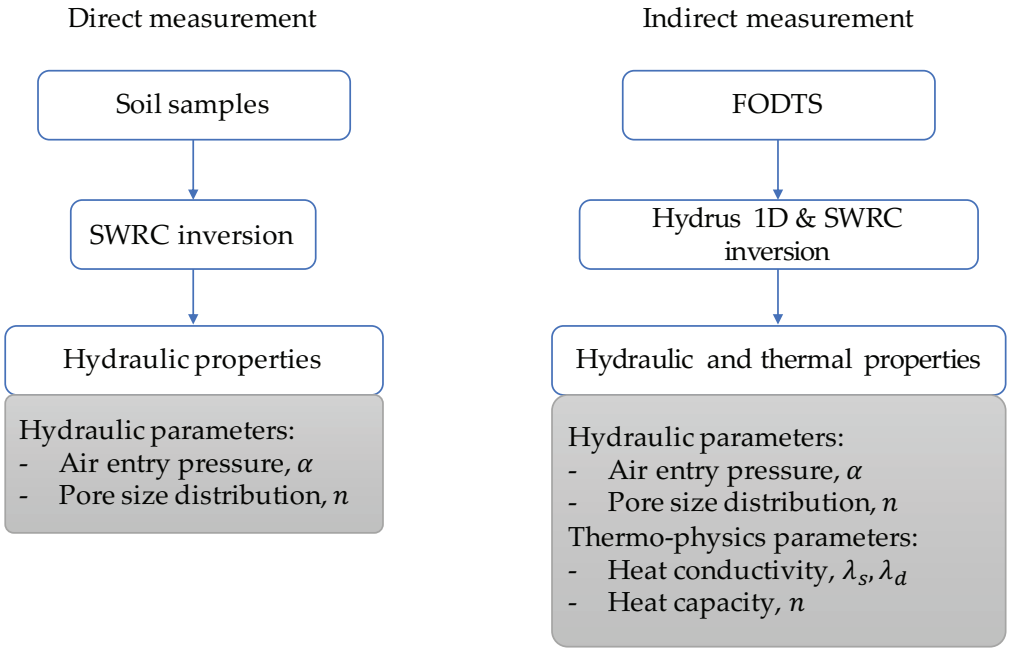

Figure 6.2 Flowchart of estimation parameters based on SWR curve and time series fitting approach. The measured soil moisture inversion is appointed as the benchmark.

The inversion of standard soil moisture measurement becomes the benchmark for indirect soil moisture inversion by using thermal observation as a proxy. The inversion result is expected to enable soil moisture model development in time series using Hydrus 1D simulation. The soil water potential, defined as the matric suction in unsaturated soil, is sensitive to environmental conditions (Fredlund, 2006). Focused on the soil water retention curve, the relationship between volumetric water content and the water suction can show hysteresis behavior (see Figure 6.3) that describes the drying and wetting processes (Hong et al., 2016). However, the soil water retention curve is mainly obtained from drying processes in laboratory measurement (Fredlund, 2006).

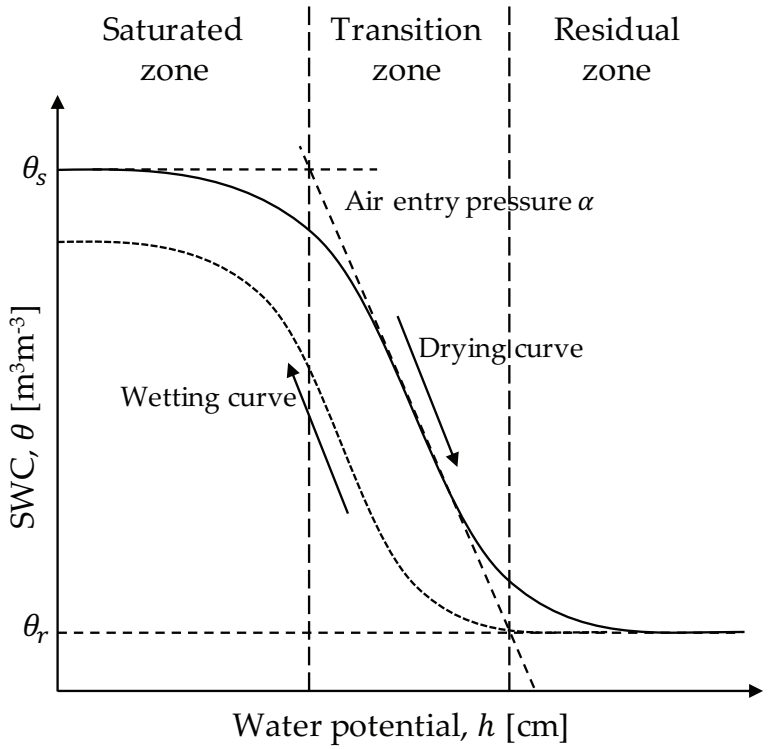

Figure 6.3 Typical hysteresis of soil water retention characteristic.

A model was designed to calculate various parameters to evaluate the water retention characteristic in unsaturated soil. Eq 6.1 expresses a Van Genuchten model (1980) of the relationship between water content and matric suction. Some parameters are estimated for fitting between the model and data measurements, such as air entry pressure and pore size distribution in unsaturated conditions.

$$\theta(h) = \theta_r + \frac{\theta_s - \theta_r}{[1 + (\alpha h)^n]^{1-1/n}} \qquad \text{Eq 6.1}$$

where θ is soil moisture (m^3/m^3), h is soil water potential (cm in logarithmic scale) and assumed to be positive, n is pore size distribution, and α is air entry pressure (cm^{-1}). The θ_s and θ_r indicate saturated and residual soil moisture values (m^3/m^3) on the water retention test, respectively. The nonlinear inversion method can be applied to estimating the parameters. The least-squares linear regression method was developed to solve the inversion problem. The differential error minimization on each estimated parameter was used to approach the parameter value. Hereafter, the model performance was evaluated by statistical analysis such as root means square error (RMSE), which compares the model and observation data.

As a comparison, the Van Genuchten parameters are also calculated by Hydrus 1D software, which uses a time series fitting approach. The standard simulation software built by Šimůnek (2013) can simulate the movement of water content, heat, and multiple solutes in variably saturated media (Šimůnek et al., 2013). The Hydrus 1D software can simulate the soil moisture changes in space and time. Local daily rainfall and atmospheric data obtained from the meteo-station at Draix are used as a time-variable boundary condition. Moreover, the water matric potential converted as the groundwater level is used as an input on Hydrus 1D simulation. It prescribes the simulation in the variable pressure head boundary condition, which fluctuates in time series (Rassam et al., 2003). Besides simulation, the Hydrus also can be used for inversion on each soil type to calculate the optimized soil parameter at the local scale (see Figure 6.4).

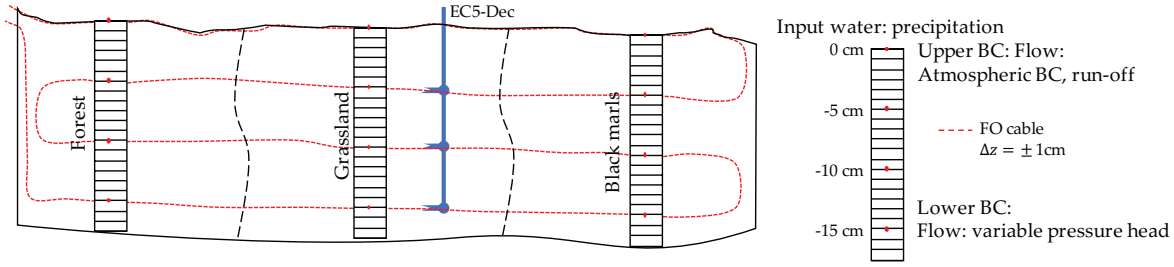

Figure 6.4 Schematic modeling and boundary condition (BC) of soil water flow simulation. The soils were assumed to have different hydraulic soil properties.

For both inversion scenarios, the input datasets are the standard measurement EC5 Decagon of 6 June to 31 July 2016 (43 days) and the calculated soil moisture from FODTS of 7 to 17 May 2016 (10 days). The appropriate soil water potential was converted to the groundwater level (GWL) to complete the inversion processes. The goodness fitting model prediction is assessed using RMS error as an absolute measure of fit and R^2 as a relative measure of fit. The 43-days datasets are used for nonlinear inversion with single decreasing soil moisture from maximum assumed as a saturated and minimum as a residual condition (see Figure 6.5).

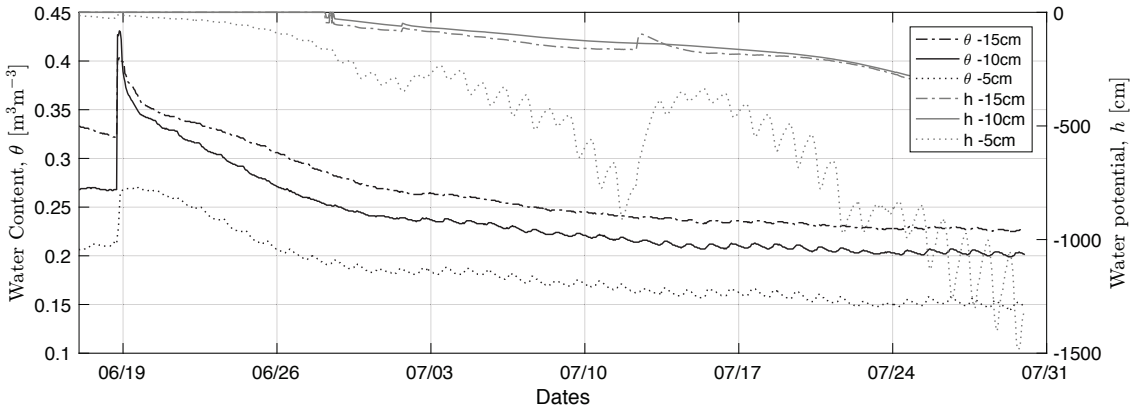

Figure 6.5 The 43-days measurement of soil moisture and soil water potential was recorded.

Furthermore, the Hydrus inversion was applied to the ten days of standard measurement and the calculated soil moisture. This strategy is used for comparing both optimized parameter results. In this inversion process, the time-series fitting approach is stressed between observed and modeled soil moisture. The Hydrus 1D simulation was developed using finite element simulation. It numerically solves Richard's equation for variably saturated water flow (Šimůnek and Van Genuchten, 1997). The input dataset had five times rainfall events in this period, which was expected to be able to describe the water flow in the soil. Afterward, the long-term (2016 to 2018) soil moisture simulations were developed based on optimized parameters as direct modeling. The simulations were built for three soil types: black marls, grassland, and soil under the forest. The adjusted hydraulic parameter is considered based on nonlinear and Hydrus inversion. The hourly time interval was used for these 669-days simulations.

6.3 Result and discussion

6.3.1 Inversion on soil moisture measurement

The previous section used the nonlinear inversion method for hydraulic parameters estimation based on a linear approach. The soil water retention curve fitting showing the relationship between soil moisture measurement versus water potential for estimating the soil hydraulic parameters is presented in Figure 6.6. While this method was run, careful attention was given to the saturated and residual soil moisture in each depth position. Despite the different saturated and residual soil moisture, each soil depth position has a relatively similar value of soil hydraulic parameter at the end of the observation. Therefore, the standard indirect measurement indicates a homogeneous soil type. The graph's differences in water flow parameters (θ_s and θ_r) may be due to clay content at each depth. Furthermore, the hydraulic parameters were optimized by Hydrus 1D as a comparison. Numerous researchers commonly use the Hydrus 1D as a standard water flow simulation and inversion.

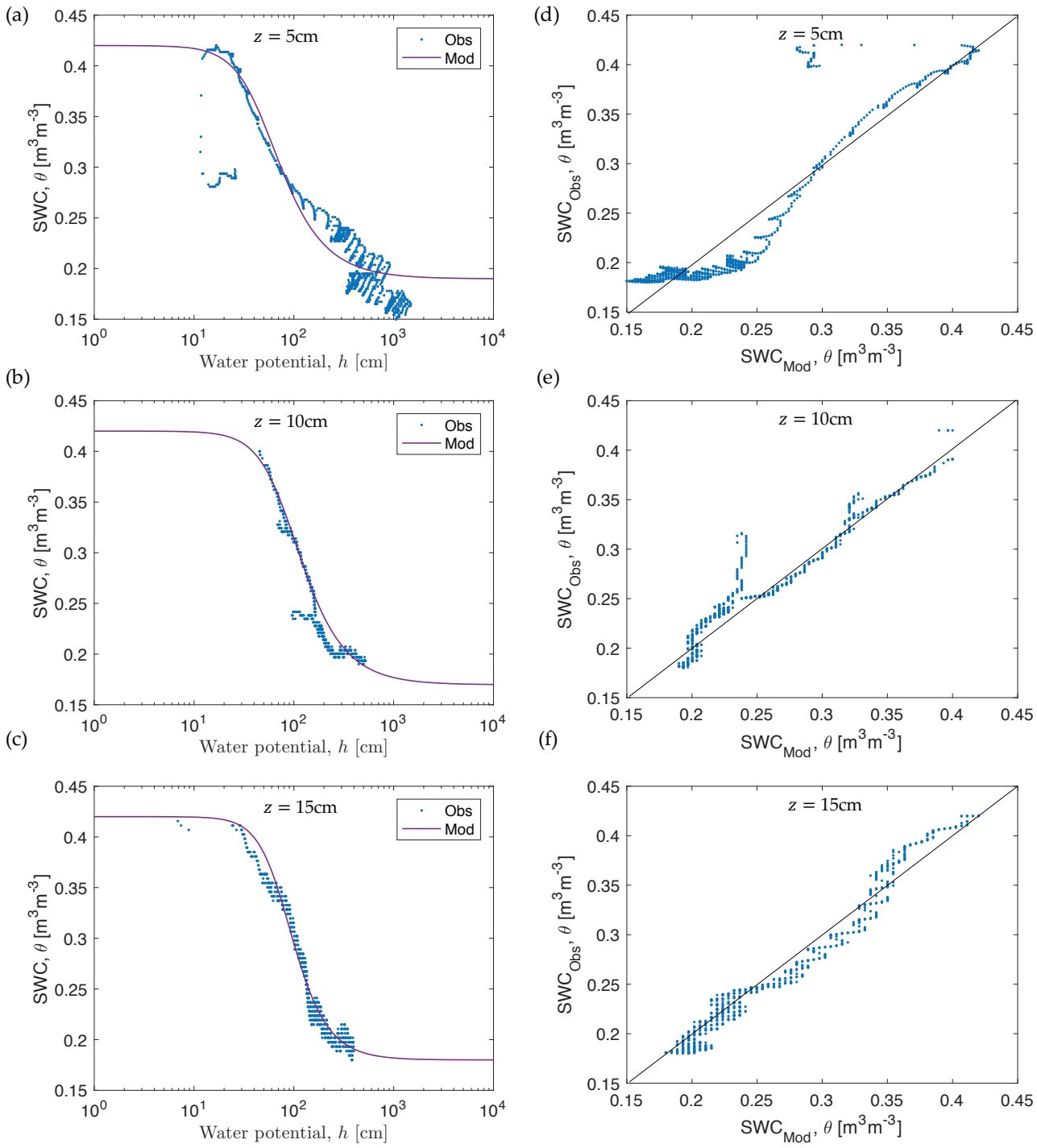

Figure 6.6 Nonlinear regression result of the SWR curve fitting approach for standard soil moisture measurement. (a-c) SWRC fitting, (d-f) the linearization of modeled and observed soil moisture.

Two optimized parameters using different concepts were applied to the soil under the forest, with the EC Decagon installation probe as a standard soil moisture measurement. The dry situation is wet due to rainfall events, and the drainage process shows a complete single-cycle environmental process (see Figure 6.5). During this flow regime, the soil's hydraulic properties are obtained (see Table 6.1). The most sensitive parameters for different underlying depths were calculated using the parameter inversion method based on non-linear, and Hydrus 1D shows that the 10 cm has the best value estimation. R^2 and RSME of calculation indicate it.

Table 6.1 The unsaturated soil hydraulic properties result from nonlinear and Hydrus 1D inversion on soil moisture measurement in soil under forest.

Depth	Parameters	Nonlinear Inv		Hydrus 1D Inv	
		Value	S.E Coeff	Value	S.E Coeff
$z = 5$ cm	α	0.01	0.00015308	0.04015	0.03521
	n	2.44	0.026857	1.85	0.46716
	R^2	0.96		0.89	
	RMSE	0.00487		0.05145	
$z = 10$ cm	α	0.02	0.00024981	0.063	0.00961
	n	2.58	0.034913	1.73	0.13531
	R^2	0.96		0.95	
	RMSE	0.00484		0.02347	
$z = 15$ cm	α	0.02	0.00053109		
	n	2.36	0.040155		
	R^2	0.91			
	RMSE	0.0114			

Using nonlinear inversion, the air entry pressure (α) and pore size distribution (n) of soil under the forest are around 0.02 and 2.56 cm^{-1}, respectively. Furthermore, the Hydrus 1D estimates that grassland's air entry pressure and pore size distribution are around 0.06 and 1.69 cm^{-1}, respectively (see Table 6.1). This means that this soil type contains clay-rich soil.

6.3.2 Inversion on fiber optic temperature observation

The inversion method was applied to the other soil type, which does not have an EC Decagon soil moisture probe sensor as a standard measurement. The soil moisture was provided by temperature observation as a proxy parameter. This indirect measurement of soil moisture was assigned to each soil type for determining high-resolution soil moisture in space and time domains. In this step, the inversions of hydraulic and heat transfer parameters were estimated simultaneously. The data inversion was the -5 and -10 cm temperatures measured by fiber optic. Furthermore, the upper and lower boundary conditions are 0 and 15 cm, measured by fiber optic cable. Moreover, the precipitation and groundwater level are also used as the time-variable boundary conditions.

The thermal conductivity equation expresses This soil heat conductivity (Chung and Horton, 1987), which depends on soil moisture. The saturated and dry thermal conductivity can be obtained by applying the saturated and residual water content (Eq 6.2). The inversion process can estimate the optimized soil heat conductivity and solid heat capacity (see Table 6.3).

$$\lambda(\theta) = B_1 + B_2\theta + B_3\theta^{0.5} \qquad \text{Eq 6.2}$$

where λ is soil heat conductivity, B_1, B_2, and B_3 are the empirical parameters of thermal conductivity. Furthermore, the saturated water content θ_s and residual water content θ_r yield saturated heat λ_s and dry heat λ_d, respectively. The solid heat capacity was optimized as well and indicated by C_n. Considering the time series fitting analysis, a temperature model seemed appropriate for the temperature observation on the soil (see Figure 6.7). The scattering plot of linearity was used to examine the fitting between modeled and observed temperatures (see Figure 6.8).

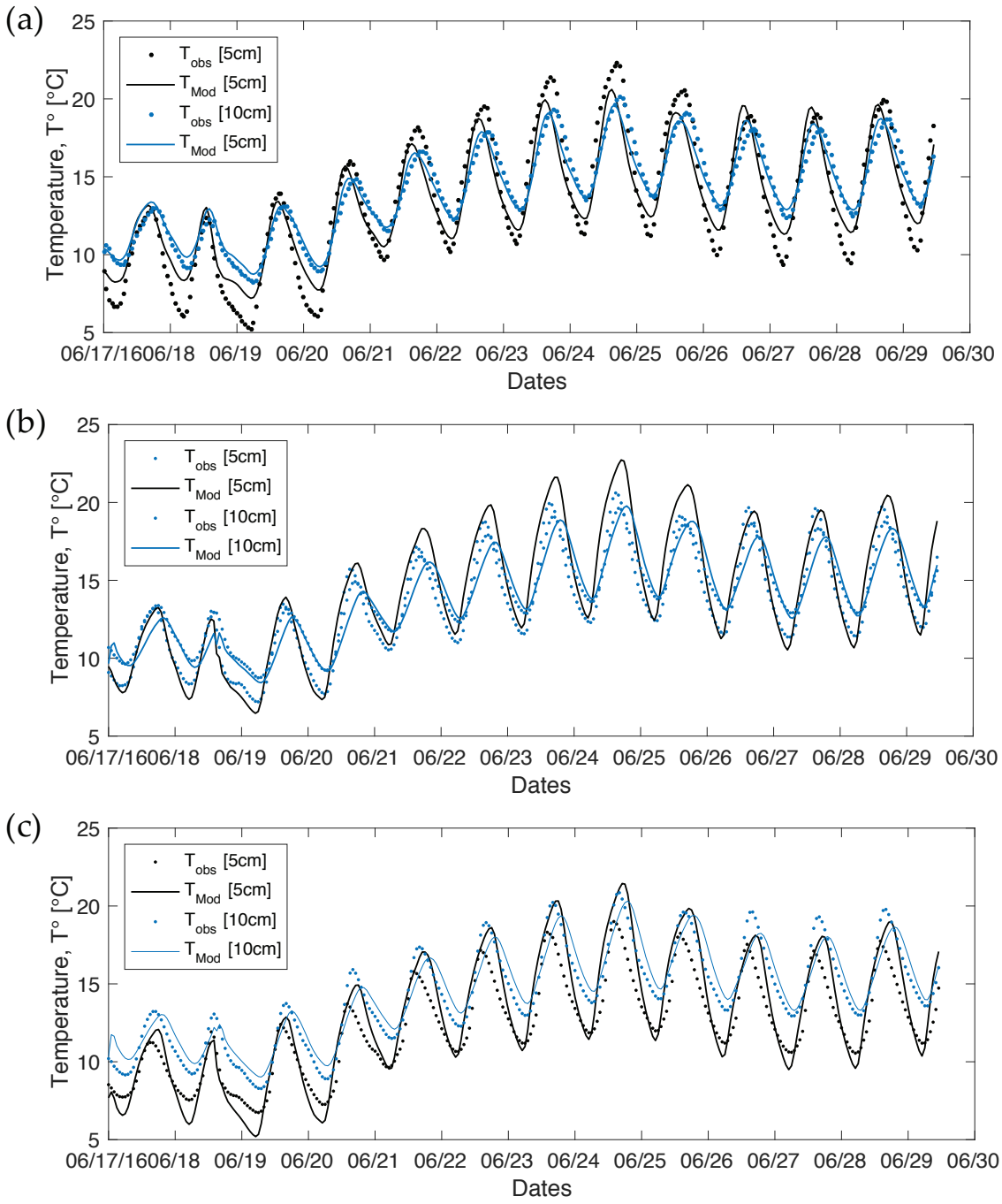

Figure 6.7 Curve fitting between modeled and observed temperature during the Hydrus simulation period consisting of dry-wet-drainage process. (a) Black marls, (b) Grassland, and (c) Forest.

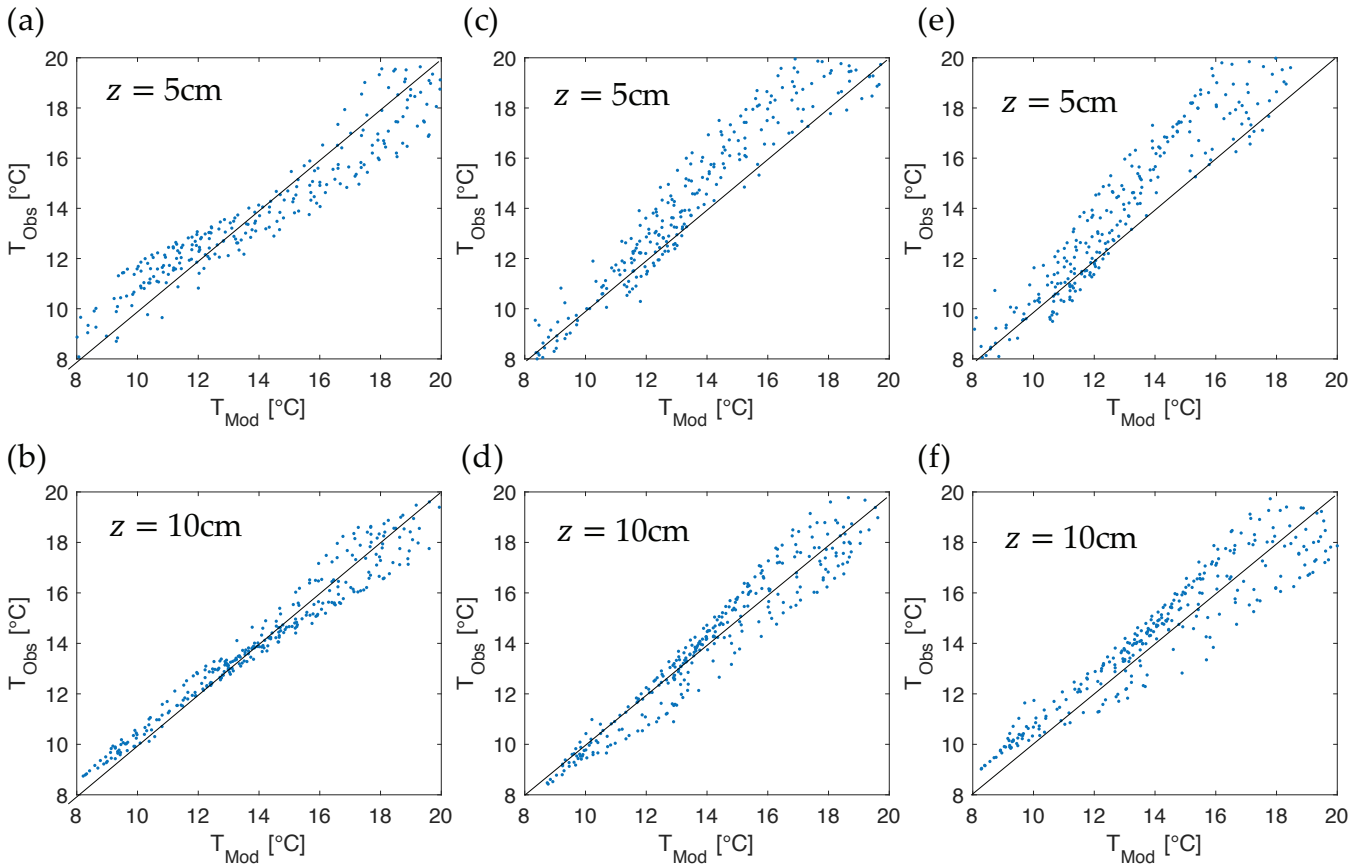

Figure 6.8 The linearization of modeled and observed temperature comes from the Hydrus 1D simulation for pada kedalaman -5 dan 10 cm. (a-b) Black marls, (c-d) Grassland, and (e-f) Forest.

Furthermore, verifying three scenarios (soil under forest, grassland, and black marls) model yields a specific hydraulic parameter (see Table 6.2). Using simultaneous inversion, the data on soil moisture as input is unnecessary. The Hydrus 1D generates soil moisture mode based on precipitation and groundwater level for estimating the optimized hydraulic parameters. Hence, the soil moisture cannot be analyzed by fitting methods between observation and model. That is why the soil moisture measurement was inverted to avoid calculation errors. The inversion on standard soil moisture measurement is used to constrain the optimized parameters' results.

Table 6.2 The soil hydraulic properties are obtained by Hydrus 1D inversion.

Parameter	Forest		Grassland		Black marls	
	Value	S.E Coeff	Value	S.E Coeff	Value	S.E Coeff
α	5.6108E-02	2.5440E-03	6.1009E-02	3.4490E-03	3.9131E-02	4.5850E-03
n	1.9907E+00	4.5931E-02	1.6895E+00	3.8717E-02	2.0139E+00	6.2214E-02
K_{sat}	5.8112E-01	6.5420E-03	1.0484E+00	9.4220E-03	3.2414E+00	2.5662E-02

Table 6.3 The soil heat transfer properties are obtained by Hydrus 1D inversion.

Soil type	Parameters	Value [Kg cm h^{-1} K^{-1}]	S.E Coeff	R^2	RMSE	λ_s [W m^{-1} K^{-1}]	λ_d [W m^{-1} K^{-1}]	Solid heat. Cap [MJ m^{-3} K^{-1}]
FR	B_1	2.7633E+08	2.8044E+07	0.76	3.67E-02	0.318	0.751	2.247
	B_2	1.0112E+11	1.1299E+10					
	B_3	5.2792E+12	2.0983E+11					
	C_n	2.9122E+11	2.1562E+10					
GR	B_1	1.7831E+11	5.4532E+10	0.86	3.03E-02	0.361	0.894	2.177
	B_2	1.8256E+12	1.2243E+11					
	B_3	4.8888E+12	1.6989E+11					
	C_n	2.8211E+11	2.4001E+10					
BM	B_1	2.3908E+11	1.8360E+10	0.87	3.07E-02	0.388	0.856	2.533
	B_2	2.8503E+11	3.7042E+11					
	B_3	5.5421E+12	1.9607E+11					
	C_n	3.2822E+11	2.0320E+10					

From the scatter graph and fitting time series, the temperature simulation was consistent with the observed one during the verification period. Based on this step, the optimized parameter can reasonably reproduce the direct soil moisture model in a time series. The soil moisture time series were constructed 5 and 10 cm for each soil type. The upper water flow boundary condition used atmospheric BC with surface runoff suitable for slope areas in a saturated situation. Then, the lower boundary condition used a variable pressure head, which used soil matric potential as a groundwater-level data input.

6.3.3 Direct modeling of soil moisture using Hydrus 1D

Based on nonlinear and Hydrus 1D inversion applied to soil moisture measurement and temperature observation, the soil hydraulic and thermal properties were obtained for soils under forest, grassland, and black marls soil types. Hereafter, direct modeling of soil moisture is developed for each soil type. Setting up a modeling scenario is important in simulating long-term soil water changes. The hourly time interval is used to develop the direct model of soil moisture. Nevertheless, temperature and atmosphere data input use a three-hour time step to avoid the overestimated value of hydraulic and thermal properties due to high-temperature variation. The total time simulation on the direct model is 19776 hours from 1 January 2016 to 3 April 2018 (see Figure 6.9).

During the hydrological year 2016/2018, modeled soil moisture at all soil profiles (Figure 6.9) presented intense seasonality temperature influences on the modeled soil moisture changes by Hydrus 1D. From April until November, soil moisture could be appropriately monitored. Nevertheless, from December until March, soil moisture seems saturated for all the wintertime. The plausible reason for this case is due to a minimal temperature difference for simulating the thermal inversion process. Hence, the overestimated diffusivity when the heat transfer inversion provokes the calculated soil moisture to be saturated value.

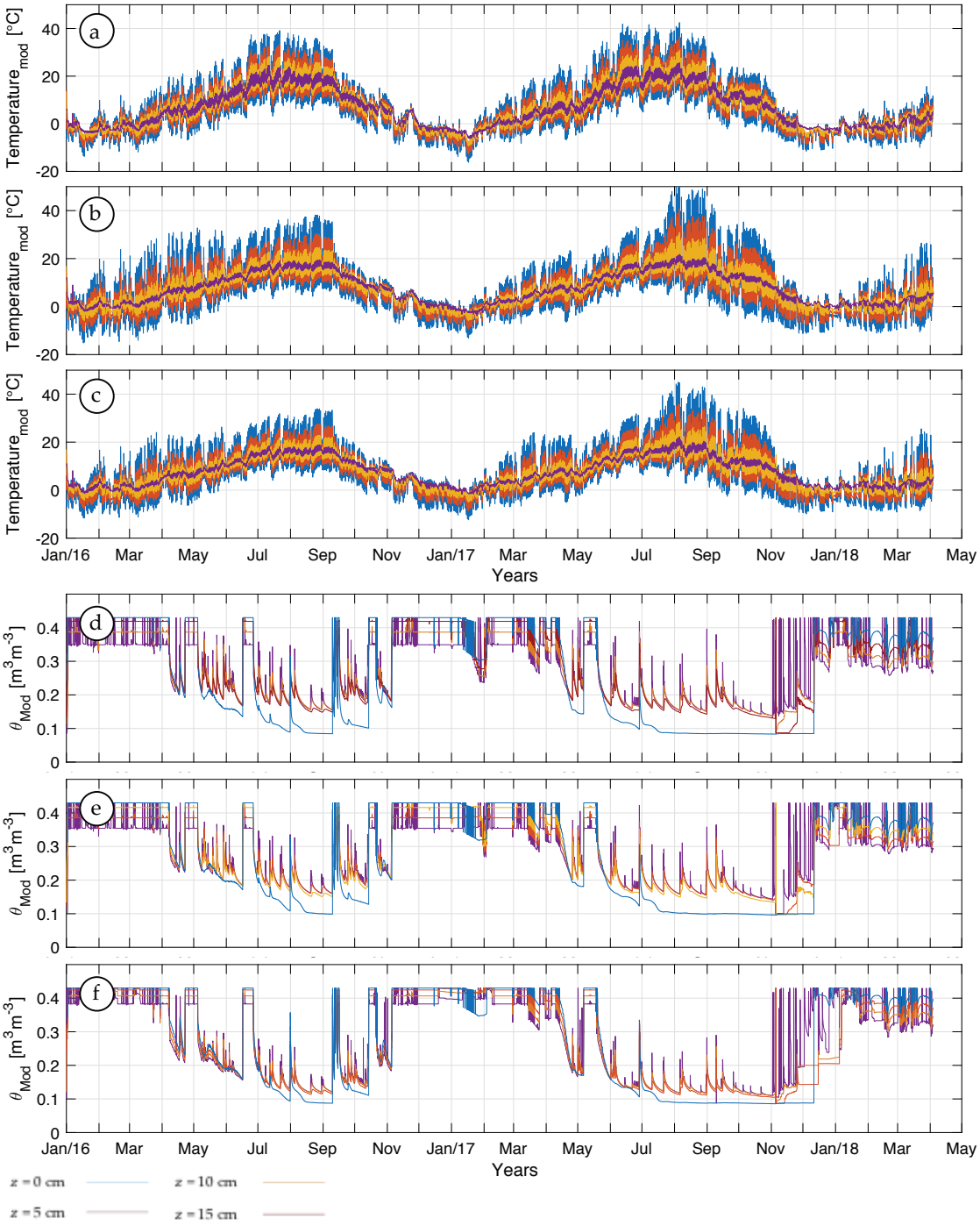

Figure 6.9 Long-term direct model simulation using hourly time interval by Hydrus 1D. (a to c) modeled temperature. (d to f) modeled soil moisture. It sequentially consists of Black marls, grassland, and soil under the forest.

In contrast to soil with plants on top, subsurface flow on black marls shows semi-arid soil during summer, and this is a noticeable difference between the soil moisture changes during the summer session for each soil type. This condition confirms that the black marls have high pore size distribution and effective K_s that represent the effect of preferential flow. Hereafter, the minimum average soil temperature that makes simulated water flow dynamically is over 2 °C. Furthermore, the soil moisture seldom exceeds field capacity due to high evapotranspiration throughout most summertime. The water flow in macrospores moves dynamically.

6.4 Conclusions and perspectives

The simulation for estimating the soil hydraulic and heat properties using different concepts was conducted in this study. The standard measurement of soil moisture is set as a constraining parameter for an indirect one. The nonlinear and Hydrus 1D inversion obtained the field parameters during the specific observation. Hereafter, it was generalized on long-term direct modeling of soil water changes. These experiment simulations addressed that temperature observation as a proxy parameter significantly influences the long-term direct model of soil water changes. The direct model performs well in simulation in the summer period but needs to be more satisfactory in the winter. This strategy can enhance soil water change monitoring in a wide observation area with limited soil moisture sensor installation as standard soil moisture measurement. Thus, distributed temperature sensing as a proxy parameter can be used as an alternative. Moreover, the long-term direct model based on temperature distributed sensing is an important component of the soil science investigation in land use or vadose zones.

This page intentionally left blank.

Chapter 7: Historical forecasting of long-term soil water content with a hydrological direct model

Abstract: The responses of the historical long-term of the soil are challenging to establish when the data observation is limited, especially on the highly fluctuated observation data, such as soil water changes. Nevertheless, this challenge can be solved using an appropriate strategy for the limited dataset. In this context, the possibility of water changes within the macrospore is considered a function of soil thermal diffusivity and depends on precipitation. In this study, we need help to assess the historical soil water changes by observing the appropriate air temperature and precipitation during the simulation period. The primary objective of this study is to explore the clay-rich soil behavior influenced by water infiltration in the past simulation period. Air and soil temperature are considered a linear time-invariant (LTI) system to infer the soil water changes. Although some LTI parameters could change over time, the simulation is expected to be able to explain the past groundwater system in general. In practice, the model parameters are acquired by direct model from the site, which uses 2016 for calibration and 2017 to 2018 for validation. Furthermore, eleven years of the hydrology period are simulated using direct modeling based on precipitation and air temperature observation to analyze the past soil water change since 2001. The correlation between precipitation and modeled water content was carried out on three soil types, under forest, grassland, and black marls, to analyze the soil-water interaction during the interested period.

Keywords: Forecasting, direct model, temperature, water content

---

Kusnahadi Susanto[1], Jean Philippe Malet[1]

[1] Institut de Physique du Globe de Strasbourg, CNRS UMR 7516/EOST – Université de Strasbourg, France ; susanto@unistra.fr

7.1 Introduction

The complexity of soil water flow in the past session is often used to understand future environmental processes. Predicting their historical behavior can be challenging due to the limited data observation. Hydrological and geomorphological investigations in clay-rich soil concluded that they have complex relationships (Malet et al., 2005). in terms of badland area, the seasonal hydrological process progressively disintegrates the black marls formation, which drives the weathered marl exposed annually (Maquaire et al., 2003; Mathys et al., 2003; Travelletti et al., 2012). The atmospheric forecasting model considers the evolution of land surface water content and temperature state (Albertson and Kiely, 2001). Numerous competing models were developed, such as land surface mode (LSM) and soil–vegetation–atmosphere-transfer (SVAT) models (Henderson-Sellers, 1996). The interaction of land surface behavior and atmospheric properties, as well as hydrological and meteorological forecasting models, is a concrete form of extensive application of ecosystem–atmospheric interactions modeling (Pielke et al., 1998).

The exciting aspect of water flow in macrospores relates to the infiltration mechanism, which is crucial for predicting runoff generation (Weiler and Naef, 2003). The macrospore is essential for wetting and drying processes, freeze-thaw cycles, or the erosive action of subsurface flow (Beven and Germann, 1982). Sometimes, the unrealistic parameterization of soil hydraulic properties influences soil water flows for prediction purposes, even though it is obtained from a specific calibration period. The hydrological model is usually used by geoscientists as a better tool for describing the relations between climate characteristics and groundwater responses (Malet et al., 2005).

In the last two decades, meteorological databases were collected to study the high-intensity hydrological process in the Draix area (Cambon et al., 2015). High quantitative reconstruction of erosion rates that cause primary sedimentation in a regional reservoir and river system were studied in an extensive area of the French Alps (Corona et al., 2011; Descroix and Gautier, 2002; Mathys et al., 2003). The water flow and infiltration were also modeled to describe the Hortonian overland flow during complex rainfall events at the exact location (Esteves et al., 2000). At the Draix site, the temperature and erosion data used to identify the following periglacial morphogenic deduced that the periglacial processes directly contributed to the annual erosion and facilitated run-off action in the guilles (Rovéra and Robert, 2005).

Although most earlier studies focused on the run-off and soil erosion typically controlled by precipitation, fewer studies have focused on the soil-water interaction, at least in the Draix area, which is the study area in this article. Hence, data availability was a major historical simulation challenge. This study analyses the historical simulation of soil water behavior using Hydrus 1D. The input simulation is precipitation and air temperature databases. Some steps are developed for generating the appropriate data input, such as soil temperature prediction in several depths. Furthermore, the simulation outcome is correlated to the climatic influences in the same study period.

7.2 Study area

The experimental site of Draix is located in the Southern French Alps, 200 km south of Grenoble. It was situated at the mean elevation of around 897 m.a.s.l (see Figure 7.1). Situated between the Alpine and Mediterranean climate systems (Oostwoud Wijdenes and Ergenzinger, 1998), the study site presented is

typically attractive to observe multidiscipline mountain erosion behavior in the Laval area as an upper part of the basin that is mainly dominated by Callovo-Oxfordian (COx) black marls (Maquaire et al., 2003).

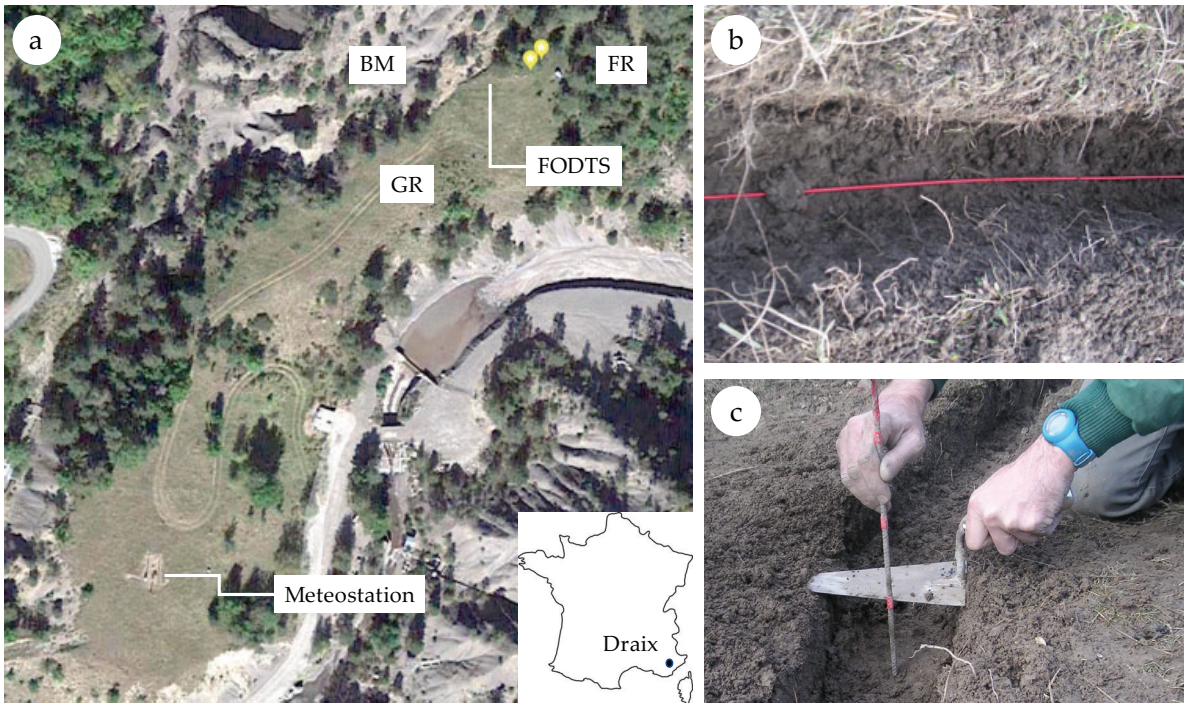

Figure 7.1 The study site of Draix. South of France. (a) aerial photographs of the Draix catchment area. (b) Fiber optic through three soil types. (c) Soil temperature profiling in different depth installations.

Several sensors (i.e., rainfall, air temperature, liquid discharge, and solid transport) have been in the measurement area since 1982 (Cambon et al., 2015). PT100 was installed to measure the air temperature. In contrast, the fiber optic distributed temperature sensor was installed through the colluvium forest, colluvium bushes, and black marls at 0cm, 5cm, 10cm, and 15cm below the surface (see Figure 7.1 b and c) to measure the soil temperature.

7.3 Material and Methods

The development and analysis of a hydrological model are carried out to forecast historical soil behavior using a long-term observation of precipitation, air temperature, and soil temperature. Concerning the unavailability of historical soil temperature in this study, a specific model is developed to calculate it using the air temperature observation. It is assumed that the characteristics of this model do not change over time so that the model can be used in the past or present. Therefore, a model with the current air temperature is simulated to obtain the soil temperature. The temperature is then compared with the measured soil temperature required from permanent fiber optic DTS in the field to ascertain the most relevant and appropriate hydrological model for the study site. A period of eleven years from 2001 to 2011, thus, is simulated to infer the soil water content.

7.3.1 Data collection

Data collection in this study consists of 2016 to 2018 and past (2001 - 2011) time observations at the Draix site. The past time collection, consisting of the air temperature, precipitation, and groundwater level data, was taken from BDOH (Base de Données des Observatoires en Hydrologie) maintained by IRSTEA (Institute national de recherche en sciences et technologies pour l'environnement), where the precipitation sensor has been continuously operated since 1982 at five locations surrounding Draix catchment area, namely Cheval blanc,

Laval, Pompe, Sevigne, and Village, as shown in Figure 7.2. The present-time collection (precipitation, air temperature, and soil temperature) was obtained from Draix site measurement using meteo-station and FO-DTS. From three locations with long-term data, this study's historical simulation period was chosen and focused on the Laval area for eleven years from 2001 to 2011 (see Figure 7.3).

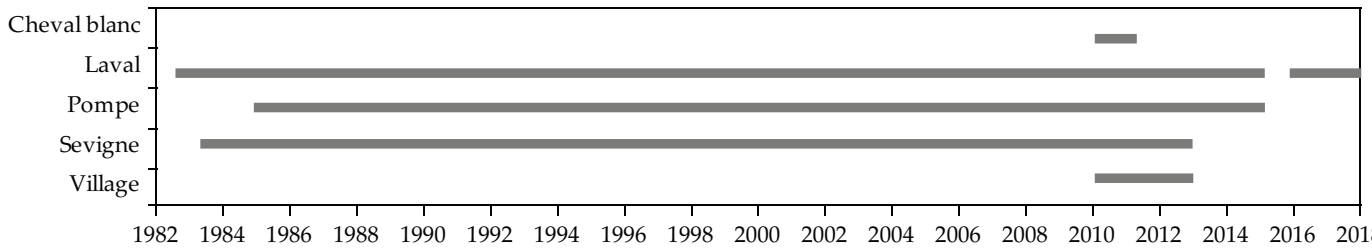

Figure 7.2 Overview of the past time observation period by IRSTEA in the five stations around the Draix catchment area.

Meteo-station provided the present-time data collection of air temperature and precipitation in the observation period from 2016 to 2018. The average annual air temperature at Draix, measured by a PT100 sensor placed 2 meters above the soil surface, was 9.41 °C. The cumulative precipitation, acquired from a permanent rain gauge Campbell Scientific sensor, reached up to 1.97×10^3 mm. The rain gauge sensor is instrumented with a tipping bucket and has a sensitivity of 0.2 mm of rain per tip. However, the rain gauge sensor did not always work well during the observation period because it was not cleaned and maintained sufficiently, or the internal battery of the data logger was dry, i.e., the abstain data in 2015. The location of the precipitation recording in that area was close to the fiber optic distributed temperature measurement, where the distance between those instruments is around 144 m.

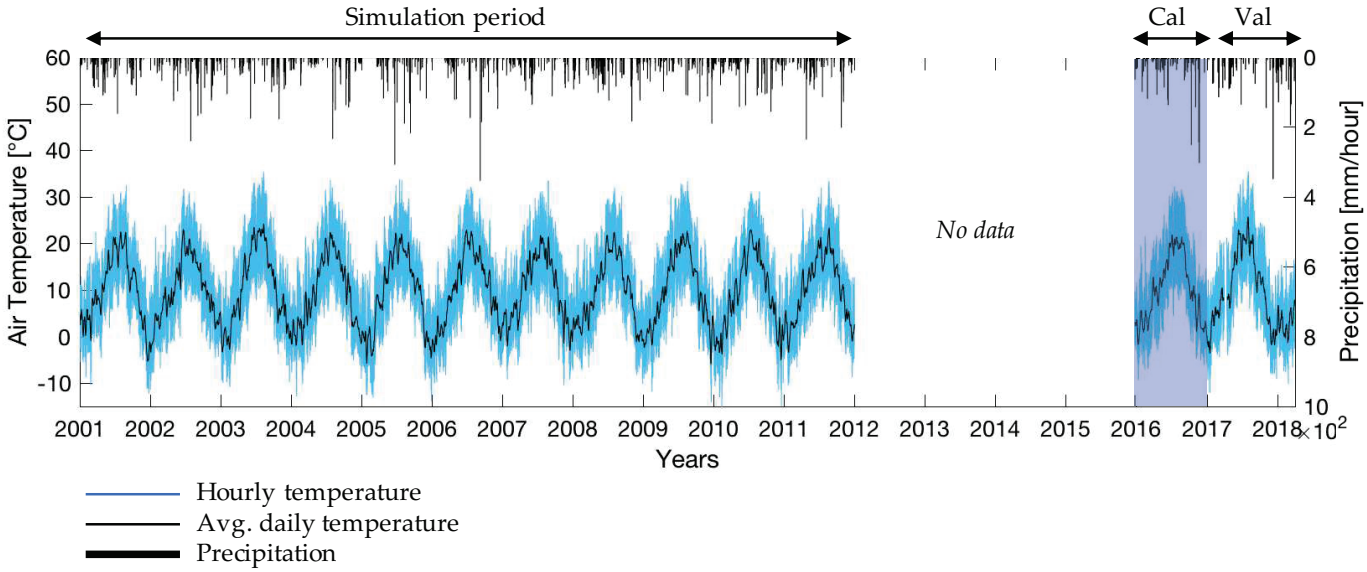

Figure 7.3 Past and present data collection of precipitation and air temperature at the Draix catchment area (Cambon et al., 2015).

Fiber optic DTS has been applied in black marls, grassland, and soil under forests to measure soil temperature within 6-minute sampling intervals since December 2015. The selection of two depths at 0 cm and 15 cm from the soil surface was carried out to provide the upper and lower boundary conditions for soil water content simulation and to define the soil characteristics. The temperature measurement points were arranged

vertically to obtain a suitable temperature profile and avoid the interpolation process. In addition, the groundwater level in the Laval area (see Figure 7.4) is included to check the soil condition when it rains. The groundwater level indicated water infiltration during rainfall occurrences represented by a strong correlation ($r = 0.86$) between the precipitation and water level in the eleven-year observation period (from 2001 to 2011).

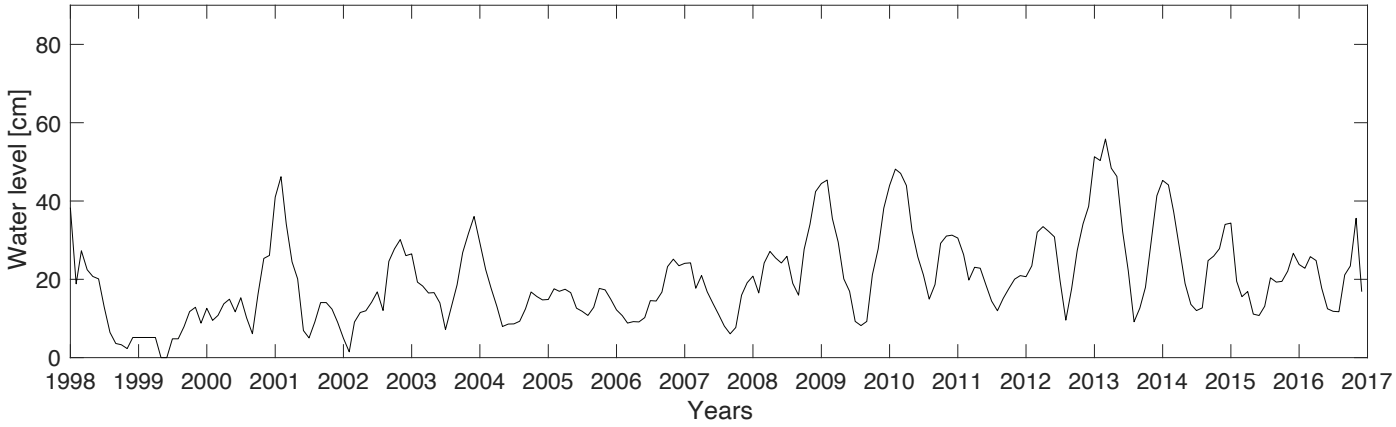

Figure 7.4 The monthly average water level recorded in the Laval area (Cambon et al., 2015).

7.3.2 Soil temperature prediction for forecasting soil water content

Soil temperature, used for predicting the soil water content (see Chapter 2 in section 2.1.3 Nonlinear inversion for hydraulic parameters estimation), can be obtained using equation Eq 7.2 applied to a model simulation (Carslaw and Jaeger, 1959). This prediction has been reported in numerous studies using soil surface temperature measurement (Barman et al., 2017; Krarti et al., 1995; Oyewole et al., 2018; P. Sharma et al., 2010; Penrod et al., 1960). Nevertheless, the time lagging factor below the surface should be estimated due to the damping depth d consideration. The damping depth is a function of the soil diffusivity, which depends on soil water content (Jong van Lier and Durigon, 2013; Krzeminska et al., 2012a).

$$ST(z,t) = T_a + ST_0 e^{(-z/d)} \sin\left(\frac{2d\pi t}{z} - \frac{z}{d}\right) \qquad \text{Eq 7.1}$$

where ST is soil temperature, T_a is average temperature, $d = \sqrt{\tau D/\pi}$, and ST_0 is the surface temperature amplitude. To simplify the soil temperature prediction, we assume that the model is invariant in the time domain and the soil is a linear system (see Figure 7.5); thus, naturally, the system can be represented as in Eq 7.2, where ST and AT are soil and air temperature, respectively. R is soil characteristic consisting of gain and frequency, and t and ω are time and frequency domains.

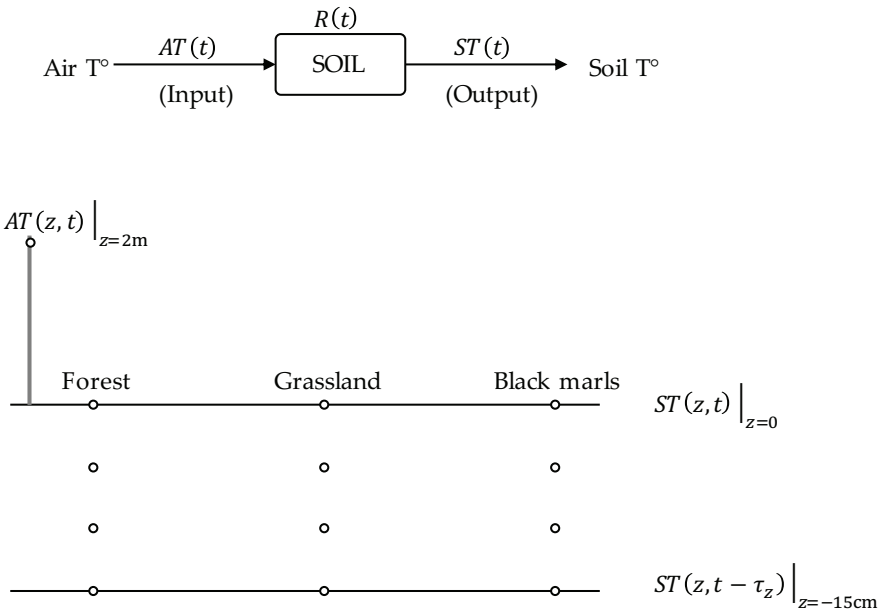

Figure 7.5 A diagram system of model assumption between air and soil temperatures and a geometrical simulation is described. $AT(t)$, $R(t)$, and $ST(t)$, respectively, are air temperature, soil characteristics, and soil temperature.

A set of arbitrary air temperature data, a multi-frequency signal, is used as the system input to obtain the soil temperature as the system output. By converting Eq 7.2 to Eq 7.3 in the frequency domain using Fast Fourier Transform (FFT) and neglecting the time lagging, the soil characteristic $R(\omega)$ is obtained by division of output $ST(\omega)$ and $AT(\omega)$. After applying the inverse of FFT, the soil temperature is directly estimated by a convolution process between air temperature $AT(t)$ and soil characteristic $R(t)$ in the time domain.

$$ST(t) = R(t) * AT(t) \qquad \text{Eq 7.2}$$

$$ST(\omega) = R(\dot{\omega}) \times AT(\omega) \qquad \text{Eq 7.3}$$

Therefore, this linear time-invariant (LTI) is easy to implement for time series observation and enables model generation (Hasfurther et al., 1972), where the system records the soil behavior reflected in the convolution function containing gain and frequency attributes. Besides local fluctuation due to rainy and cloudy situations, the environmental temperature has diurnal and annual frequencies. Thus, a full-wave temperature response in a single hydrological cycle determines a minimum requirement for modeling the LTI soil system. We used one year of observation in 2016 and the next two years as the calibration and validation periods, respectively. Meanwhile, the average temperature in one daily cycle and soil surface temperature amplitude ST_0 can be neglected because they have already been implied in characteristic soil $R(t)$ calculation.

7.4 Result and Discussion

This section describes the simulation of historical soil water content from 2001 to 2011 using the 1D Hydrus model, as explained in section 7.4.2, where datasets of predicted soil temperatures at depths of 0 cm and 15 cm were applied to the simulation. Those datasets were obtained from a convolution process between historical air temperature (2001-2011) and soil characteristics. This soil characteristic resulted in deconvolution between soil temperature at two depths and air temperature at present (2016). The calibration was carried out

by comparing the soil temperatures from the convolution result and the fiber optic measurement in 2016. The validation process was carried out by comparing the soil temperature dataset 2017, as illustrated in section 7.4.1.

7.4.1 Calibration and validation of soil temperature

The calibration process was prepared by implementing linear time-invariant to complete the hydrological process in one year using data from the 2016 period. A full-wave soil temperature was deconvoluted with air temperature to result in the soil characteristic, where the average air temperature in 2016 was 11.54 °C. A convolution process was done between soil characteristics and the air temperature to generate the predicted soil temperature. The predicted soil temperatures, which depend on the depths of 0 cm and 15 cm, in Black marls, Grassland, and forest soil, respectively, are 11.22 °C and 10.33 °C, 11.37 °C and 9.92 °C, and 11.01 °C and 9.80 °C. The measured soil temperature dataset was compared with the predicted ones for calibration purposes, as shown on the left side of Figure 7.6. The temperature fluctuated significantly throughout the whole year. It influences the weathering soil process, especially in the marls slope area (Gance et al., 2016).

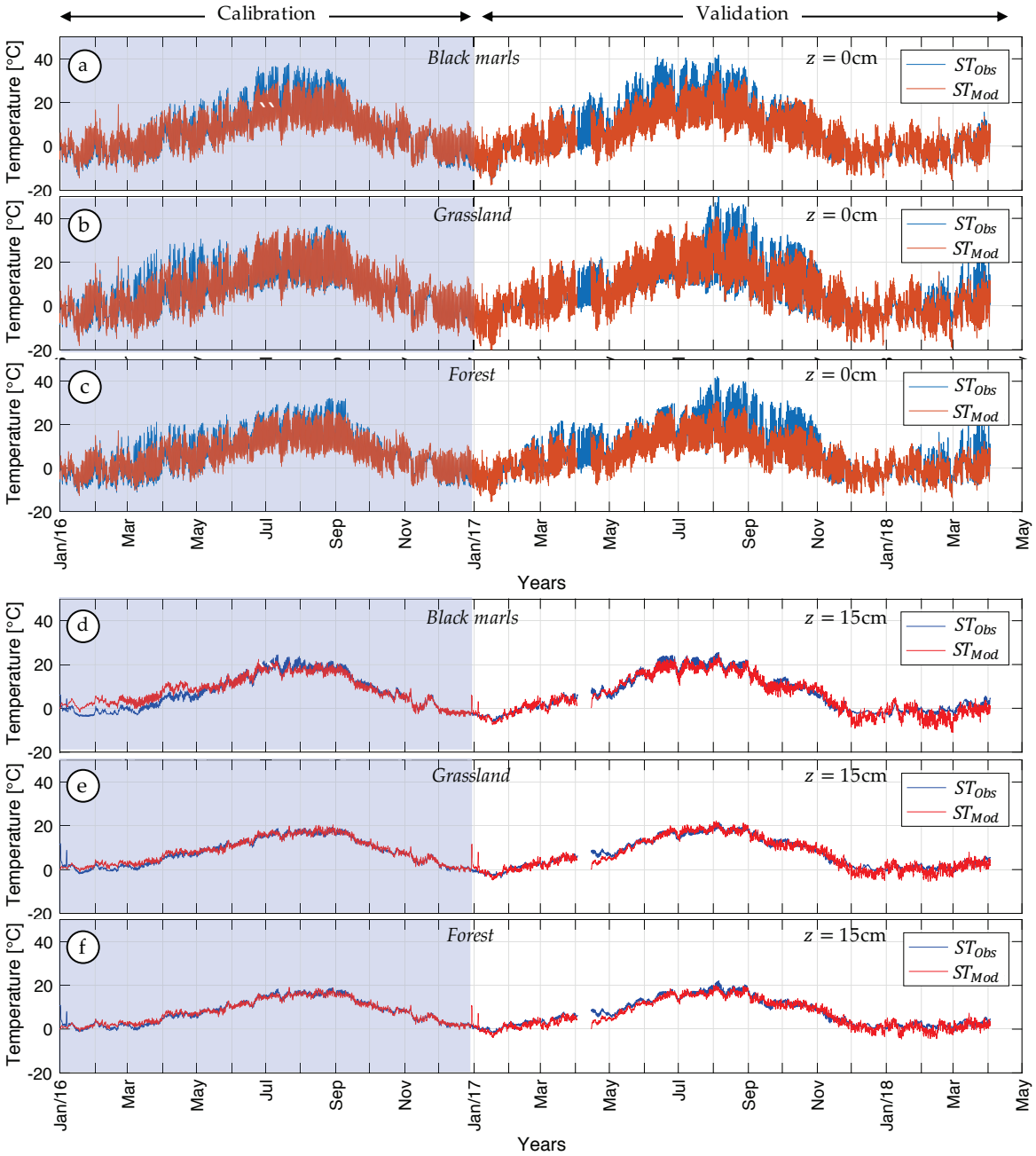

Figure 7.6 Time series period for calibrating and validating soil temperature (ST). (a to c) the depth is 0 cm. (d to f) the depth is 15 cm. The structure images are sequentially Black marls, Grassland, and soil under a forest.

For the validation process, a more extensive validation period compared to the calibration period was chosen to achieve higher precision of the predicted soil temperature and to check the robustness of soil characteristics. The soil characteristic could be implemented for a longer historical time series of temperature databases. The predicted soil temperature was calculated by convoluting the air temperature and the soil characteristics for 16 months from 2017 to 2018, where the average air temperature was 11.76 °C. The predicted soil temperatures at the depths of 0 cm and 15 cm in Black marls, Grassland, and forest soil, respectively, are 11.43 °C and 10.31 °C, 11.51 °C and 9.81 °C and 11.02 °C and 9.77 °C. Furthermore, as shown in Figure 7.6, the comparisons between the measured temperatures in the same measurement period and the predicted ones in all soil types aimed to examine whether the LTI system worked adequately in predicting the soil temperature.

As we know, the condition of the soil surface is also affected by climatic or environmental factors such as solar radiation and wind speed. However, the effect of damping depth reduced the noisy temperature amplitude during the heat transfer process Eq 7.1). It is shown by comparing the temperature at a depth of 15 cm, slightly better than 0 cm. To analyze the LTI result, the measured and predicted soil temperature are analyzed by comparison analysis, such as the determination coefficient of linear regression, R^2, root means squared error (RMSE), and correlation analysis. Table 6.1 presents the quantitative result of the comparison. The ranges of R^2 values between measured and predicted soil temperatures for all soil types in calibration and validation indicated the excellent performance of the work of the LTI system, i.e., 0.91 - 0.94 and 0.89 - 0.94, respectively.

Meanwhile, the best fittings for the temperature comparisons were analyzed by the scattering plots in Figure 7.7 for calibration and Figure 7.8 for validation. The plots showed that the distributed points were close to the linearity line. In other words, it indicated that the predicted temperature was relatively close to the measured one.

Table 7.1 Comparison analysis of measured and predicted soil temperature on calibration and validation period (2016 to 2018)

	Depth [cm]	Calibration				Validation				Ratio RMSE Val/Cal
		R^2. Cal	RMSE. Cal	Max. Correl	Time delay [hour]	R^2. Val	RMSE. Val	Max. Correl	Time delay [hour]	
FR	0	0.93	2.39	0.98	0-1	0.91	3.00	0.93	0-1	1.26
	15	0.94	1.56	0.99	0	0.93	1.59	0.97	0	1.02
GR	0	0.91	3.10	0.97	0-1	0.89	3.67	0.92	0	1.18
	15	0.94	1.56	0.99	0	0.94	1.58	0.95	0	1.01
BM	0	0.92	2.97	0.98	0	0.92	3.25	0.91	0-1	1.09
	15	0.94	0.94	0.97	0	0.93	2.28	0.95	0	2.43

As we know, the LTI system produces a time delay between the output and input systems. This unexpected circumstance may also occur on the measured and predicted soil temperatures. The cross-correlation was performed in this analysis to quantify the unexpected time delay. The cross-correlation results in Table 7.1 show that the delay is less than 1 hour. In addition, the similarity of signals (between predicted and measured temperature) is examined by the root means square error (RMSE). In this case, the maximum RMSEs are 3.1 for calibration and 3.25 for the validation period.

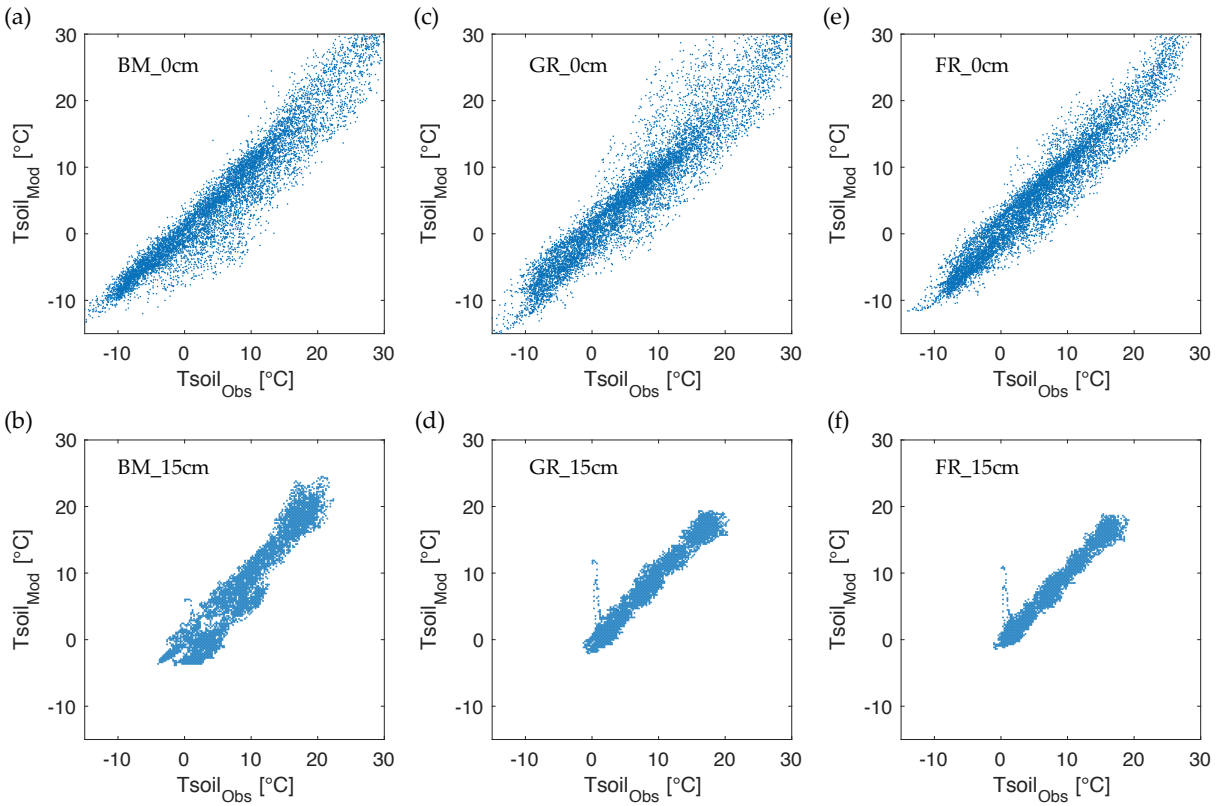

Figure 7.7 The scatter plots of measured and predicted temperatures in the calibration period (2016).

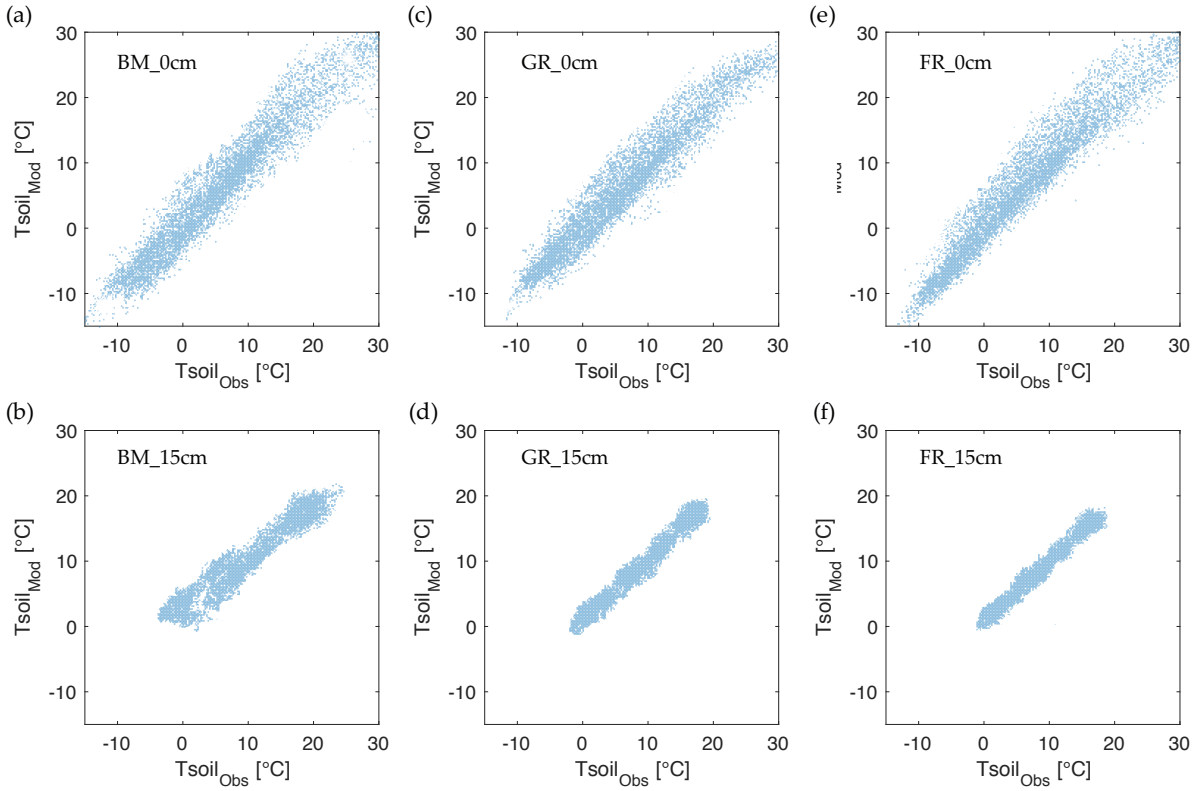

Figure 7.8 The scatter plots of measured and predicted temperatures in the validation period (January 2017 – April 2018).

7.4.2 Historical simulation of Draix hydrology

The model simulation is simplified by assuming that the hydrological parameters do not change over time. The parameters were obtained from arid soil to totally wet soil and went to drainage processes optimized by the inversion method. The inversion period of calibration started from 6 to 17 May 2016. The optimized parameters consist of air entry pressure (α), pore size distribution (n), and hydraulic conductivity (K_{sat}) as soil hydraulic parameters, the dry and saturated heat conductivity (λ_s and λ_d)) and the heat capacity (C_s) as soil thermal properties (see Table 7.2).

Table 7.2 Overview of optimized parameters of soil hydraulic and heat properties.

	Soil hydraulic properties			Soil heat properties		
	Air entry press α (cm $^{-1}$)	Pore size dist n (-)	Hydraulic cond K_{sat} (cm hr $^{-1}$)	Dry thermal cond λ_d (W m^{-1} K^{-1})	Sat thermal cond λ_s (W m^{-1} K^{-1})	Solid heat. Cap C_n (MJ m^{-3} K^{-1})
FR	0.056108	1.9907	0.58112	0.318	0.751	2.247
GR	0.061009	1.6895	1.0484	0.361	0.894	2.177
BM	0.039131	2.0139E	3.2414	0.388	0.856	2.533

Furthermore, the optimized parameters were applied to eleven eleven-year simulation period from 2001 to 2011 (see Figure 7.3). To simulate the hydrology modeling, two important inputs of the model are necessary: precipitation and soil temperature. As described above, the soil temperature at the surface and bottom was predicted based on the air temperature around the site. Hydrus 1D simulated the historical water content at specific depths (5 cm and 10 cm). The 5 cm simulation of depth is noisier than the 10 cm due to the dynamic upper surface. Hence, the soil water content analysis is focused on 10 cm of depth, as presented in Figure 7.9.

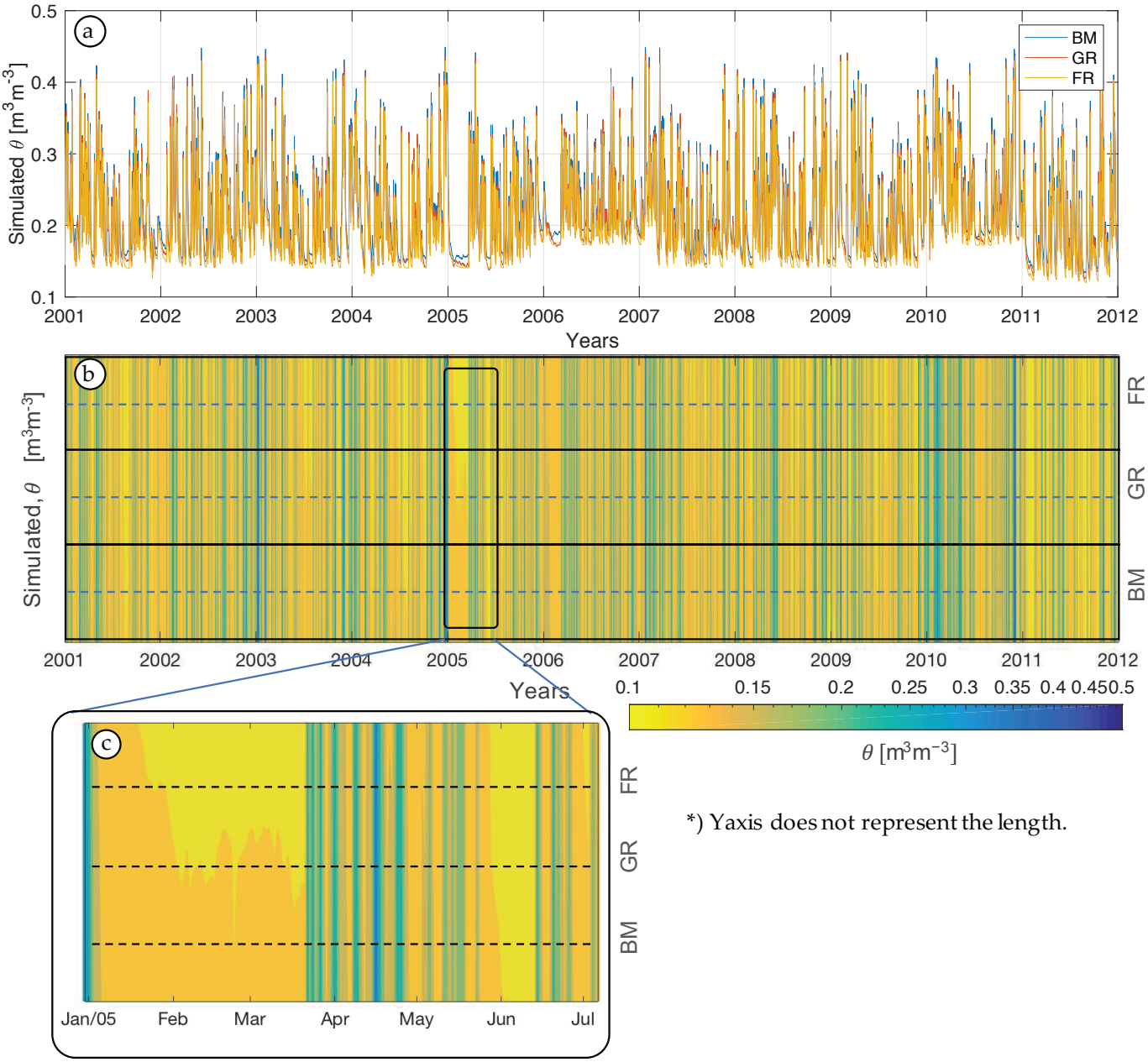

Figure 7.9 Simulated historical soil water content from 2001 to 2011. **) The hourly data is too big to be displayed entirely. The monthly selection is shown.

The Hydrus 1D model simulated soil water content according to the schematization described in Figure 7.5 with the hourly time interval. It was divided into two practical simulations. These are in calibration-validation and the past time simulation period. Figure 7.9a shows the simulation result for historical soil water content simulated in two different depths. A qualitative analysis of the response pattern shows the performance of the Hydrus 1D model. The fluctuation of simulated water content follows the rainfall event. Although the response pattern of the soil water content has a good correlation with rainfall events, the water needs time to infiltrate the soil and reach specific depths. The time lag between water infiltration and precipitation is analyzed by cross-correlation function.

Three scenarios of soil types have different response behaviors when precipitation events come. Figure 7.9b shows the distribution of simulated water content in the past time. For instance, we can see a variation in

soil water content in a few months in 2005 for each soil type (see Figure 7.9c). The simulated soil water content in the soil forest indicates the driest condition compared to the others. The values of soil water content were about 0.13 in that period. A wet period occurred in 2010, which indicated that, by average minimum, the soil water content values were around 0.189 m^3/m^3. Furthermore, the driest soil water content also occurred in 2011, as shown by the average soil water content of around 0.123 m^3/m^3.

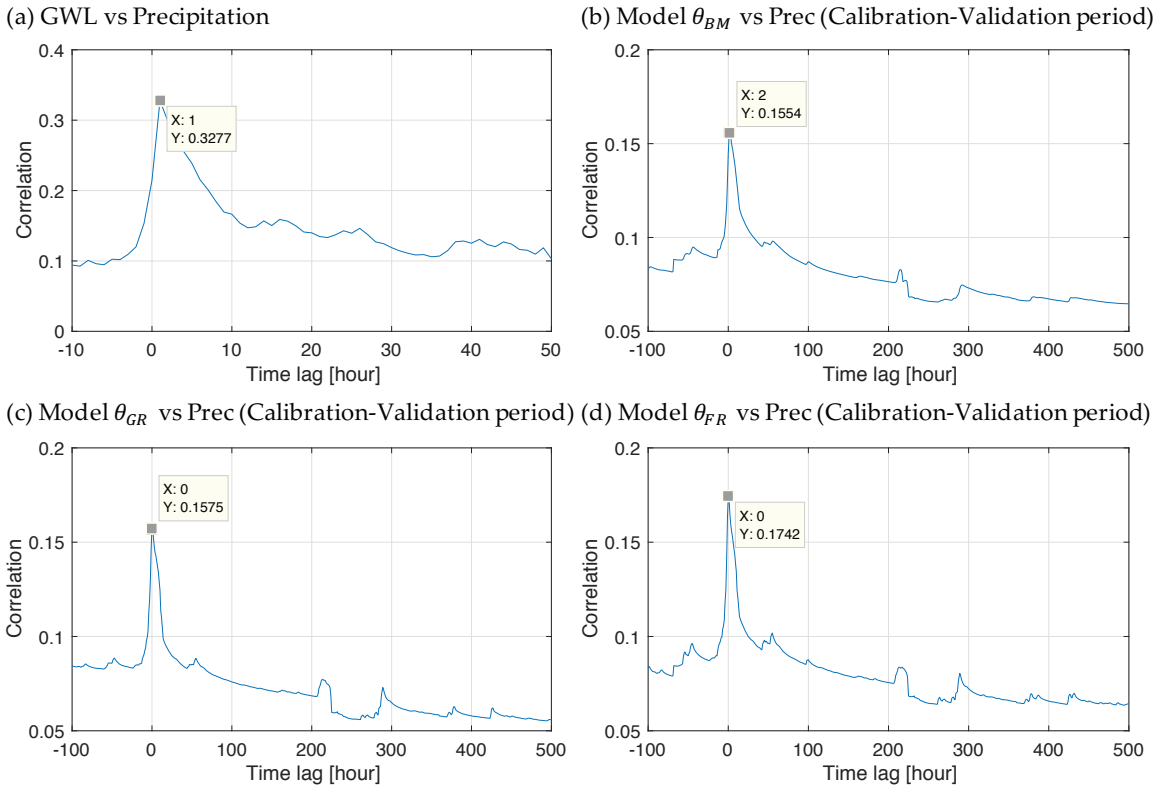

Figure 7.10 Cross-correlation between (a) the precipitation groundwater level. Then, soil water content vs. precipitation in the calibration-validation periods. (b) at the black marls, (c) grassland, and (d) soil under the forest.

The time lag is stressed to describe soil water infiltration. Figure 7.10 shows the cross-correlation between simulated soil water content response and rainfall events in the calibration and validation period. The cross-correlation is performed at 10 cm of depth. The first practical simulation was performed during the calibration-validation period (2016-2018). The time lagging water penetration reached up to 2 hours on black marls longer than soil under forest and grassland. The water infiltration at grassland and forest can be a maximum of 1 hour. The absence of roots and the high clay content in black marls can be plausible reasons.

Other factors like the soil water level on the site influence the water pressure in the soil column and contribute to the soil water behavior. The soil water level was also examined in calibration-validation (Figure 7.10a) and simulation period (Figure 7.11a) to validate the simulated water flow after the precipitation events. The comparison of time lagging between precipitation with water level and precipitation with simulated water content denotes a consistent value. The time lag between precipitation and the soil water level is around 1-2 hours for the Draix study site. Therefore, we deduced that the simulated water content has a good relationship with the precipitation and measured soil water level.

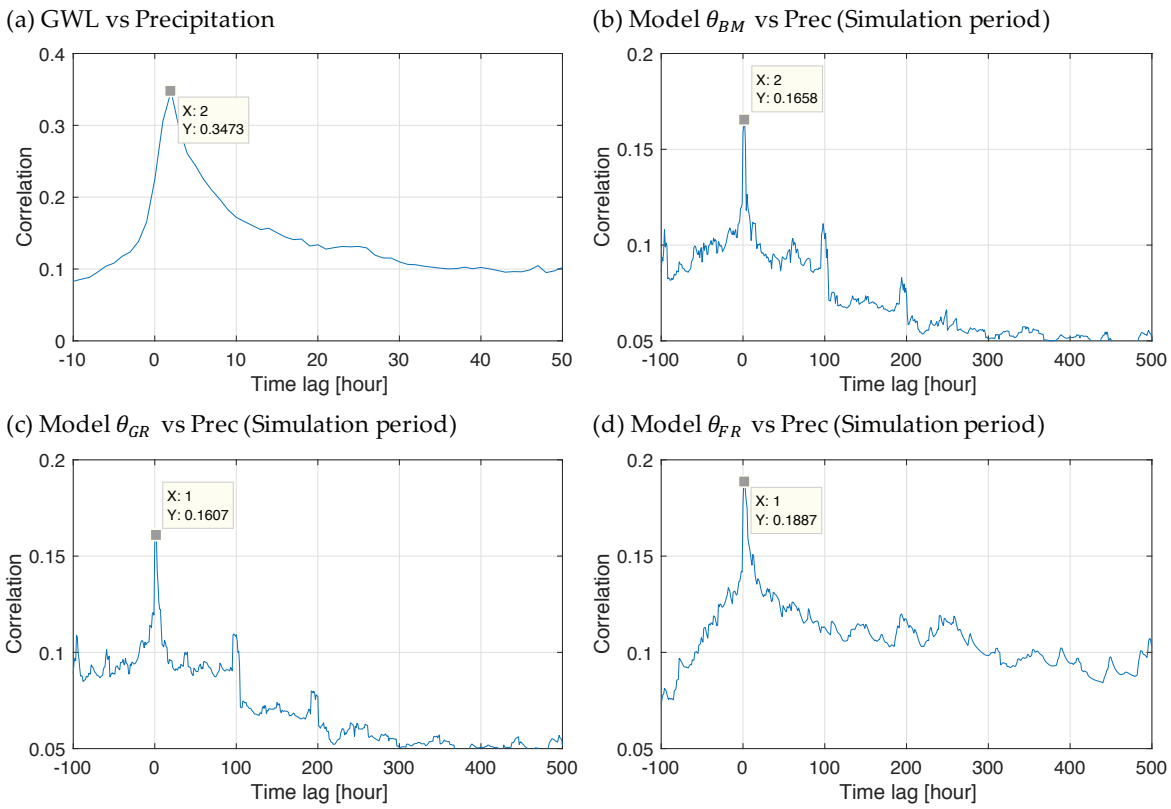

Figure 7.11 Cross-correlation between (a) the precipitation groundwater level. Then, soil water content vs precipitation in the simulation periods. (b) at the black marls, (c) grassland, and (d) soil under the forest.

The second practical simulation was performed during the past historical period. Figure 7.11 shows the cross-correlation between precipitation and soil water content in the past simulation period. Among these other soil behaviors, the black marls have a consistent time lagging and are like the calibration-validation period. Nevertheless, the grassland and soil under the forest have a 1-hour time lag in this simulation period. We deduce that the soil with roots is more dynamic than the black marls without roots. As we know, the appearance of roots influences the volumetric water content besides the clay content. Moreover, the percentage of roots might influence the time of water infiltration.

According to the simulation at hourly time resolution, each soil type's water infiltration was slightly longer for the black marls to infiltrate the water. However, it has a higher hydraulic conductivity than the others. Other than that, the longer time lagging can also be interpreted as a faster drying rate on the surface because the high hydraulic conductivity provokes faster evapotranspiration at the soil surface. Hence, the vertical water flow cannot pass through specific depths.

7.5 Conclusions

The dynamic time series of simulation results show a direct impact of precipitation events on the soil water changes. The evolution of soil water content in Draix during the past time simulation period shows that the optimized parameters are sufficiently well enough for long-term simulation. At 10 cm of soil depth, each soil unit has a different soil-water interaction behavior. The upper soil column between 0 and 10 cm contributes to water infiltration besides the intrinsic soil hydraulic parameters. The existence of roots and clay content on the upper surface can restrain or even increase the water flow rates.

In this historical simulation, the upper and lower soil temperatures as inputs for the atmospheric boundary condition are well predicted using the linear time-invariant and applying the Fourier series method to the soil heat characteristics. However, the damping depth factor should be emphasized carefully. Thus, the phase shifting of temperature penetration from the surface to the bottom side is not neglected. This complexity of steps enables the realistic soil temperature at specific depths.

The assessment of the past time hydrological behavior describes the dynamic soil-water interaction. The simulated soil water content captures the hydrological phenomena such as water flow time lagging that is specific for each soil type at the same depths with sufficient accuracy in the past time simulation to provide the qualitative description of hydrological behavior. Although the simulation result of soil water content was in reasonable agreement with precipitation events and soil water level measurement, the results may need to be more generalized because these are affected by several model simplifications.

Chapter 8: General discussions

8.1 The temperature to soil moisture

The work presented in this thesis relates to the development of fiber optic distributed sensing technologies for long-term soil observation. Numerous antecedent types of research were conducted to extend the understanding of water-flow interaction in macrospores and preferential flow in the soils. Béhaegel, Sailhac and Marquis, (2007) addressed the possibility of fiber optic DTS application in clay-rich soil to assess soil moisture. Soil moisture can be obtained using high-resolution temperature measurement as a proxy parameter. Van de Giesen (2012) has already explained the usage guidelines of fiber optic DTS applications. Double-ended and single-ended configurations were obvious techniques for obtaining the temperature along the fiber optic cable.

Nevertheless, another correction was conducted to reduce the measurement error, especially on the fiber cable directly hit by solar radiation. The quantification of solar radiation on the fiber cable was clearly explained by Sigmund (2017). He presented the influences of solar radiation concerning the aerial coiled-fiber-optic distributed temperature sensing deployments and how to make a correction on it. This technique should be combined with meteorological data observation around the fiber optic deployment.

Unlike soil moisture probe sensors, the fiber optic DTS application can be applied to a wide observation area by spreading the fiber cable. Moreover, the length of fiber cable can reach up to 4 Km with a temperature resolution of 0.8 °C, spatial resolution of 1 m, and acquisition time of 200 seconds (Schenato, 2017). The developed fiber-optic sensors provide a promising alternative in the longest space measurement. In this research, the 354 m fiber cable was buried using a vertical gridding configuration through three soil types: black marls, grassland, and soil under the forest. Each soil was observed at four depth positions: 0 cm, 5 cm, 10 cm, and 15 cm. Statistic and spectrum analyses were used to assess the temperature reading quality. They were applied to certain depth positions. The signal-to-noise ratio indicates that the temperature recorded by fiber optics is pretty good in the annual and diurnal periods. The annual SNR of temperature is more than 50 dB, and the diurnal one is more than 30 dB.

This study found that the temperature strongly influenced the soil type and depth in a series of texture-contrast soils at Draix Bléone. The thermal soil properties lead us to define soil-water interaction. When soils were wet, the soil thermal diffusivity indicated an increasing value. On the other hand, the dry soil indicated the decreasing value of the soil diffusivity. When soils were wet, the soil thermal diffusivity indicated an increasing value. However, the soil diffusivity calculation was not as simple as expected. The difficulty is that the temperature gradient in the time domain also produces the fluctuated diffusivity in the half-diurnal period (see Figure 8.1). Steele-Dunne (2010) used the *fminsearch* function in MATLAB that was applied to window 24-hour temperature measurement to find the diffusivity value. This function minimizes the root-mean-square error between the simulated and observed temperature at a depth of the upper cable. Anyhow, the fluctuated soil diffusivity due to temperature gradient in time can be reduced by signal filtering technique, but this strategy influences the other diffusivity values.

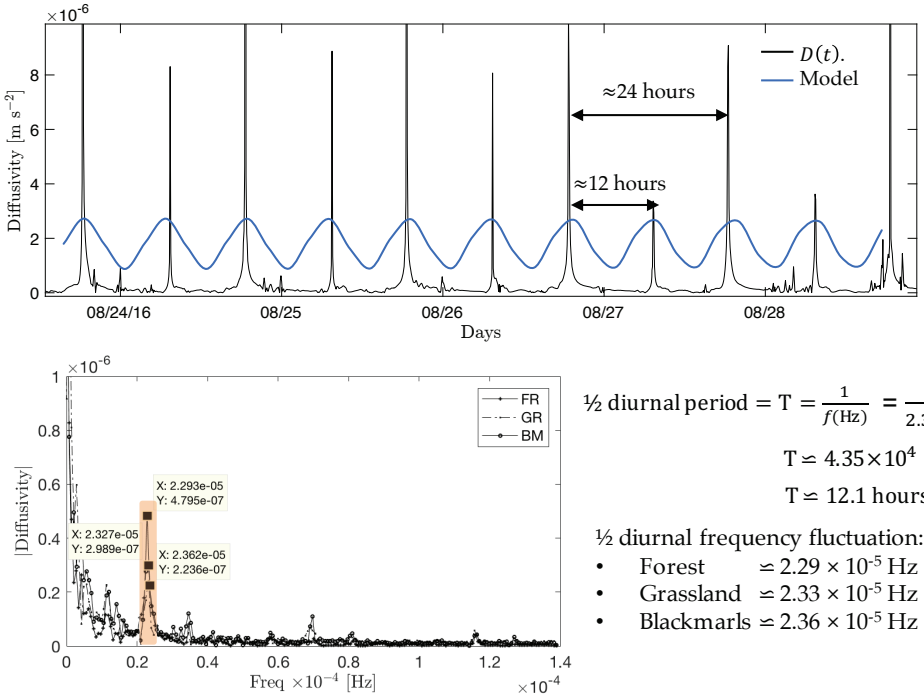

Figure 8.1 Effect of temperature gradient in the morning and the afternoon session on diffusivity calculation that is determined as an artifact inside the diffusivity signal response.

The half-diurnal effect (≈12.1 hours) is always found on calculated diffusivity based on passively heated fiber optic (PHFO) using the sinusoid model. Generally, the diffusivity response enormously increases at sunrise and sunset time. Eventually, the half-diurnal effect is a deterministic artifact inside the diffusivity signal response that should be refined. Therefore, we conclude that the diffusivity time series $D(t)$ contains multiple responses, such as water content and diurnal temperature changes (see Eq 8.1). The aperiodic signal is maintained according to rainfall events and recharges time series.

$$D(t) = D_{rain}(t) + D_{diurnal}(t) + D_{annual}(t) \qquad \text{Eq 8.1}$$

Aperiodic (events) — Periodic Very low frequency

The nonlinear inversion is used to solve the Johansen model (1975) to obtain the soil moisture based on temperature observation, which mathematically relates the soil thermal diffusivity and soil moisture. Kersten coefficient (1949) is also used to solve heat conductivity in a dry and saturated situation. In this work, the soil heat conductivity was obtained by applying nonlinear inversion, which uses actual soil moisture and observed temperature as the input. The soil moisture was measured by a standard soil moisture probe sensor such as EC5 Decagon installed at specific soil types and depths. Besides, the soil moisture EC5-decagon is also used to compare calculated soil moisture based on fiber optic DTS. The nonlinear inversion results that the dry soil conductivity (λ_d) is 0.53 W m^{-1} K^{-1}, soil saturated conductivity (λ_s) is 2.51 W m^{-1} K^{-1} and soil heat capacity (C_s) is 2.8 MJ m^{-3} K^{-1} and the RMSE is 9.3×10^{-8}, and R^2 is 0.85. In general, the value of thermal soil properties that have already been calculated is suitable for clay-rich soil. In the end, the soil diffusivity was obtained for each soil type over time that follows the water infiltration due to rainfall events.

Statistically, the black marls has the highest average soil thermal diffusivity on this observation term, followed by the soil under forest and grassland as the lowest diffusivity. The average diffusivity is 3.8×10^{-7},

2.2×10^{-7}, and 1.8×10^{-7} m^2/s for black marls, the soil under forest and grassland, respectively. Furthermore, this soil diffusivity is proportional to soil moisture following the Johansen model curve. The soil moisture in the black marls is higher than others, especially after a rainfall event. The clay in black marl is 28.66% based on the soil sampling experiment, with the highest clay content.

8.2 The importance of soil moisture in slope hydrology

The interaction of soil, topography, vegetation, and precipitation govern the hydrology in the shallow soil surface. The interlinked soil variability and landscape features are crucial to understanding the soil-water-environment relationship (Becker et al., 2004; Mohanty, 2000). Mohanty (2000) said measuring hydraulic properties cutting across different soil types, slopes, vegetation, and precipitation fields along the slope was scarce, whereas the soil properties might vary. Besides, the water run-off generation is influenced by water flow in macrospores as an essential mechanism of infiltration (Weiler and Naef, 2003). The soil moisture and run-off experiment has already been conducted to explore the switching between climate and soil water balance as the controls over actual evapotranspiration qualitatively and quantitatively by Longobardi and Khaertdinova (2014). He experimented with the terrain feature, which has a smooth 35° slope with a flat area in the upper portion (Longobardi and Khaertdinova, 2014). This experiment aligns with Mohanty and Markus's research to follow up the hill-slope characteristic feature across different soil types.

The presence of roots significantly influenced the water volume infiltration in the soil surface due to clay-rich soil (0-30 cm). Black marls that have less vegetation above show different soil moisture behavior than grassland and soil under the forest that has dense vegetation. Using fiber optic DTS, the calculated soil moisture was obtained from 2016 to the end of 2017. Furthermore, the soil moisture was analyzed in five scenarios: 23 studied months, winter session, summer session, wetting, and drying processes. Statistically, the characterization of black marls has the highest soil moisture than the grassland and soil under forest in the observation period.

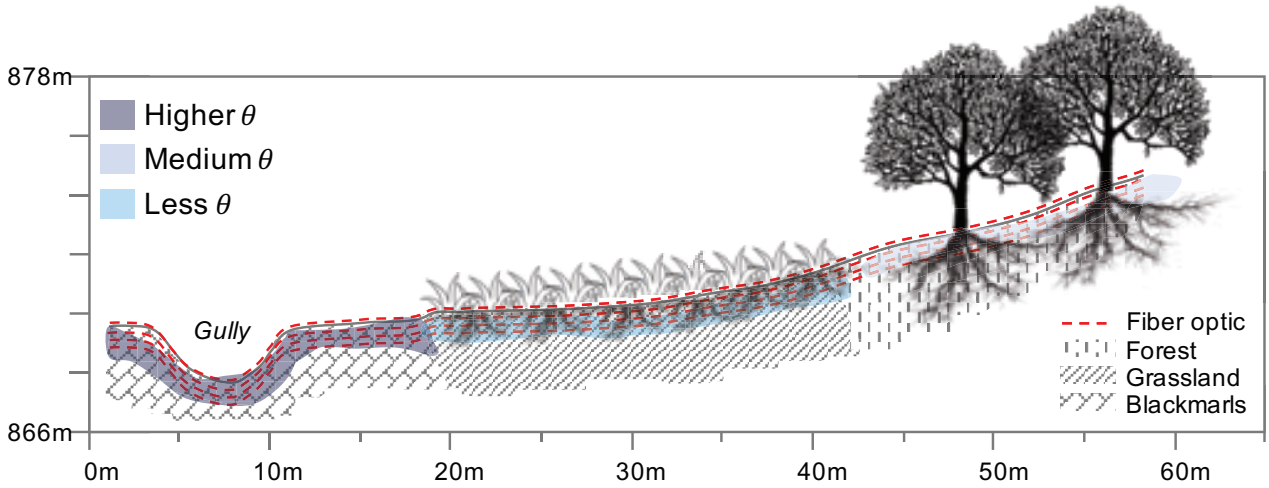

Figure 8.2 Conceptual reconstruction of average soil moisture distribution retained in the effective root zone (0-30 cm).

Figure 8.2 presents the conceptual average soil moisture distribution in slope hydrology based on long-term observation. The average soil moisture in black marls is 0.171 m^3/m^3 in 23 studied months, followed by the soil under forest at 0.136 m^3/m^3 and grassland at 0.119 m^3/m^3. The plausible explanation is that black marls do not have vegetation on the topsoil. Hence, the evapotranspiration rate in the black marls is very low. On the

other hand, the average soil moisture on grassland is lower than the soil in the forest due to the more intensive evapotranspiration process by the grassroots. The soil moisture analysis is not separated from meteorological observation and consists of precipitation, evapotranspiration, air temperature, and wind speed measurements. At the Draix study site, as a Mediterranean climate system, the average daily air temperature ranges from -7.15 to 29.37 °C for winter and summer, respectively, and its highly variable and irregular rainfall regime. Further, the precipitation sensor recorded 343 rain days from January 2016 to April 2018, and the cumulative precipitation was 1913 mm, which is 2.3 mm/day on average. At least two winter storms were reported in November 2016 and December 2017, with a rainfall intensity of more than 70 mm/day.

The results are coherent while the soil thermal diffusivity, calculated soil moisture, and precipitation were compared. The lack of results is a time lag between rain occurrences and calculation responses. These variables give us a better understanding of soil moisture over time and soil types, even for different temperature magnitudes and vegetation conditions. The distributed probability function applied in the winter-summer session and wetting-drying processes phenomenon for each soil unit describes the distinction of soil moisture evidence. The result can be helpful in studies utilizing fiber optics for soil moisture estimation representing water in the catchment scale.

8.3 Soil water modeling and comparison

The determination of soil hydraulic properties has been developed for several years. These soil hydraulic components are primarily based on more or less simple regression analysis (Scheuermann and Bieberstein, 2007). Numerous strategies have been developed to assess hydraulic properties. They were proposed due to the complexity of hydraulic soil assessment in a dynamic field scale (Negm et al., 2017). The soil moisture change concerning matric suction in the unsaturated zone is sensitive to environmental conditions (Fredlund, D.G.; Rahardjo, 1993). This relationship becomes an essential aspect of discovering the soil hydraulic parameters such as air entry pressure, pore size distribution, and soil hydraulic conductivity, especially at the Draix study site, which is a clay-rich soil area and highly reactive to rainfall pulse (Garel et al., 2012; Travelletti et al., 2012).

Two approaches are applied to obtain the optimized soil hydraulic parameters, which can lead us to develop soil water modeling. The first approach is nonlinear inversion on the soil water retention curve (SWRC), which emphasizes calculating the best curve-fitting approach. This method yields the optimized soil hydraulic properties with R^2 around 0.94. The second approach is the Hydrus 1D simulation, which emphasizes calculating the best time series fitting approach. This method yields the optimized soil hydraulic properties with R^2 around 0.92. In addition, the averaged Root Mean Square Error (RMSE) is 0.007 m^3/m^3 for the SWRC model and 0.04 m^3/m^3 for the Hydrus model approach. Both SWRC and Hydrus 1D simulations were tested on the soil under the forest and applied to standard soil moisture measurement, and the soil moisture was calculated based on temperature observation. The testing was run through a dry situation that goes wet due to high rainfall events and the drainage process as a single-cycle infiltration. This experiment result gives preliminary soil hydraulic information at the study site. Furthermore, the soil hydraulic properties are calculated for each soil type to get more specific values from the calculated soil moisture based on temperature observation. The Hydrus 1D software can simultaneously calculate the soil's hydraulic and thermal properties.

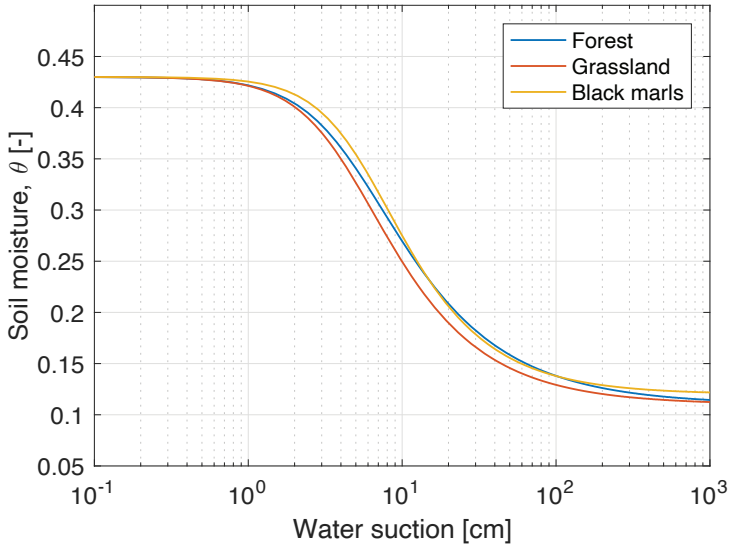

Figure 8.3 Comparison of each soil type's water retention curve model at the Draix study site.

Generally, the value of the optimized parameter is consistent with the experimental particle analyzer that interprets the soil classification. The soil texture determines the particle size distribution, proportioning with the clay, silt, and sand weight. Further, clay is defined by the diameter of a grain less than 2 μm. The simulation yields that the black marls has the lowest air entry pressure (0.04 cm^{-1}) and is appropriate with the soil sampling experiment, which presents 28.66% clay content. In other words, the black marls retain more water than the others.

On the contrary, the soil under the forest has an air entry pressure of about 0.06 cm^{-1}, and it contains only 19.89 % clay, presented by the soil sampling experiment. It means the water can quickly move inside the soil's pores when applying pressure. Nevertheless, the soil under the forest retains the water because it has 51.44% silt, with a grain size diameter range of 2-50 μm. Furthermore, the pore size distribution index of all soil types has values ranging from 1.7 to 2.0, which means that the water will flow relatively in similar pressure conditions, as presented in Figure 8.3.

The long-term soil moisture model is simulated during the hydrological year (2016 to 2018) by Hydrus 1D simulation to simultaneously examine the influence of soil moisture and temperature. The precipitation and soil temperature databases lead the simulation over time. Geometrically, the simulation was designed by using 15 cm of depth and a 0.01 cm grid cell vertically. Then, the upper and lower water flow boundary conditions are atmospheric BC with surface run-off and variable pressure head, respectively. From April until November, soil moisture could be appropriately monitored.

Nevertheless, from December until March, soil moisture seems saturated for all wintertime. The plausible reason for this case is due to a tiny temperature difference for simulating the thermal inversion process. Hence, the overestimated diffusivity when the heat transfer inversion provokes the calculated soil moisture to be saturated value.

Regarding soil moisture comparison, three observation methods, Hydrus simulation, Hymenet soil moisture sensor, and EC5 Decagon soil moisture sensor, present different value levels. However, it was observed in a similar soil type and depth. The comparison is conducted on Florian's experiment using EC5 Decagon from May 2015 to November 2016, the Hydrus simulation from January 2016 to November 2017, and the Hymenet

experiment from January 2017 to November 2017. The maximum soil moisture of EC5 Decagon and Hydrus simulation is relatively similar in the range between 0.39 and 0.43 m^3/m^3, but the Hymenet reaches up to 0.55 m^3/m^3. Further, the minimum soil moisture of EC5 Decagon is 0.22 m^3/m^3, Hydrus simulation is 1.9 m^3/m^3, and Hymenet is 0.31 m^3/m^3. This circumstance presents the soil moisture overestimation on the Hymenet sensor and the underestimation on the Hydrus simulation.

Nevertheless, the Hydrus simulation seems more sensitive to response to the water infiltration according to rainfall events. In terms of low-temperature periods along the winter session, the Hydrus and Hymenet result in the saturated estimation. Otherwise, the EC5 Decagon is more stable as long as the observation period.

8.4 Prediction of historical soil moisture

Calculating the soil moisture to provide information about historical soil water behavior has recently been scrutinized for estimating hydrological and geomorphological investigations. In terms of clay-rich soil, the complexity of both has been concluded by many researchers (Malet et al., 2005). The groundwater evolution in shallow surface, temperature state, and soil-atmosphere interactions was considered to develop a forecasting model (Albertson and Kiely, 2001; Ochsner et al., 2013). The soil surface behavior concerning atmospheric properties, hydrological, and meteorological forecasting models have been developed as a concrete form of extensive application of ecosystem–atmospheric interactions modeling (Pielke et al., 1998). Regarding meteorological or hydrologic forecasting, soil moisture shows promise, but significant spatial and temporal data variability challenges remain.

In Draix's context, most of the earlier studies focused on the current soil erosion and water run-off that is typically controlled by precipitation databases. The historical soil moisture simulation in the past still needs to be improved to build historical predictions and future forecast modeling. Hydrus 1D simulation can be used to estimate the soil moisture prediction over time, but it needs precipitation and soil temperature as boundary conditions. At the same time, the soil historical temperature database is only available at the Draix observatory if precipitation and air temperature databases are used. Therefore, A simple simulation model is proposed to predict the historical soil moisture behavior over time using the precipitation and air temperature databases already measured for long-time observation. Numerous studies have been published to predict soil temperature with depth using soil surface temperature measurement (Barman et al., 2017; Krarti et al., 1995; Oyewole et al., 2018; P. Sharma et al., 2010; Penrod et al., 1960). To simplify the soil temperature prediction, we assume that the soil is a linear system invariant in the time domain, which is easy to implement for time series observation. It enables model generation (Hasfurther et al., 1972).

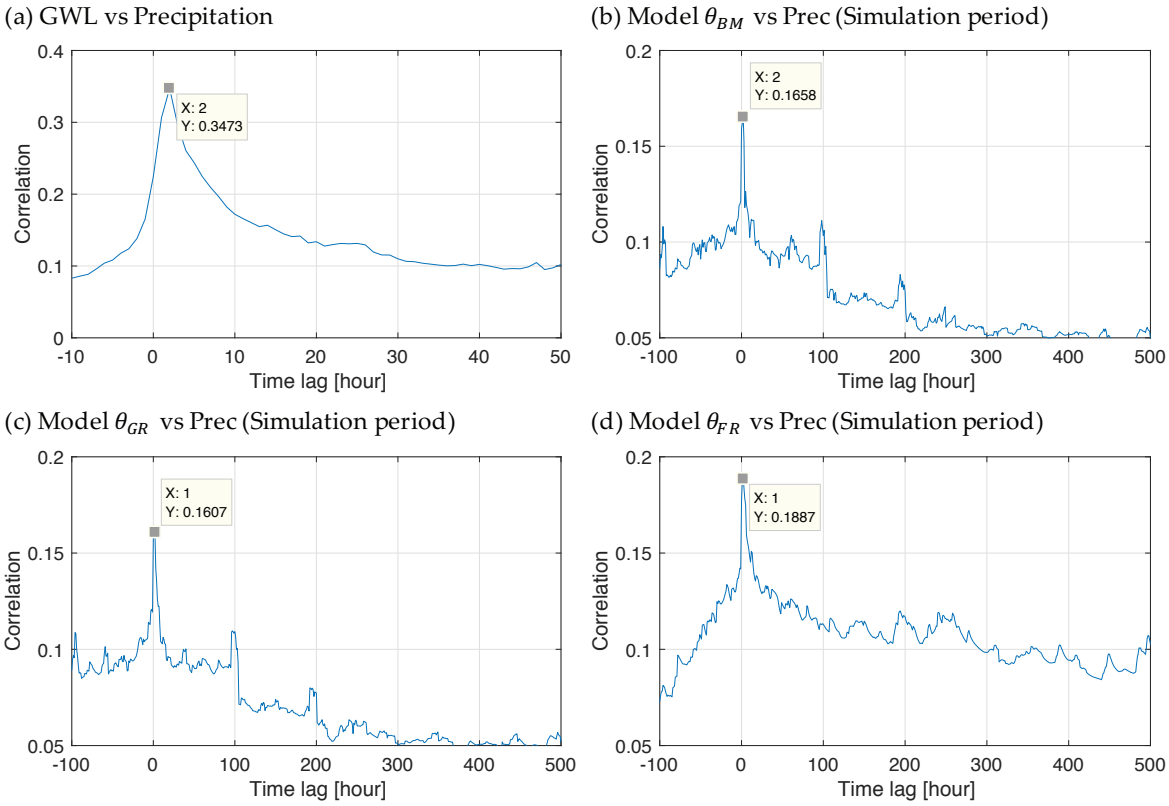

Figure 8.4 Cross-correlation between (a) the precipitation groundwater level. Then, soil moisture vs. precipitation in the 11-year simulation periods (2001 to 2011). (b) at the black marls, (c) grassland, and (d) soil under the forest.

The estimated soil temperature is compared with the observed temperature in the calibration and validation period to analyze the soil temperature estimation method before the method is applied to predict historical soil temperature in amplitude and time variation. The R^2 between measured and predicted soil temperature for all six positions (two depth positions for each soil type, 0 and 15 cm) ranged from 0.91 to 0.94 on calibration (2016) and 0.91 to 0.97 on validation period (Jan 2017 to Apr 2018). Then, the ratio of RMSE between validation and calibration ranged from 1.01 and 2.43. the regression analysis shows that the amplitude of the estimated soil temperature is close to the observed one. In addition, cross-correlation presents that the averaged time lagging both the estimated and the observed temperature is about 0.3 hours or 20 minutes (three times the sampling period, the temperature sampling period is 6 minutes). This situation is still tolerable for hourly simulation (see Figure 8.4).

Furthermore, the historical simulation result shows soil moisture variability from 2001 to 2011. The simulation is run for three soil types: black marls, grassland, and soil under the forest. Generally, the average soil moisture is 0.13 m^3/m^3 for an 11-year simulated period. A wet period is predicted in 2010, with average soil moisture around 0.19 m^3/m^3. On the contrary, the driest soil moisture occurred in 2011, shown by the average soil moisture of around 0.123 m^3m^3. The time lag between precipitation and predicted soil moisture response is examined to describe the water infiltration after rainfall events. The cross-correlation result presents that the water needed around 2 hours for black marls and 1 hour for grassland and soil under the forest to infiltrate along 10 cm of depths in the past.

Regarding flow, the water infiltration was longer in the past than in the calibration and validation period. We deduce that the soil behavior has already changed over time. The erosion and weathering process may change soil-water behavior.

Besides, if we compare the time lagging of each soil type, we will find that the water needs more extended time in black marls than grassland or soil under the forest. This situation occurred not only in the calibration-validation period but also in the historical simulation period. The comparison of time lagging denotes a consistent infiltration time for each soil type. The absence of roots and the high clay content in black marls can be plausible reasons. The examination of the result of the model revealed a satisfactory correspondence between precipitation and soil moisture in the historical simulation provided by time-lagging quantification. Although the simulation result of soil moisture was in reasonable agreement with precipitation events and soil water level measurement, the results may need to be more generalized because these are affected by several model simplifications.

Chapter 9: Conclusions and perspectives

9.1 General conclusion

Knowing water content dynamics in the soil surface provides valuable information on soil-water interaction and groundwater changes. The direct and indirect methods can measure this variability. This thesis discusses the long-term soil temperature observation concerning soil moisture changes over time. Temperature observation is an indirect method to understand the hydrological and thermophysical soil during water flow occurrences. To improve the knowledge regarding soil water interaction in shallow surfaces, fiber optic DTS technology was applied to measure the soil temperature over a long time. This strategy expects to collect more detailed hydrological information. This field experiment considered three soil types: colluvium forest, colluvium bushes or grassland, and black marls. This expectation raises the following question as the research objectives stated in **Chapter 1**:

1. How to monitor the soil moisture and quantify soil hydrological properties based on indirect methods?
2. What information on the tree soil types can we deduce from the spatial and temporal distribution of temperature observation?
3. Can the temperature datasets be used to indirectly calculate the soil hydraulic properties coupled with other variables?
4. Can we understand historical soil behavior based on past time simulation and prediction?

Chapter 2 presents a literature review of fiber optic DTS application for hydrological studies and the basic concept of distributed technology. The technical data treatment is also presented to increase the measurement sensitivity. The temperature correction and calibration are described to avoid measurement error due to internal fiber cable disturbance and external environmental disturbances such as solar radiation. The length of fiber optic has an attenuation along the fiber that reduces the energy excitation of the light throughout the cable. This phenomenon influences the amplitude of Raman back-scattering as a denotation of temperature detection.

The frequency shifting of the light, such as on Brillouin back-scattering, is not a problem. However, the attenuation can disturb the temperature measurement because the Raman back-scattering uses the amplitude shifting of the light. Furthermore, the aerial solar radiation has to be quantified to make a temperature correction for the fiber cable installed on the soil surface. The soil surface installation was designed to measure the interface temperature between air and soil, which is then used for upper boundary conditions on the simulation. However, the specialized data treatment has to be done as a standard procedure of temperature measurement using fiber optic DTS.

Chapter 3 focuses on field observation, data collection, and methods. Draix site is an exciting catchment area. Located in the Alps, Draix was situated between the Alpine and Mediterranean climate systems, which have been studied for several decades. Numerous geoscientists have already researched this area. Generally, the geological setting of Draix is mountainous and dominated by black marls formation called "badland," which is highly affected by climatic conditions.

Consequently, the soil experiences periglacial erosion, contributing to topography and morphology. This chapter describes the permanent installation of fiber optic DTS and other instruments to measure the

hydrological and meteorological parameters. Draix's techno setup is expected to be able to provide high-resolution measurements and demonstrate the importance of sampling resolution on the location. The data collection was measured with a very high resolution. The soil temperature was measured by fiber optic DTS every 6 minutes in 354 m of length, and then the meteorological station operated with 5 minutes per data sampling. Draix's techno setup was equipped with the established network communication that allows remote sensing and monitoring. Hereafter, the observed dataset is processed to estimate the hydrological and thermophysical properties and make the historical simulation. The parameters were estimated using the Hydrus 1D simulation software package and the advanced nonlinear inversion.

Furthermore, a detailed discussion was written in the four chapters. The **Chapter 7** shows the strategy for improving long-term volumetric water content (VWC) estimation accuracy using passively heated fiber optic distributed temperature sensing (FO-DTS). We improve the accuracy of the soil thermal diffusivity calculation using a method combining numerical discretization and signal processing to perform a validation procedure. After simulation and examination, this strategy is convenient for use in passively heated experiments using diurnal heat sources, where reliable thermal diffusivity and VWC data can be obtained without active application sources and with appropriate adjustments to increase its performance.

The **Chapter 5** describes the technical setup of permanent high-resolution temperature observation using FO-DTS to monitor soil water changes in a Mediterranean catchment. The long-term temperature and calculated soil moisture in the time series are also analyzed. This chapter concludes that the time series pattern of the calculated soil moisture, temperature, and precipitation events are coherent. The investigation of seasonal hydrological cycles shows the differences in soil water behavior for each soil type. This preliminary result might give insight into the seasonal influences of the Draix site study.

The **Chapter 6** presents directly modeling soil moisture in the Mediterranean area. Indirect soil moisture measurement needs some inversion method for estimating the optimized parameters. In this case, the air entry pressure, pore size distribution, and hydraulic conductivity were optimized and used on direct modeling to simulate the soil moisture in Draix. The soil hydrological properties are particular for each soil type. Hence, they cannot be generalized due to differences in clay content and other factors. We assume that the soil hydrological properties do not change over time for long-term direct modeling simplification. Hereafter, this article concludes that these experiment simulations addressed that temperature observation as a proxy parameter significantly influences the long-term direct model of soil water changes.

The **Chapter 7** presents the past soil moisture simulations. The direct hydrological model predicts long-term historical soil behavior. The precipitation and air temperature databases are used as the primary input of the simulation. However, the historical soil temperature is unavailable due to unestablished measurements in the past time. Therefore, the LTI system is used to characterize the soil system. It is conducted during the calibration period and then tested during the validation period before it is applied for developing historical soil temperature. Several statistical analyses are used to examine the method. Furthermore, the historical soil temperature can be predicted based on air temperature measurements. The result of the simulation shows that precipitation events have a direct impact on the dynamic time series of soil water changes. The time lagging of soil water flow and temperature propagation to the position of the specific depth is discussed. Although the

simulation result of soil moisture was in reasonable agreement with precipitation events and soil water level measurement, the results may not be generalized because these are affected by several model simplifications.

Finally, this thesis is closed by a general discussion in **Chapter 8**, which addresses long-term temperature observation concerning soil moisture simulation. Some physical properties are described to clarify the three soil types which are studied. **Chapter 9** is made for the conclusion and perspective of the research, which wraps up the thesis manuscript.

9.2 Perspectives

This research work, the application of fiber optic distributed temperature sensing (FODTS) for understanding the shallow surface's groundwater behavior, is ongoing. The following perspectives are recommended for further hydrological research:

- Fiber optics actively heated to track groundwater flow in the hydrological process must be designed further, considering power consumption.
- In the deep groundwater level, the pressure head in the soil vertical soil column should be considered as a factor influencing the soil moisture model, especially in the historical simulation.
- Due to soil morphology alteration, the dynamic hydrological and thermophysical properties should be considered further. As is generally known, high-intensity erosion can occur all the time, which changes the soil properties.

Methodological Perspective on the Use of FO-DTS

In this study, soil temperature data were collected using passive heating FO-DTS. The long-term temperature measurements generally demonstrate good accuracy and reliability. However, measuring soil temperature during winter presented specific challenges. The analysis of soil water content based on winter temperature observations yielded less satisfactory results. In contrast, observations conducted during the summer produced more favorable outcomes. These seasonal differences highlight the impact of environmental conditions on the effectiveness of FO-DTS for soil moisture analysis.

Using passive heating mode in FO-DTS could effectively improve soil temperature observations and soil water content measurements during the summer. Enhancing temperature readings may lead to better data quality in warmer seasons. When applied only at specific times (such as during summer), the passive heating mode in FO-DTS can also help reduce power consumption. This selective use conserves energy while still capturing essential data. Conversely, using the active heating mode in FO-DTS at certain times (such as winter) may improve observation quality. Implementing this mode selectively during colder seasons could address measurement challenges caused by low temperatures. Such a targeted approach allows researchers to optimize data quality and power efficiency across seasons. The combination of passive and active heating modes could enhance FO-DTS application in seasonal soil monitoring.

A heating coil can be applied as an active heating source to support the observation of soil temperature and changes in soil water content using FO-DTS. This setup could provide consistent and reliable temperature data under various conditions. Integrating active and passive heating modes in FO-DTS could offer a

comprehensive approach for year-round monitoring. Researchers can capture accurate measurements throughout different seasons by combining these two heating methods. Such a dual approach may enhance the precision and reliability of soil moisture data. This combination could be precious for long-term, sustainable soil water content monitoring research. Therefore, the active-passive FO-DTS approach is worth considering for future sustainable studies on soil water content.

Methodological Perspective in Observational Data Processing

Estimating changes in soil water content based on soil temperature measurements presents several challenges. One of these challenges is the fluctuation in soil temperature before rainfall events and the variations caused by diurnal cycles. Temperature variability due to diurnal changes can be analyzed using signal processing techniques. A straightforward strategy to reduce the daily response is to apply a band-stop filter to the time series observational data. This filtering method helps isolate the primary signals by removing periodic daily fluctuations. However, temperature variability caused by random noise is much harder to reduce. The most accessible approach for eliminating random temperature responses is through filtering processes. These methods aim to enhance the clarity and reliability of soil temperature data for better soil moisture estimation.

In estimating soil water content based on soil temperature measurements, the Johansen Model (1975) provides a straightforward approach. This method relies on the relationship between soil water content and soil thermal diffusivity. Achieving accurate diffusivity parameters requires careful discretization of geometry and time in the measurement data. The closer the spacing in distance and time for soil temperature measurements, the better the soil water content variability estimates. An inversion method is applied to link soil temperature data with soil thermal diffusivity using a function that minimizes errors. This study's spatial intervals are 50 cm horizontally and 5 cm vertically. In our approach, soil thermal diffusivity is calculated every 6 minutes. Theoretically, this allows for detecting thermal diffusivity and water content changes between two estimations with a 6-minute resolution. In practice, however, the actual resolution of thermal diffusivity and water content is higher and variable, as it depends on the frequency content of the input temperature signal and the thermal diffusivity value itself. Our dataset estimates the minimal resolution to be around 12 hours.

Methodological Perspective in Historical Data Processing and Forecasting

This study considers air and soil temperatures as a linear time-invariant (LTI) system to infer soil water changes. While some LTI parameters may change, the simulation will provide a general understanding of the historical groundwater system. The complexity of past soil water flow patterns often serves as a basis for understanding future environmental processes. Hydrological and geomorphological studies in clay-rich soils have shown that these soils have intricate relationships with water flow. In practice, the behavior of the LTI system creates a time delay between the output and input signals. This time lag may also appear between the measured and predicted soil temperatures. Despite these delays, the simulation results for soil water content show a reasonable correlation with precipitation events and soil moisture measurements. However, the results require careful interpretation due to various model simplifications. These simplifications might limit the broader

application of the findings. Therefore, further adjustments and validations are recommended for a more generalized forecasting model.

Reference

Adams, W.M., Watts, G., Mason, G., 1976. Estimation of thermal diffusivity from field observations of temperature as a function of time and depth. Am. Mineral. 6, 560–568.

Al-kayssi, A.W., Al-karaghouli, A.A., Hasson, A.M., Beker, S.A., 1990. Influence of Soil Moisture Content on Soil Temperature and Heat Storage under Greenhouse Conditions. J. Agric. Eng. Res. 45, 241–252. https://doi.org/10.1016/S0021-8634(05)80152-0

Albertson, J.D., Kiely, G., 2001. On the structure of soil moisture time series in the context of land surface models. J. Hydrol. 243, 101–119. https://doi.org/10.1016/S0022-1694(00)00405-4

An, K., Wang, W., Zhao, Y., Huang, W., Chen, L., Zhang, Z., Wang, Q., Li, W., 2016. Estimation from Soil Temperature of Soil Thermal Diffusivity and Heat Flux in Sub-surface Layers. Boundary-Layer Meteorol. 158, 473–488. https://doi.org/10.1007/s10546-015-0096-7

Antoine, P., Giraud, A., Meunier, M., Van Asch, T., 1995. Geological and geotechnical properties of the "Terres Noires" in southeastern France: Weathering, erosion, solid transport and instability. Eng. Geol. 40, 223–234. https://doi.org/10.1016/0013-7952(95)00053-4

AP Sensing Linear Pro DTS-N4386B, 2013. AP Sensing Linear Pro Series DTS – N4386B User ' s Guide. AP Sensing GmbH, Boeblingen Germany.

Assouline, S., Tessier, D., Bruand, A., 1998. A conceptual model of the soil water retention curve. Water Resour. Res. 34, 223–231.

Bao, X., Chen, L., 2012. Recent progress in distributed fiber optic sensors. Sensors (Basel) 12, 8601–8639. https://doi.org/10.3390/s120708601

Barman, D., Kundu, D.K., Pal, Soumen, Pal, Susanto, Chakraborty, A.K., Jha, A.K., Mazumdar, S.P., Saha, R., Bhattacharyya, P., 2017. Soil temperature prediction from air temperature for alluvial soils in lower Indo-Gangetic plain. Int. Agrophysics 31, 9–22. https://doi.org/10.1515/intag-2016-0034

Bechkit, M.A., Flageul, S., Guerin, R., Tabbagh, A., 2014. Monitoring soil water content by vertical temperature variations. Ground Water 52, 566–72. https://doi.org/10.1111/gwat.12090

Becker, M.W., Georgian, T., Ambrose, H., Siniscalchi, J., Fredrick, K., 2004. Estimating flow and flux of ground water discharge using water temperature and velocity. J. Hydrol. 296, 221–233. https://doi.org/10.1016/j.jhydrol.2004.03.025

Béhaegel, M., Sailhac, P., Marquis, G., 2007. On the use of surface and ground temperature data to recover soil water content information. J. Appl. Geophys. 62, 234–243. https://doi.org/10.1016/j.jappgeo.2006.11.005

Benítez-buelga, J., Sayde, C., Rodríguez-, L., Selker, J.S., 2014. Heated Fiber Optic Distributed Temperature Sensing : A Dual- Probe Heat-Pulse Approach. Vadose Zo. J. 13, vzj2014.02.0014-vzj2014.02.0014. https://doi.org/10.2136/vzj2014.02.0014

Bense, V.F., Read, T., Bour, O., Borgne, T. Le, Coleman, T., Krause, S., Chalari, A., Mondanos, M., Ciocca, F.,

Selker, J.S., 2016. Distributed temperature sensing as a down-hole tool in hydrogeology. Water Resour. Res. 9259–9273. https://doi.org/10.1002/2016WR018869.

Bense, V. F., Read, T., Verhoef, A., 2016. Using distributed temperature sensing to monitor field scale dynamics of ground surface temperature and related substrate heat flux. Agric. For. Meteorol. 220, 207–215. https://doi.org/10.1016/j.agrformet.2016.01.138

Bergvall, M., Grip, H., Sjöström, J., Laudon, H., 2011. Modeling subsurface transport in extensive glaciofluvial and littoral sediments to remediate a municipal drinking water aquifer. Hydrol. Earth Syst. Sci. 15, 2229–2244. https://doi.org/10.5194/hess-15-2229-2011

Beven, K., Germann, P., 1982. Macropores and water flow in soils. Water Resour. Res. 18, 1311–1325. https://doi.org/10.1029/WR018i005p01311

Bogaard, T.A., Antoine, P., Desvarreux, P., Giraud, A., Van Asch, T.W.J., 2000. The slope movements within the Mondores graben (Drome, France); the interaction between geology, hydrology and typology. Eng. Geol. 55, 297–312. https://doi.org/10.1016/S0013-7952(99)00084-8

Bogaard, T.A., Van Asch, T.W.J., 2002. The role of the soil moisture balance in the unsaturated zone on movement and stability of the Beline landslide, France. Earth Surf. Process. Landforms 27, 1177–1188. https://doi.org/10.1002/esp.419

Bohy Provost, C., 2016. Étude de l ' état hydrique des sols en zone de montagne. Avignon.

Bolognini, G., Hartog, A., 2013. Raman-based fibre sensors: Trends and applications. Opt. Fiber Technol. 19, 678–688. https://doi.org/10.1016/j.yofte.2013.08.003

Cambon, Malet., J.P., Esteves, M., Klotz, S., Bouteiller, C. Le, Legout, C., Liebault, F., Mathys, N., Meunier, M., Olivier, J.-E., Richard, D., 2015. Observatoire hydrosedimentaire de montagne Draix-Bleone. Irstea [WWW Document]. URL https://doi.org/10.17180/obs.draix

Campbell, G.S., Calissendorff, C., Williams, J.H., 1991. Probe for measuring soil specific heat using a heat-pulse method. Soil Sci. Soc. Am. J. 55, 291–293.

Campbell, G.S., Norman, J.M., 1998. An Introduction to Envionmental Biophysics, Springer-Verlag New York, Inc.

Caris, J.P.T., Van Asch, T.W.J., 1991. Geophysical, geotechnical and hydrological investigations of a small landslide in the French Alps. Eng. Geol. 31, 249–276. https://doi.org/10.1016/0013-7952(1)90011-9

Carslaw, H.S., Jaeger, J.C., 1959. Conduction of Heat in Solids, 2nd ed. Oxford Univiversity Press, New York.

Castle, R.O., Elliott, R., 1999. Estimation of surface heat flux and an index of soil moisture using adjoint-state surface energy balance. WATER Resour. Res. VOL. 35, 3115–3125.

Castro-Jiménez, J., Berrojalbiz, N., Mejanelle, L., Dachs, J., 2013. Sources, transport and deposition of atmospheric organic pollutants in the mediterranean sea. ACS Symp. Ser. 1149, 231–260. https://doi.org/10.1021/bk-2013-1149.ch011

Chavanne, X., Frangi, J.P., 2017. Autonomous sensors for measuring continuously the moisture and salinity of a porous medium. Sensors (Switzerland) 17, 1–17. https://doi.org/10.3390/s17051094

Chavanne, X., Jean-Pierre, F., 2014. Presentation of a complex permittivity-meter with applications for sensing the moisture and salinity of a porous media. Sensors (Switzerland) 14, 15815–15835. https://doi.org/10.3390/s140915815

Cheng, H., 2014. Fiber optic sensors for metrology , geophysics and strain measurements.

Chung, S. -O, Horton, R., 1987. Soil heat and water flow with a partial surface mulch. Water Resour. Res. 23, 2175–2186. https://doi.org/10.1029/WR023i012p02175

Ciocca, F., Lunati, I., Van de Giesen, N., Parlange, M.B., 2012. Heated Optical Fiber for Distributed Soil-Moisture Measurements: A Lysimeter Experiment. Vadose Zo. J. 11, 0. https://doi.org/10.2136/vzj2011.0199

Clothier, B.E., White, I., 2010. Measurement of Sorptivity and Soil Water Diffusivity in the Field1. Soil Sci. Soc. Am. J. 45, 241. https://doi.org/10.2136/sssaj1981.03615995004500020003x

Corona, C., Lopez Saez, J., Rovéra, G., Stoffel, M., Astrade, L., Berger, F., 2011. High resolution, quantitative reconstruction of erosion rates based on anatomical changes in exposed roots at Draix, Alpes de Haute-Provence - critical review of existing approaches and independent quality control of results. Geomorphology 125, 433–444. https://doi.org/10.1016/j.geomorph.2010.10.030

De Jong, S.A.P., Slingerland, J.D., Van De Giesen, N.C., 2015. Fiber optic distributed temperature sensing for the determination of air temperature. Atmos. Meas. Tech. 8, 335–339. https://doi.org/10.5194/amt-8-335-2015

Dehghan, M., 2004. Weighted finite difference techniques for the one-dimensional advection-diffusion equation. Appl. Math. Comput. 147, 307–319. https://doi.org/10.1016/S0096-3003(02)00667-7

Descroix, L., Claude, J.C., 2002. Spatial and temporal factors of erosion by water of black marls in the badlands of the French southern Alps. Hydrol. Sci. J. 47, 227–242. https://doi.org/10.1080/02626660209492926

Descroix, L., Gautier, E., 2002. Water erosion in the southern French Alps: Climatic and human mechanisms. Catena 50, 53–85. https://doi.org/10.1016/S0341-8162(02)00068-1

Dorleus, J., Zhang, Y., Ning, J., Koscica, T., Li, H., Cui, H.L., 2009. A Fiber Optic Seismic Sensor for Unattended Ground Sensing Applications 30, 455–460.

Durner, W., Lipsius, K., 2005. Determining Soil Hydraulic Properties. Encycl. Hydrol. Sci.

Esteves, M., Descroix, L., Mathys, N., Lapetite, J.M., 2005. Soil hydraulic properties in a marly gully catchment (Draix, France). Catena 63, 282–298. https://doi.org/10.1016/j.catena.2005.06.006

Esteves, M., Faucher, X., Galle, S., Vauclin, M., 2000. Overland flow and infiltration modelling for small plots during unsteady rain: Numerical results versus observed values. J. Hydrol. 228, 265–282. https://doi.org/10.1016/S0022-1694(00)00155-4

Farahani, M.A., Gogolla, T., 1999. Spontaneous Raman scattering in optical fibers with modulated probe light for distributed temperature Raman remote sensing. J. Light. Technol. 17, 1379–1391. https://doi.org/10.1109/50.779159

Fernandez Fernandez, A., Rodeghiero, P., Brichard, B., Berghmans, F., Hartog, A.H., Hughes, P., Williams, K., Leach, A.P., 2005. Radiation-tolerant Raman Distributed Temperature monitoring system for large nuclear infrastructures. IEEE Trans. Nucl. Sci. 52, 2689–2694. https://doi.org/10.1109/TNS.2005.860736

Ficklin, D.L., Letsinger, S.L., Gholizadeh, H., Maxwell, J.T., 2015. Incorporation of the Penman-Monteith potential evapotranspiration method into a Palmer Drought Severity Index Tool. Comput. Geosci. 85, 136–141. https://doi.org/10.1016/j.cageo.2015.09.013

Fredlund, D.G.; Rahardjo, H., 1993. Soil Mechanics for Unsaturated Soils. John Wiley & Sons, Ltd, New York, NY, USA.

Fredlund, D.G., 2006. Unsaturated soil mechanics in engineering practice. J. Geotech. Geoenvironmental Eng. 132, 286–321. https://doi.org/10.1061/(ASCE)1090-0241(2006)132:3(286)

Gaikwad, P., Devendrachari, M.C., Thimmappa, R., Paswan, B., Raja Kottaichamy, A., Makri Nimbegondi Kotresh, H., Thotiyl, M.O., 2015. Galvanic Cell Type Sensor for Soil Moisture Analysis. Anal. Chem. 87, 7439–7445. https://doi.org/10.1021/acs.analchem.5b01653

Gallage, C., Kodikara, J., Uchimura, T., 2013. Laboratory measurement of hydraulic conductivity functions of two unsaturated sandy soils during drying and wetting processes. Soils Found. 53, 417–430. https://doi.org/10.1016/j.sandf.2013.04.004

Gance, J., Malet, J.P., Supper, R., Sailhac, P., Ottowitz, D., Jochum, B., 2016. Permanent electrical resistivity measurements for monitoring water circulation in clayey landslides. J. Appl. Geophys. 126, 98–115. https://doi.org/10.1016/j.jappgeo.2016.01.011

Garel, E., Marc, V., Ruy, S., Cognard-Plancq, A.L., Klotz, S., Emblanch, C., Simler, R., 2012. Large scale rainfall simulation to investigate infiltration processes in a small landslide under dry initial conditions: The Draix hillslope experiment. Hydrol. Process. 26, 2171–2186. https://doi.org/10.1002/hyp.9273

Goran, K., Vesna, C.-B., 2013. A sensor for the measurement of the moisture of undisturbed soil samples. Sensors (Switzerland) 13, 1692–1705. https://doi.org/10.3390/s130201692

Green, J.K., Seneviratne, S.I., Berg, A.M., Findell, K.L., Hagemann, S., Lawrence, D.M., Gentine, P., 2019. Large influence of soil moisture on long-term terrestrial carbon uptake. Nature 565, 476–479. https://doi.org/10.1038/s41586-018-0848-x

Hasfurther, V., Burman, R.D., Nunn, J., 1972. A model for predicting soil temperature from air temperature. Laramie, Wyoming.

Hausner, M.B., Kobs, S., 2016. Identifying and Correcting Step Losses in Single-Ended Fiber-Optic Distributed Temperature Sensing Data. J. Sensors 2016. https://doi.org/10.1155/2016/7073619

Hausner, M.B., Suárez, F., Glander, K.E., van de Giesen, N., Selker, J.S., Tyler, S.W., 2011. Calibrating single-ended fiber-optic raman spectra distributed temperature sensing data. Sensors 11, 10859–10879. https://doi.org/10.3390/s111110859

Henderson-Sellers, A., 1996. Soil moisture: A critical focus for global change studies. Glob. Planet. Change 13,

3–9. https://doi.org/10.1016/0921-8181(95)00034-8

Hilgersom, K., Van Emmerik, T., Solcerova, A., Berghuijs, W., Selker, J., Van De Giesen, N., 2016. Practical considerations for enhanced-resolution coil-wrapped distributed temperature sensing. Geosci. Instrumentation, Methods Data Syst. 5, 151–162. https://doi.org/10.5194/gi-5-151-2016

Hillel, D., 2004. Introduction to Environmental Soil Physics. Elsevier Sci. XXXIII, 81–87. https://doi.org/10.1007/s13398-014-0173-7.2

Hoffman, L., Müller, M.S., Krämer, S., Giebel, M., Schwotzer, G., Wieduwilt, T., 2007. Applications of fibre optic temperature measurement. Proc. Est. Acad. Sci. Eng. 13, 363–378.

Hong, W.T., Jung, Y.S., Kang, S., Lee, J.S., 2016. Estimation of soil-water characteristic curves in multiple-cycles using membrane and TDR system. Materials (Basel). 9. https://doi.org/10.3390/ma9121019

Iverson, R.M., 2000. Landslide triggering by rain infiltration. Water Resour. Res. 36, 1897. https://doi.org/10.1029/2000WR900090

Jansen, J., Stive, P.M., van de Giesen, N., Tyler, S., Steele-Dunne, S.C., Williamson, L., 2011. Estimating soil heat flux using Distributed Temperature Sensing. GRACE, Remote Sens. Ground-based Methods Multi-Scale Hydrol. 140–144.

Jong van Lier, Q. de, Durigon, A., 2013. Soil thermal diffusivity estimated from data of soil temperature and single soil component properties. Rev. Bras. Ciência do Solo 37, 106–112. https://doi.org/10.1590/S0100-06832013000100011

Kato, C., Nishimura, T., Imoto, H., Miyazaki, T., 2010. Applicability of HYDRUS to predict soil moisture and temperature in vadose zone of arable land under monsoonal climate region, Tokyo. 19th World Congr. Soil Sci. Soil Solut. a Chang. World 6–9.

Kauffmann, T.H., Kokanyan, N., Fontana, M.D., 2019. Use of Stokes and anti-Stokes Raman scattering for new applications. J. Raman Spectrosc. 50, 418–424. https://doi.org/10.1002/jrs.5523

Keller, C.A., Huwald, H., Vollmer, M.K., Wenger, A., Hill, M., Parlange, M.B., Reimann, S., 2011. Fiber optic distributed temperature sensing for the determination of the nocturnal atmospheric boundary layer height. Atmos. Meas. Tech. 4, 143–149. https://doi.org/10.5194/amt-4-143-2011

Kersten, M., 1949. Thermal properties of soils. Eng. Exp. Stn. Bull. 1–226.

Koudelka, P., Petrujova, B., Latal, J., Hanacek, F., Siska, P., Skapa, J., Vasinek, V., 2010. Optical fiber distributed sensing system applied in cement concrete commixture research. Radioengineering 19, 172–177.

Krarti, M., Claridge, D.E., Kreider, J.F., 1995. Analytical model to predict nonhomogeneous soil temperature variation. J. Sol. Energy Eng. Trans. ASME 117, 100–107. https://doi.org/10.1115/1.2870823

Krause, S., Taylor, S.L., Weatherill, J., Haffenden, A., Levy, A., Cassidy, N.J., Thomas, P.A., 2013. Fibre-optic distributed temperature sensing for characterizing the impacts of vegetation coverage on thermal patterns in woodlands. Ecohydrology 6, 754–764. https://doi.org/10.1002/eco.1296

Krzeminska, D.M., Steele-Dunne, S.C., Bogaard, T.A., Rutten, M.M., Sailhac, P., Geraud, Y., 2012a. High-resolution temperature observations to monitor soil thermal properties as a proxy for soil moisture

condition in clay-shale landslide. Hydrol. Process. 26, 2143–2156. https://doi.org/10.1002/hyp.7980

Krzeminska, D.M., Steele-Dunne, S.C., Bogaard, T.A., Rutten, M.M., Sailhac, P., Geraud, Y., 2012b. High-resolution temperature observations to monitor soil thermal properties as a proxy for soil moisture condition in clay-shale landslide. Hydrol. Process. 26, 2143–2156. https://doi.org/10.1002/hyp.7980

Lane, J.W., Day-lewis, F.D., Johnson, C.D., Dawson, C.B., Nelms, D.L., Eddy-miller, C.A., Wheeler, J.D., Harvey, C.F., 2008. Fiber-optic distributed temperature sensing: A new tool for assessment and monitoring of hydrologic processes. Symp. Appl. Geophys. to Eng. Environ. Probl. Philadelph, 1–9. https://doi.org/10.4133/1.2963272

Lehmann, P., Or, D., 2012. Hydromechanical triggering of landslides: From progressive local failures to mass release. Water Resour. Res. 48, 1–24. https://doi.org/10.1029/2011WR010947

Lienhart, W., 2015. Case studies of high-sensitivity monitoring of natural and engineered slopes. J. Rock Mech. Geotech. Eng. 7, 379–384. https://doi.org/10.1016/j.jrmge.2015.04.002

Liu, Y.-Z., Ou, Z.-H., Dai, Z.-Y., Zhang, L.-X., Zhou, C., 2008. Landslide monitoring based on high-resolution distributed fiber optic stress sensor. Proc. 1st Asia-Pacific Opt. Fiber Sensors Conf. APOS '08 6, 1–4. https://doi.org/10.1109/APOS.2008.5226289

Longobardi, A., Khaertdinova, E., 2014. Relating soil moisture and air temperature to evapotranspiration fluxes during inter-storm periods at a Mediterranean experimental site. J. Arid Land 7, 27–36. https://doi.org/10.1007/s40333-014-0075-8

Malet, J.-P., van Asch, T.W.J., van Beek, R., Maquaire, O., 2005. Forecasting the behaviour of complex landslides with a spatially distributed hydrological model. Nat. Hazards Earth Syst. Sci. 5, 71–85. https://doi.org/10.5194/nhess-5-71-2005

Mallet, M.F., 2018. Spatialisation et modélisation de l ' état hydrique des sols pour l ' étude des processus de formation des écoulements en contexte torrentiel : application au bassin versant marneux du Laval (ORE Draix-Bléone , Alpes-De-Haute-Provence , France) To cite .

Mamer, E.A., Lowry, C.S., 2013. Locating and quantifying spatially distributed groundwater / surface water interactions using temperature signals with paired fiber-optic cables 49, 7670–7680. https://doi.org/10.1002/2013WR014235

Maquaire, O., Malet, J.P., Remaître, A., Locat, J., Klotz, S., Guillon, J., 2003. Instability conditions of marly hillslopes: Towards landsliding or gullying? The case of the Barcelonnette Basin, South East France. Eng. Geol. 70, 109–130. https://doi.org/10.1016/S0013-7952(03)00086-3

Maquaire, O., Ritzenthaler, A., Fabre, D., Ambroise, B., Thiery, Y., Truchet, E., Malet, J.P., Monnet, J., 2002. Caractérisation des profils de formations superficielles par pénétrométrie dynamique à énergie variable: Application aux marnes noires de Draix (Alpes-de-Haute-Provence, France). Comptes Rendus - Geosci. 334, 835–841. https://doi.org/10.1016/S1631-0713(02)01788-1

Marasigan, R.A., Olivar, R.E.R., 2015. Distributing Access to Geohazard Information Using Web GIS for EDC Geothermal Field Sites. World Geotherm. Congr. 2015 19–25.

Marc, V., Bertrand, C., Malet, J.P., Carry, N., Simler, R., Cervi, F., 2017a. Groundwater—Surface waters interactions at slope and catchment scales: implications for landsliding in clay-rich slopes. Hydrol. Process. 31, 364–381. https://doi.org/10.1002/hyp.11030

Marc, V., Bertrand, C., Malet, J.P., Carry, N., Simler, R., Cervi, F., 2017b. Groundwater—Surface waters interactions at slope and catchment scales: implications for landsliding in clay-rich slopes. Hydrol. Process. 31, 364–381. https://doi.org/10.1002/hyp.11030

Martin, R., 2016. Etude de l ' ét at hydrique des sols en zone de montagne . Avignon.

Mathys, N., Brochot, S., Meunier, M., Richard, D., 2003. Erosion quantification in the small marly experimental catchments of Draix (Alpes de Haute Provence, France). Calibration of the ETC rainfall-runoff-erosion model. Catena 50, 527–548. https://doi.org/10.1016/S0341-8162(02)00122-4

Mathys, N., Klotz, S., Esteves, M., Descroix, L., Lapetite, J.M., 2005. Runoff and erosion in the Black Marls of the French Alps: Observations and measurements at the plot scale. Catena 63, 261–281. https://doi.org/10.1016/j.catena.2005.06.010

Mittelbach, H., Lehner, I., Seneviratne, S.I., 2012. Comparison of four soil moisture sensor types under field conditions in Switzerland. J. Hydrol. 430–431, 39–49. https://doi.org/10.1016/j.jhydrol.2012.01.041

Mohanty, B.P., 2000. Saturated hydraulic conductivity and soil water retention properties across a soil-slope transition orthogonal. Water Resour. Res. 36, 3311–3324.

Monsberger, C., Woschitz, H., Hayden, M., 2016. Deformation Measurement of a Driven Pile Using Distributed Fibre-optic Sensing, Journal of Applied Geodesy. Vienna. https://doi.org/10.1515/jag-2015-0021

Mualem, Y., 1978. Hydraulic conductivity of unsaturated porous media: Generalized macroscopic appraoch. Water Resour. Res. 14, 325–334.

Negm, A., Capodici, F., Ciraolo, G., Maltese, A., Provenzano, G., Rallo, G., 2017. Assessing the performance of thermal inertia and Hydrus models to estimate surface soil water content. Appl. Sci. 7, 1–16. https://doi.org/10.3390/app7100975

Neilson, B.T., Hatch, C.E., Ban, H., Tyler, S.W., 2010. Solar radiative heating of fiber-optic cables used to monitor temperatures in water. Water Resour. Res. 46, 1–17. https://doi.org/10.1029/2009WR008354

Nikles, M., Vogel, B., Briffod, F., Grosswig, S., Sauser, F., Luebbecke, S., Bals, A., Pfeiffer, T., 2004. Leakage detection using fiber optics distributed temperature monitoring. Symp. A Q. J. Mod. Foreign Lit.

O'Donnell Meininger, T., Selker, J.S., 2015. Bed conduction impact on fiber optic distributed temperature sensing water temperature measurements. Geosci. Instrumentation, Methods Data Syst. 4, 19–22. https://doi.org/10.5194/gi-4-19-2015

Ochsner, T.E., Cosh, M.H., Cuenca, R.H., Dorigo, W. a., Draper, C.S., Hagimoto, Y., Kerr, Y.H., Njoku, E.G., Small, E.E., Zreda, M., 2013. State of the Art in Large-Scale Soil Moisture Monitoring. Soil Sci. Soc. Am. J. 77, 1888. https://doi.org/10.2136/sssaj2013.03.0093

Oh, S., Kim, Y.K., Kim, J.W., 2015. A modified van Genuchten-Mualem model of hydraulic conductivity in Korean residual soils. Water (Switzerland) 7, 5487–5502. https://doi.org/10.3390/w7105487

Oostwoud Wijdenes, D.J., Ergenzinger, P., 1998. Erosion and sediment transport on steep marly experimental field study. Catena 33, 179–200.

Otto, R.G., Gerking, S.D., 1973. Heat tolerance of a Death Valley pupfish (genus Cyprinodon). Physiol. Zool. 46, 43–49.

Oyewole, J., Olasupo, T., Akinpelu, J., Faboro, E., 2018. Prediction of Soil Temperature at Various Depths Using a Mathematical Model. J. Appl. Sci. Environ. Manag. 22, 1417. https://doi.org/10.4314/jasem.v22i9.09

P. Sharma, M. K. Shukla, T. W. Sammis, 2010. Predicting Soil Temperature Using Air Temperature and Soil, Crop, and Meteorological Parameters for Three Specialty Crops in Southern New Mexico. Appl. Eng. Agric. 26, 47–58. https://doi.org/10.13031/2013.29474

Paulsson, B.N.P., Toko, J.L., Thornburg, J.A., Slopko, F., He, R., Zhang, C., 2013. A HIGH PERFORMANCE FIBER OPTIC SEISMIC SENSOR SYSTEM.

Peñarrocha, D., Estrela, M.J., Millán, M., 2002. Classification of daily rainfall patterns in a Mediterranean area with extreme intensity levels: The Valencia region. Int. J. Climatol. 22, 677–695. https://doi.org/10.1002/joc.747

Penrod, E.B., Elliott, J.M., Brown, W.K., 1960. Soil temperature variation (1952–1956) at lexington, kentucky. Soil Sci. 90, 275–283. https://doi.org/10.1097/00010694-196011000-00003

Peterson, A.M., Helgason, W.D., Ireson, A.M., 2016. Estimating field-scale root zone soil moisture using the cosmic-ray neutron probe. Hydrol. Earth Syst. Sci. 20, 1373–1385. https://doi.org/10.5194/hess-20-1373-2016

Pielke, R.A., Avissar, R., Raupach, M., Dolman, A.J., Zeng, X., Denning, A.S., 1998. Interactions between the atmosphere and terrestrial ecosystems: influence on weather and climate. Glob. Chang. Biol. 4, 461–475. https://doi.org/10.1046/j.1365-2486.1998.00176.x

Raffelli, G., Previati, M., Canone, D., Gisolo, D., Bevilacqua, I., Capello, G., Biddoccu, M., Cavallo, E., Deiana, R., Cassiani, G., Ferraris, S., 2017. Local- and plot-scale measurements of soil moisture: Time and spatially resolved field techniques in plain, hill and mountain sites. Water (Switzerland) 9. https://doi.org/10.3390/w9090706

Rassam, D., Šim, J., Genuchten, M.T. Van, 2003. Modelling Variably Saturated Flow with Hydrus-2D. Brisbane.

Richard, D., Mathys, N., 1999. Historique, contexte technique et scientifique des BVRE de Draix. Caractéristiques, données disponibles et principaux résultats acquis au cours des dix ans de suivi. Les bassins versants expérimentaux Draix, Lab. d'étude l'érosion en Mont. 11–28.

Riggs, A.C., Deacon, J.E., 2002. Connectivity in desert aquatic ecosystems : The Devils Hole Story. Spring-fed Wetl. Important Sci. Cult. Resour. Intermt. Reg.

Rizkalla, S.H., 1997. Fiber-optic Bragg Grating Sensors for Bridge Monitoring 19, 21–33.

Rogers, A., 1999. Distributed optical-fibre sensing. Meas. Sci. Technol. 10, R75–R99.

Ross, P.J., 2014. Estimation of Soil Thermal Properties in Two and Three Dimensions. Vadose Zo. J. 13,

vzj2013.07.0143-vzj2013.07.0143.

Rovéra, G., Robert, Y., 2005. Winter Climatic Conditions and Periglacial Erosion Processes in the CONDITIONS CLIMATIQUES HIVERNALES ET PROCESSUS D ' É ROSION P É RIGLACIAIRES DANS LES BAD-LANDS. Géographie Phys. Quat. 59, 31–48.

Rutten, M.M., Steele-Dunne, S.C., Judge, J., van de Giesen, N., 2010. Understanding Heat Transfer in the Shallow Subsurface Using Temperature Observations. Vadose Zo. J. 9, 1034. https://doi.org/10.2136/vzj2009.0174

Sándor, R., Fodor, N., 2012. Simulation of soil temperature dynamics with models using different concepts. Sci. World J. 2012. https://doi.org/10.1100/2012/590287

Sayde, C., Buelga, J.B., Rodriguez-Sinobas, L., El Khoury, L., English, M., Van De Giesen, N., Selker, J.S., 2014. Mapping variability of soil water content and flux across 1-1000 m scales using the actively heated fiber optic method. Water Resour. Res. 50, 7302–7317. https://doi.org/10.1002/2013WR014983

Sayde, C., Gregory, C., Gil-Rodriguez, M., Tufillaro, N., Tyler, S., Van De Giesen, N., English, M., Cuenca, R., Selker, J.S., 2010. Feasibility of soil moisture monitoring with heated fiber optics. Water Resour. Res. 46, 1–8. https://doi.org/10.1029/2009WR007846

Sayde, C., Thomas, C.K., Wagner, J., Selker, J., 2015. High-resolution wind speed measurements using actively heated fiber optics. Geophys. Res. Lett. 42, 10064–10073. https://doi.org/10.1002/2015GL066729

Schaap, M.G., Van Genuchten, M.T., 2006. A modified Mualem-van Genuchten formulation for improved description of the hydraulic conductivity near saturation. Vadose Zo. J. 5, 27–34. https://doi.org/10.2136/vzj2005.0005

Schenato, L., 2017. A Review of Distributed Fibre Optic Sensors for Geo-Hydrological Applications, Applied Sciences. https://doi.org/10.3390/app7090896

Schenato, L., Palmieri, L., Camporese, M., Bersan, S., Cola, S., Pasuto, A., Galtarossa, A., Salandin, P., Simonini, P., 2017. Distributed optical fibre sensing for early detection of shallow landslides triggering. Sci. Rep. 7, 1–7. https://doi.org/10.1038/s41598-017-12610-1

Scheuermann, A., Bieberstein, A., 2007. Determination of the Soil Water Retention Curve and the Unsaturated Hydraulic Conductivity from the Particle Size Distribution. Exp. Unsaturated Soil Mech. Springer Proc. Phys. Vol. 112 112, 421–433. https://doi.org/10.1007/3-540-69873-6

Selker, J., van de Giesen, N.C., Westhoff, M., Luxemburg, W., Parlange, M.B., 2006. Fiber optics opens window on stream dynamics. Geophys. Res. Lett. 33, 6–9. https://doi.org/10.1029/2006GL027979

Selker, J.S., Thévenaz, L., Huwald, H., Mallet, A., Luxemburg, W., Van De Giesen, N., Stejskal, M., Zeman, J., Westhoff, M., Parlange, M.B., 2006. Distributed fiber-optic temperature sensing for hydrologic systems. Water Resour. Res. 42, 1–8. https://doi.org/10.1029/2006WR005326

Seneviratne, S.I., Corti, T., Davin, E.L., Hirschi, M., Jaeger, E.B., Lehner, I., Orlowsky, B., Teuling, A.J., 2010. Investigating soil moisture-climate interactions in a changing climate: A review. Earth-Science Rev. 99, 125–161. https://doi.org/10.1016/j.earscirev.2010.02.004

Seyfried, M., Link, T., Marks, D., Murdock, M., 2016. Soil Temperature Variability in Complex Terrain Measured

Using Fiber-Optic Distributed Temperature Sensing. Vadose Zo. J. 15, 1–18. https://doi.org/10.2136/vzj2015.09.0128

Sigmund, A., Pfister, L., Sayde, C., Thomas, C.K., 2017. Quantitative analysis of the radiation error for aerial coiled-fiber-optic distributed temperature sensing deployments using reinforcing fabric as support structure. Atmos. Meas. Tech. 10, 2149–2162. https://doi.org/10.5194/amt-10-2149-2017

Šimůnek, J., Šejna, M., Saito, H., Sakai, M., Genuchten, M.T. van, 2013. The HYDRUS-1D Software Package for Simulating the One-Dimensional Movement of Water, Heat, and Multiple Solutes in Variably-Saturated Media. RIVERSIDE, CALIFORNIA.

Šimůnek, J., Van Genuchten, M.T., 1997. Estimating unsaturated soil hydraulic properties from multiple tension disc infiltrometer data. Soil Sci. 162, 383–398. https://doi.org/10.1097/00010694-199706000-00001

Smettem, K.R.J., Ross, P.J., 1992. Measurement and prediction of water movement in a field soil: The matrix-macropore dichotomy. Hydrol. Process. 6, 1–10. https://doi.org/10.1002/hyp.3360060102

Steele-Dunne, S.C., Rutten, M.M., Krzeminska, D.M., Hausner, M., Tyler, S.W., Selker, J., Bogaard, T.A., Van De Giesen, N.C., 2010. Feasibility of soil moisture estimation using passive distributed temperature sensing. Water Resour. Res. 46, 1–12. https://doi.org/10.1029/2009WR008272

Stoddart, P.R., Cadusch, P.J., Pearce, J.B., Vukovic, D., Nagarajah, C.R., Booth, D.J., 2005. Fibre optic distributed temperature sensor with an integrated background correction function. Meas. Sci. Technol. 16, 1299–1304. https://doi.org/10.1088/0957-0233/16/6/009

Striegl, A.M., Loheide, S.P., 2012. Heated Distributed Temperature Sensing for Field Scale Soil Moisture Monitoring. Ground Water 50, 340–347. https://doi.org/10.1111/j.1745-6584.2012.00928.x

Suárez, F., Hausner, M.B., Dozier, J., Selker, J.S., Tyler, S.W., 2011. Heat Transfer in the Environment : Development and Use of Fiber-optic Distributed Temperature Sensing.

Susanto, K., Malet, J.-P., Gance, J., Marc, V., 2017. Fiber Optics Distributed Temperature Sensing (FO-DTS) for long-term monitoring of soil water changes in the subsoil, in: EAGE/DGG Workshop on Fibre Optic Technology in Geophysics. Postdam.

Thomas, C.K., Kennedy, A.M., Selker, J.S., Moretti, A., Schroth, M.H., Smoot, A.R., Tufillaro, N.B., Zeeman, M.J., 2012. High-Resolution Fibre-Optic Temperature Sensing: A New Tool to Study the Two-Dimensional Structure of Atmospheric Surface-Layer Flow. Boundary-Layer Meteorol. 142, 177–192. https://doi.org/10.1007/s10546-011-9672-7

Travelletti, J., Sailhac, P., Malet, J.P., Grandjean, G., Ponton, J., 2012. Hydrological response of weathered clay-shale slopes: Water infiltration monitoring with time-lapse electrical resistivity tomography. Hydrol. Process. 26, 2106–2119. https://doi.org/10.1002/hyp.7983

Tyler, S.W., Selker, J.S., Hausner, M.B., Hatch, C.E., Torgersen, T., Thodal, C.E., Schladow, S.G., 2009. Environmental temperature sensing using Raman spectra DTS fiber-optic methods. Water Resour. Res. 45, W00D23. https://doi.org/10.1029/2008WR007052

Ukil, A., Braendle, H., Krippner, P., 2012. Distributed temperature sensing: Review of technology and applications. IEEE Sens. J. 12, 885–892. https://doi.org/10.1109/JSEN.2011.2162060

van de Giesen, N., Steele-Dunne, S.C., Jansen, J., Hoes, O., Hausner, M.B., Tyler, S., Selker, J., 2012a. Double-ended calibration of fiber-optic raman spectra distributed temperature sensing data. Sensors (Switzerland) 12, 5471–5485. https://doi.org/10.3390/s120505471

van de Giesen, N., Steele-Dunne, S.C., Jansen, J., Hoes, O., Hausner, M.B., Tyler, S., Selker, J., 2012b. Double-ended calibration of fiber-optic raman spectra distributed temperature sensing data. Sensors (Switzerland) 12, 5471–5485. https://doi.org/10.3390/s120505471

van Genuchtan M, T., 1980. A closed form equation for predicting the hydraulic conductivity of unsaturated soils. Soil Sci. Soc. Am.

Vandersteen, G., Schneidewind, U., Anibas, C., Schmidt, C., Seuntjens, P., Batelaan, O., 2015. Determining groundwater-surface water exchange from temperature-time series: Combining a local polynomial method with a maximum likelihood estimator. J. Am. Water Resour. Assoc. 5, 922–393.

Vandervaere, J.-P., Vauclin, M., Elrick, D.E., 2000. Transient flow from tension infiltrometers: II. Four methods to determine sorptivity and conductivity. Soil Sci. Soc. Am. J. 64, 1272–1284. https://doi.org/10.2136/sssaj2000.6441272x

Vercauteren, N., Huwald, H., Bou-zeid, E., Selker, J.S., Lemmin, U., Parlange, M.B., Lunati, I., 2011. Evolution of superficial lake water temperature profile under diurnal radiative forcing 47, 1–10. https://doi.org/10.1029/2011WR010529

Vereecken, H., Huisman, J.A., Bogena, H., Vanderborght, J., Vrugt, J.A., Hopmans, J.W., 2008. On the value of soil moisture measurements in vadose zone hydrology: A review. Water Resour. Res. 46, 1–21. https://doi.org/10.1029/2008WR006829

Vogt, T., Schirmer, M., Cirpka, O.A., 2012. Investigating riparian groundwater flow close to a losing river using diurnal temperature oscillations at high vertical resolution. Hydrol. Earth Syst. Sci. 16, 473–487. https://doi.org/10.5194/hess-16-473-2012

Weiler, M., Naef, F., 2003. An experimental tracer study of the role of macropores in infiltration in grassland soils. Hydrol. Process. 17, 477–493. https://doi.org/10.1002/hyp.1136

Weiss, J.D., 2003. Using fiber optics to detect moisture intrusion into a landfill cap consisting of a vegetative soil barrier. J. Air Waste Manag. Assoc. 53, 1130–1148. https://doi.org/10.1080/10473289.2003.10466268

Weng, Y., Qiao, X., Guo, T., Hu, M., Feng, Z., Wang, R., 2011. A Robust and Compact Fiber Bragg Grating Vibration Sensor for Seismic Measurement 12, 800–804.

Westhoff, M.C., Savenjie, H.H.G., Luxemburg, W.M.J., Stelling, G.S., Van De Giesen, N.C., Selker, J.S., Pfister, L., Uhlenbrook, S., 2007. A distributed stream temperature model using high resolution temperature observations. Hydrol. Earth Syst. Sci. 11, 1469–1480. https://doi.org/10.5194/hess-11-1469-2007

Wildung, R.E., Garland, T.R., Buschbom, R.L., 1975. The interdependent effects of soil temperature and water content on soil respiration rate and plant root decomposition in arid grassland soils. Soil Biol. Biochem. 7,

373–378. https://doi.org/10.1016/0038-0717(75)90052-8

Yilmaz, G., Karlik, S.E., 2006. A distributed optical fiber sensor for temperature detection in power cables. Sensors Actuators, A Phys. 125, 148–155. https://doi.org/10.1016/j.sna.2005.06.024

Zeni, L., Picarelli, L., Avolio, B., Coscetta, A., Papa, R., Zeni, G., Di Maio, C., Vassallo, R., Minardo, A., 2015. Brillouin optical time-domain analysis for geotechnical monitoring. J. Rock Mech. Geotech. Eng. 7, 458–462. https://doi.org/10.1016/j.jrmge.2015.01.008

Zhou, D.P., Li, W., Chen, L., Bao, X., 2013. Distributed temperature and strain discrimination with stimulated brillouin scattering and rayleigh backscatter in an optical fiber. Sensors (Switzerland) 13, 1836–1845. https://doi.org/10.3390/s130201836

Zribi, M., Paris Anguela, T., Duchemin, B., Lili, Z., Wagner, W., Hasenauer, S., Chehbouni, a., 2010. Relationship between soil moisture and vegetation in the Kairouan plain region of Tunisia using low spatial resolution ;our. Res. 46,